Micro-deformation and Texture in Engineering Materials

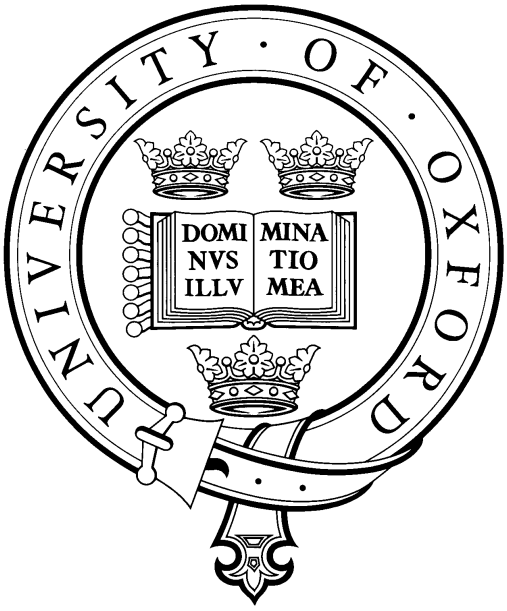
Robert Kiwanuka

Christ Church

Solid Mechanics and Materials Engineering Research Group

Department of Engineering Science

University of Oxford



A thesis submitted for the degree of

Doctor of Philosophy

Supervisor: Prof. F.P.E Dunne

Co-Supervisor: Prof. J. Lin (Imperial)

Hilary Term 2013

Micro-deformation and Texture in Engineering Materials

Robert Kiwanuka

Christ Church

Submitted for Doctor of Philosophy

Hilary 2013

This DPhil project is set in the context of single crystal elasticity-plasticity finite element modelling. Its core objective was to develop and implement a methodology for predicting the evolution of texture in single and dual-phase material systems. This core objective has been successfully achieved. Modelling texture evolution entails essentially modelling large deformations (as accurately as possible) and taking account of the deformation mechanisms that cause texture to change. The most important deformation mechanisms are slip and twinning. Slip has been modelled in this project and care has been taken to explore conditions where it is the dominant deformation mechanism for the materials studied. Modelling slip demands that one also models dislocations since slip is assumed to occur by the movement of dislocations. In this project a model for geometrically necessary dislocations has been developed and validated against experimental measurements.

A texture homogenisation technique which relies on interpretation of EBSD data in order to allocate orientation frequencies based on representative area fractions has been developed. This has been coupled with a polycrystal plasticity RVE framework allowing for arbitrarily sized RVEs and corresponding allocation of crystallographic orientation. This has enabled input of experimentally measured initial textures into the CPFE model allowing for comparison of predictions against measured post-deformation textures, with good agreement obtained. The effect of texture on polycrystal physical properties has also been studied. It has been confirmed that texture indeed has a significant role in determining the average physical properties of a polycrystal.

The thesis contributes to the following areas of micro-mechanics materials research: (i) 3D small deformation crystal plasticity finite element (CPFE) modelling, (ii) geometrically necessary dislocation modelling, (iii) 3D large deformation CPFE modelling, (iv) texture homogenisation methods, (v) single and dual phase texture evolution modelling, (vi) prediction of polycrystal physical properties, (vii) systematic calibration of the power law for slip based on experimental data, and (viii) texture analysis software development (pole figures and Kearns factors).

Contents

Acknowledgements **5**

1 Introduction **8**
1.1 Texture representation . . . 10
1.1.1 Pole figures . . . 10
1.1.2 Orientation distribution functions . . . 11
1.1.3 Kearns texture factors . . . 13
1.2 Deformation mechanisms . . . 14
1.2.1 Deformation by slip . . . 15
1.2.2 Slip versus twinning . . . 17
1.3 Texture evolution modelling . . . 19
1.3.1 Reference frames and crystal plasticity . . . 19
1.3.2 Grain interaction models . . . 21
1.3.3 Updating crystal orientation . . . 24

2 Large deformation theory **28**
2.1 Executive summary . . . 28
2.2 The Problem . . . 28
2.3 Tangent Stiffness Matrix $\boldsymbol{K}_T$ . . . 29
2.3.1 $\boldsymbol{K}_T$ with respect to other stress and strain measures . . . 35
2.4 Implicit Integration of constitutive equations . . . 38
2.5 Results . . . 41
2.6 Conclusion . . . 42

3 Pole figure construction **44**
3.1 Executive summary . . . 44
3.2 Introduction . . . 44
3.2.1 The Pole and the Spherical Projection . . . 44
3.2.2 The Stereographic Projection . . . 47
3.2.3 Crystal and sample axes . . . 48
3.3 Macroscopic symmetry elements . . . 48
3.4 HCP planes and directions . . . 51
3.5 Implementation . . . 53
3.6 Discussion and conclusions . . . 56

4 Geometrically necessary dislocation modelling **59**
4.1 Executive summary . . . 59
4.2 Introduction . . . 59
4.3 Dislocation tensors . . . 63
4.3.1 Reconciling dislocation measures . . . 67
4.3.2 Curl of a second order tensor $\boldsymbol{T}$ . . . 70
4.3.3 GNDs in hcp crystals . . . 72
4.4 Crystal plasticity FE implementation . . . 76
4.4.1 The CPFE gradient implementation . . . 76
4.5 Analysis of hcp single and polycrystal GND development . . . 79
4.5.1 Single element: uniaxial loading . . . 80

4.5.2 Four point bending . . . 80
4.5.3 Hcp polycrystal (random orientation) . . . 82
4.6 Conclusion . . . 90

5 Strain, lattice rotation and GND density in a nickel alloy 92
5.1 Executive summary . . . 92
5.2 Introduction . . . 93
5.3 Material, experimental EBSD and crystal plasticity methodology . . . 95
5.3.1 Crystal plasticity model . . . 96
5.4 Strain, lattice rotation and GND density analyses of Ni sample . . . 100
5.4.1 Comparison between the GND coupled and uncoupled models . 107
5.5 Discussion and conclusions . . . 113

6 Texture evolution modelling 115
6.1 Executive summary . . . 115
6.2 Introduction . . . 115
6.3 New stress and texture update methodology . . . 118
6.3.1 Stress update . . . 119
6.3.2 Texture development . . . 122
6.3.3 Numerical Stability Control . . . 124
6.4 Model validation: hcp crystal simulations . . . 125
6.4.1 Single crystal uniaxial compression to 90% . . . 125
6.4.2 Single crystal shearing to 45° . . . 126
6.4.3 Single crystal uniaxial compression to 65% . . . 126
6.4.4 Hcp polycrystal test . . . 134
6.5 Allowable time-step and the slip rule . . . 135
6.6 Determination of slip rule parameters . . . 138
6.6.1 The yield point: τ_c and $\dot{\gamma}_0$ . . . 139
6.6.2 Strain rate sensitivity: n . . . 141
6.6.3 Stress-strain curve shape . . . 143
6.6.4 Results . . . 146
6.7 Conclusion . . . 148

7 Texture homogenization and evolution 150
7.1 Executive summary . . . 150
7.2 Introduction . . . 150
7.3 Texture homogenization from EBSD measurements . . . 153
7.3.1 Representative volume elements . . . 155
7.3.2 Texture evolution using homogenized RVEs . . . 157
7.4 Measured texture after deformation . . . 160
7.5 RVE dependence of average stress-strain response . . . 163
7.6 Conclusions . . . 165

8 Texture effects on polycrystal physical properties 168
8.1 Executive summary . . . 168
8.2 Introduction . . . 169
8.3 Thermal expansivity calculation . . . 171
8.4 Systematic study of texture effects on expansivity . . . 177
8.4.1 Investigating texture realisation effects . . . 181
8.5 Texture effects on mechanical properties . . . 184
8.6 Conclusions . . . 187

9 Two-phase texture evolution 189
9.1 Executive summary . . . 189
9.2 Introduction . . . 189
9.3 Dual phase material model . . . 190
9.4 Experimental data . . . 191

9.5 Two-phase texture homogenisation . . . 193
9.6 Two-phase (hcp+bcc) texture evolution . . . 195
9.6.1 Block vs. uniform phase assignment . . . 195
9.6.2 RVE size effect on texture evolution . . . 198
9.7 Bcc single phase texture evolution . . . 200
9.8 The effect of the second phase . . . 202
9.9 Discussion and conclusions . . . 205

10 Conclusions and future work **207**
10.1 Conclusions . . . 207
10.1.1 Geometrically necessary dislocation modelling . . . 208
10.1.2 GND effects in micro-deformation modelling . . . 208
10.1.3 Texture homogenisation and evolution modelling . . . 209
10.1.4 Texture effects on physical properties . . . 210
10.2 Future work . . . 211
10.2.1 Orientation distribution realisations . . . 211
10.2.2 Deformation mechanisms . . . 212
10.2.3 Temperature dependence of physical properties . . . 212

Appendix A Euler angles **214**
A.1 Roe, Bunge and Kocks angles . . . 214
A.2 Roe's system . . . 214

Appendix B Slip systems **217**
B.1 BCC Slip Systems . . . 217
B.1.1 {110} family . . . 217
B.1.2 {112} family . . . 217
B.1.3 {123} family . . . 218
B.2 FCC Slip Systems . . . 218
B.3 HCP Slip Systems . . . 218

References **225**

Acknowledgements

I would like to thank my supervisor, **Professor Fionn Dunne**, for his patience with me and for the guidance and encouragement he has given me throughout the duration of this project. I am especially thankful for his guidance on my written and oral presentation skills in addition to sharpening my general research skills. I would also like to thank my co-supervisor **Professor Jianguo Lin** for providing his software from Imperial College London for various uses at the start of the project.

I would like to thank **Professor David Rugg** from Rolls-Royce plc for various insightful and inspiring discussions which have in many ways shaped the emphasis of the work in this thesis, especially with regard to texture evolution. His industrial perspective on various issues has motivated and provided great momentum for this project and made the whole research experience a pleasurable one.

I am grateful for experimental data received from **Luke Bradley** of Rolls-Royce plc. This data has been the focus for the work in the second half of the thesis. I am also grateful for various meetings and email exchanges which have been useful for setting various targets and milestones for the project with the result that all the work for this project was completed well within three years.

Thanks also to **Dr Angus Wilkinson, Dr T Ben Britton** and **Philip Littlewood** from the Oxford Department of Materials for various helpful discussions and for providing the experimental data for the GND and Nickel particle studies which are a major part of this thesis. Thanks indeed to the whole micromechanics working group

- with members from the Engineering department (under Professor Fionn Dunne) and Oxford Department of Materials (under Dr Angus Wilkinson) - for the regular meetings and discussions, which in many ways enabled me to remain focussed.

Special thanks to **Rolls-Royce plc** for providing the bulk of the funding for this project: all the tuition fees for three years at an overseas rate and maintenance for two years. I am also grateful for the Centenary scholarship from the **Man Group** which helped with maintenance in the third year of this project. I would also like to thank **Christ Church** for electing me to a college lectureship during the third year which further helped to rectify my then unhealthy financial situation.

I am eternally grateful to my college advisor **Professor David Nowell** for support at various difficult points in this project. I am especially grateful for his gracious mediation efforts at a time when various factors almost made it necessary to terminate the research project just before I could transfer from PRS to DPhil status at the end of my first year.

I am indebted to the Dean of Christ Church, **The Very Reverend Christopher Lewis** for providing me with a generous morale boost when he off-loaded my financial burden by authorising funds to enable my mum and sister to visit me from Uganda. That was their first ever visit to the United Kingdom despite my continuous residence in the country for seven years by the time of their visit. They will never forget this. Neither will I. I also thank my **mum, Josephine Namuyimbwa** for her unrelenting support throughout my time at Christ Church even while she is thousands of miles away in Uganda.

I am thankful to **Jon Gregory** for his technical support. I am also thankful for the various discussions with many present and past members of the **Solid Mechanics and Materials Engineering group**. I would also like to thank the **Department of Engineering Science** for providing me with an excellent research office space and a

generally conducive research environment, and to thank **Christ Church** for providing excellent accommodation and general welfare support, all of which has been vital for the success of my research.

I have been very blessed with a wonderful office community with whom I have shared a truly wonderful life. Both its ups and downs. Looking back, I think one of the best decisions I made at the start of my project was to surround myself with this community, none of whom is even a member of my Solid Mechanics and Materials Engineering research group. Together they have provided the perfect balance of discussions away from materials engineering. They have in fact enabled me to remain broad-based in my search for knowledge as I have often ended up deeply discussing subjects and projects far-removed from my research area. But most importantly, together we have definitely enjoyed life to the full extent a research student should enjoy it! These awesome people include: **Katherine Glover (UK), Pharima Pongpairoj (Singapore), Xiafu Shi (China), Aimee Guha Roy (USA), Timothy Mbasuen (Nigeria), Julian David Hunt (Brazil), Tamara Etmannski (Canada), Edward Pitt (UK), Hassan El-Houjeiri (Lebanon), and Kim Wu (Hong Kong).**

Last but not least I am thankful for the many amazing people who have brought great joy to my life in Oxford. These include a great number of graduates and undergraduates from Christ Church and various other colleges, Christ Church support staff from the different departments of the college, as well as from the awe-inspiring postgraduate community from my church, St Aldates. I cannot even start listing names as this would quickly turn into a chapter of its own. I am grateful to all for making my life complete and a continuous joy indeed despite all the challenges along the way.

Chapter 1

Introduction

Plastic deformation causes the crystallographic orientations of crystals and grains to change. The resulting orientation of the grains (or crystals) may not be random, but may be clustered about a particular orientation called a *preferred orientation* or *texture*. If the orientation is random then the material is said to have no texture - although this is often conveniently referred to as a random texture. Texture is usually presented in terms of at least three well established techniques: pole figures, orientation distribution functions [37], and Kearns' factors [3, 47]. In addition to plastic deformation, texture can also develop as a result of grain growth, phase transformations, solidification, and recrystallization [40, 64].

Deformation induced texture evolution is affected by many parameters, including: the initial texture before deformation; the number of active slip systems; localised shearing, which can lead to large changes in local crystallographic orientations; the (distribution of) deformation temperature; strain rate and strain [37].

Modelling texture evolution therefore entails getting three essential components right: modelling the deformation mechanisms (slip and twinning - ignore diffusional processes), modelling grain interaction (essential for dealing effectively and correctly with grain growth, phase transformations, and recrystallisation), and updating texture correctly.

Current research and development involves efforts to improve the understanding of large-strain plasticity of metals and alloys, and to develop predictive models to describe the deformation microstructure and texture [37]. Understanding texture evolution and its effects on microstructure and mechanical properties is of industrial importance because such knowledge can enable a materials designer to deliberately manipulate

and control a material's behaviour for a predetermined purpose, e.g., designing for high temperature application where thermal expansivity is of interest or for high numbers of stress cycles (i.e. long life).

The work done in this project was indeed requested by Rolls-Royce plc who wish to understand the effect of texture evolution on the mechanical and thermal physical properties of materials used in nuclear reactors and jet engines. Such materials include Zr-2.5%wtNb which is used for nuclear fuel rods, and Ti-6Al-4V which is used in the fan blades of jet engines. Fan blades experience large deflections at the top which result in texture change. In addition to texture change due to large strains, Zr textures have been observed to change drastically when samples are heat treated.

There are many factors that affect the hardness and strength of a material during high temperature deformation processes. Hardness typically increases due to strain-hardening as a result of an increase in the density of dislocations. This hardening may, however, be counteracted by softening due to dynamic recovery resulting from elimination of dislocations and due to dynamic recrystallisation as a result of the continuous nucleation and growth of new grains. With rapid dynamic recovery, the flow stress increases progressively up to a steady value at which the stress-strain curve levels off; but the stress-strain curve may exhibit a maximum, which is eventually followed by a steady state stress, if dynamic recrystallisation also occurs [64].

Prediction of this behaviour requires improved understanding of the fundamentals of texture evolution, as well as improved modelling techniques for plastic deformation, e.g. modelling of dislocations. Prediction of the evolution of crystalline anisotropy during plastic deformation has so far remained a problem; it "is necessary since crystals individually rotate during deformation owing to the nonsymmetry of the displacement gradients created by crystal slip" [67].

1.1 Texture representation

1.1.1 Pole figures

Pole figures are a form of stereographic projection used to show the texture of a polycrystal. Typically the preferred orientation can be presented by showing the scatter of some convenient type of pole (unsigned normal to the plane through the center of a reference sphere), e.g. only {100} or {111}. If say, {111} is plotted, it is called a {111} pole figure. The plot is thus used to show the orientation of a large number of grains relative to some preferred set of external reference axes. Such reference axes could, for example, be the rolling direction, transverse direction, and the normal to the rolling plane. With a large number of grains, contours can then be drawn to show equal density of a the plotted pole per solid angle. A single pole is not enough to fully determine the orientation of an object as it is unchanged under a rotation about the normal. Full determination of texture requires two pole figures corresponding to planes that are not parallel and that do not have the same diffraction angle, i.e., that have different interplanar distance [40, 64]. Such planes will therefore not be symmetrically equivalent.

Inverse pole diagrams also exist in which preferred orientations may be presented by plotting the external reference axes on a standard crystallographic projection. For a polycrystal, a number of points would then be required to represent the reference axis of the specimen relative to the crystal axes of different grains. If there is more than one reference axis of importance (e.g. RD, TD, ND), it may then be necessary to plot more than one inverse pole figure for each such direction [40]. Inverse pole figures mainly find application in cases of axially symmetric textures e.g in tensile tests.

Pole figures are usually obtained experimentally by use of such techniques as x-ray diffraction. It is worth emphasising that for (direct) pole figures only one crystallo-

graphic form of the poles, e.g. only {100}, is plotted but for many crystals/grains [64]. It also does not matter whether the physical planes and directions of interest intersect at a common point. Any plane and all planes parallel to it will be plotted through the same point [40]. In other words, only relative orientation but not position is captured. The procedure for constructing pole figures is outlined in Chapter 3.

1.1.2 Orientation distribution functions

Pole figures are a two-dimensional plot of a three-dimensional texture. Except for very simple textures, the orientations present are very difficult to determine quantitatively from pole figures or inverse pole figures with certainty. Pole figures do not provide the complete orientation distribution but only the distribution of poles. Only a three dimensional plot of orientations can fully describe a texture.

To fully describe an orientation, three angles (Euler angles) are required. Two commonly used systems of angles for describing the orientation of crystal axes ([100],[010],[001]) relative to the external (x, y, z) axes are those proposed by Bunge and Roe which have been shown to be similar [40]. The relationship between the angles of the two systems are given in appendix A.1. Roe's system is described in appendix A.2.

The orientation distribution function (ODF), $f(\boldsymbol{g})$, is a probability density function of orientation $\boldsymbol{g}$, expressed, for example in Euler angles φ_1,Φ, and φ_2. It is the volume fraction of grains oriented along a certain direction $\boldsymbol{g}$. Mathematically it can be expressed as follows [68]:

$$\frac{dV}{V} = f(\boldsymbol{g})d(\boldsymbol{g}), \text{ with } d(\boldsymbol{g}) = \frac{1}{8\pi^2} sin\Phi d\varphi_1 d\Phi d\varphi_2 \text{ and } \oint f(\boldsymbol{g})d(\boldsymbol{g}) = 1 \qquad (1.1)$$

where $\boldsymbol{g}$ is the orientation, V is the sample volume and dV is the volume of all crystallites with the orientation $\boldsymbol{g}$. The Euler angles describe the transition from the sample's reference frame into the crystallographic reference frame of each individual grain of the

polycrystal. The distribution of crystal orientations over a suitable space defined by these angles comprises the ODF.

Traditionally both X-ray diffraction and EBSD may collect pole figures. The ODF cannot be measured directly by any technique. Instead it is achieved through evaluation of a set of pole figures or diffraction spectra. Subsequently, all pole figures can be derived from the ODF. The relationship between the ODF and the pole figure is such that, for an arbitrary pole (hkl), the pole figure is obtained by integrating the ODF, $f(\boldsymbol{g})$, along a path Γ corresponding to a 2π rotation of a crystal about its (hkl) pole, see equation (1.2), i.e., a 2π rotation about the diffraction vector. The pole figure may generally be considered a projection of the ODF along this path. This path will not, in general, correspond to a simple route in Euler space - it is only simple for the (100) pole where $\Theta = \alpha$ and $\Phi = \beta$. (α and β are the polar and azimuthal angle respectively, which describe the position of a pole on the surface of a reference sphere). It is relatively trivial to compute any pole figure when given the ODF. The more difficult task is the inverse of this, i.e., to compute the ODF given the pole figure [49, 68].

$$p_{(hkl)}(\alpha, \beta) = \frac{1}{2\pi} \int_0^{2\pi} f(\Phi, \Theta, \psi) d\Gamma \tag{1.2}$$

Different methodologies exist to obtain the ODF from the pole figures or data in general. Some of the most common methods of pole figure inversion include: the series expansion method, which employs spherical harmonic functions - computations are performed in Fourier space; and direct or discrete methods in which computations are perfomed directly in orientation space. They all have their advantages and disadvantages. A full overview of these is provided by Kocks et al. [49] and Randle and Engler [68].

In many experimental procedures for obtaining pole figures, only incomplete pole

figures are obtained so that not the entire pole figure range is covered reducing the texture information available in such a pole figure. To overcome the ambiguities introduced by this and thus to permit quantitative texture evaluation necessitates description of orientation density of a polycrystal in an appropriate 3-D representation, i.e., in terms of an ODF [68]. ODFs are also useful for obtaining missing pole figures, i.e. pole figures that cannot be measured directly from experiment.

If a pole figure is measured in reflection geometry, the errors strongly increase with the pole figure angle α, so that the inner circles of the figure can be obtained without much correction while outer parts either need strong corrections or are not accessible ($\alpha \approx 90^o$). The reverse is true for pole figures measured in transmission geometry. Therefore, *complete pole figures* are obtained by combining two pole figures measured in the different geometries. Such combination entails intensity adaptations to bring the two measurements to the same intensity scale. Due to extra work involved in this, it is usual for only *incomplete pole figures* to be measured, and when necessary the complete pole figures are derived by recalculation from a 3D orientation distribution function [68].

For experimental texture determination, it is evident from the above that one needs to employ one of the available methods to compute the ODF in order to be able to recalculate pole figures, or even determine pole figures that could not otherwise be determined experimentally. Since this project is focused on texture evolution modelling, it would be of no added value to engage with the involved procedures for obtaining ODFs. As such, presentation will be limited to pole figures assuming the availability of the Euler angles describing the texture in question.

1.1.3 Kearns texture factors

Kearns texture factors provide another way to quantitatively present texture information. They are traditionally used for the hcp crystal type and can be defined for various types of poles, e.g. the basal pole, or a prismatic pole. Any choice of pole can be related to the basal pole [35, 47], hence in this work we shall restrict ourselves to working only with that pole. With respect to the basal pole, the Kearns factors describe the effective volume fraction of crystallites with their c-axis aligned along a specified direction [3, 47], normally defined with respect to three mutually orthogonal directions such as the sample's rolling, transverse, and normal directions. Therefore there are three such factors, one for each of the directions. They are defined as follows [3, 74]:

$$\begin{aligned} f_1 &= \int_0^{\pi/2} \int_0^{2\pi} q(\theta,\psi) \sin^3(\theta) \cos^2(\psi)\, \mathrm{d}\psi\, \mathrm{d}\theta \\ f_2 &= \int_0^{\pi/2} \int_0^{2\pi} q(\theta,\psi) \sin^3(\theta) \sin^2(\psi)\, \mathrm{d}\psi\, \mathrm{d}\theta \\ f_3 &= \int_0^{\pi/2} \int_0^{2\pi} q(\theta,\psi) \sin(\theta) \cos^2(\theta)\, \mathrm{d}\psi\, \mathrm{d}\theta \end{aligned} \tag{1.3}$$

where the angles θ and ψ correspond to the usual spherical coordinates with θ the polar angle and ψ the azimuthal angle, and $q(\theta,\psi)$ represents the number of poles with the orientation (θ,ψ) as a fraction of the total number of poles (or crystals/crystallites) being considered, i.e. the pole density [74]. These Kearns factors are essentially the quantitative equivalent of the basal pole figure, i.e. the pole figure given in terms of numbers where each orientation on the pole figure is resolved to give its components in the three mutually orthogonal directions.

1.2 Deformation mechanisms

In order to understand and model texture evolution we need to understand the underlying deformation mechanisms that cause it. Slip and twinning are the two most important deformation mechanisms in plastic deformation where large strains are involved. Crystals and crystalline grains making up a metal or alloy usually deform plastically primarily by slip and to a lesser extent by twinning. Some materials under certain conditions (temperature and strain rate) may experience only (or nearly only) deformation by slip while others (such as hcp materials) will experience a combination of slip and twinning deformation. Therefore theoretical and experimental analyses of the slip patterns (i.e., number and type of slip systems) are mandatory in order to understand deformation-induced changes in microstructure, texture and mechanical behaviour [37, 64].

1.2.1 Deformation by slip

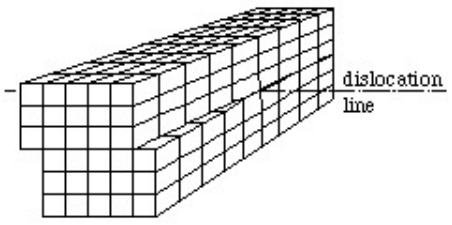


Figure 1.1: An illustration of slip showing a (screw) dislocation line.

Slip is defined as the ultimate shear displacement of discrete sections of a crystal relative to other adjacent sections. It primarily occurs due to the movement of dislocations. The dislocations include statistically stored dislocations (SSDs) - dislocations which accumulate by trapping each other randomly [31] - and geometrically necessary dislocations (GNDs). Figure 1.1 is an illustration of slip showing a dislocation line. Slip usually takes place on the closest-packed atomic planes and in the densest atomic directions, i.e. directions with the shortest Burgers vector (because the strain energy

around a dislocation is proportional to b^2 [41]), which are also the directions in which atoms touch [64].

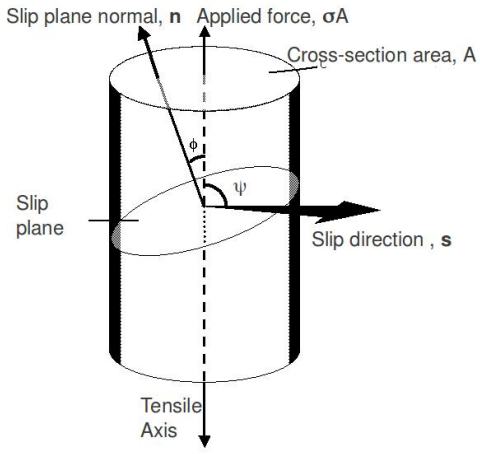


Figure 1.2: An illustration of Schmidt's law showing the slip direction, slip plane normal, the direction of the applied force, and the angles between them as used to calculate the Schmidt factor.

Deformation by slip is normally described in terms of a slip plane and slip direction (i.e. a slip system) - illustrated in Figure 1.2 - and a critical resolved shear stress (CRSS) needed to overcome resistance to dislocation motion. Depending on the loading state, different slip systems can get activated and some slip systems will dominate plastic deformation depending on their Schmidt factors. The value of the critical resolved shear stress is determined according to Schmidt's law, which states that slip will occur when the resolved shear stress, τ , on any slip system reaches a critical value, known as the CRSS. The system α whose τ^α reaches the critical value is then said to be activated.

$$\tau^\alpha = \sigma cos\psi cos\phi = \sigma(\boldsymbol{s}^\alpha \cdot \boldsymbol{p}^\alpha)(\boldsymbol{n}^\alpha \cdot \boldsymbol{p}^\alpha) \tag{1.4}$$

where ψ is the angle between the loading direction $\boldsymbol{p}^\alpha$ and the slip direction $\boldsymbol{s}^\alpha$, and ϕ is the angle between the loading direction and the normal to the plane $\boldsymbol{n}^\alpha$. The Schmidt factor for slip system α is defined as $cos\psi cos\phi$ $(= \boldsymbol{s}^\alpha \cdot \boldsymbol{p}^\alpha)$. See Figure 1.2, where $\boldsymbol{p}^\alpha$ is

defined parallel to the applied force.

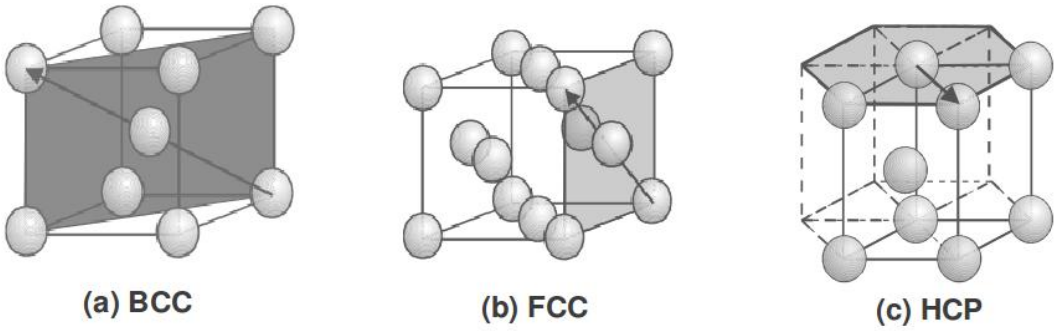


Figure 1.3: Schematics of the bcc, fcc, and hcp crystal types showing atomic arrangement, example slip planes and slip directions.

The observed dominant slip systems found in hcp are $\{0001\} < 11\bar{2}0 >$. Other observed slip systems for Ti include $\{10\bar{1}0\} < 11\bar{2}0 >$ and $\{10\bar{1}1\} < 11\bar{2}0 >$ [64]. A full list of possible slip systems for hcp materials is given in appendix B.3. Appendix B gives a comprehensive list of possible slip systems for the three main crystal types that will be of interest in this project: bcc, fcc (or ccp - cubic close pack) and hcp. Figure 1.3 shows a schematic of these crystal types. The dominance of certain slip systems relative to others in hcp materials implies that such slip system families have different tendencies in their resistance to dislocation motion so that they require different critical resolved shear stresses to activate.

1.2.2 Slip versus twinning

The amount of gross deformation produced by twinning is small, for example, the maximum extension when an entire zinc crystal is converted into a twin on the $(10\bar{1}2)$ type planes is only 7.39%. The important role of twinning in plastic deformation is not from the strain produced, but from the fact that orientation changes resulting from twinning may place new slip systems in more favourable orientation with respect to the stress axis, so that additional slip can occur. Thus twinning is important in hcp metals like titanium and magnesium [64].

Deformation twinning is favoured over slip as a deformation mode when there are few slip systems available, e.g. in low symmetry crystal structures, and at high strain rates. Hcp metals deform both by slip and twinning. The relative amount of the components varies with temperature. The tendency for twinning generally increases as the deformation temperature is lowered and strain rate is increased.

The CRSS also increases as the temperature decreases so that slip becomes more difficult making the role of twinning more significant. Because of this CRSS-temperature relationship one expects higher stresses in a sample as one lowers the temperature (i.e. ones expects to see apparent hardening due to a reduction in temperature).

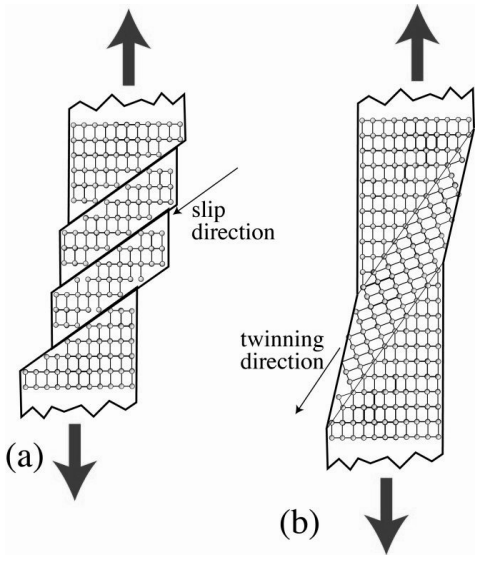


Figure 1.4: Schematic of shape changes arising from (a) slip and (b) deformation twinning due to an applied stress. Slip tends to take place by repeated passage of dislocations on specific slip planes. For deformation twinning, on the other hand, the simultaneous, rapid displacement of a large number of neighbouring atoms, all in the same direction, also creates a (shear) displacement of the lattice, although in this case the sheared region has a different orientation from that of the parent crystal. In fact, the structure is a mirror image of the parent, reflected across the twin plane. Courtesy of DoITPoMS[24]

Figure 1.4 shows a schematic of shape changes arising from slip and deformation twinning. Both slip and twinning are deformation mechanisms involving shear displacements on specific crystallographic planes and in specific crystallographic directions; but there are important differences [40]: with slip, the magnitude of shear displacement is variable but it is always an integral number of interatomic repeat distance and it

occurs on only a few of the parallel planes (which are separated by large distances), with twinning, the shear displacement is a fraction of an interatomic spacing repeat distance and involves shear between every successive plane; twinning shear is always directional unlike slip, e.g. twinning in fcc crystals occurs by shear on the (111) plane in the $[11\bar{2}]$ direction but not in the $[\bar{1}\bar{1}2]$ direction but in the same crystals slip can occur on a (111) plane in either $[\bar{1}10]$ or the $[1\bar{1}0]$ directions; slip leaves the lattice virtually unchanged, and lattice rotation is gradual but twinning abruptly reorients the lattice.

In this work we model only the most important deformation mechanism: slip. Where experimental data has been used it has been selected to deliberately avoid deformation regimes where twinning is prevalent.

1.3 Texture evolution modelling

This section introduces some of the key considerations required for modelling the evolution of texture, in additional to the deformation mechanisms already discussed. The two main considerations of interest are the grain interaction models, and the methods for updating crystallographic orientation. The section presents both a literature review on these issues and suggestions for potential improvements on what is suggested by the literature.

1.3.1 Reference frames and crystal plasticity

When plotting pole figures, there are in general two reference frames to consider: the crystallographic axes c - each crystal's own orthogonal (not necessarily natural for non-cubic ones) set of axes - and the sample axes s. Description of texture (or crystallographic orientation) specifically concerns defining the orientation matrix $\boldsymbol{g}$ (or an equivalent representation) needed to describe the sample axes in terms of each crystal's crystallographic axes and vice versa.

In numerical evaluation of constitutive equations and other quantities of interest, there are usually three frames of interest: the initial frame (also typically called the undeformed reference frame or global frame), s; an intermediate frame; and the current (local/deformed) frame, l. The undeformed frame (Langrangian) and the deformed frame (Eulerian) are related by the deformation gradient $\boldsymbol{F}$, defined as:

$$\boldsymbol{F} = \frac{\partial \boldsymbol{x}}{\partial \boldsymbol{X}} \tag{1.5}$$

How any of these two frames is related to the intermediate frame depends on how one choses to define that intermediate frame, and hence how one decomposes $\boldsymbol{F}$.

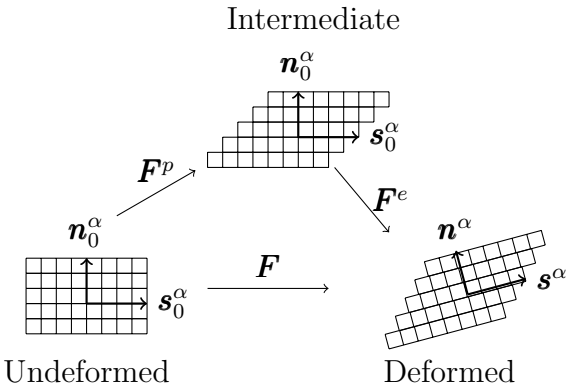


Figure 1.5: Schematic of the Kroner-Lee [51, 53] multiplicative decomposition of the deformation gradient $\boldsymbol{F}$ showing the relationship between the deformed, intermediate, and undeformed configurations and how components of $\boldsymbol{F}$, i.e. $\boldsymbol{F}^e$ and $\boldsymbol{F}^p$, map the different configurations to each other.

In crystal plasticity theory, which is a quantitative description of plastic deformation in single crystals based on crystallographic slip, it is usual to decompose $\boldsymbol{F}$ as [51, 53]:

$$\boldsymbol{F} = \boldsymbol{F}^e \boldsymbol{F}^p \tag{1.6}$$

A schematic of this decomposition is given in Figure 1.5. In this case $\boldsymbol{F}^p$ maps the deformation state from the initial frame to the intermediate frame (also called the relaxed configuration or lattice configuration). $\boldsymbol{F}^e$ then maps the deformation state

from the intermediate state to the deformed frame. $\boldsymbol{F}^e$ is assumed to account for all the rigid body rotation and the elastic stretch. The plastic part of the deformation gradient $\boldsymbol{F}^p$ evolves as given in equation 1.7:

$$\dot{\boldsymbol{F}}^p = \boldsymbol{L}^p \boldsymbol{F}^p \quad \text{with} \quad \boldsymbol{L}^p = \sum_{i=1}^{n} \dot{\gamma}^i \boldsymbol{s}^i \otimes \boldsymbol{n}^i \tag{1.7}$$

where the plastic part of the velocity gradient $\boldsymbol{L}^p$ incorporates the crystallographic slip from the active slip systems i, with normal vector $\boldsymbol{n}^i$ and slip direction vector $\boldsymbol{s}^i$, and $\dot{\gamma}^i$ is computed according to a slip rule. One of the slip rules used in this project is that developed by Gibbs [33], which is based on a combination of thermodynamics and statistical mechanics principles. This slip rule was further developed by Dunne et al. [26], and is used here in the following form:

$$\begin{aligned} &\dot{\gamma}^i = \rho_S^m \nu {b^i}^2 \exp\left(\frac{-\Delta F}{kT}\right) \sinh\left(\frac{(\tau^i - \tau_c^i)\gamma_0^i \Delta V^i}{kT}\right), \\ &\text{where} \quad \Delta V^i = l{b^i}^2, \quad l = \frac{1}{\sqrt{\psi(\rho_S^s + \rho_G)}} \end{aligned} \tag{1.8}$$

where ρ_S^m, ρ_S^s are the mobile and immobile SSD densities respectively, ρ_G is the overall GND density, ν the frequency of attempts (successful or otherwise) by dislocations to jump the energy barrier, b^i the Burger's vector magnitude for slip system i, ΔF the Helmholtz free energy, k the Boltzman constant, T the temperature in Kelvin (K), τ^i the resolved shear stress, τ_c^i the critical resolved shear stress (a slip system is considered active when $\tau^i \geq \tau_c^i$), γ_0 the shear strain that is work conjugate to the resolved shear stress, ΔV the activation volume, l the pinning distance, and ψ is a coefficient that indicates that not all sessile dislocations (SSDs or GNDs) necessarily act as pinning points. The superscript i indicates the quantity appropriate to the i^{th} active slip system (for example, the Burger's vector for a-type slip is different to that for c+a-type slip

in hcp materials). The subsequent implicit integration of constitutive equations and the determination of the consistent elastic - plastic tangent stiffness are also detailed in Dunne et al. [26].

1.3.2 Grain interaction models

In modelling texture evolution and deformation in general, there are various considerations given to boundary conditions with regard to stress and strain, i.e. equilibrium and compatibility. The different considerations lead to different grain interaction models. Such models include the full constraint (Taylor) model, the relaxed constraints model, the viscoplastic self-consistent model, and the Lamel model [76].

In the Taylor model, the macroscale (polycrystal) kinematics and that of a crystal are linked by assuming that the average deformation rate of the polycrystal $\boldsymbol{D}^s$ is the same as that of the crystal $\boldsymbol{D}^c$. Additionally it is assumed that the spin of a grain in the sample frame $\boldsymbol{W}^s$ gives the average of spin over the polycrystal [9]. In this case no effort is made to satisfy equilibrium conditions among the crystals.

The relaxed constraints model (flat-grain limit) treats the interface between two grains "A" and "B" as flat in the limit. Such grain arrangements can be expected in rolling to large reductions. The grains are taken to meet in a single plane with the normal in the 3-direction with equilibrium and compatibility being satisfied in this plane. The local equilibrium equations are [9, 49]

$$\sigma_{33}^A = \sigma_{33}^B, \qquad \sigma_{31}^A = \sigma_{31}^B \qquad \text{and} \qquad \sigma_{32}^A = \sigma_{32}^B \tag{1.9}$$

and the compatibility requirements are

$$D_{11}^A = D_{11}^B, \qquad D_{22}^A = D_{22}^B \qquad \text{and} \qquad D_{12}^A = D_{12}^B \tag{1.10}$$

This is relaxed constraints because there are some components of the deformation tensor, for example D_{31}, which are left unconstrained or unspecified thus allowing neighbouring grains in the free direction to potentially develop from independent deformation processes without constraints at the boundary [49].

In the viscoplastic self-consistent model, a grain is treated as a viscoplastic inclusion in a homogeneous medium. Loading at the surface of the medium leads to a non-uniform stress field around the inclusion. The relevant constitutive behaviour in this case is given in Kocks et al. [49] and Beaudoin and Engler [9].

In full constraint models, an upper bound on stress necessary to achieve a specified macroscopic strain can be obtained by assuring compatibility throughout the body and ignoring the satisfaction of local equilibrium, for example by assuming uniform strain - as is the case for the Taylor model of plasticity. Similarly a lower bound can be achieved by assuming uniform stress and ignoring local compatibility conditions. A lower bound solution is not reasonable in the case of large plastic strains because of the random distributions of orientations at any one time, unless it is coupled with high strain rate hardening [49].

Since uniform distributions of stress and strain give bounds to the solution, a general distribution of strains gives a measure of deviation from the Taylor model. Conversely a low dispersion of stresses resulting from a Taylor calculation indicates that equilibrium is not significantly violated. Grain-to-grain variation of stress and strain must result from the specific interaction of a grain and its particular surroundings. This introduces a stochastic (probabilistic) effect into any model that assumes quasi-homogeneity. Prediction of overall stress-strain response may not be sensitive to these variations, however, there may be a correlation between neighbouring orientations, which could lead to specific grain interaction models which have so far been formulated abstractly [49]. Van Houtte et al. [76] provide comprehensive comparisons of the

different grain interaction models.

Finite element (FE) polycrystal plasticity formulations provide another way to account for grain interactions [76]. Unlike the above grain interaction models, finite element formulations are made to ensure that both equilibrium and compatibility are satisfied for every finite element. "The FE method does not only take the interactions between adjacent elements into account (i.e. the grain-to-first-neighbour interactions), but also long range interactions," Van Houtte et al. [76]. Considering the limitations on the above models, and the ability of the FE method to account for grain interactions, the FE formulations are perhaps the best alternative for developing models for texture evolution.

Various authors (e.g. Bate and Quinta da Fonseca [7], Van Houtte et al. [76]) have compared finite element methods (FEM) with some of the models above and concluded that finite element predictions are better. This project will thus waste no further time in making such comparisons. The FEM with crystal plasticity constitutive laws (CPFEM) will be used.

In the CPFEM a polycrystal is spatially discretized into component crystals/grains and each crystal is discretized into one or more finite elements. For purposes of modeling texture evolution, Bate and Quinta da Fonseca [7] suggest that a grain should consist of at least more than one finite element; otherwise the results over a single finite element would be very rough estimates and cannot be used satisfactorily to make conclusions about the intragranular deformation behaviour, which may not be homogeneous.

1.3.3 Updating crystal orientation

Updating the crystallographic orientation implies updating the slip systems' orientation. According to Kocks et al. [49] and Beaudoin and Engler [9], the evolution of

the crystallographic orientation of a crystal with deformation is given by

$$\dot{\boldsymbol{R}}^e = \boldsymbol{W}^e \cdot \boldsymbol{R}^e \quad \text{from} \quad \boldsymbol{W}^e = \dot{\boldsymbol{R}}^e \cdot \boldsymbol{R}^{e-1} \quad \text{where} \quad \boldsymbol{F} = \boldsymbol{R}^e \cdot \boldsymbol{F}^p \tag{1.11}$$

where $\boldsymbol{R}^e$ is the rotation part from a polar decomposition of $\boldsymbol{F}^e$ and $\boldsymbol{W}^e$ is the elastic part of the continuum spin $\boldsymbol{W}$. $\boldsymbol{W}$ is the asymmetric part of the velocity gradient $\boldsymbol{L}$.

They assume that in large deformation the elastic strains are small so that $\boldsymbol{F}^e \approx \boldsymbol{R}^e$. With the same assumption, Molinari [65] states that the slip systems can be updated according to the following relations:

$$\dot{\boldsymbol{s}}^\alpha = \boldsymbol{W}^e \boldsymbol{s}^\alpha \quad \text{and} \quad \dot{\boldsymbol{n}}^\alpha = \boldsymbol{W}^e \boldsymbol{n}^\alpha \quad \text{where} \quad \boldsymbol{W}^e = \dot{\boldsymbol{F}}^e \boldsymbol{F}^{e-1} \tag{1.12}$$

where $\boldsymbol{s}^\alpha$ and $\boldsymbol{n}^\alpha$ are the slip direction and slip normal respectively for slip system α at any time t. This is equivalent to

$$\boldsymbol{s}_t^\alpha = \boldsymbol{F}_t^e \boldsymbol{s}_0^\alpha \quad \text{and} \quad \boldsymbol{n}_t^\alpha = \boldsymbol{F}_t^e \boldsymbol{n}_0^\alpha \tag{1.13}$$

where the subscript 0 implies initial directions. Equation 1.13 is also stated by Molinari [65] and Kalidindi et al. [43], and it bears the same meaning as equation 1.11. If time-steps are assumed small then, from equation 1.11, it can be shown that the orientation matrix $\boldsymbol{T} = \boldsymbol{g}^{-1}$ - inverse because $\boldsymbol{g} = \boldsymbol{R}(Z, \varphi_2)\boldsymbol{R}(X, \Phi)\boldsymbol{R}(Z, \varphi_1)$, where $\boldsymbol{R}(Z, \theta)$ implies a rotation of angle θ about the Z axis, is defined as a mapping from the sample orientation to the crystal orientation - can be incremented as follows

$$\boldsymbol{T}_{t+1} = \boldsymbol{T}_t + \boldsymbol{W}^e \boldsymbol{T}_t \Delta t \tag{1.14}$$

Otherwise a fully implicit time-integration scheme is given as follows (compare with

the implicit time-integration for $\boldsymbol{F}^p$ given by Kalidindi et al. [43]),

$$\boldsymbol{T}_{t+1} = \exp(\boldsymbol{W}^e_{t+1}\Delta t)\boldsymbol{T}_t \approx \left(\boldsymbol{I} - \boldsymbol{W}^e_{t+1}\Delta t)\right)^{-1}\boldsymbol{T}_t \tag{1.15}$$

Equation 1.11 suggests that given a polycrystal, the change in orientation of any given crystal is a function of the rigid body rotation that crystal experiences. Changes in rigid body rotation are usually captured, in rate form, by the elastic part of the continuum spin $\boldsymbol{W}^e$ (as already noted) often given as

$$\boldsymbol{W}^e = \boldsymbol{W} - \boldsymbol{W}^p \tag{1.16}$$

where the continuum spin $\boldsymbol{W}$ and its plastic part $\boldsymbol{W}^p$ are the asymmetric parts of the velocity gradient $\boldsymbol{L}$ and its plastic part $\boldsymbol{L}^p$ respectively. Eqn 1.16 is, however, not a satisfactory representation of $\boldsymbol{W}^e$. Consider the following:

$$\begin{aligned}
&\boldsymbol{L} = \dot{\boldsymbol{F}}\boldsymbol{F}^{-1}, \quad \boldsymbol{L}^p = \dot{\boldsymbol{F}}^p\boldsymbol{F}^{p-1}, \quad \boldsymbol{W}^e = \dot{\boldsymbol{F}}^e\boldsymbol{F}^{e-1} \quad \text{and} \quad \boldsymbol{F} = \boldsymbol{F}^e\boldsymbol{F}^p \\
&\boldsymbol{L} = \dot{\boldsymbol{F}}\boldsymbol{F}^{-1} = \frac{\partial}{\partial t}\left(\boldsymbol{F}^e\boldsymbol{F}^p\right)\left(\boldsymbol{F}^e\boldsymbol{F}^p\right)^{-1} = \left(\dot{\boldsymbol{F}}^e\boldsymbol{F}^p + \boldsymbol{F}^e\dot{\boldsymbol{F}}^p\right)\boldsymbol{F}^{p-1}\boldsymbol{F}^{e-1} \\
&\boldsymbol{L} = \dot{\boldsymbol{F}}^e\boldsymbol{F}^{e-1} + \boldsymbol{F}^e\dot{\boldsymbol{F}}^p\boldsymbol{F}^{p-1}\boldsymbol{F}^{e-1} = \boldsymbol{W}^e + \boldsymbol{F}^e\boldsymbol{L}^p\boldsymbol{F}^{e-1} \quad \text{therefore} \\
&\boldsymbol{W}^e = \boldsymbol{L} - \boldsymbol{F}^e\boldsymbol{L}^p\boldsymbol{F}^{e-1}
\end{aligned} \tag{1.17}$$

As it is, equation 1.17 is difficult to reconcile with equation 1.16. Note that the expression $\boldsymbol{W}^e = \dot{\boldsymbol{F}}^e\boldsymbol{F}^{e-1}$ is a direct consequence of assuming that elastic strains are small; otherwise we would have that $\boldsymbol{L}^e = \dot{\boldsymbol{F}}^e\boldsymbol{F}^{e-1}$, and our final result in eqn 1.17 would have to be

$$\boldsymbol{W}^e = \text{asym}(\boldsymbol{L}^e) = \text{asym}(\boldsymbol{L} - \boldsymbol{F}^e\boldsymbol{L}^p\boldsymbol{F}^{e-1}) \tag{1.18}$$

Even with that taken into account, eqn 1.16 would give the correct answer only if $\boldsymbol{F}^e = \boldsymbol{I}$, i.e. only in the absence of any rigid body rotations, since these are assumed to be lumped into $\boldsymbol{F}^e$. Eqn 1.16 may, therefore, not be used in cases where rigid body rotations are expected. Eqn 1.18 together with eqn 1.15 have been in used in the work presented in Chapters 4 and 5 which involve relatively small deformations. A non-incremental approach to updating texture is later developed in Chapter 6 which is then used for much larger deformation in the subsequent chapters.

Other approaches to updating texture exist (such as Raabe and Roters [67]) where an attempt is made to formulate an orientation dependent constitutive law which is then embedded into the crystal plasticity finite element code. In such cases, the aim is generally to move away from working with individual single orientations to working with representative volume averages. This approach is good when dealing with samples containing say up to 10^{10} single crystals/grains. We will not deal with such huge samples in this project so a grain-by-grain approach will suffice for our purposes.

Chapter 2

Large deformation theory

2.1 Executive summary

In derivations of the constitutive behaviour of materials, it is usually assumed that displacements and strains are small. This enables the use of first order, infinitesimal linear strain approximations. However, these approximations do not always produce very accurate results in practice due to geometric non-linearities. For example, physically large displacements can occur without causing large strains. In such a case, the strains are non-linearly related to the displacements. Whether the displacements (or strains) are large or small, equilibrium between the external and internal loading must be satisfied. This chapter reviews the relevant theory for large deformations and its implementation into a finite element code. Specifically the derivation for the tangent stiffness matrix and the implicit integration of constitutive equations are discussed.

2.2 The Problem

Satisfying equilibrium between the external and internal loading can be stated mathematically as follows

$$\boldsymbol{F}^{ext} - \boldsymbol{F}^{int} = 0 \tag{2.1}$$

where $\boldsymbol{F}^{ext}$ represents the applied loading and $\boldsymbol{F}^{int}$ the internal loads. Eqn 2.1 represents a set of non-linear equations which may be solved iteratively using a Newton-type scheme. For an implicit integration scheme, a residual $\boldsymbol{\psi}$ can be defined such that

$$\boldsymbol{\psi} = \boldsymbol{F}^{ext} - \boldsymbol{F}^{int} \tag{2.2}$$

Eqn 2.2 would then be solved by a Newton iterative scheme until a prescribed tolerance for $\boldsymbol{\psi}$ is achieved with the updated displacements obtained from

$$\boldsymbol{u}_{t+\Delta t} = \boldsymbol{u}_t - \left[\frac{\partial \boldsymbol{\psi}(\boldsymbol{u}_t)}{\partial \boldsymbol{u}}\right]^{-1} \boldsymbol{\psi}(\boldsymbol{u}_t) \tag{2.3}$$

The partial derivative term above is the tangent stiffness matrix $\boldsymbol{K}_T$, that is

$$\boldsymbol{K}_T = \frac{\partial \boldsymbol{\psi}(\boldsymbol{u}_t)}{\partial \boldsymbol{u}} \tag{2.4}$$

In our case, we work with Abaqus' user element subroutine (UEL). The routine must be provided with $\boldsymbol{K}_T$ and the internal force $\boldsymbol{F}^{int}$ so that the Abaqus software (Abaqus/Standard) estimates the displacement $\boldsymbol{u}_{t+\Delta t}$. Following is the derivation for the tangent stiffness matrix.

2.3 Tangent Stiffness Matrix $\boldsymbol{K}_T$

Perhaps the most important concept in developing the theory of large deformations is the need to remember and make clear distinction between different frames of reference relative to which the various quantities, e.g. stress and strain measures, are defined. This is a very basic point but one that is worth repeating and keeping to the fore of the mind as one thinks about large deformation formulations. Figure 2.1 shows that the two main reference frames are related by the deformation gradient, which is defined as $\boldsymbol{F} = \frac{\partial \boldsymbol{x}}{\partial \boldsymbol{X}}$.

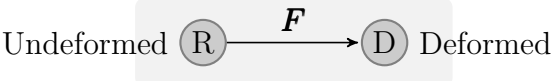


Figure 2.1: Relationship between the deformed and undeformed configurations defined by the deformation gradient $\boldsymbol{F}$. The distinction between the two frames is important for defining quantities used in large deformation modelling unlike in the case of small deformations.

Zienkiewicz [89] gives a straight forward methodology for taking account of the effects of geometric non-linearity, which is further expounded by Zienkiewicz and Taylor [90] and is summarised below for completeness. If the displacements are prescribed by a finite number of nodal parameters $\tilde{\boldsymbol{u}}$, then a force residual $\boldsymbol{\psi}$ is given as

$$\boldsymbol{\psi}(\tilde{\boldsymbol{u}}) = \int_V \bar{\boldsymbol{B}}^T \boldsymbol{S} \mathrm{d}V - \boldsymbol{F}^{ext} \tag{2.5}$$

where $\boldsymbol{F}^{ext}$ represents all the external forces due to imposed loads and $\boldsymbol{S}$ is the second Piola-Kirchoff stress, defined relative to the undeformed configuration - see Figure 2.1. $\boldsymbol{S}$ is related to the Cauchy stress $\boldsymbol{\sigma}$ - which is defined relative to the deformed configuration - according to equation 2.6

$$\boldsymbol{S} = J\boldsymbol{F}^{-1}\boldsymbol{\sigma}\boldsymbol{F}^{-T} \qquad \text{where} \qquad J = \det(\boldsymbol{F}) \tag{2.6}$$

$\bar{\boldsymbol{B}}$ is defined as

$$\mathrm{d}\boldsymbol{E} = \bar{\boldsymbol{B}}\mathrm{d}\tilde{\boldsymbol{u}} \tag{2.7}$$

and the bar on $\bar{\boldsymbol{B}}$ is added to emphasise the non-linear dependence of the strains on displacements so that $\bar{\boldsymbol{B}}$ is dependent on $\tilde{\boldsymbol{u}}$ due to large displacements. The derivatives in $\bar{\boldsymbol{B}}$, the volume V and the Green-Lagrange strain $\boldsymbol{E}$ are defined relative to the undeformed coordinates $\boldsymbol{X}$, i.e. in the R-frame in Figure 2.1. $\bar{\boldsymbol{B}}$ can be written as two components $\boldsymbol{B}_0$ and $\boldsymbol{B}_L$ where $\boldsymbol{B}_0$ is the usual small displacement $\boldsymbol{B}$-matrix, and $\boldsymbol{B}_L$ is the component due to large displacements that is dependent on the nodal displacements

$$\bar{\boldsymbol{B}} = \boldsymbol{B}_0 + \boldsymbol{B}_L(\tilde{\boldsymbol{u}}) \tag{2.8}$$

The stress strain relation is given by

$$\boldsymbol{S} - \boldsymbol{S}_0 = \hat{\boldsymbol{D}}(\boldsymbol{E} - \boldsymbol{E}_0) \tag{2.9}$$

where $\hat{\boldsymbol{D}}$ is the 4^{th} order elasticity tensor. $\boldsymbol{S}_0$ and $\boldsymbol{E}_0$ represent the initial stress and strain respectively. To establish the tangential stiffness matrix, we can linearise equation 2.5, assuming constant external loading so that $\mathrm{d}\boldsymbol{F}^{ext}$ is zero. This can be formally written as

$$\mathrm{d}\boldsymbol{\psi} = \int_V [\mathrm{d}(\bar{\boldsymbol{B}}^T)\boldsymbol{S} + \bar{\boldsymbol{B}}^T \mathrm{d}(\boldsymbol{S})]\mathrm{d}V \tag{2.10}$$

From equations 2.9, 2.7, and 2.8,

$$\mathrm{d}\boldsymbol{S} = \hat{\boldsymbol{D}}\mathrm{d}\boldsymbol{E} = \hat{\boldsymbol{D}}\bar{\boldsymbol{B}}\mathrm{d}\tilde{\boldsymbol{u}} \qquad \text{and} \qquad \mathrm{d}\bar{\boldsymbol{B}} = \mathrm{d}\boldsymbol{B_L} \tag{2.11}$$

Equation 2.10 therefore becomes

$$\mathrm{d}\boldsymbol{\psi} = \int_V [\mathrm{d}(\boldsymbol{B_L}^T)\boldsymbol{S} + \bar{\boldsymbol{B}}^T\hat{\boldsymbol{D}}\bar{\boldsymbol{B}}\mathrm{d}\tilde{\boldsymbol{u}}]\mathrm{d}V = \int_V \mathrm{d}(\boldsymbol{B_L}^T)\boldsymbol{S}\mathrm{d}V + \bar{\boldsymbol{K}}\mathrm{d}\tilde{\boldsymbol{u}} \tag{2.12}$$

where

$$\bar{\boldsymbol{K}} = \int_V \bar{\boldsymbol{B}}^T\hat{\boldsymbol{D}}\bar{\boldsymbol{B}}\mathrm{d}V \tag{2.13}$$

$\bar{\boldsymbol{K}}$ is the large displacement matrix or initial displacement matrix. It can be split in the same fashion as $\bar{\boldsymbol{B}}$ in equation 2.8. In this case the component $\boldsymbol{K}_0$ is given as

$$\boldsymbol{K_0} = \int_V \boldsymbol{B_0}^T\hat{\boldsymbol{D}}\boldsymbol{B_0}\mathrm{d}V \tag{2.14}$$

and $\boldsymbol{K}_L$ is given as

$$\boldsymbol{K_L} = \int_V (\boldsymbol{B_0}^T \hat{\boldsymbol{D}} \boldsymbol{B_L} + \boldsymbol{B_L}^T \hat{\boldsymbol{D}} \boldsymbol{B_L} + \boldsymbol{B_L}^T \hat{\boldsymbol{D}} \boldsymbol{B_0}) \mathrm{d}V \tag{2.15}$$

The remaining part of equation 2.12 can be written as

$$\int_V \mathrm{d}(\boldsymbol{B_L}^T) \boldsymbol{S} \mathrm{d}V = \boldsymbol{K}_\sigma \mathrm{d}\tilde{\boldsymbol{u}} \tag{2.16}$$

where $\boldsymbol{K}_\sigma$ is symmetric and dependent on the stress level. It is known as the geometric (or initial stress) matrix and is given, according to Crisfield [20], by.

$$\boldsymbol{K_\sigma} = \int_V \boldsymbol{G}(\boldsymbol{X})^T \hat{\boldsymbol{S}} \boldsymbol{G}(\boldsymbol{X}) \mathrm{d}V \tag{2.17}$$

where $\boldsymbol{G}(\boldsymbol{X})$ is defined as in equation 2.18 and $\boldsymbol{X}$ indicates that the derivatives all defined with respect to the undeformed configuration

$$\boldsymbol{G} = \begin{bmatrix} N_{a,1} & 0 & 0 & \dots \\ N_{a,2} & 0 & 0 & \dots \\ N_{a,3} & 0 & 0 & \dots \\ 0 & N_{a,1} & 0 & \dots \\ 0 & N_{a,2} & 0 & \dots \\ 0 & N_{a,3} & 0 & \dots \\ 0 & 0 & N_{a,1} & \dots \\ 0 & 0 & N_{a,2} & \dots \\ 0 & 0 & N_{a,3} & \dots \end{bmatrix} \tag{2.18}$$

N_a is the shape function defined at node a, $N_{a,I}$ is a shorthand for the derivative of N_a with respect to I, and the "..." imply that the given three columns should be repeated

as many times as there are nodes i.e. only one node a is given. Also in equation 2.17 $\hat{\boldsymbol{S}}$ is defined as in equation 2.19

$$\hat{\boldsymbol{S}} = \begin{bmatrix} \bar{\boldsymbol{S}} & \mathbf{0} & \mathbf{0} \\ \mathbf{0} & \bar{\boldsymbol{S}} & \mathbf{0} \\ \mathbf{0} & \mathbf{0} & \bar{\boldsymbol{S}} \end{bmatrix}; \quad \text{where} \qquad \bar{\boldsymbol{S}} = \begin{bmatrix} S_{11} & S_{12} & S_{13} \\ S_{12} & S_{22} & S_{23} \\ S_{13} & S_{23} & S_{33} \end{bmatrix} \tag{2.19}$$

The tangential stiffness matrix $\boldsymbol{K}_T (= \bar{\boldsymbol{K}} + \boldsymbol{K}_{\boldsymbol{\sigma}})$ is thus given as

$$\boldsymbol{K_T} = \int_V \left[\bar{\boldsymbol{B}}(\boldsymbol{X})^T \hat{\boldsymbol{D}} \bar{\boldsymbol{B}}(\boldsymbol{X}) + \boldsymbol{G}(\boldsymbol{X})^T \hat{\boldsymbol{S}} \boldsymbol{G}(\boldsymbol{X}) \right] \mathrm{d}V \tag{2.20}$$

In a finite element formulation, positions and displacements anywhere can be approximated from nodal values as

$$x = \sum_a N_a(\boldsymbol{\zeta}) x_N^a \qquad \text{and} \qquad u = \sum_a N_a(\boldsymbol{\zeta}) \tilde{u}^a \qquad \Longrightarrow \qquad u_{i,I} = N_{a,I} \tilde{u}_i^a \tag{2.21}$$

The last expression implies summation over a. The Green-Lagrange strain tensor is written as

$$\boldsymbol{E} = \frac{1}{2} \left(\boldsymbol{F}^T \boldsymbol{F} - \boldsymbol{I} \right) \tag{2.22}$$

and we can write the deformation gradient in elemental form as follows

$$F_{iJ} = \delta_{iJ} + \frac{\partial u_i}{\partial X_J} = \delta_{iJ} + u_{i,J} \tag{2.23}$$

where δ_{iJ} is the Kronecker delta. It follows from above that

$$\delta F_{iJ} = \frac{\partial \delta u_i}{\partial X_J} = \delta u_{i,J} \tag{2.24}$$

Therefore, using equation 2.22, we have

$$E_{IJ} = \frac{1}{2}\left(F_{iI}F_{iJ} - \delta_{IJ}\right) \tag{2.25}$$

from which

$$\delta E_{IJ} = \frac{1}{2}\left(\delta F_{iI}F_{iJ} + F_{iI}\delta F_{iJ}\right) = \frac{1}{2}\left(\delta u_{i,I}F_{iJ} + F_{iI}\delta u_{i,J}\right) \tag{2.26}$$

The Green-Lagrange strain tensor is written in Voigt notation as

$$\boldsymbol{E} = [E_{11}, E_{22}, E_{33}, 2E_{12}, 2E_{13}, 2E_{23}]^T \tag{2.27}$$

hence

$$\delta\boldsymbol{E} = [\delta E_{11}, \delta E_{22}, \delta E_{33}, 2\delta E_{12}, 2\delta E_{13}, 2\delta E_{23}]^T \tag{2.28}$$

Substituting equation 2.26 into equation 2.28 gives

$$\delta\boldsymbol{E} = \begin{bmatrix} F_{i1}\delta u_{i,1} \\ F_{i2}\delta u_{i,2} \\ F_{i3}\delta u_{i,3} \\ F_{i1}\delta u_{i,2} + F_{i2}\delta u_{i,1} \\ F_{i3}\delta u_{i,1} + F_{i1}\delta u_{i,3} \\ F_{i2}\delta u_{i,3} + F_{i3}\delta u_{i,2} \end{bmatrix} \tag{2.29}$$

Equations 2.21 and 2.29 combine to give the $\bar{B}$ matrix for a given node a, from $\delta \boldsymbol{E} = \bar{B}\delta \boldsymbol{u}^a$ as follows

$$\delta \boldsymbol{E} = \begin{bmatrix} F_{11}N_{a,1} & F_{21}N_{a,1} & F_{31}N_{a,1} \\ F_{12}N_{a,2} & F_{22}N_{a,2} & F_{32}N_{a,2} \\ F_{13}N_{a,3} & F_{23}N_{a,3} & F_{33}N_{a,3} \\ F_{11}N_{a,2} + F_{12}N_{a,1} & F_{21}N_{a,2} + F_{22}N_{a,1} & F_{31}N_{a,2} + F_{32}N_{a,1} \\ F_{13}N_{a,1} + F_{11}N_{a,3} & F_{23}N_{a,1} + F_{21}N_{a,3} & F_{33}N_{a,1} + F_{31}N_{a,3} \\ F_{12}N_{a,3} + F_{13}N_{a,2} & F_{22}N_{a,3} + F_{23}N_{a,2} & F_{32}N_{a,3} + F_{33}N_{a,2} \end{bmatrix} \begin{pmatrix} \delta\tilde{u}_1^a \\ \delta\tilde{u}_2^a \\ \delta\tilde{u}_3^a \end{pmatrix} \quad (2.30)$$

and by using equations 2.23 to replace F in the $\bar{B}$ matrix one can easily split it into the small and large displacement components according to equation 2.8.

The above Lagrangian derivation is the more natural way of approaching the problem of geometric non-linearity but it introduces a complicated strain-displacement $\bar{\boldsymbol{B}}$ matrix as can be seen in equation 2.30. If one has been working with small strain formulations, then one has to reprogram all the finite element routines in order to implement this. Zienkiewicz and Taylor [90] carefully show that, taking advantage of the chain rule for differentiation, i.e.

$$\frac{\partial(.)}{\partial X_I} = \frac{\partial(.)}{\partial x_i}\frac{\partial(x_i)}{\partial X_I} = \frac{\partial(.)}{\partial x_i}F_{iI} \qquad \text{i.e.} \qquad \frac{\partial(.)}{\partial \boldsymbol{X}} = \frac{\partial(.)}{\partial \boldsymbol{x}}\boldsymbol{F} \quad (2.31)$$

the above derivations can be transformed to an equivalent deformed configuration formulation, which makes finite element implementation much easier.

2.3.1 $\boldsymbol{K}_T$ with respect to other stress and strain measures

A number of other representations of the tangent stiffness matrix for various conjugate stress and strain measures are given by Crisfield [20]. The one given for the Eulerian (deformed configuration) formulation, using the Jaumann rate of Cauchy

stress is as follows

$$\boldsymbol{K_t} = \int_{\omega} \left[\boldsymbol{B}(\boldsymbol{x})^T(\boldsymbol{C}^{JC} - \tilde{\boldsymbol{\sigma}} + \check{\boldsymbol{\sigma}})\boldsymbol{B}(\boldsymbol{x}) + \boldsymbol{G}(\boldsymbol{x})^T\hat{\boldsymbol{\sigma}}\boldsymbol{G}(\boldsymbol{x})\right] \mathrm{d}\omega \tag{2.32}$$

where $\boldsymbol{B}$ is the small strain B-matrix, $\boldsymbol{C}^{JC}$ is the elastic stiffness matrix appropriate for the Jaumann rate of Cauchy stress, ω is the volume defined with respect to the deformed coordinates $\boldsymbol{x}$, and the other terms are given as follows

$$\tilde{\boldsymbol{\sigma}} = \begin{bmatrix} 2\sigma_{11} & 0 & 0 & \sigma_{12} & \sigma_{13} & 0 \\ 0 & 2\sigma_{22} & 0 & \sigma_{21} & 0 & \sigma_{23} \\ 0 & 0 & 2\sigma_{33} & 0 & \sigma_{31} & \sigma_{32} \\ \sigma_{21} & \sigma_{12} & 0 & \tilde{\sigma}_{12} & \sigma_{23} & \sigma_{13} \\ \sigma_{31} & 0 & \sigma_{13} & \sigma_{32} & \tilde{\sigma}_{13} & \sigma_{12} \\ 0 & \sigma_{32} & \sigma_{23} & \sigma_{31} & \sigma_{21} & \tilde{\sigma}_{23} \end{bmatrix} \qquad \text{where} \qquad \tilde{\sigma}_{ij} = \frac{1}{2}(\sigma_{ii} + \sigma_{jj}) \tag{2.33}$$

$$\check{\boldsymbol{\sigma}} = \begin{bmatrix} \sigma_{11} & \sigma_{11} & \sigma_{11} & 0 & 0 & 0 \\ \sigma_{22} & \sigma_{22} & \sigma_{22} & 0 & 0 & 0 \\ \sigma_{33} & \sigma_{33} & \sigma_{33} & 0 & 0 & 0 \\ \sigma_{12} & \sigma_{12} & \sigma_{12} & 0 & 0 & 0 \\ \sigma_{13} & \sigma_{13} & \sigma_{13} & 0 & 0 & 0 \\ \sigma_{23} & \sigma_{23} & \sigma_{23} & 0 & 0 & 0 \end{bmatrix} \tag{2.34}$$

$$\hat{\boldsymbol{\sigma}} = \begin{bmatrix} \bar{\boldsymbol{\sigma}} & \mathbf{0} & \mathbf{0} \\ \mathbf{0} & \bar{\boldsymbol{\sigma}} & \mathbf{0} \\ \mathbf{0} & \mathbf{0} & \bar{\boldsymbol{\sigma}} \end{bmatrix}; \qquad \bar{\boldsymbol{\sigma}} = \begin{bmatrix} \sigma_{11} & \sigma_{12} & \sigma_{13} \\ \sigma_{12} & \sigma_{22} & \sigma_{23} \\ \sigma_{13} & \sigma_{23} & \sigma_{33} \end{bmatrix} \tag{2.35}$$

$$\boldsymbol{G} = \begin{bmatrix} N_{a,1} & 0 & 0 & \dots \\ N_{a,2} & 0 & 0 & \dots \\ N_{a,3} & 0 & 0 & \dots \\ 0 & N_{a,1} & 0 & \dots \\ 0 & N_{a,2} & 0 & \dots \\ 0 & N_{a,3} & 0 & \dots \\ 0 & 0 & N_{a,1} & \dots \\ 0 & 0 & N_{a,2} & \dots \\ 0 & 0 & N_{a,3} & \dots \end{bmatrix}; \quad \boldsymbol{B} = \boldsymbol{H}\boldsymbol{G}; \quad \boldsymbol{H} = \begin{bmatrix} 1 & 0 & 0 & 0 & 0 & 0 & 0 & 0 & 0 \\ 0 & 0 & 0 & 0 & 1 & 0 & 0 & 0 & 0 \\ 0 & 0 & 0 & 0 & 0 & 0 & 0 & 0 & 1 \\ 0 & 1 & 0 & 1 & 0 & 0 & 0 & 0 & 0 \\ 0 & 0 & 1 & 0 & 0 & 0 & 1 & 0 & 0 \\ 0 & 0 & 0 & 0 & 0 & 1 & 0 & 1 & 0 \end{bmatrix} \tag{2.36}$$

where the derivatives of the shape functions are with respect to the deformed configuration. Note that $\check{\boldsymbol{\sigma}}$ is not symmetric.

The elastic stiffness matrix $\boldsymbol{C}$- which is the inverse of the compliance $\boldsymbol{k}$ (below) - is defined in the crystallographic orientation and has to be transformed to any frame of reference where it may be needed according to the transformation matrices that map the respective frames to each other.

$$\boldsymbol{k} = \begin{bmatrix} 1/E_1 & -\nu_{12}/E_1 & -\nu_{13}/E_1 & 0 & 0 & 0 \\ -\nu_{12}/E_1 & 1/E_2 & -\nu_{23}/E_2 & 0 & 0 & 0 \\ -\nu_{13}/E_1 & -\nu_{23}/E_2 & 1/E_3 & 0 & 0 & 0 \\ 0 & 0 & 0 & 1/G_{12} & 0 & 0 \\ 0 & 0 & 0 & 0 & 1/G_{13} & 0 \\ 0 & 0 & 0 & 0 & 0 & 1/G_{23} \end{bmatrix} \tag{2.37}$$

In the present implementation, the result of applying the crystallographic orientation to $\boldsymbol{C}$ yields the required $\boldsymbol{C}^{JC}-$matrix. Meissonnier et al. [62] also give a derivation

for an appropriate $\boldsymbol{C}^{JC}-$matrix for use in eqn 2.32. Their derivation suggests that extra terms beyond the simple application of rotations above are required to get $\boldsymbol{C}^{JC}$ right. However, for the current configuration based formulation used here, when the extra correction terms were added, the simulation collapsed. Noteworthy, however, is the fact that to the point of collapse, the results obtained were exactly the same as those obtained without the correction terms. This is not surprising since (as both Meissonnier et al. [62] and Crisfield [20] state) $\boldsymbol{K}_T$ plays a fundamental role in the rate of convergence but has no effect on the accuracy of the converged solution. Since Meissonnier et al. [62] use an implicit solution procedure based on the intermediate configuration, it may be that these extra terms are useful if one uses such a scheme.

The following section discusses the implicit integration of constitutive equations that is performed in an Abaqus UMAT subroutine and which is separate from the above solution for $\boldsymbol{K}_T$ which is provided in the UEL subroutine and used by the Abaqus kernel to estimate the displacements.

2.4 Implicit Integration of constitutive equations

In order to perform the implicit integration of constitutive equations with respect to the deformed configuration for large deformation, it is necessary to take care of the fact that as well as the usual response to straining, the Cauchy stress $\boldsymbol{\sigma}$ also changes due to rigid body rotations [8]. A summary of a small deformation stress update [26] is given below followed by a modification to the same to account for rigid body rotations.

For small deformation

$$\begin{aligned}
\boldsymbol{\sigma}_{t+\Delta t} &= \boldsymbol{C}\boldsymbol{\epsilon}^e_{t+\Delta t} = \boldsymbol{C}\boldsymbol{\epsilon}^e_t + \boldsymbol{C}\Delta\boldsymbol{\epsilon}^e = \boldsymbol{C}\boldsymbol{\epsilon}^e_t + \boldsymbol{C}\dot{\boldsymbol{\epsilon}}^e\Delta t \\
&= \boldsymbol{C}\boldsymbol{\epsilon}^e_t + \boldsymbol{C}(\dot{\boldsymbol{\epsilon}} - \dot{\boldsymbol{\epsilon}}^p)\Delta t = \boldsymbol{\sigma}_t + \boldsymbol{C}\dot{\boldsymbol{\epsilon}}\Delta t - \boldsymbol{C}\dot{\boldsymbol{\epsilon}}^p\Delta t \\
&= \boldsymbol{\sigma}^{tr} - \boldsymbol{C}\dot{\boldsymbol{\epsilon}}^p\Delta t
\end{aligned} \tag{2.38}$$

where the superscript tr implies the trial stress at $t = t + \Delta t$. In the case of large deformation, using the Jaumann rate of Cauchy stress,

$$\begin{aligned} \dot{\boldsymbol{\sigma}}_{t+\Delta t} &= \boldsymbol{C}\boldsymbol{D}^e + \boldsymbol{W}\boldsymbol{\sigma}_t - \boldsymbol{\sigma}_t\boldsymbol{W} = \boldsymbol{C}\boldsymbol{D}^e + \dot{\boldsymbol{\sigma}}^R \\ &= \boldsymbol{C}(\boldsymbol{D} - \boldsymbol{D}^p) + \dot{\boldsymbol{\sigma}}^R = \boldsymbol{C}\boldsymbol{D} + \dot{\boldsymbol{\sigma}}^R - \boldsymbol{C}\boldsymbol{D}^p \end{aligned} \tag{2.39}$$

This gives the following result

$$\begin{aligned} \boldsymbol{\sigma}_{t+\Delta t} &= \boldsymbol{\sigma}_t + (\boldsymbol{C}\boldsymbol{D} + \dot{\boldsymbol{\sigma}}^R)\Delta t - \boldsymbol{C}\boldsymbol{D}^p\Delta t \\ &= \boldsymbol{\sigma}^{tr} + \dot{\boldsymbol{\sigma}}^R\Delta t - \boldsymbol{C}\boldsymbol{D}^p\Delta t \end{aligned} \tag{2.40}$$

where $\dot{\boldsymbol{\sigma}}^R\Delta t$ is a stress increment during the time Δt due to rigid body rotation. Notice that the only difference between the small and large deformation formulations is the introduction of a term that expresses the change in Cauchy stress due to rigid body rotations during the time Δt. In both cases the (rate of) plastic strain increment $\boldsymbol{D}^p$ can be computed from the symmetric part of the plastic velocity gradient. The scheme used to compute $\boldsymbol{D}^p$ is detailed by Dunne et al. [26].

During the implicit iteration to solve for $\boldsymbol{D}^p$, a residual $\boldsymbol{\phi}$ is defined so that from eqn 2.38 we have

$$\boldsymbol{\phi} = \boldsymbol{\sigma}_{t+\Delta t} - (\boldsymbol{\sigma}^{tr} - \boldsymbol{C}\boldsymbol{D}^p\Delta t) \tag{2.41}$$

The iteration is done to find a $\boldsymbol{D}^p$ such that $\boldsymbol{\phi}$ achieves a prescribed tolerance. The point to note about this iteration scheme is that only stresses determined from material straining are to be used in order to achieve the correct value of the plastic strain increment. The increment in stress due to rigid body rotations should therefore only be added on (in obtaining $\boldsymbol{\sigma}_{t+\Delta t}$) after the plastic strain increment has been determined.

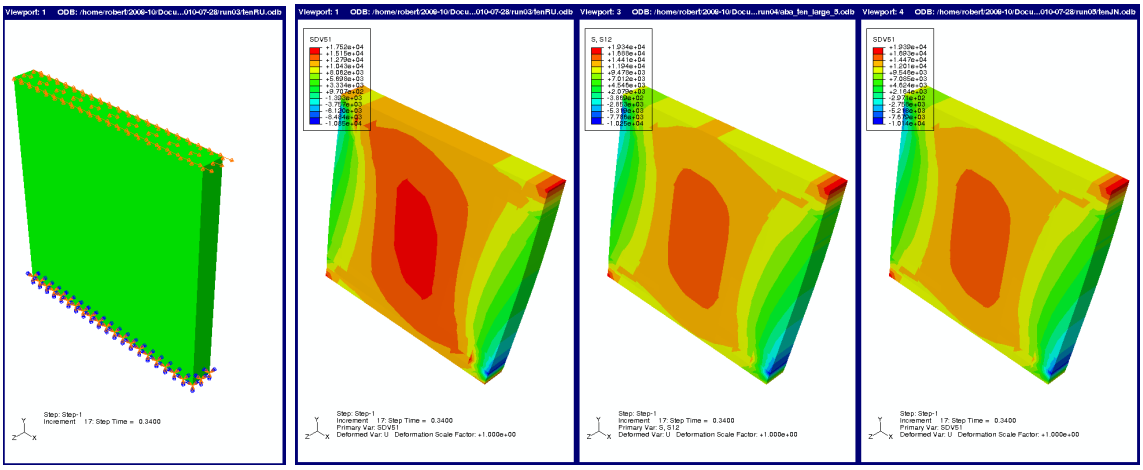
However, it should be noted that the stress $\boldsymbol{\sigma}_{t+\Delta t}$ used in the iteration process already contains a component that is due to rigid body rotations, from any previous time increments. This introduces a complication that may require extra storage if we are to truly use only the stresses determined from material straining in order to achieve the correct value of the plastic strain increment.

The above scheme gives better results than have been achieved in the previously used scheme, as seen in the results below (Figure 2.2), but it is still unsatisfactory that we have to separately account for contributions due to rotation, something we cannot avoid as long as we directly work with the Cauchy stress tensor for the time-integration of the constitutive equations. Moreover with this scheme it is difficult to simulate strain that is large enough for texture evolution without employing complicated remeshing algorithms - attempts to simulate larger strains, beyond applied compressive nominal strain of about 10%, with this scheme led to simulation collapse with Abaqus reporting the cause of failure as excessive mesh distortion.

Results could potentially be improved even further by using stress and strain measures more suited to finite strain formulations. A commonly used such measure, in the literature pertaining to crystal plasticity, is the second Piola-Kirchoff stress $\boldsymbol{S}$ and its work conjugate the Green-Lagrange strain $\boldsymbol{E}$ [38, 43, 62, 65, 67], which are usually utilised to update stress in an intermediate (relaxed) configuration defined by the usual multiplicative decomposition of the deformation gradient $\boldsymbol{F} = \boldsymbol{F}^e\boldsymbol{F}^p$ so that this configuration is located $\boldsymbol{F}^e$ away from the deformed configuration and $\boldsymbol{F}^p$ away from the undeformed configuration, see Section 1.3.1. The Cauchy stress is then obtained from eqn 2.6, with the relevant modification, for use in the expression for $\boldsymbol{K}_T$, eqn 2.32. This approach to stress-strain update is explored in Chapters 6 to 9 where very large deformation is desired in order to simulate texture evolution. In the meantime the scheme developed here is employed in the following chapters (4 and 5) where relatively

low strain suffices for our needs.

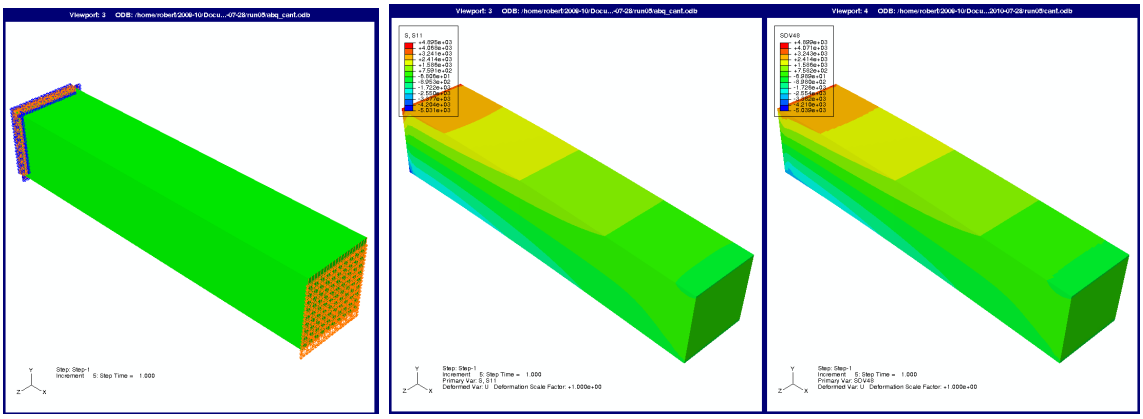
2.5 Results



(a) Loading (b) σ_{xy}:intermediate config, Abaqus, new scheme

Max values: 1.752×10^4 | 1.934×10^4 |$1.939 \times 10^4 MPa$
Min values: -1.085×10^4 |-1.025×10^4 |$-1.014 \times 10^4 MPa$

Figure 2.2: Elastic shear loading: $100 \times 100 \times 10 \mu m$; top deflection: $65 \mu m$.



(a) Loading (b) σ_{xx}: Abaqus, new scheme

Max values: 4.895×10^3 |$4.899 \times 10^3 MPa$
Min values: -5.031×10^3 |$-5.039 \times 10^3 MPa$

Figure 2.3: Cantilever bending: $100 \times 20 \times 20 \mu m$; End deflection of $5 \mu m$. Abaqus and deformed config comparisons only

Elastic large deformation comparisons were made between this deformed configuration stress update scheme and the one in use until this point in the project, which was based on update in an intermediate configuration defined by the polar decomposition,

i.e. located $\boldsymbol{U}$ away from the undeformed reference frame ($\boldsymbol{U} = \boldsymbol{R}^{-1}\boldsymbol{F}$) - see Liang [56, chap. 4] for full details on this intermediate configuration update scheme. The two were also compared against Abaqus/standard elasticity for shear loading and for a cantilever. Shear loading was selected because it results in fairly large rigid body rotations. Cantilever bending is also a fairly complex loading state since stresses vary both along the length and the height of the cantilever. Both cases thus provide very good tests for the stress update schemes. The results are given in Figures 2.2 and 2.3.

2.6 Conclusion

This chapter has reviewed the theory of large deformations involving large strains and large rotations. Specifically the derivation of the tangent stiffness matrix and its implementation into finite element code have been discussed for the choices of stress and strain measures relevant to the question the thesis seeks to answer, i.e. modelling texture evolution.

The implicit integration of constitutive equations is also discussed and improvements proposed to a Cauchy stress-based scheme that has been in use up to this point in the project in order to account for the effects of rigid body rotations on the Cauchy stress with a view to modelling very large strains. The improvements led to better results compared to the previous scheme when benchmarked against Abaqus/Standard results. However, they were not sufficient to address the need for simulating the very large strains needed to model texture evolution without resorting to complex remeshing algorithms or using continuation simulations, i.e. a series of simulations where a previous simulation's output is used as input for a following simulation.

The overall compressive strain, of <10% nominal strain, achievable with the improved scheme is sufficient for studies involving relatively small strains. The code developed is therefore used for the studies in Chapters 4 and 5. A more robust code is

later developed in Chapter 6 for use in the texture evolution studies thereafter.

Chapter 3

Pole figure construction

3.1 Executive summary

In order to fully explore and understand pole figures, a program was written in the Python programming language to produce pole figures (and inverse pole figures). This chapter presents the theory used in constructing the pole figures and ends by presenting some results produced by the developed Python program, as well as giving a short description of how the program works. The program developed in this chapter has been used to produce all the pole figures in the rest of the thesis, as a convenient alternative to commercial solutions.

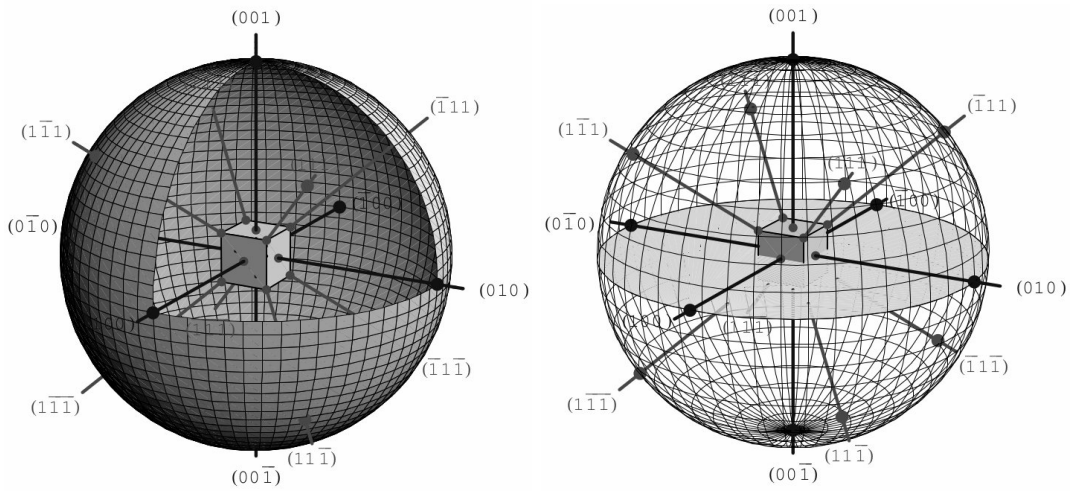
3.2 Introduction

Pole figures may be constructed as either a stereographic or equal area projection. Given Euler angles describing a texture, representation of it on a pole figure involves four main stages: (i) converting the pole into an equivalent cartesian unit vector, (ii) defining the relevant symmetry elements, (iii) obtaining a spherical projection of the pole, (iv) projecting the pole onto a plane of the sphere parallel to the equatorial plane: an equatorial plane projection is a stereographic pole figure while a polar plane projection defines an equal area pole figure.

3.2.1 The Pole and the Spherical Projection

A pole is an unsigned normal to a plane. More strictly, it is the point where the unsigned normal to a plane strikes the surface of a sphere if this normal is drawn through the centre of the sphere. The significance of the "unsignedness" is that for a given plane, whether we chose to plot the end of the normal that is in the northern

hemisphere of the projection sphere (which if we made it signed we could call the positive end) or the end in the southern hemisphere (which could consequently be called the negative end), we will be plotting the same pole [49].



(a) Sphere of projection (b) Poles

Figure 3.1: Pole figure construction: illustration of the sphere of projection and poles.

Imagine a crystal to be positioned at the centre of a unit sphere - called a *sphere of projection* - and draw normals to crystal planes through the centre of the sphere to intersect the surface of the sphere, say at P; see Figure 3.1(a) for example. P is called the *pole* of the plane for which OP is the normal. A direction can also be represented by a point on the sphere defined as the point where the line parallel to the direction passing through the centre of the sphere strikes the surface of the sphere. A crystal plane can be represented by drawing a parallel plane through the centre of the sphere and extending it until it strikes the sphere. Since the plane goes through the centre of the sphere it is a diametral plane and the line of the intersection of the sphere and such a plane is called the *great circle*: a circle on the surface of a sphere with radius equal to the radius of the sphere. Representing the directions in the crystal, i.e. normals to lattice planes or lattice directions, by points (poles) on the surface of the sphere results in a *spherical projection* of the crystal [48]; see for Figure 3.1(b) example.

For a specified plane (hkl), the normal to this plane is not generally the same

as the direction [hkl]. Indeed it is only in cubic crystal systems that direction [hkl] necessarily coincides with the normal to the plane (hkl) for all h,k,l [48]. In other crystal systems, this may only be true for one or more special lattice planes, but not in general. In an orthorhombic crystal, for example, a normal to the plane (221), i.e. its pole, is also commonly labeled (221); it corresponds to a vector in "reciprocal space" Bhadeshia [10]. However the direction [221] is not parallel to the pole (221): it is not perpendicular to the plane (221) [49].

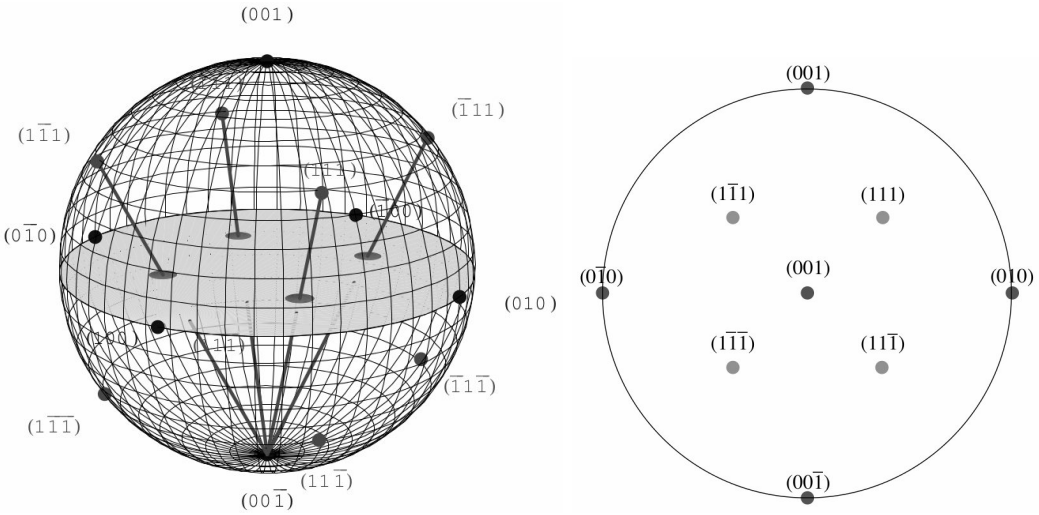
A north pole is defined, where the z-axis exits the sphere, and a standard meridian is defined e.g. where the x and z-planes meet (the Greenwich). Two angles Ψ and Θ are needed which describe a point on the surface of the unit sphere. The longitudes (Θ) are defined to be increasing/positive according to the right hand rule. Ψ and Θ can also be introduced as a series of two specific rotations e.g. first a clockwise rotation of Ψ about the positive z-axis and then a clockwise rotation of Θ about the new positive y-axis. These are therefore two "Euler angles" for locations on the surface of a sphere [49].

The point to be plotted can be chosen in two ways (since poles are unsigned normals). So we pick a hemisphere - usually the northern hemisphere in materials science - and plot the end of the pole that appears in that hemisphere. Every point on the hemisphere can then be mapped onto the inside of a circle. The representation of directions on the surface of a unit sphere is especially convenient when we have many crystals in one polycrystalline sample: their relative orientation is immediately evident, and the local density of points reflects exactly the number of grains in a given interval of directions: the orientation distribution.

One needs two numbers to specify an direction; they are most conveniently chosen as the coordinates on the surface of: a sphere, if they are signed directions; a hemisphere if they are unsigned. The latter may be mapped onto the area of a circle and the former

onto two circles [49].

3.2.2 The Stereographic Projection



(a) Intersecting equatorial plane (b) Pole figure

Figure 3.2: Pole figure construction: illustration of pole projection from the northern hemisphere to the south pole and the resulting pole figure.

If we choose to project the pole P in the northern hemisphere from the south pole S, the point P' where line PS intersects the equatorial plane (i.e. the primitive circle or simply primitive) is then defined as the stereographic projection of P; see Figure 3.6 for example.

All poles in the northern hemisphere give stereographic projections inside the primitive. Poles in the southern hemisphere project outside the primitive. It is inconvenient to work with poles outside the primitive and to avoid this, a pole in the southern hemisphere may be projected from the north pole to give a projected pole inside the primitive. This new pole is normally distinguished from the *true* projection - which is outside the primitive - by using an open circle instead of a dot.

The stereographic projection is important in crystallography because it is angle true, i.e. angles on the sphere of projection project as equal angles. Also all circles (great or small) on the surface of the sphere of projection project as circles [48]

3.2.3 Orientation relationship between crystal and sample axes

The orientation matrix $\boldsymbol{g}$ describing a crystal's orientation relative to sample axes (and vice versa) is constructed from three Euler Angles in a specified notation e.g Bunge, Roe or symmetric Kocks angles. This involves construction of $\boldsymbol{g}$ according to the ZXZ route: anticlockwise rotations about Z, then the new X and the finally the new Z (see appendix A.1 for a fuller review of these). Other routes are also possible e.g. using Cardan angles, Nautical angles, etc which may involve rotation sequences such as ZYZ, XYX, XZY etc [79].

Traditionally, $\boldsymbol{g}$ is defined such that it represents a rotation from the sample axes to the crystal axes. Thus it describes the crystal axes (rows) expressed in terms of the sample axes (columns). Figure 3.3 illustrates Bunge Euler angles used to define $\boldsymbol{g}$. To start the process for constructing the pole figure, the transpose of $\boldsymbol{g}$ is applied to the given pole which transforms it from the crystal to the sample axes. The rotated pole can then be referred to the unit sphere to construct the pole diagram.

3.3 Macroscopic symmetry elements

The most basic form of structural symmetry is that contained in a crystal structure since the crystal structure is the basic structural element common to most materials. A material is crystalline if its structure can be idealised into having discrete translation symmetry at the atomic level [49].

The existence of translation symmetry limits the number of symmetry elements that can be present. The macroscopically measured properties of a crystal can be defined and understood without reference to the translational symmetry elements defined by the lattice. If translational symmetry of the crystal is disregarded, the remaining symmetry elements (i.e., rotational symmetry, mirror planes, and the centre of inversion

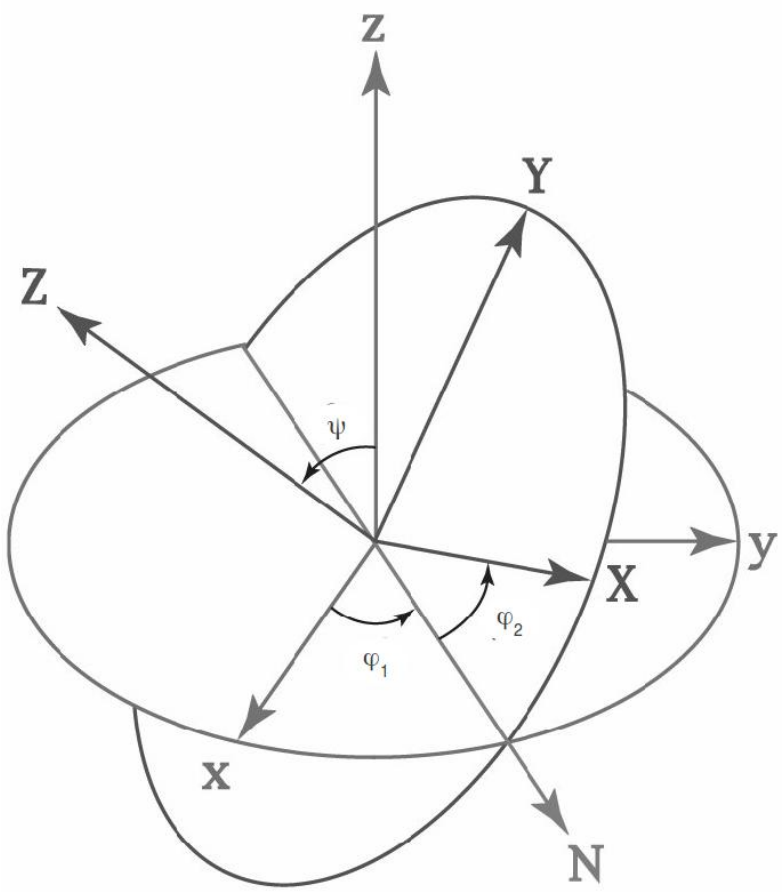


Figure 3.3: An illustration of Bunge Euler angles.

- the centre of the sphere of projection) can be arranged into 32 consistent groups: the 32 crystallographic *point groups* or *crystal classes*. They are so-called because all of the symmetry elements in a group pass through a single point and the operation of these elements leaves just one point unmoved - the point through which they pass. A "group" of symmetry elements consists of all elements that, if applied in succession (or again), give an element that is aready a member of the set. Knowlegde of this group is useful for enforcing all applicable symmetries in a calculation. These point groups are called macroscopic symmetry elements because their presence or absence can be deduced from macroscopic tests such as the symmetry of physical properties or the arrangement of external faces [48, 49]. The various different combinations of pure rotation axes $(1, 2, 3, 4, 5, 6)$ and rotoinversion axes $(\bar{1}, \bar{2}, \bar{3}, \bar{4}, \bar{5}, \bar{6})$ constitute the 32 crystal classes. The 32 classes are grouped into systems (i.e. triclinic, monoclinic,

orthorhombic, trigonal, tetragonal, hexagonal and cubic) according to the presence of symmetry elements [48]. The nomenclature of the crystal classes is as follows. X and $\bar{X}$ indicate a rotation axis and inversion axis respectively. X/m is a rotation axis normal to a mirror plane, Xm is a rotation axis with a mirror plane parallel to it, $X2$ is a rotation axis with a diad (2) normal to it. X/mm indicates a rotation axis with a mirror plane normal to it and another parallel to it. $\bar{X}m$ is an inversion axis with a parallel plane of symmetry. A plane of symmetry is an alternative description of a mirror plane.

A full description of the crystal's symmetry involves a description of the spatial distribution of the symmetry elements, i.e. a combination of point groups and translations. There are 230 crystallographic space groups and each one of them gives the fullest description of the symmetry of the crystal possessing that space group. For discussion of imperfections in crystals and for texture analysis, space groups are not of interest [48, 49].

All lattices are centrosymmetric and so are all crystals with a single atom in the motif. Those with a multi-atom motif at each lattice point generally have lower symmetry than that of the lattice but they nevertheless have an inversion centre. A Laue group is the crystal class formed when a centre of inversion is added to the symmetry elements already present. There are 11 such classes [48, 49].

Symmetry operators of rotation groups are listed in chapter 1, table II of Kocks et al. [49] and in an appendix in Randle and Engler [68]. The different groups and their significance for the different crystal systems are detailed in chapter 2 of Kelly and Groves [48] and chapter 1 of Kocks et al. [49]. These symmetries have to be taken into account when one constructs the pole diagrams. For this project, attention is drawn to the symmetries applicable to cubic and hexagonal crystal systems - since it is intended to look at single and combined phase systems where the two apply.

3.4 HCP planes and directions

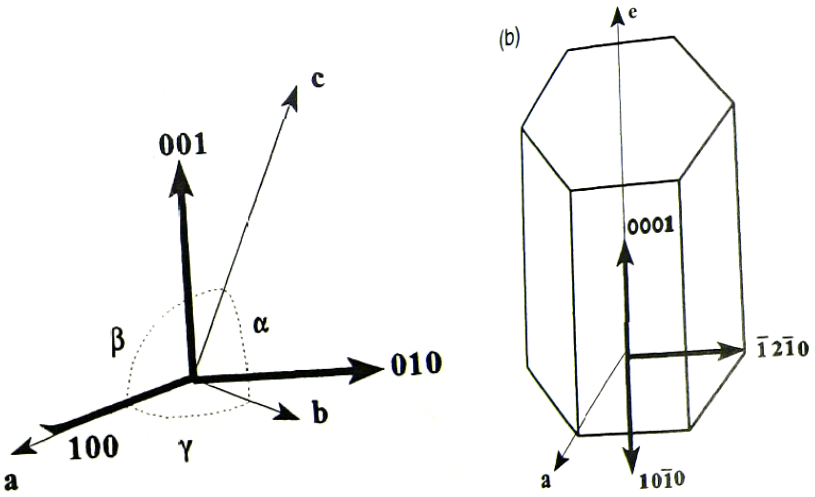


Figure 3.4: For HCP it is necessary to convert from the Miller-Bravais 4-index notaion to an equivalent 3-index orthogonal set for projection. Courtesy of Randle and Engler [68].

For planes in the hexagonal crystal system, the index can be represented by using the Miller index notation or the Miller-Bravais notation where a fourth index is introduced such that (hkl) becomes (hkil) where $i = -(h + k)$. To change from the four to the three index notation one only has to delete the third index. For example the following are equivalent pairs: $(\bar{1}\bar{1}0), (\bar{1}\bar{1}20)$; $(\bar{1}00), (\bar{1}010)$; $(2\bar{1}0), (2\bar{1}\bar{1}0)$.

The Miller-Bravais system can also be used for directions such that [uvw] becomes [uvtw] with t bearing the same relationship to u,v as i to h,k for planes. However, care has to be taken in this case to ensure that the result of a three index notation are the same as those of a four one. Directions are specified by taking steps along all three axes and arranging that the step along the u-axis is of such length that the number of unit repeat vectors moved along the t-direction is equal to the negative of (u+v). For example the following are equivalent pairs: $[100], [2\bar{1}\bar{1}0]$; $[11\bar{2}0], [110]$; $[01\bar{1}0], [120]$; $[1\bar{2}13], [0\bar{1}1]$. It should be noted that the Miller-Bravais index cannot always be immediately written down from the first two indices of the three index

triplet, as is the case for a plane [48]. In this case if one started with a four index value, one can get two possible permutations of a three index notation that give the same direction as the four index one, i.e. some ambiguity is introduced.

Since in a cubic system the plane Miller indices also specify the direction of the normal to the plane, one just needs to normalise this and apply the orientaion matrix to it in order to construct the pole figure, as previously described. However, for HCP, since the axes in the plane are not at right angles to one another, and since the three axes are not of equal length (i.e. the system is not an orthonormal one), care has to be taken in order to determine the normal to a plane.

Determining the normal is straight forward for basal and prismatic planes. For the basal plane (0001), the normal is simply [001]. For the prismatics ($hki0$), it is always true that the first three indices of the plane describe a direction $[hki]$ normal to the plane [49].

For the pyramidal planes, it is best to work out the normal from first principles (i.e. by referring to the definition of the indices of the plane). First, all the axes $\boldsymbol{a}_1, \boldsymbol{a}_2, \boldsymbol{a}_3, \boldsymbol{c}$ are expressed as vectors in the usual cartesian coordinate system. Then given a plane $(hkil)$, each non-zero member of $(hkil)$ is inverted and multiplied by the vector of the axis in its direction giving vectors in the cartesion system of the form: $\boldsymbol{a}_1/h, \boldsymbol{a}_2/k, \boldsymbol{a}_3/i, \boldsymbol{c}/l$. From this, two vectors in the plane can be computed with normal vector arithmetic, e.g. $\boldsymbol{v}_1 = \boldsymbol{a}_1/h - \boldsymbol{a}_2/k$ and $\boldsymbol{v}_2 = \boldsymbol{a}_1/h - \boldsymbol{c}/l$. A normal to the plane is the cross product of $\boldsymbol{v}_1$ and $\boldsymbol{v}_2$. Because of symmetry, the order of the two vectors in taking the cross product is immaterial. The opposite pole will always be produced by the inversion centre symmetry element.

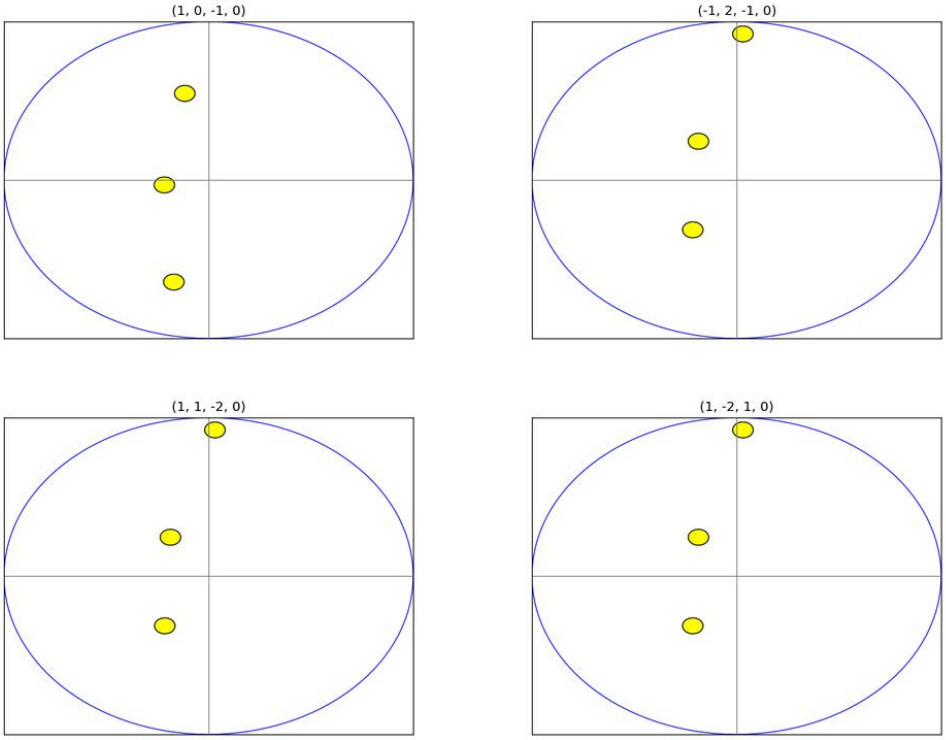
Other schemes for finding the normal to planes are available, although one has to be careful when utilising them. One such scheme is that proposed by Randle and Engler [68]. In this scheme, the Miller-Bravais plane index is converted into three index

notation as described above. A matrix L (as defined in Randle and Engler [68] chapter 2) is then applied to the result. This is then expected to transform the hexagonal reference system to an orthonormal one like that of a cubic. This kind of operation would enable all crystal systems to basically have the same form of crystal coordinate system, i.e. orthonormal. This scheme was attempted but it was found that there are some slight inconsistencies in the results it produces.

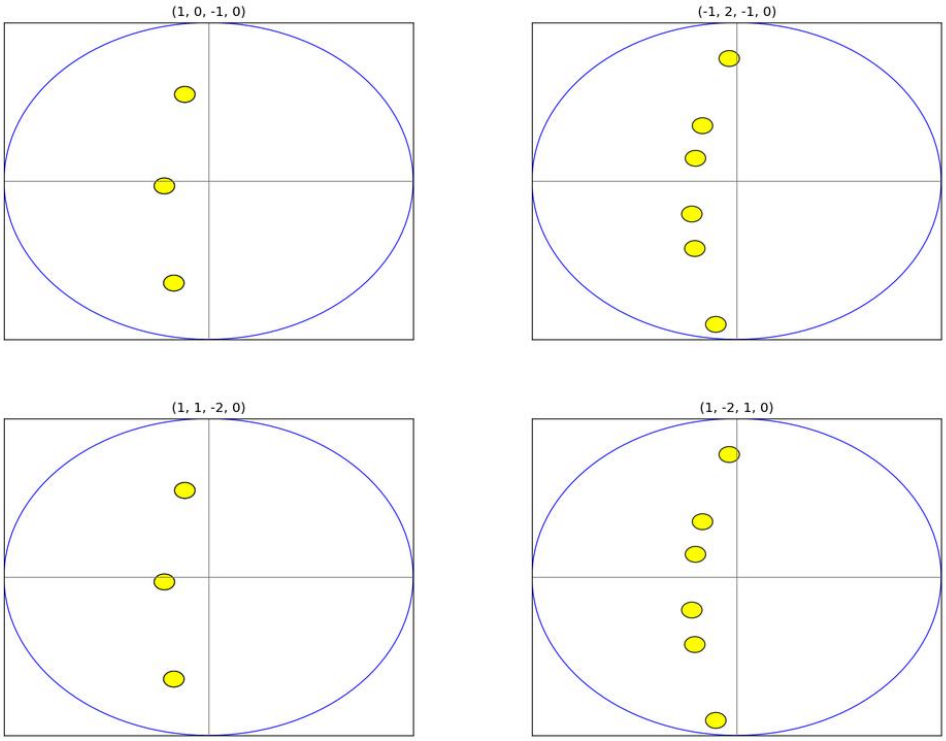
Consider Figure 3.5 where the two schemes above have been applied to a single HCP crystal whose orientation is given by the Bunge Euler angles $(6.21, 1.99, 2.53)$ - in radians. Figure 3.5(a) gives results from the first principles scheme while (b) gives those from the L-matrix scheme. Pole figures for the following prismatic planes are shown in the figure, respectively: $(10\bar{1}0)$, $(\bar{1}2\bar{1}0)$, $(11\bar{2}0)$ and $(1\bar{2}10)$. There are two things to note in the figures: in (a), $(\bar{1}2\bar{1}0)$, $(11\bar{2}0)$ and $(1\bar{2}10)$ are the same and $(10\bar{1}0)$ is different than them; in (b), $(\bar{1}2\bar{1}0)$ and $(1\bar{2}10)$ are the same and different than $(10\bar{1}0)$ and $(\bar{1}2\bar{1}0)$, which are also the same. From the crystal geometry of the HCP crystal, we know that $(10\bar{1}0)$ and $(\bar{1}2\bar{1}0)$ should not be the same. We also know that $(\bar{1}2\bar{1}0)$, $(11\bar{2}0)$ and $(1\bar{2}10)$ are symmetrically equivalent and therefore should give exactly the same results. All the symmetry elements for the HCP (and for the cubics -separately) were incorporated into the program developed to produce these pole figures. It is obvious that there is an error introduced by the combination of the L-matrix and the use of the three index notation for HCP. The source of this error is a factor worth investigating in future since the use of such a matrix is a neat solution and one worth polishing if possible.

3.5 Implementation

A program has been developed in the Python programming language to produce the pole figures (and inverse pole figures) using the methodology described in this section.



(a) First principles scheme



(b) L-matrix scheme

Figure 3.5: Comparison of symmetry results for the calculation from first principles and that based on the L-Matrix given by Randle and Engler [68].

Given texture information in the form of Euler angles (for either cubic or hexagonal crystal geometry), the program computes the relevant $\boldsymbol{g}$ matrices, determines which geometry it has received, i.e. either cubic or hexagonal, and then chooses the course of action. For cubics, it normalises the pole given and then generates the xy coordinates for the poles in the unit circle after computing all the relevant cubic symmetries. For hexagonals, it chooses a scheme to implement the conversion from four to three indices (it is enabled to choose between the two systems described in this chapter) and normalises the result. It then deals with the result in the same manner as for the cubic. The points are then plotted with Python's graphing library matplotlib.

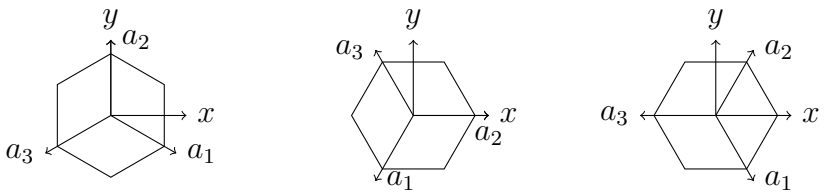
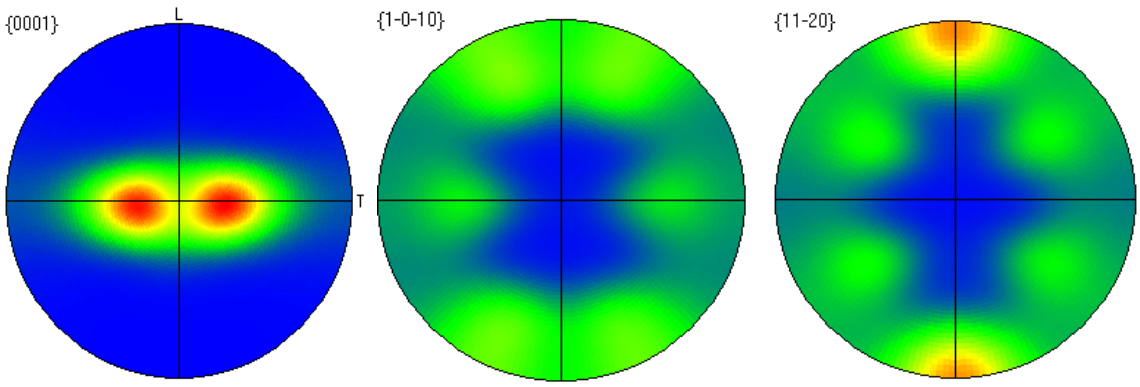


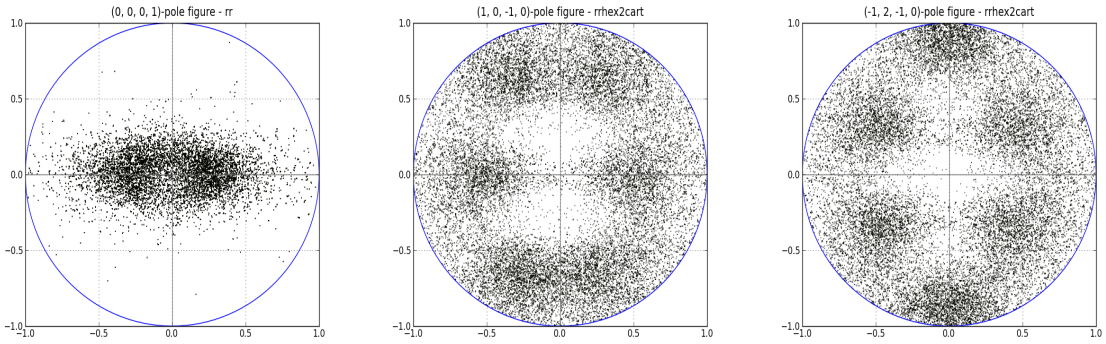
Figure 3.6: Defining the cartesian axes relative to the natural crystallographic axes for hcp crystal geometry. The leftmost system is required to faithfully represent received pole figures. The other alternative configurations are also generally used in the literature.

Care must be taken when defining the cartesian axes relative to the crystallographic axes in the case of hexagonal geometry, otherwise pole figures may get swapped, e.g.$(10\bar{1}0)$ may get plotted as $(11\bar{2}0)$. The following three options were found in the literature (see Figure 3.6): (i) $X_1 = [10\bar{1}0]$, $Y_1 = [\bar{1}2\bar{1}0]$, $Z = [0001]$; (ii) $X_2 = [11\bar{2}0]$, $Y_2 = [\bar{1}100]$, $Z = [0001]$; and (iii) $X_3 = [\bar{1}2\bar{1}0]$, $Y_3 = [\bar{1}010]$, $Z = [0001]$. Option (i) was used to match the pole figures provided by Rolls-Royce, fig 3.7. FCC Nickel data was also obtained from Ben Britton[1]. Fig 3.8 shows the images obtained from Ben for FCC Nickel in smoothed and unsmoothed form alongside those obtained from the program developed here.

[1]Ben Britton was working with A.J. Wilkinson at Oxford's Department of Materials at the time.



(a) 0001 (b) $10\bar{1}0$ (c) $\bar{1}2\bar{1}0$



(d) 0001 (e) $10\bar{1}0$ (f) $\bar{1}2\bar{1}0$

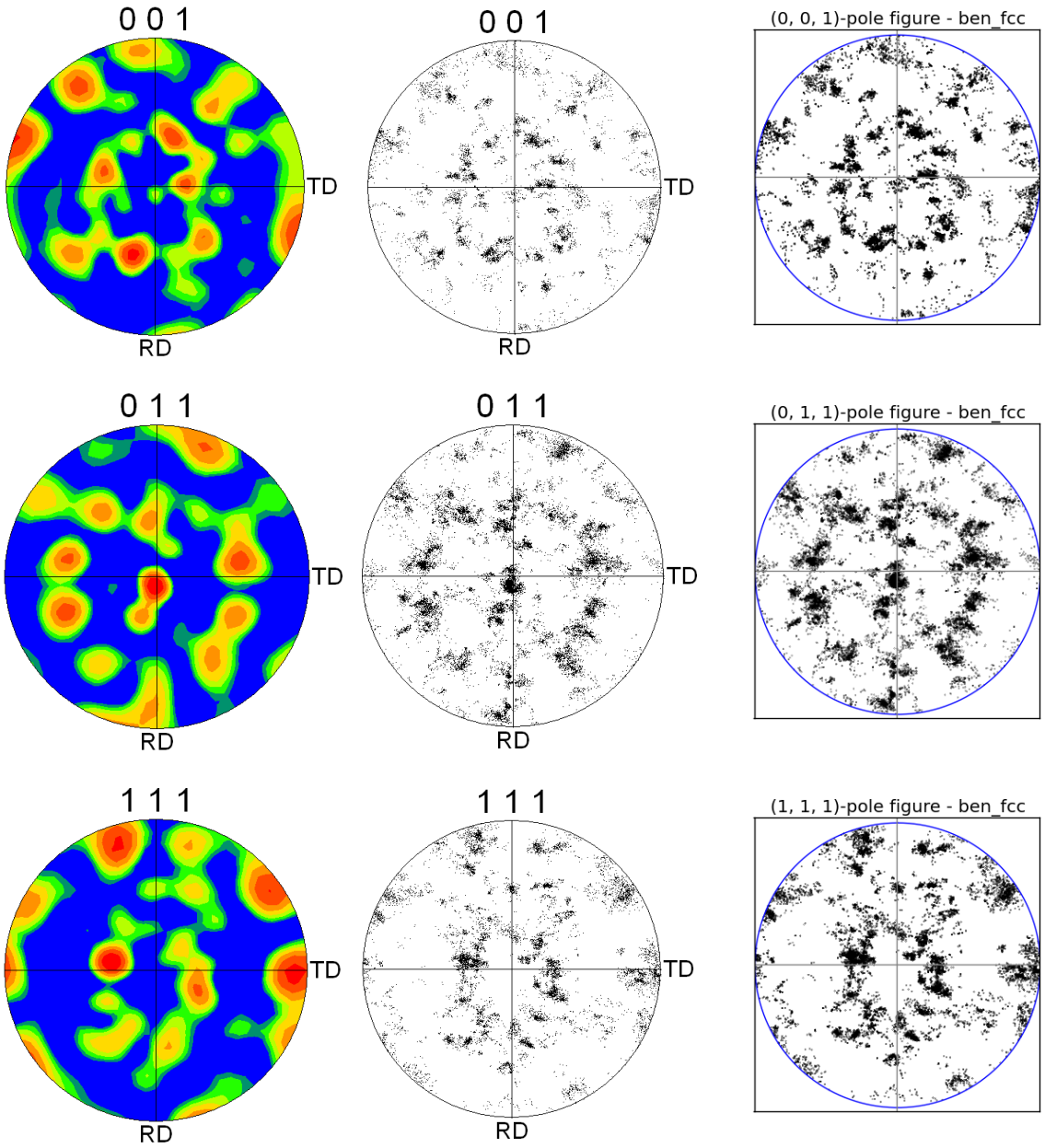
Figure 3.7: Comparison of pole figures obtained from Rolls-Royce (a–c) with those obtained by the program developed here (d–f).

3.6 Discussion and conclusions

This chapter has reviewed the theory needed in the construction of pole figures and presents some pole figures for hcp and cubic materials that have been constructed with a Python programme developed here based on the theory that has been discussed.

For purposes of comparison with commercial pole figure software packages, data was received from two sources (as stated in Section 3.5) both as Euler angles in text files for use to construct the pole figures with the software developed here, and as pole figures constructed by the commercial pole figure software packages. Good qualitative comparison between the received pole figures and those developed by the software developed here has been obtained.

For hcp materials, it is concluded that it is better to work from first principles



(g) Ben's figures smoothed (h) Ben's figures not smoothed (i) Figures from the program

Figure 3.8: Comparison of Pole figures obtained from Ben's Ni experiments with those obtained by the program developed here.

than from the L-matrix scheme available from literature. The L-matrix scheme has been shown to lead to errors. It would, however, be useful to investigate the source of this error in future because the idea of a single L-matrix would be a neat solution for purposes of constructing pole figures.

It is also noted, for hcp crystals, that care must be taken when choosing the relationship between the orthogonal cartesian set of axes and the natural crystals axes

- which are not an orthogonal set. Different choices could lead to swapping of pole figures when compared to pole figures from different pole figure software packages. Normally user manuals for any selected pole figure software package should state what relationship between these two sets of axes is implemented.

For purposes of texture evolution modelling, the practice of reproducing initial pole figures as received from experimentalists is worth doing every time new data is received as it enables the modeller to confirm that model reference axes are consistent with those expected by experimentalists. Failure to do this basic check could lead to specifying a model loading direction (as normally defined by the rolling, transverse, and normal directions on pole figures) that is different from the direction used in the experiments. This would have the effect of working with essentially different initial textures, which is undesirable.

Chapter 4

Geometrically necessary dislocation modelling

4.1 Executive summary

The geometric dislocation tensor has been derived in forms suitable for both deformed and undeformed configuration formulations, and reconciled with the various suggestions of its form in the literature. The result, together with Nye's slip-systemwise-discrete tensor, has been implemented in crystal plasticity finite element code to enable determination of GND accumulation on the active and independent a-type basal, prismatic and pyramidal and c+a-type pyramidal slip systems in hcp crystals. The GND density is fully coupled with the crystal slip rule.

A model near-α Ti polycrystal under deformation has been analysed using this approach to determine the GND densities developing on the a- and c+a-type slip systems and compared with independent experimental observations. Good agreement is obtained and in particular the experiments support the model prediction that c+a-type slip system GND densities are an order of magnitude lower than those for a-type slip.

4.2 Introduction

A dislocation may be defined in one of two ways. First, as a boundary or a line in the slip plane separating regions where slip has occurred from those where it has not. Consequently, a dislocation must possess many of the characteristics of other boundaries such as on a map, i.e., they cannot terminate inside a crystal but must be

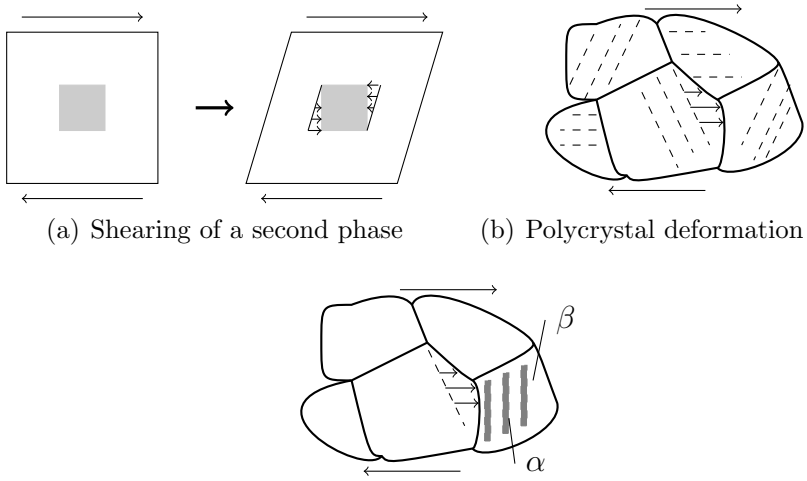
continuous and form a closed loop, terminate on other dislocations (in a junction or node) or on a surface. This is a manifestation of the general *principle of conservation of the Burger's vector*, which can be stated as follows: if the directions of all the dislocation lines are taken to run out from the node, then the sum of the Burger's vectors of all the dislocations is zero. Second, a dislocation may be defined as a line defect in a crystal in which the coordination differs systematically from the regular or ideal arrangement of atoms [48, 64]. Both definitions show that a dislocation is a lattice imperfection in a crystal structure which affects structure-sensitive properties such as strength, hardness, ductility and toughness.

The dislocations can be screw, edge or mixed. Screw dislocations are dislocations where the direction of the dislocation line is parallel to the slip direction. Edge dislocations are those with the direction of the dislocation line perpendicular to the slip direction. If the direction of the dislocation line has a component parallel to the slip direction and another normal to it, it is referred to as a mixed dislocation. Crystals normally contain a great number of dislocations even before plastic deformation occurs. These are generally statistically distributed, and are referred to as statistically stored dislocations (SSDs).

In addition to SSDs, there is another important type: the geometrically necessary dislocation (GND). GNDs were proposed primarily to accommodate strain gradients which result from the inhomogeneous plastic deformation of neighbouring grains [5]. The extent of the strain gradients for a given polycrystal depends on the size of the grains in such a way that polycrystals with smaller grain size generate strain gradients which develop further into the grain, giving a harder stress-strain response during plasticity (Cheong et al. [17]). Cheong et al. [17] showed that except for large polycrystal grains, where strain gradient effects are expected to be small, there is a significant difference between the stress-strain response of a polycrystal with and without the

evolution of GNDs. GNDs lead to further macroscopic strengthening of the material [31, 32].

Since GNDs are required to support plastic strain gradients, they do not exist in situations involving homogeneous plastic strain, that is, they only exist in the presence of a plastic strain gradient. Conditions necessitating GNDs arise in many circumstances in practice. Figure 4.1 shows some cases where GNDs would be required to satisfy geometric compatibility at grain boundaries as well as at interfaces of multi-phase systems such as alloys. Length scale dependent plasticity, based on the development of



(a) Shearing of a second phase (b) Polycrystal deformation

(c) Two-phase alloy

Figure 4.1: In this figure, 4.1(a) shows an idealised two phase situation where a rigid particle in a sheared matrix experiences a plastic strain gradient. Figure 4.1(b) shows a case of deformation at the grain boundaries of a polycrystal; the incompatibility of strain at the grain boundary (strain gradient) necessitates GNDs to satisfy it. Figure 4.1(c) shows a two phase alloy such as Ti-6Al-4V; α lath structures exist throughout the β phase with similar consequences to that in 4.1(a).

geometrically necessary dislocations, is becoming increasingly used in understanding micro-deformation, fatigue crack nucleation, crack propagation and recrystallization to name a few examples. However, what remains a significant shortcoming is microstructural validation of the ability of such modelling, usually crystal plasticity based, to capture correctly the densities of geometrically necessary dislocations developed, and their spatial distribution. Without such detailed validation, these modelling techniques will never gain the confidence of experimentalists nor of model users, be they

researchers or industrial practitioners. In addition, limited work has been reported on the modelling of GND development in hcp polycrystals. Specifically, the slip anisotropy in hcp crystals is significantly different to that in fcc and bcc systems because of the c- and a-type slip having differing Burger's vectors and vastly different critical resolved shear stresses. Slip in such systems occurs on basal, prismatic and pyramidal systems (a-type), and on first- and second-order pyramidal systems (c+a-type). Experimental observations [13, 45, 82] show that c+a-type slip may occur at a resolved shear stress of 2.5–3.0 times that for a-type slip [34]. A consequence of this is that the densities of GNDs developing on the different slip systems during deformation have been measured to be orders of magnitude different[13]. This poses challenges for crystal plasticity coupled GND modelling techniques which have not as yet been addressed.

This chapter therefore focuses on the particular matter of GND development in hcp polycrystals. The physically-based crystal plasticity model of Dunne et al. [26] is employed, which is fully length scale dependent and contains explicitly the coupling between GND density and slip rate. We present a methodology for determination of the GND densities on the individual basal, prismatic and pyramidal slip systems and importantly, present for the first time detailed comparisons of GND activity on the different systems with experimental EBSD observations for a Ti alloy polycrystal. In passing, we note the various uses and definitions of the curl tensor used in determining GND density and present a rationalization and comparison of the approaches described in the literature. In the following sections, we first review the Nye tensor and the various approaches for describing dislocation content, and present a comparison of the approaches. We go on to detail the methodology employed for addressing the well-known non-uniqueness problem (e.g. [4]) and describe the coupling of the GND evolution model with our crystal plasticity slip rule and the corresponding finite element implementation. Finally, we present an analysis of a Ti polycrystal subjected

to deformation in which we assess the development of GND densities on the basal, prismatic and pyramidal slip systems and we compare the results obtained in some detail with independent experimental observations. We provide, therefore, a detailed assessment of the ability of GND-based crystal plasticity to capture correctly experimentally observed behaviour in hcp polycrystals.

4.3 Dislocation tensors

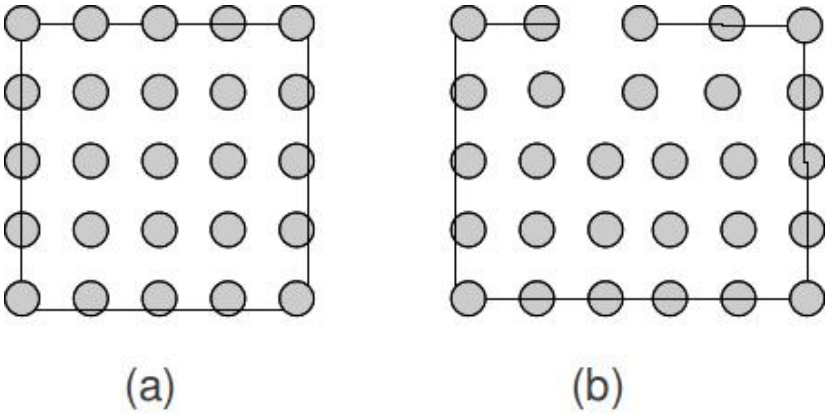


Figure 4.2: Sketch of a closed path in a plane (a) that in (b) fails to close due to the introduction of a dislocation in the plane. The path in both (a) and (b) is 16 inter-atomic spaces long.

In this section, we address the various measures of geometrically necessary dislocation content.

The deformation gradient $\boldsymbol{F}$ is defined as a mapping between the deformed and undeformed configurations such that it maps an initial undeformed path element $\mathrm{d}\boldsymbol{X}$ to a deformed path element $\mathrm{d}\boldsymbol{x}$ as $\mathrm{d}\boldsymbol{x} = \boldsymbol{F}\,\mathrm{d}\boldsymbol{X}$ (see Section 1.3.1). Nye [66] defined the closure failure (or discontinuity or opening of an initially closed path following deformation) due to dislocations generated in a particular plane per unit area as

$$B_i = \alpha_{ij} l_j \quad \text{with} \quad \alpha_{ij} = n b_i r_j \tag{4.1}$$

where B_i is the closure failure, l_j is a unit vector normal to the unit area, b_i is the

Burger's vector, n the number density of dislocations, and r_j is a unit vector along the dislocation line. Figure 4.2 shows a sketch to illustrate a closure failure due to dislocations in a plane. If all the dislocations are parallel the two definitions of density (i.e. total length of dislocation per unit volume or number of dislocations intersecting a unit area) give the same value, but for a completely random arrangement the volume density is twice the surface density [41].

Defining $\rho_j = nr_j$ from eqn 4.1 so that $\alpha_{ij} = nb_i r_j$ becomes $\alpha_{ij} = b_i \rho_j$, we can re-write Nye's slip-systemwise-discrete dislocation tensor, $\boldsymbol{\alpha}$, for multi-slip as

$$\alpha_{ij} = b_i^\beta \rho_j^\beta \quad \Longrightarrow \quad \boldsymbol{\alpha} = \sum_\beta \left(\boldsymbol{b}^\beta \otimes \boldsymbol{\rho}^\beta \right) \tag{4.2}$$

where β is a general active slip plane. The dislocation tensor $\boldsymbol{\alpha}$ specifies the state of dislocation of the region for which the closure failure is defined [66]. The closure failure, $\boldsymbol{B}_C$, can thus be written for this region (or volume) as

$$\boldsymbol{B}_C = \iint_S \left(\sum_\beta \left(\boldsymbol{b}^\beta \otimes \boldsymbol{\rho}^\beta \right) \right) \boldsymbol{n} \, \mathrm{d}S \tag{4.3}$$

where S is a surface that bounds the region and $\boldsymbol{n}$ is the normal to the surface.

An alternative description of the state of dislocation of a region can be made purely in terms of the kinematics of the deformation under consideration. The closure failure can be described over the region (or volume) by considering the change in the length of a path on the surface due to the generation of dislocations in the volume. This results in a field quantity $\boldsymbol{G}$ which describes the dislocation content of the volume in a similar way to Nye's slip-systemwise-discrete dislocation tensor $\boldsymbol{\alpha}$. Acharya and Bassani [1] while dealing with the subject of lattice incompatibility proposed a definition of this closure failure with respect to the deformed configuration $\boldsymbol{C}$ as the existence of at least one closed curve in $\boldsymbol{C}$ for which the *cumulative Burger's vector* is *non-vanishing*. They

define the cumulative Burger's vector, $\boldsymbol{b}_C$, of all dislocation lines that belong within the closed curve C on $\boldsymbol{C}$ by

$$\boldsymbol{b}_C = \oint_C \boldsymbol{F}^{e-1}\,\mathrm{d}\boldsymbol{x} \tag{4.4}$$

and they interpret a non-vanishing Burger's vector at a point of $\boldsymbol{C}$ as the closure failure associated with the projection of the closed curve C, that bounds an infinitesimal element of area containing that point, in the intermediate configuration (or relaxed configuration).

Starting with eqn 4.4, in which the integration is performed with respect to the deformed configuration, and using Stokes' theorem, the line integral can be converted into an integral over the whole surface of the volume for which the path above is a periphery resulting in eqn 4.5, where "curl" implies the operation "$\nabla\times$" performed with respect to the deformed (or spatial) coordinates $\boldsymbol{x}$, where $\boldsymbol{x} = \boldsymbol{X} + \boldsymbol{u}$. "Curl" will be used when referring to the undeformed (or material) coordinates $\boldsymbol{X}$.

$$\boldsymbol{b}_C = \oint_C \boldsymbol{F}^{e-1}\,\mathrm{d}\boldsymbol{x} = \iint_S \left(\mathrm{curl}\boldsymbol{F}^{e-1}\right)^T \boldsymbol{n}\,\mathrm{d}S = \iint_S \boldsymbol{G}_D^{eT}\boldsymbol{n}\,\mathrm{d}S \quad \text{where} \quad \boldsymbol{G}_D^e = \mathrm{curl}\boldsymbol{F}^{e-1} \tag{4.5}$$

Superscipts e and D are just reminders that $\boldsymbol{G}$, the dislocation content tensor introduced above, is defined in terms of $\boldsymbol{F}^e$ and the derivatives are performed with respect to the deformed coordinates $\boldsymbol{x}$ respectively. Note that the curl term is transposed unlike when Stokes' theorem is applied to vectors. Cermelli and Gurtin [16] provide the relevant proof for the origin of the transpose which can be summarised as follows. Given the identity $(\mathrm{curl}\boldsymbol{T})\boldsymbol{c} = \mathrm{curl}(\boldsymbol{T}^T\boldsymbol{c})$ for all constant vectors $\boldsymbol{c}$ and a tensor field $\boldsymbol{T}$;

for a smooth vector field $\boldsymbol{f}$ Stokes' theorem applies as

$$\oint_C \boldsymbol{f} \cdot \mathrm{d}\boldsymbol{x} = \iint_S \mathrm{curl}\boldsymbol{f} \cdot \mathrm{d}\boldsymbol{S} \tag{4.6}$$

If $\boldsymbol{f} = \boldsymbol{T}^T\boldsymbol{c}$, then

$$\oint_C \boldsymbol{T}^T\boldsymbol{c} \cdot \mathrm{d}\boldsymbol{x} = \iint_S \mathrm{curl}\left(\boldsymbol{T}^T\boldsymbol{c}\right) \cdot \mathrm{d}\boldsymbol{S} = \iint_S \left(\mathrm{curl}\boldsymbol{T}\right)\boldsymbol{c} \cdot \mathrm{d}\boldsymbol{S} \tag{4.7}$$

but $\boldsymbol{c}$ is constant hence

$$\oint_C \boldsymbol{T}\,\mathrm{d}\boldsymbol{x} = \iint_S \left(\mathrm{curl}\boldsymbol{T}\right)^T \mathrm{d}\boldsymbol{S} \tag{4.8}$$

If we wish to obtain $\boldsymbol{G}$ with respect to the undeformed configuration, we can re-write eqn 4.4 so that the integration is referred to the undeformed coordinates as follows:

$$\boldsymbol{b}_C = \oint_C \boldsymbol{F}^{e-1}\,\mathrm{d}\boldsymbol{x} = \oint_C \boldsymbol{F}^p\boldsymbol{F}^{-1}\boldsymbol{F}\,\mathrm{d}\boldsymbol{X} = \oint_C \boldsymbol{F}^p\,\mathrm{d}\boldsymbol{X} \tag{4.9}$$

where the relations $\boldsymbol{F} = \boldsymbol{F}^e\boldsymbol{F}^p$ and $\mathrm{d}\boldsymbol{x} = \boldsymbol{F}\,\mathrm{d}\boldsymbol{X}$ have been used. In this case we get

$$\boldsymbol{b}_C = \oint_C \boldsymbol{F}^p\,\mathrm{d}\boldsymbol{X} = \iint_{S_R} \left(\mathrm{Curl}\boldsymbol{F}^p\right)^T \mathrm{d}\boldsymbol{S}_R = \iint_{S_R} \boldsymbol{G}_R^{pT}\boldsymbol{n}_R\,\mathrm{d}S_R \quad \text{where} \quad \boldsymbol{G}_R^p = \mathrm{Curl}\boldsymbol{F}^p \tag{4.10}$$

where now $\boldsymbol{G}_R^p$ is the geometric dislocation tensor as a function of $\boldsymbol{F}^p$ and the derivatives are performed with respect to the undeformed coordinates $\boldsymbol{X}$; subscript R implies the undeformed configuration.

By equating the closure failure as defined by eqns 4.3 and 4.4, i.e. $\boldsymbol{B}_C = \boldsymbol{b}_C$, it can be seen that if the surface element in eqn 4.3 refers to the deformed configuration

(hence all crystal lattice directions included in $\boldsymbol{b}$ and $\boldsymbol{\rho}$ will have to be referred to the deformed configuration), then

$$\iint_S \left(\sum_\beta \left(\boldsymbol{b}^\beta \otimes \boldsymbol{\rho}^\beta \right) \right) \boldsymbol{n} \, \mathrm{d}S = \iint_S \left(\mathrm{curl} \boldsymbol{F}^{e-1} \right)^T \boldsymbol{n} \, \mathrm{d}S \Longrightarrow \sum_\beta \left(\boldsymbol{b}^\beta \otimes \boldsymbol{\rho}^\beta \right) = \left(\mathrm{curl} \boldsymbol{F}^{e-1} \right)^T \tag{4.11}$$

Similarly, if the surface element in eqn 4.3 refers to the undeformed configuration then

$$\iint_{S_R} \left(\sum_\beta \left(\boldsymbol{b}_R^\beta \otimes \boldsymbol{\rho}_R^\beta \right) \right) \boldsymbol{n}_R \, \mathrm{d}S_R = \iint_{S_R} (\mathrm{Curl} \boldsymbol{F}^p)^T \, \mathrm{d}\boldsymbol{S}_R \Longrightarrow \sum_\beta \left(\boldsymbol{b}_R^\beta \otimes \boldsymbol{\rho}_R^\beta \right) = (\mathrm{Curl} \boldsymbol{F}^p)^T \tag{4.12}$$

where the subscript R on $\boldsymbol{b}$ and $\boldsymbol{\rho}$ indicates that the crystal lattice directions included have to be referred to the undeformed configuration. This subscript will be omitted in all mention of $\boldsymbol{b}$ and $\boldsymbol{\rho}$ from this point on, but the reader should remember to assume the deformed or undeformed configuration depending on whether $\mathrm{curl} \boldsymbol{F}^{e-1}$ or $\mathrm{Curl} \boldsymbol{F}^p$ is used according to eqns 4.11 and 4.12 respectively. Since FE code implementations are normally set up with respect to either the deformed coordinates ($\boldsymbol{x}$) or undeformed coordinates ($\boldsymbol{X}$), this in practice determines which form is most appropriate to use.

In the case of infinitesimal deformation, the deformed and undeformed configurations collapse onto each other since $\boldsymbol{x} \approx \boldsymbol{X}$ which implies curl $\approx$ Curl and $\boldsymbol{F} \approx \boldsymbol{I}$. Hence, from $\boldsymbol{F} = \boldsymbol{F}^e \boldsymbol{F}^p$, $\boldsymbol{I} \approx \boldsymbol{F}^e \boldsymbol{F}^p \Longrightarrow \boldsymbol{F}^{e-1} \approx \boldsymbol{F}^p$ so that $\mathrm{curl} \boldsymbol{F}^{e-1} \approx \mathrm{Curl} \boldsymbol{F}^p$.

4.3.1 Reconciling dislocation measures

In the literature there have been various representations of the geometric dislocation tensor. An extended list of these is given by Cermelli and Gurtin [16]. In this section we attempt to reconcile some of them with the tensors obtained above. Busso et al.

[14] provided the tensor $\boldsymbol{\Lambda}_1 = \text{curl}\boldsymbol{F}^p$ which can be derived as $\boldsymbol{G}^p_R$ in eqn 4.10 but without the transpose and without specifying the configuration with respect to which the derivatives are to be performed - although this distinction is not necessary for the kind of small deformations they were working with. Acharya [2] also provided the tensor $\boldsymbol{\Lambda}_2 = -\text{curl}\boldsymbol{F}^{e-1}$ which can be derived as $\boldsymbol{G}^e_D$ in eqn 4.5 again without the transpose, but also with a negative sign that arises from the definition of the "true" Burger's vector according to Willis' [85] convention. Therefore if the transpose, resulting from the application of Stokes' theorem to a second order tensor (eqn 4.8) rather than to a vector (eqn 4.6), is applied and care is taken to identify the configuration with respect to which the derivatives are carried out, the measures $\boldsymbol{\Lambda}_1$ and $\boldsymbol{\Lambda}_2$ become the same as $\boldsymbol{G}^p_R$ and $\boldsymbol{G}^e_D$ respectively.

Cermelli and Gurtin [16] also start with eqn 4.10, i.e.,

$$\boldsymbol{b}_C = \oint_C \boldsymbol{F}^p \,\mathrm{d}\boldsymbol{X} = \iint_{S_R} (\text{Curl}\boldsymbol{F}^p)^T \,\mathrm{d}\boldsymbol{S}_R = \iint_{S_R} (\text{Curl}\boldsymbol{F}^p)^T \,\boldsymbol{n}_R \,\mathrm{d}S_R \tag{4.13}$$

They then argue that since $(\text{Curl}\boldsymbol{F}^p)^T \,\boldsymbol{n}_R$ lies in the intermediate configuration and $\boldsymbol{n}_R \,\mathrm{d}S_R$ lies in the undeformed configuration, it would be incorrect to associate $(\text{Curl}\boldsymbol{F}^p)^T \,\boldsymbol{n}_R \,\mathrm{d}S_R$ with the Burger's vector corresponding to the boundary curve of a surface element with normal $\boldsymbol{n}_R$. They propose to rectify the situation with $\boldsymbol{n}_I \,\mathrm{d}S_I = J^p \boldsymbol{F}^{p-T} \boldsymbol{n}_R \,\mathrm{d}S_R$, where $\boldsymbol{n} \,\mathrm{d}S_I$ is a surface element in the intermediate configuration I and J^p is the determinant of $\boldsymbol{F}^p$, so that

$$(\text{Curl}\boldsymbol{F}^p)^T \,\boldsymbol{n}_R \,\mathrm{d}S_R = \frac{1}{J^p} (\text{Curl}\boldsymbol{F}^p)^T \,\boldsymbol{F}^{pT} \boldsymbol{n}_I \,\mathrm{d}S_I \tag{4.14}$$

This results [16] in $\boldsymbol{G}$ defined in the intermediate configuration, i.e. $\boldsymbol{G}^p_I$, with the form

$$\boldsymbol{G}^p_I = \frac{1}{J^p} \boldsymbol{F}^p \text{Curl}\boldsymbol{F}^p \tag{4.15}$$

and the equivalent $\boldsymbol{G}$ in the undeformed configuration of the form

$$\boldsymbol{G}_R^{p*} = J_p \boldsymbol{F}^{p-1} \boldsymbol{G}_I^p \boldsymbol{F}^{p-T} = (\mathrm{Curl}\boldsymbol{F}^p)\, \boldsymbol{F}^{p-T} \tag{4.16}$$

where the superscript $*$ only serves to differentiate this $\boldsymbol{G}_R^p$ from that defined in eqn 4.10. A similar argument leads to

$$\boldsymbol{G}_I^e = J^e \boldsymbol{F}^{e-1} \mathrm{curl}\boldsymbol{F}^{e-1} \quad \text{and} \quad \boldsymbol{G}_D^{e*} = \frac{1}{J_e} \boldsymbol{F}^e \boldsymbol{G}_I^e \boldsymbol{F}^{eT} = (\mathrm{curl}\boldsymbol{F}^{e-1}) \boldsymbol{F}^{eT} \tag{4.17}$$

where J^e is the determinant of $\boldsymbol{F}^e$ and the superscript $*$ serves to differentiate this $\boldsymbol{G}_D^e$ from that defined in eqn 4.5

It can be seen that the tensors $\boldsymbol{G}_D^{e*}$ and $\boldsymbol{G}_R^{p*}$ look rather different to $\boldsymbol{G}_D^e$ and $\boldsymbol{G}_R^p$ respectively and are difficult to reconcile with those suggested by Acharya [2] and Busso et al. [14]. This is a result of the specific assumption that it would be incorrect to associate $(\mathrm{Curl}\boldsymbol{F}^p)^T \boldsymbol{n}_R \, \mathrm{d}S_R$ with the Burger's vector corresponding to the boundary curve of a surface element with normal $\boldsymbol{n}_R$ and the consequent introduction of $\boldsymbol{n}\, \mathrm{d}S_I = J^p \boldsymbol{F}^{p-T} \boldsymbol{n}_R \, \mathrm{d}S_R$ to define a surface element in the intermediate configuration in order to rectify the situation. As can be seen in eqn 4.13 although $\boldsymbol{b}_C$ is defined in the intermediate configuration, it is appropriate for it to be determined entirely in terms of undeformed coordinates, implied in $\mathrm{d}\boldsymbol{X}$. This does not change for $\mathrm{d}\boldsymbol{S}$ after the application of Stokes' theorem, i.e. $\boldsymbol{b}_C$ is still determined entirely in terms of undeformed coordinates, implied in $\mathrm{d}\boldsymbol{S}$ and in $\mathrm{Curl}\boldsymbol{F}^p (= \boldsymbol{\varepsilon} \frac{d\boldsymbol{F}^p}{d\boldsymbol{X}}$, where $\boldsymbol{\varepsilon}$ is the permutation tensor). However the right hand side of eqn 4.14 is defined in a mixture of coordinates, i.e. undeformed coordinates in the Curl, and 'intermediate coordinates' implied in $\mathrm{d}S_I$. This can be rectified with the chain rule for intermediate coordinates defined

as $\mathrm{d}\boldsymbol{x}_I = \boldsymbol{F}^p\,\mathrm{d}\boldsymbol{X}$

$$\boldsymbol{\varepsilon}\frac{d}{d\boldsymbol{X}} = \boldsymbol{\varepsilon}\frac{d}{d\boldsymbol{x}_I}\frac{d\boldsymbol{x}_I}{d\boldsymbol{X}} = \boldsymbol{\varepsilon}\frac{d}{d\boldsymbol{x}_I}\boldsymbol{F}^p \quad \text{hence in eqn 4.14} \tag{4.18}$$

$$(\mathrm{Curl}\boldsymbol{F}^p)^T\,\boldsymbol{n}_R\,\mathrm{d}S_R = \left(\boldsymbol{\varepsilon}\frac{d\boldsymbol{F}^p}{d\boldsymbol{X}}\right)^T\boldsymbol{n}_R\,\mathrm{d}S_R = \frac{1}{J^p}\left(\boldsymbol{\varepsilon}\frac{d\boldsymbol{F}^p}{d\boldsymbol{x}_I}\boldsymbol{F}^p\right)^T\boldsymbol{F}^{pT}\boldsymbol{n}_I\,\mathrm{d}S_I \tag{4.19}$$

$$= \frac{1}{J^p}\boldsymbol{F}^{pT}\left(\boldsymbol{\varepsilon}\frac{d\boldsymbol{F}^p}{d\boldsymbol{x}_I}\right)^T\boldsymbol{F}^{pT}\boldsymbol{n}_I\,\mathrm{d}S_I = \frac{1}{J^p}\boldsymbol{F}^{pT}\left(\mathrm{curl}_I\boldsymbol{F}^p\right)^T\boldsymbol{F}^{pT}\boldsymbol{n}_I\,\mathrm{d}S_I \tag{4.20}$$

where curl_I implies the "$\nabla\times$" operation performed with respect to intermediate coordinates. This would lead to $\boldsymbol{G}_I^p$ defined as follows, instead of eqn 4.15

$$\boldsymbol{G}_I^p = \frac{1}{J^p}\boldsymbol{F}^p\left(\mathrm{curl}_I\boldsymbol{F}^p\right)\boldsymbol{F}^p \tag{4.21}$$

For implementation into finite element code, it is normally preferable to work with the deformed or undeformed coordinates and so from here on, we adopt the dislocation tensors given in eqns 4.5 and 4.10.

4.3.2 Curl of a second order tensor $\boldsymbol{T}$

A survey of literature in the area of dislocation modelling shows that there are various definitions currently in use for the curl of a second order tensor, curl($\boldsymbol{T}$). The following definitions were found as shown in Table 4.1. The summation convention is used and ε is the permutation tensor or alternating tensor. The permutation tensor, ε_{hki}, is a pseudotensor which is antisymmetric under the interchange of any two indices [19].

However, since this is a mathematical problem, it is reasonable to suggest that not all the forms shown in the table may be necessary and here, we attempt to reconcile

Table 4.1: Definitions of curl($\boldsymbol{T}$)

	Definition	Author(s)/reference
1	$(\text{curl}\boldsymbol{T})_{ij} = \varepsilon_{jkh}T_{ik,h}$	Meissonnier et al. [62], Malvern [59, p.60, $\boldsymbol{T} \times \overleftarrow{\nabla}$]
2	$(\text{curl}\boldsymbol{T})_{ij} = \varepsilon_{ikh}T_{jh,k}$	Arsenlis and Parks [4], Sun et al. [73]
		Cermelli and Gurtin [16]
3	$(\text{curl}\boldsymbol{T})_{ij} = \varepsilon_{ikh}T_{jk,h}$	Willis [85]: *This is the negative of 2, and transpose of 1*
4	$(\text{curl}\boldsymbol{T})_{ij} = \varepsilon_{jkh}T_{ih,k}$	Acharya [2]: *This is the negative of 1, and transpose of 2*
5	$(\text{curl}\boldsymbol{T})_{ij} = \varepsilon_{ikh}T_{hj,k}$	Malvern [59, p.60, $\overrightarrow{\nabla} \times \boldsymbol{T}$]:*Transpose* $\boldsymbol{T}$ *to make same as 2*

the various definitions in use.

Normally we know how to define the curl of a vector, curl($\boldsymbol{v}$). Starting with this, we can consistently define the curl of a second order tensor as follows. Define the basis vectors of a cartesian coordinate system as $\boldsymbol{e}_1, \boldsymbol{e}_2$, and $\boldsymbol{e}_3$. Then we can define the curl of a vector $\boldsymbol{v}$ as

$$\nabla \times \boldsymbol{v} = \varepsilon_{hki} v_{k,h} \boldsymbol{e}_i \tag{4.22}$$

To define the curl of a second order tensor $\boldsymbol{T}$, consider an arbitrary constant vector $\boldsymbol{c}$. We can write

$$\boldsymbol{c} \cdot \boldsymbol{T} = c_j T_{jk} \boldsymbol{e}_k \tag{4.23}$$

The inner product given in eqn 4.23 defines a vector. We can therefore use eqn 4.22 to write the curl of this product. Therefore

$$\nabla \times (\boldsymbol{c} \cdot \boldsymbol{T}) = \varepsilon_{hki} c_j T_{jk,h} \boldsymbol{e}_i = (\varepsilon_{hki} T_{jk,h} \boldsymbol{e}_i \otimes \boldsymbol{e}_j) \cdot \boldsymbol{c} = (\nabla \times \boldsymbol{T}) \cdot \boldsymbol{c} \tag{4.24}$$

where $c_j = \boldsymbol{e}_j \cdot \boldsymbol{c}$ has been used. Hence

$$\nabla \times \boldsymbol{T} = \varepsilon_{hki} T_{jk,h} \boldsymbol{e}_i \otimes \boldsymbol{e}_j \quad \text{or} \quad (\nabla \times \boldsymbol{T})_{ij} = \varepsilon_{hki} T_{jk,h} = \varepsilon_{ikh} T_{jh,k} \tag{4.25}$$

If we define another second order tensor $\boldsymbol{H} = \boldsymbol{T}^T$, it follows that $\boldsymbol{H} \cdot \boldsymbol{c} = \boldsymbol{T}^T \cdot \boldsymbol{c} = \boldsymbol{c} \cdot \boldsymbol{T}$, hence $\nabla \times \boldsymbol{H}$ would be the same as the $\overrightarrow{\nabla} \times \boldsymbol{T}$ form given by Malvern [59] (item 5 in Table 4.1). Comparing eqn 4.25 against the terms in Table 4.1, it is clear that the second definition is the mathematically most appropriate one, and this definition is used henceforth in this chapter. Eqn 4.25 is written out in full form in terms of cartesian coordinates x, y, z as follows:

$$\nabla \times \boldsymbol{T} = \begin{bmatrix} \frac{\partial T_{xz}}{\partial y} - \frac{\partial T_{xy}}{\partial z} & \frac{\partial T_{yz}}{\partial y} - \frac{\partial T_{yy}}{\partial z} & \frac{\partial T_{zz}}{\partial y} - \frac{\partial T_{zy}}{\partial z} \\ \frac{\partial T_{xx}}{\partial z} - \frac{\partial T_{xz}}{\partial x} & \frac{\partial T_{yx}}{\partial z} - \frac{\partial T_{yz}}{\partial x} & \frac{\partial T_{zx}}{\partial z} - \frac{\partial T_{zz}}{\partial x} \\ \frac{\partial T_{xy}}{\partial x} - \frac{\partial T_{xx}}{\partial y} & \frac{\partial T_{yy}}{\partial x} - \frac{\partial T_{yx}}{\partial y} & \frac{\partial T_{zy}}{\partial x} - \frac{\partial T_{zx}}{\partial y} \end{bmatrix}$$

4.3.3 GNDs in hcp crystals

We now focus in this section on the application of the above to the determination of densities of GNDs in hcp crystals in particular. For this system, it is necessary to differentiate between a- and c+a-type slip as a result of both the differing critical resolved shear stresses (CRSS) and Burger's vectors which apply.

We start with eqn 4.11 or 4.12, and identify that the problem to solve in order to obtain the GND densities is the following:

$$\sum_{\alpha=1}^{N} \boldsymbol{b}^\alpha \otimes \boldsymbol{\rho}^\alpha = \boldsymbol{G}^T \qquad \text{or} \qquad \sum_{\alpha=1}^{N} \boldsymbol{\rho}^\alpha \otimes \boldsymbol{b}^\alpha = \boldsymbol{G} \tag{4.26}$$

where N is the number of active slip systems. In crystals with high degrees of symmetry the geometric constraints on dislocation density, imposed by the plastic slip gradient field, can be satisfied with many different dislocation configurations [4] the same way a given plastic deformation can be performed by different combinations of slip systems [48]. In crystals of such symmetry the number of distinct dislocation types may exceed

the nine independent components of the Nye tensor, hence a unique solution for the dislocation density may not be possible. Therefore, once $\boldsymbol{G}$ is obtained, the densities may be obtained by solving eqn 4.26 in such a way as to minimise the error between the right and left hand sides, i.e., find $\boldsymbol{\rho}^{\alpha}$ such that the error $\boldsymbol{\xi}$ is minimum, e.g. for least squares minimisation: minimise($||\boldsymbol{\xi}||_2$), where

$$\boldsymbol{\xi} = \boldsymbol{G} - \sum_{\alpha} \boldsymbol{\rho}^{\alpha} \otimes \boldsymbol{b}^{\alpha} \tag{4.27}$$

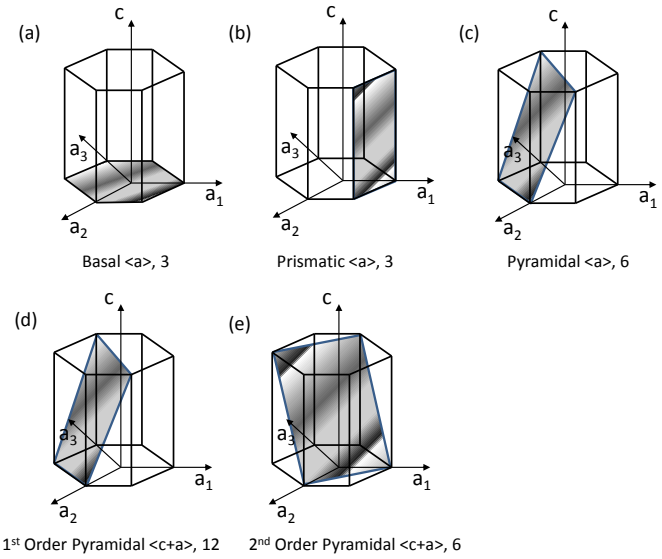


Figure 4.3: Hcp slip systems. Courtesy of Hasija et al. [38].

Here the problem is solved for hcp materials for which slip occurs on basal, prismatic, and pyramidal slip systems. The relevant slip systems are detailed by Hasija et al. [38] and are reproduced in Figure 4.3 for completeness. A-type slip occurs on the basal, prismatic and a-pyramidal slip systems, while c+a-type slip occurs on the primary (1^{st} order) and secondary (2^{nd} order) c+a-pyramidal slip systems as shown in fig 4.3. The Burger's vectors $\boldsymbol{b}^{\alpha}$ for a-type slip ($\boldsymbol{b}_a^{\alpha}$) and c+a-type slip ($\boldsymbol{b}_c^{\alpha}$) differ by the c/a ratio. Similarly the critical resolved shear stress (CRSS) required to initiate slip on the a-type (τ_c^a) and c+a-type (τ_c^{c+a}) slip systems differs. Experimental observations

show that c+a-type slip may occur at a resolved shear stress of 2.5–3.0 times that for a-type slip [34].

We solve the problem by keeping the different dislocation line components, i.e. edge (ρ_e^α) and screw (ρ_s^α), separate so that eqn 4.26 can be rewritten as follows

$$\sum_{\alpha=1}^{N_a} (\rho_e^\alpha \boldsymbol{t}^\alpha \otimes \boldsymbol{b}_a^\alpha + \rho_s^\alpha \boldsymbol{s}^\alpha \otimes \boldsymbol{b}_a^\alpha) + \sum_{\beta=1}^{N_c} \left(\rho_e^\beta \boldsymbol{t}^\beta \otimes \boldsymbol{b}_c^\beta + \rho_s^\beta \boldsymbol{s}^\beta \otimes \boldsymbol{b}_c^\beta\right) = \boldsymbol{G} \tag{4.28}$$

where the first and second terms on the left hand side of eqn 4.28 are the contribution to the dislocation content from a-type and c+a-type slip respectively, and N_a and N_c are the corresponding number of active slip systems so that the total number of active slip systems N is given as $N = N_a + N_c$. $\boldsymbol{t}^\alpha$ is defined from the slip direction $\boldsymbol{s}^\alpha$ and normal $\boldsymbol{n}^\alpha$ as $\boldsymbol{t}^\alpha = \boldsymbol{s}^\alpha \times \boldsymbol{n}^\alpha$. Depending on the active slip systems α and β, the available number of screw types varies. The maximum number of screw types for the hcp crystal type is 9, if we don't distinguish between negative and positive dislocations. The number of edge type is always equal to the number of active slip systems N.

Once the active edge and screw have been established, eqn 4.28 may be written as a linear set of equations $\boldsymbol{Ax} = \boldsymbol{b}$ in which $\boldsymbol{A}(m, n)$ has dimension $m = 9$ and $n = n_e + n_s$, where n_e and n_s are the number of edge types ($n_e = N$) and the number of screw types respectively. We then have a problem of ($m = 9$) linear equations with (n) unknowns. n may be such that $n \leq m$ or $n > m$ depending on the number of active slip systems.

For the screw components a scheme has to be adopted to enable the screw density component for a given slip direction to be shared among the active slip systems having the corresponding slip direction. In this case the sharing is performed linearly among the systems according to their activity, where the extent of activity η for slip system α is defined as $\eta^\alpha = \tau^\alpha / \tau_c^\alpha$ – a slip system is not active if $\eta^\alpha < 1$. For example, if three systems 1, 2, and 3 have the same slip direction and have extents of activity

$\eta^1 \geq 1, \eta^2 \geq 1$, and $\eta^3 < 1$ and if the screw density obtained for this slip direction is ρ_s, then the screw densities on the three slip systems are: $\rho_s^1 = \rho_s\eta^1/(\eta^1 + \eta^2)$, $\rho_s^2 = \rho_s\eta^2/(\eta^1 + \eta^2)$, and $\rho_s^3 = 0$.

Arsenlis and Parks [4] suggested two ways of solving the above problem (eqn 4.27): one geometrically motivated (L^2) and the other energetically motivated (L^1). These involve minimising L^1 or L^2, which are defined as follows [52], where the w are possible weightings.

$$L^1 = \sum_{\alpha=1}^{N} |\rho^\alpha w^\alpha| \quad \text{and} \quad L^2 = \left[\sum_{\alpha=1}^{N} [\rho^\alpha w^\alpha]^2\right]^{\frac{1}{2}} \tag{4.29}$$

The L^1-scheme can be implemented as a linear programming (LP) minimisation using the simplex algorithm, where L^1 is the cost function and the weightings w are chosen according to the energy of the different dislocation types (see Hull and Bacon [41, \$4.4] for the complete dislocation energy equations). Britton et al. [12] used the energy motivated LP scheme to calculate GND densities from measured (i.e. experimental) curvatures using MATLAB.

Least squares (LS) minimisation can also be used as a third alternative. The LS scheme minimises the sum of squares of the resulting dislocation densities. It is essentially a special case of the L^2 minimisation for which $w = 1$. For LS minimisation, one can either use the LAPACK libraries [11] or achieve the same result via the Moore-Penrose pseudoinverse. Whatever the choice, one obtains the exact solution to $\boldsymbol{Ax} = \boldsymbol{b}$ for $m \geq n$. The case for $m < n$ gives the solution to $min(||\boldsymbol{Ax} - \boldsymbol{b}||_2)$, and if there are multiple such solutions, the solution $||\boldsymbol{x}||_2$ is returned. Geometrically, this means finding the shortest possible dislocation line lengths. Using the Moore-Penrose pseu-

doinverse

$$\boldsymbol{x} = \boldsymbol{A}^{+}\boldsymbol{b} \tag{4.30}$$

where

$$\begin{aligned} \boldsymbol{A}^{+} &= \boldsymbol{A}^{T}(\boldsymbol{A}\boldsymbol{A}^{T})^{-1} \quad \text{for} \quad m < n \\ \boldsymbol{A}^{+} &= (\boldsymbol{A}^{T}\boldsymbol{A})^{-1}\boldsymbol{A}^{T} \quad \text{for} \quad m > n \quad \text{and} \\ \boldsymbol{A}^{+} &= \boldsymbol{A}^{-1} \quad \text{for} \quad m = n \end{aligned} \tag{4.31}$$

The LS scheme has been implemented into crystal plasticity finite element (CPFE) code. Arsenlis and Parks [4] argue that the differences between this approach and the LP scheme are likely to be small. Kysar et al. [52], however, show that differences can become significant under conditions of plane strain. In the following section the crystal plasticity finite element implementation is presented.

4.4 Crystal plasticity FE implementation

In this section, we outline the finite element approach used in order to obtain the plastic strain gradients from which $\boldsymbol{G}$ in eqn 4.28 may be obtained such that the GND densities discussed above for hcp crystals may be determined.

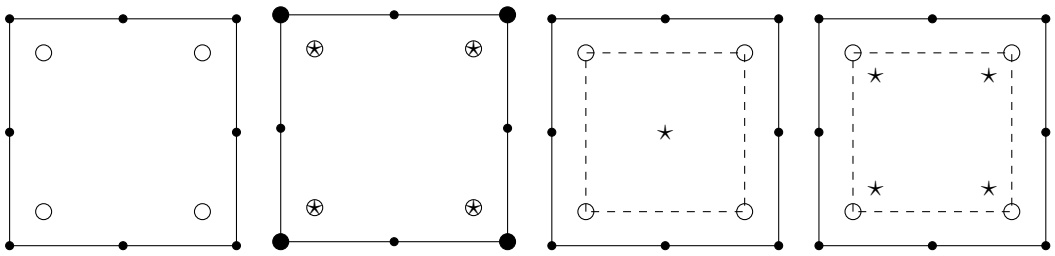
4.4.1 The CPFE gradient implementation

From Section 4.3, we see that it is necessary to determine terms of the form curl $(\boldsymbol{T})$ in which $\boldsymbol{T}$ may be $\boldsymbol{F}^{p}$ or $\boldsymbol{F}^{e-1}$. The quantity to be differentiated $\boldsymbol{T}$ is known only at the eight integration points of the 20-noded reduced integration element (defined as C3D20R in Abaqus/standard), Figure 4.4(a), adopted in the present analysis. The aim is to obtain curl $(\boldsymbol{T})$ at the same eight integration points of this element (open

circles ○ in Figure 4.4(a)), with the ability to capture variations of slip gradient *within the element* so as to considerably increase the accuracy of calculations compared with constant element gradient assumptions [14]. In the literature, several methods have been reported for the determination of the gradients of the plastic deformation. The approach of Busso et al. [14], Meissonnier et al. [62] and Cheong et al. [17] involves three steps: (i) linear extrapolation of $\boldsymbol{T}$ from the integration points of the C3D20R element (open circles ○ in Figure 4.4(b)) to its corner nodes (filled circles ● in the same subfigure); (ii) (full $2 \times 2 \times 2$ integration) evaluation of curl $(\boldsymbol{T})$ at the eight integration points of the eight-noded linear element defined by the corner nodes ($\star$), with linear shape functions ; (iii) assigning the values obtained to the eight integration points of the C3D20R element (open circles ○). An alternative simplified approach is given in [26] which also involves three steps: (i) defining an eight-noded linear element with nodes at the integration points of the C3D20R element (open circles ○ in Figure 4.4(c)), so that this element naturally finds itself with the values of $\boldsymbol{T}$ at its nodes; (ii) (reduced integration) evaluation of curl $(\boldsymbol{T})$ at one integration point of the eight-noded inner linear element ($\star$ in the same subfigure), with linear shape functions; (iii) assigning the values obtained to the eight integration points of the C3D20R element (open circles ○). Since $\boldsymbol{T}$ is known at the integration points, the linear element definition with nodes at these integration points is preferred but reduced integration together with simply assigning the values from the single integration point of the inner element to the eight integration points of the C3D20R element means that curl $(\boldsymbol{T})$ is forced to be constant throughout the element.

Here we define an inner linear 3-D element with nodes at the integration points of the C3D20R element as in the second alternative above but we compute the derivatives over its eight integration points, that is, full (2x2x2) integration ($\star$ in Figure 4.4(d)). The results from the eight integration points of this inner element are then extrapolated

to its nodes (open circles ○, which are also the C3D20R element's integration points) with linear shape functions as described below.



(a) Reduced integration element (b) Full integration outer element (c) Reduced integration inner element (d) Full integration inner element

Figure 4.4: Computation of strain gradients in a C3D20R Abaqus/standard element. The element is 3-D although the figures here present it as viewed on one face - hence the 2-D equivalent.

For any finite element nodal positions, $\tilde{\boldsymbol{x}}$, it is appropriate to write:

$$\boldsymbol{x} = \boldsymbol{N}\tilde{\boldsymbol{x}} \tag{4.32}$$

Define $\boldsymbol{Z} = curl\,(\boldsymbol{T})$. With respect to the inner element, $\boldsymbol{T}$ is known at its nodal points (open circles ○ in Figure 4.4(d) which are also the integration points of the outer element as already observed above). $\boldsymbol{Z}$ at the integration points of the inner element ($\star$ in Figure 4.4(d)) is then obtained as

$$\boldsymbol{Z} = \varepsilon\frac{\partial \boldsymbol{T}}{\partial \boldsymbol{x}} = \varepsilon\tilde{\boldsymbol{T}}\frac{\partial \boldsymbol{N}}{\partial \boldsymbol{\zeta}}\left(\tilde{\boldsymbol{x}}\frac{\partial \boldsymbol{N}}{\partial \boldsymbol{\zeta}}\right)^{-1} \tag{4.33}$$

where $\boldsymbol{\varepsilon}$ is the permutation tensor and $\boldsymbol{\zeta}$ are the natural coordinates of the inner element. $\boldsymbol{x}$ is obtained for the nodes of the inner element from the outer element according to eqn 4.32. The $\tilde{(.)}$ in eqn 4.33 should be understood to refer to the nodes of the inner element. Eqn 4.25 gives $\boldsymbol{Z}$ in index notation. We may also relate $\boldsymbol{Z}$ at the integration

points of the inner element to its nodal values by

$$\boldsymbol{Z} = \boldsymbol{M}\tilde{\boldsymbol{Z}} \tag{4.34}$$

Since we are treating each component of $\boldsymbol{Z}$ separately, $\boldsymbol{M}$ is different in form to $\boldsymbol{N}$. Finally, $\tilde{\boldsymbol{Z}}$ at the nodal points of the inner element, or equivalently, at the integration points of the 20-noded outer element may be determined from

$$\tilde{\boldsymbol{Z}} = \boldsymbol{M}^{-1}\boldsymbol{Z} \tag{4.35}$$

It is recognised that the above approach makes use only of information available for a given finite element in order to determine strain gradients. Alternative techniques which use non-local approaches are known to be superior (e.g. [36]). However, in the present work, in the interest of simplicity and computational efficiency, the scheme adopted allows for piecewise linear variation of strain gradient and suitable mesh refinement minimises significant errors resulting from the linear approximation.

4.5 Analysis of hcp single and polycrystal GND development

In this section, we analyse the development of geometrically necessary dislocations within an hcp Ti alloy polycrystal using the GND-coupled crystal plasticity formulation described above. We then compare the results obtained with those from independent experimental observations [13] in particular addressing the GND generation during deformation on the various hcp a- and c+a-type slip systems.

The material considered is taken to be a near-α polycrystal titanium alloy. The material properties arising in the slip rule in eqn 1.8 are detailed below. Where freedom

exists to specify properties (the critical resolved shear stress and activation energy), these have been chosen to ensure that uniaxial stress-strain behaviour resulting for a polycrystal sample under strain controlled loading is reproduced, including the moderate strain rate sensitivity observed in these materials even at room temperature [26]. The properties used in eqn 1.8 are as summarised in Table 4.2 for a-slip. In the equation $\rho_S^m = \rho_S^s$ and $T = 293K$. The following relations apply between a-slip and c+a-slip: c/a ratio is 1.593, $b^{c+a} = c/a \times b^a$, $\tau_c^{c+a} = 2.5\tau_c^a$, and γ_0 has been fixed for simplicity to $\gamma_0^i = b^i/d$ for slip system i with d a characteristic length set to be the average grain size.

Table 4.2: Material properties

Slip Rule							
τ_c^a MPa	$b^a\mu$m	k JK^{-1}	ΔF J	νs^{-1}	$\rho_{ssd}^m\mu$m^{-2}	d μm	ψ
200	3.2e−4	1.381e−23	3.456e−20	10^{11}	0.05	30	1.5e−4
Elastic Moduli							
		E_{11} GPa	E_{33} GPa	ν_{12}	ν_{13}	G_{13} GPa	
Near-α Ti alloy		104.4	143.3	0.48	0.20	46.7	

Briefly before considering polycrystal behaviour, we apply the technique above for the purposes of validation to two very simple problems; namely single crystal uniform deformation and a single-crystal beam subjected to four-point bending in order to produce a linear variation of plastic strain and hence develop a constant GND density field of known slip activity.

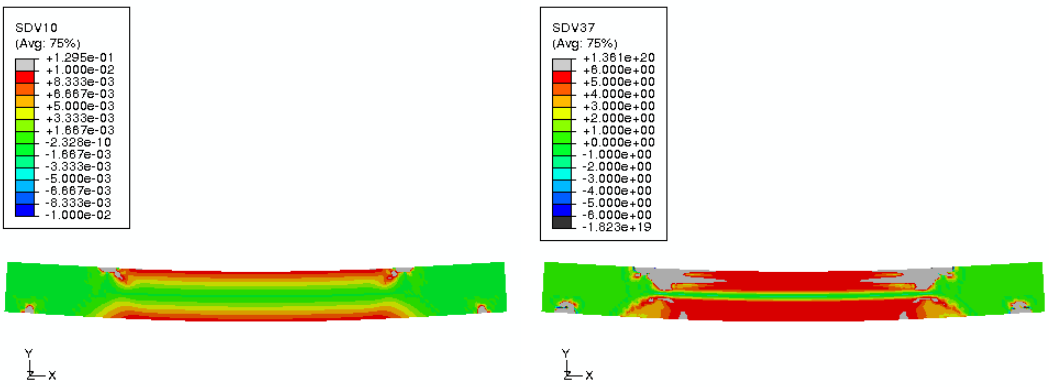
4.5.1 Single element: uniaxial loading

Here we subject a single element to displacement-controlled, uniaxial straining in a direction normal to the crystal c-axis. Figure 4.3 on page 73 shows sketches of hcp crystals showing the c-axis and a-axes as well as the possible slip systems. We therefore expect to observe the resulting uniform stress-strain behaviour which reproduces that for homogeneous a-type slip without the development of plastic strain gradients nor GND densities. The resulting stress-strain curve obtained reproduced the expected

behaviour.

4.5.2 Four point bending

A four-point (4pt) single crystal bending analysis provides a validity test of the model because of the known form of the strain and stress fields developed between the loading points. The linear variation of strain through the beam section is anticipated to lead to a constant plastic strain gradient and consequently GND density within the plastic zone. The (single) crystal orientation is specified such that the c-axis is normal to the beam axis, i.e. parallel to z-axis in Figure 4.5, so that prismatic slip only is anticipated. The hcp single crystal beam with dimensions of 200x20x20μm, is supported and loaded (under displacement control) at distances of $0.5h$ and $2h$ respectively from the end, where h is the height of the beam. A deflection of $2\mu m$ is applied, and the beam is constrained in the z-direction such that a state of plane strain is imposed. Figure 4.5 shows the results obtained for effective plastic strain and overall GND density.



(a) Effective plastic strain (b) GND density(μm^{-2})

Figure 4.5: Hcp 200x20x20μm - 4pt beam with reference crystal orientation under $2\mu m$ deflection.

Firstly it was confirmed that the field variation of the geometric dislocation tensor, $\boldsymbol{G}$, given in eqns 4.5 and 4.10 and determined with respect to deformed and undeformed configurations respectively, were identical.

In addition, the GND density was found to be constant through the thickness in the plastic regime in the pure bending region. This is expected since the plastic strains are linear through the thickness so that the GND density, which is derived from their gradients, would be expected to be constant. The magnitudes are within the expected range with the maximum being approximately $10^3 \mu m^{-2}$ (see, for example, Hull and Bacon [41, \$1.4]). Fleck et al. [31] also gave a one-dimensional single slip approximation for the density of GNDs, eqn 4.36.

$$\rho_G = \frac{1}{b}\frac{\partial \gamma}{\partial x} \tag{4.36}$$

The maximum effective plastic strain within the beam centre is about 0.01, the depth of the plastic region is about $10\mu m$ and $b = 3.20 \times 10^{-4} \mu m$. Hence $\rho_G \approx 0.01/(3.20 \times 10^{-4} \times 10) = 3.13 \mu m^{-2}$. In Figure 4.5(b), the corresponding value of ρ_G, which has been determined at the beam centre (i.e. away from the loading points) to be consistent with this calculation, is about $5 \mu m^{-2}$. Hence the predictions are physically reasonable.

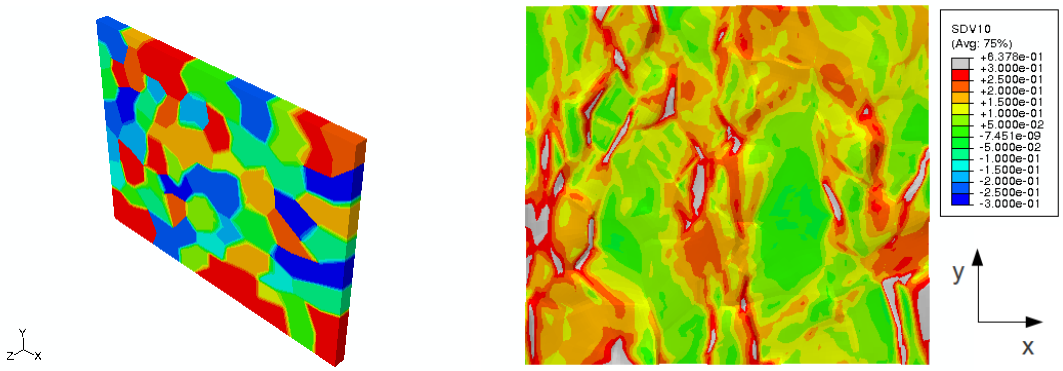
The GND density is calculated and stored according to the contribution from each individual slip system. In this problem only the prismatic slip systems contribute to the density for the prescribed conditions, as expected.

4.5.3 Hcp polycrystal (random orientation)

The GND-coupled crystal plasticity model is applied to the study of GND development in a model Ti polycrystal. The grain morphology for this polycrystal was generated by drawing the desired grain shapes on an x-y plane in Abaqus/CAE, and then extruding these shapes into the z-direction. The polycrystal is subjected to uniaxial straining up to a strain of about 12%. The resulting generation of GND densities on the various hcp slip systems are compared with those obtained independently from high resolution EBSD carried out on a similarly near-alpha titanium alloy previously

subjected to deformation by rolling [13]. Clearly, the deformation histories applied for the model polycrystal and in the experiment are different but it remains useful to carry out qualitative comparisons of the results obtained.

The model polycrystal comprises sixty nine grains with random initial orientation, as shown in Figure 4.6(a). The variable shown is one of the nine components of the orientation matrix $\boldsymbol{g}$ (i.e. $g^{-1}(1,2)$), where $\boldsymbol{g}$ is the orientattion matrix as defined in standard texts on texture analysis, e.g. Kocks et al. [49, pg. 65] and Randle and Engler [68, pg. 35]. Figure 4.6(b) shows the effective plastic strain developed in the polycrystal which is constrained not to move in x on the negative x-face, in y on the negative y-face, in z on the negative z-face, and loaded in compression on the positive x-face.



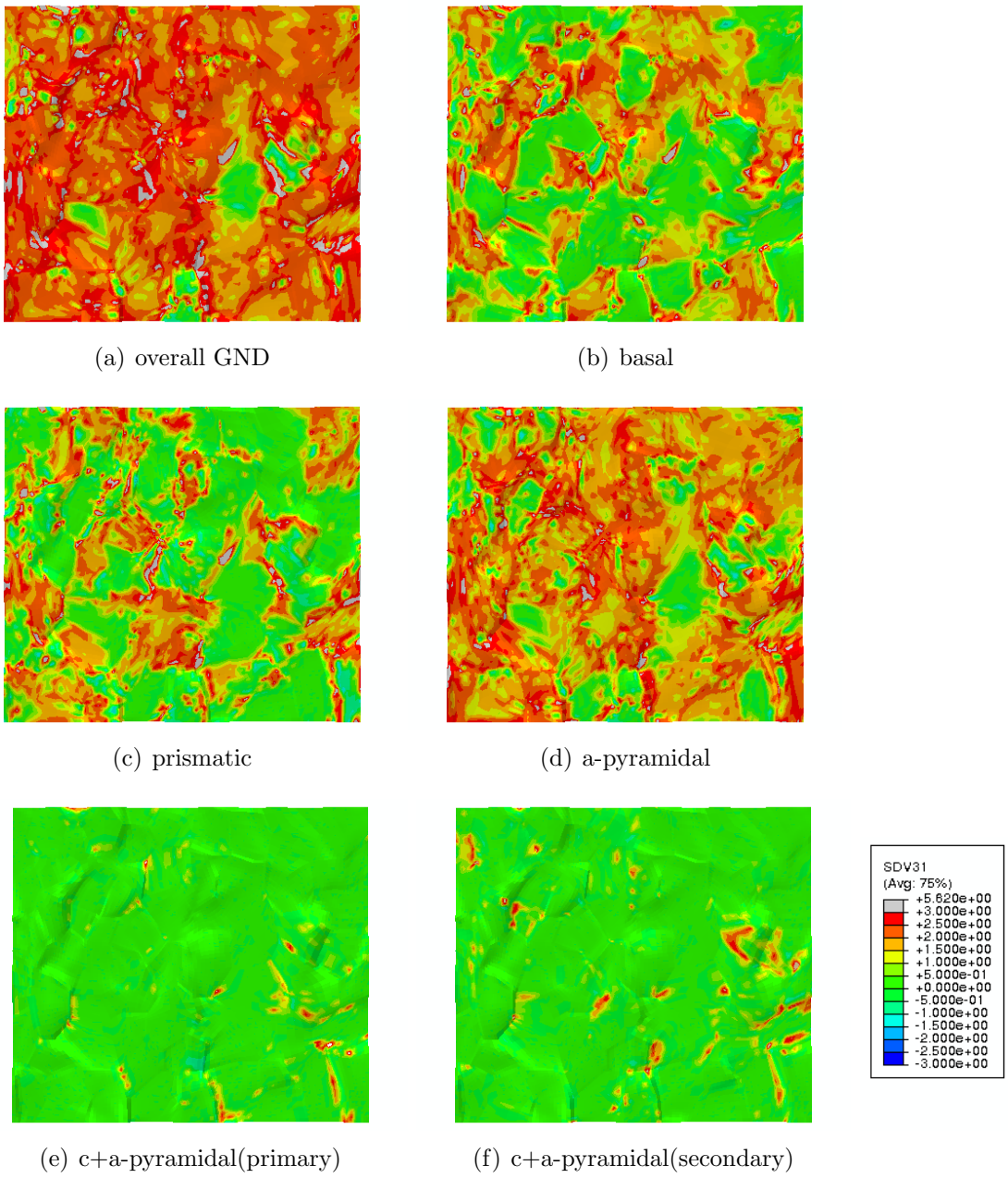
(a) $g^{-1}(1,2)$ (b) Effective plastic strain

Figure 4.6: Hcp 240x180x10μm polycrystal under applied compression of 192.0μm on the positive x-face, with a strain rate of $10^{-3}s^{-1}$ at a strain of 12%

Observations and discussion

Figure 4.7 shows the field variation of GND densities obtained. It is observed that the basal, prismatic, and a-pyramidal slip systems have the highest contribution to GND density. From Figure 4.7, it is clear that c+a slip systems provide a much smaller contribution compared to the others. This is in good qualitative agreement with experiments as reported by Britton et al. [13, fig. 2].

Pole figures (Figure 4.8) also suggest that although the initial orientation is gener-



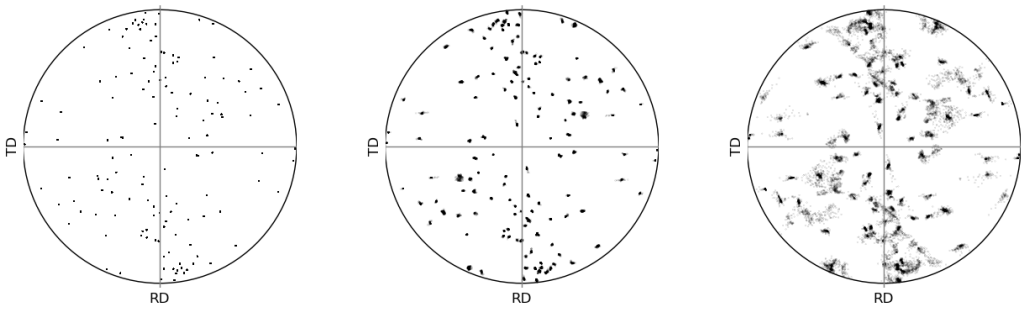
(a) overall GND (b) basal

(c) prismatic (d) a-pyramidal

(e) c+a-pyramidal(primary) (f) c+a-pyramidal(secondary)

Figure 4.7: Logarithmic GND density results for the hcp polycrystal shown in Figure 4.6, in μm^{-2} after an applied strain of 12.0%.

ally random, there is increasing density of crystals with c-axes in, or mostly oriented towards, the y-z plane than towards the x-z plane as the deformation increases. Since we are loading in the x-direction, we expect a decreasing rate of activation of c+a-slip. Indeed as Figure 4.8(c) shows, as the deformation proceeds, many crystals rotate so that their c-axes turn towards the z-direction (and there is also significant rotation towards the y-direction). This is in keeping with the nature of the loading and boundary conditions as detailed above.



(a) Initial orientation (b) orientation at $\epsilon_{xx} \sim 3.2\%$ (c) orientation at $\epsilon_{xx} \sim 12.0\%$

Figure 4.8: Hcp polycrystal. 0001 pole figure before, part way through, and at the end of the deformation.

Statistical analysis

In this section histograms are presented comparing the results of a statistical analysis of data predicted by the GND model developed here with that obtained by experiments performed by Wilkinson et al. [84]. Some results from the experiments have now been published [13]. The sample shown in that paper is the same as that from which the experimental data presented here was generated. In Figure 4.9 the vertical axis shows the number of pixels (for the experimental data) or elements (for the simulation results) as a fraction of the total against the GND densities shown on the horizontal axis. It therefore gives an indication of the coverage over the sample for any given GND type under observation. Dislocation densities less than $0.1\mu m^{-2}$ have not been included in the figure.

It is observed that the GND distributions change over time in response to the corresponding level of deformation. Figure 4.10 shows the development of the histograms as the applied strain develops. The predicted histogram given in Figure 4.9 corresponds to an applied strain of about 12%. The following observations are made.

(i) For both predicted and experimental data, each set of densities corresponding to each independent slip system type or dislocation type is distributed such that it

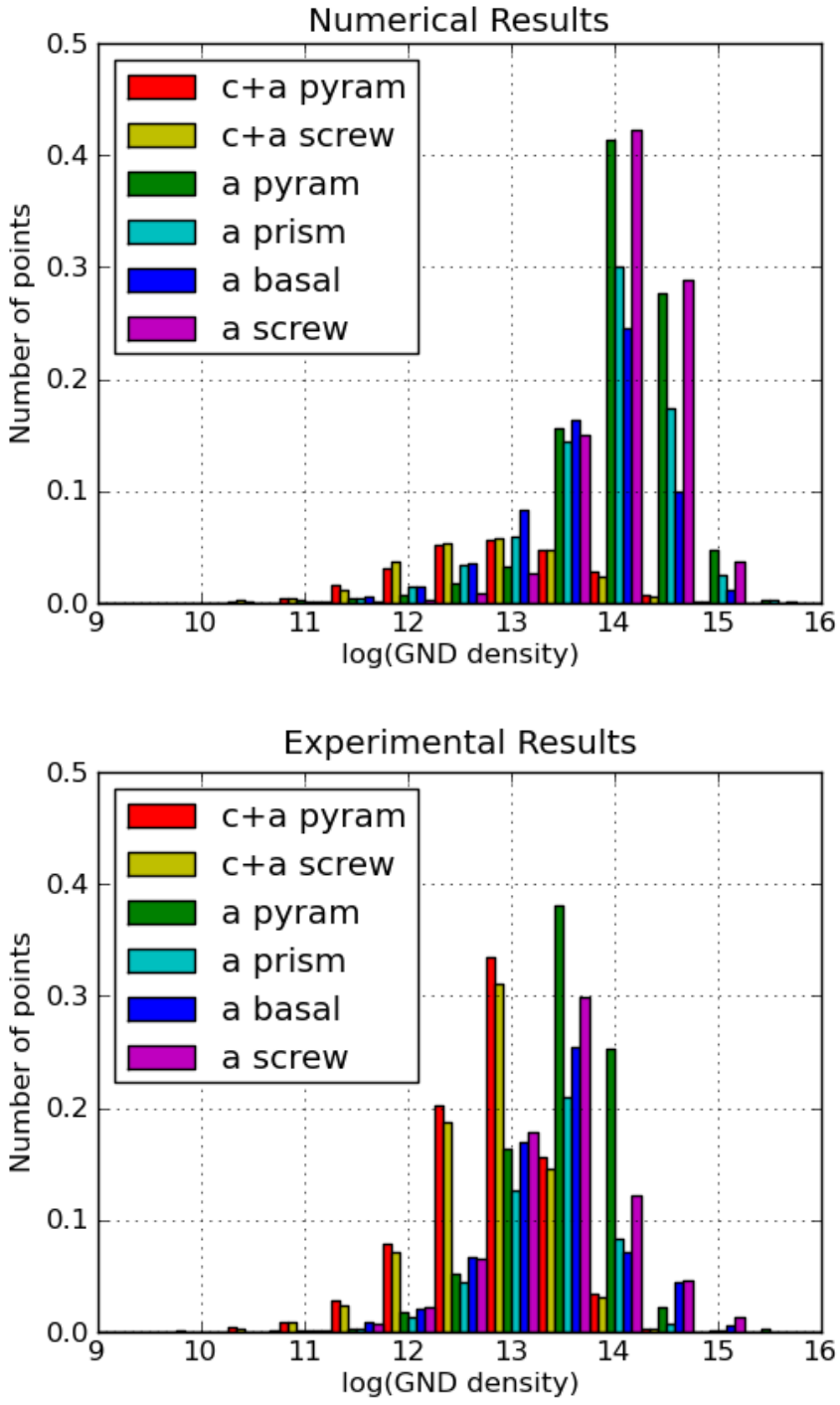
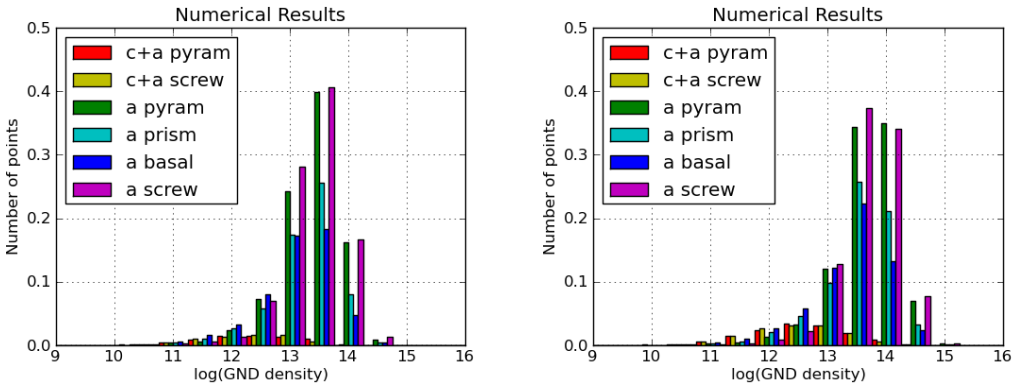


Figure 4.9: Predicted and experimental distributions of GND density (m^{-2}). The horizontal axis is logarithmic (base 10). Each range of values starts with red (c+a pyram) and ends with magenta (a screw), and the width of the range is 0.5. The top figure shows the predicted results while the lower figure shows the experimental results, courtesy of Wilkinson et al. [84]. The vertical axis shows the number of points (pixels or elements) normalised to the total of the same in the sample/model.

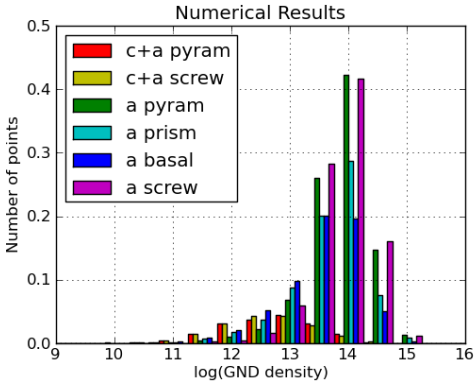
can be represented approximately as a skewed normal distribution.

(ii) In both the predicted and experimental results it is observed that the density of GNDs for c+a-slip is an order of magnitude lower than that for a-slip.

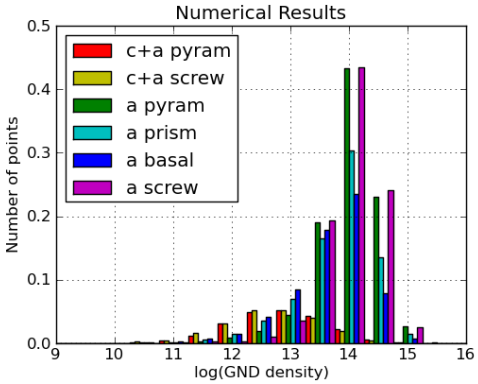


(a) $\epsilon_{xx} \sim 3.2\%$

(b) $\epsilon_{xx} \sim 5.6\%$



(c) $\epsilon_{xx} \sim 8.0\%$



(d) $\epsilon_{xx} \sim 10.4\%$

Figure 4.10: GND variation with applied strain. Data shifts right and overall coverage increases as more material experiences plasticity.

(iii) It is observed from histograms taken at different times through the duration of the simulation (Figure 4.10) that the GND densities increase and the volume of material experiencing GND activity increases. Following each grouping of density in the histograms (i.e. a single colour) reveals essentially a moving skewed normal distribution.

(iv) The experimental data shows more widespread c+a activity than the simulation.

(v) It is observed in both cases that a-pyramidal edge dislocations are the dominant type. The a-screw dislocations appear significant too but it should be noted that they include all screw contributions from all a-slip systems: a-pyramidal, basal, and prismatic systems. Basal and prismatic systems contribute by about the same amount in both the experimental data and simulations.

(vi) It is also clear from the histograms that all the simulated density magnitudes fall within the physically expected range both according to the literature and as the experimental results corroborate. Overall there is good qualitative agreement between the two sets of data.

Discussion

The polycrystal in the simulation is not necessarily completely representative of the experimental sample as will become more clear in the following points. The experimental sample referred to here is shown in [13].

In computing the GND density from the experimentally measured curvatures [13], it was assumed that all slip systems were active. This is a very unlikely occurrence for an hcp crystal. In the numerical simulation, only the active slip systems are accounted for. This factor has a bearing on the solution for the densities as it means that in the experimental data analysis, the number of unknowns (the densities) was always assumed to be higher than in reality. The method used for GND analysis in the experiment is detailed in Britton et al. [12]. This difference probably offers the best explanation for the observation that the c+a coverage is higher for the experimental results than that from the simulation. As the pole figures (Figure 4.8) show, the texture is changing in such a away as to become less favourable to c+a-slip. This change is not captured by assuming that all systems are always present, as in the experimental analysis.

In addition to the above, in the numerical simulation, there is full knowledge of the strain gradients (i.e. all the nine components of Nye's tensor are known); in the experiment, only six of the nine components can be obtained [12] and the assumption of plane stress has been made. No such assumption or approximation is needed in the calculations presented here.

The size, geometry, grain size distribution, and number of grains of the experimen-

tal sample were not the same as those used for the simulation, compare [13, fig. 1] with Figure 4.6(a) above. Since the GND density is size dependent, we should expect differences. Another size related factor is the fact that in the experiments, the pixel (point) size is $0.28\mu m$ while the characteristic element size for the simulation is $4\mu m$. This brings into perspective an aspect of length scales - in this case with reference only to the level of resolution - which could result in differences. This finite element resolution related size effect was checked by Mayama et al. [60] who studied the organization of the GND structure in an FCC bicrystal subjected to cyclic loading. His results showed that a higher mesh resolution led to a higher predicted GND density but qualitatively the spatial distribution was not affected. Other length scales are also discussed by Kysar et al. [52] who state that it is necessary to choose a characteristic length scale for the volume under consideration so that the calculated value of the geometrically necessary dislocation density converges to a meaningful value.

In addition to size differences, the numerical model uses a randomly chosen initial texture as indicated in Figure 4.8. That is, not the same orientation distribution as that for the experimental sample [13, figs. 1 and 2]. Orientation affects activity and strain gradients, and hence GND magnitudes. This may also be part of the reason the experimental data shows more widespread c+a activity than the simulation (i.e. peak number of points for c+a about 33% for the experiment and about 5% for the simulation).

Despite these potential sources of difference, it is clear from the data that there is good qualitative agreement between simulations and the experiment. It is to be noted again that in the data analysis performed after the experiments, an energy based minimisation was performed to compute the GND densities while a least squares approach (which is geometrically motivated to minimise dislocation line length) has been used here. The level of agreement obtained suggests that the minimisation approach used

may not be very significant in determining the result.

The unexpected result, however, is the dominance of the a-pyramidal slip in contributing to the GND density. In a separate test, it was observed that if a-pyramidal systems were assigned the same CRSS as the c+a pyramidals they would never become activated. Energy considerations make it sensible that they should have similar CRSS to that of the basals and prismatics; this state gives the observed results as already noted and this is in agreement with the experiment. What is not clear then is why they have a greater influence than the prismatic or the basal systems. It may be due to the fact that a-pyramidal slip can easily be activated both for orientation suitable for basal slip and for prismatic slip, so that it is possible over a wider range of crystal orientations than either of basal or prismatic slip.

4.6 Conclusion

The geometric dislocation tensor has been derived in forms suitable for both deformed and undeformed configuration formulations, and reconciled with the various suggestions of its form in the literature.

This tensor is given by the *curl* of a second order tensor. It was found that various authors use different definitions for the *curl* of a second order tensor. A mathematically consistent definition of this operation has been derived based on the starting definition of the *curl* of a vector.

Existing numerical techniques which address the well known non-uniqueness problem have been developed for the particular use of hcp crystals in which GND density is assumed to develop on all the active independent slip systems. A technique has been presented for accounting for the slip systems shared by screw-type dislocations. GND density is fully coupled with the crystal slip rule adopted.

Analyses have been carried out of a model near-α Ti polycrystal subject to de-

formation. The development of GND densities on the a- and c+a-type slip systems (basal, prismatic and pyramidal) has been compared with corresponding experimental measurements. In particular, the model prediction that a-type densities are an order of magnitude higher than c+a-type is entirely in keeping with experimental observations. The predicted distribution of a-type basal, prismatic and pyramidal and c+a-type pyramidal GND densities are found to show good agreement with experimental observations.

Chapter 5

Strain, lattice rotation and GND density in a nickel alloy

5.1 Executive summary

A single-crystal nickel alloy sample containing carbide particles of size $\sim 20\mu$m has been subjected to cooling from 870°C to 20°C from a nominally stress-free state thus causing the development of thermal mismatch strains as a result of the differing thermal expansivities of the Ni matrix and the carbide particle. High-resolution EBSD has been employed to determine the resulting elastic strains, lattice rotations and densities of geometrically necessary dislocations (GNDs) close to a particular carbide particle. A representative gradient-enhanced crystal plasticity finite element (CPFE) model has been developed for the same sample and loading conditions, and detailed comparisons of the predicted strains, rotations and GND densities are presented. In addition, the same analysis is carried out in which the GND density is decoupled from the crystal slip rule, and the results obtained also compared with those from the gradient-enhanced model and with the experimental data. Qualitatively good agreement is achieved between the coupled and decoupled model elastic strains with the EBSD measurements, but lattice rotations and GND densities are quantitatively well-predicted by the coupled crystal model but are less well captured by the decoupled model. In addition, the GND coupling is found to lead to reduced lattice rotations and plastic strains in the region of highest heterogeneity close to the Ni matrix/particle interface, which are in agreement with the experimental measurements. The results presented provide objective evidence of the effectiveness of gradient-enhanced CPFE and demonstrate that GND coupling is

required in order to capture strains and lattice rotations in regions of high heterogeneity.

5.2 Introduction

It is becoming increasingly desirable to calculate strain and stress response at progressively smaller length scales. Major drivers for this are in, for example, development of understanding of deformation, fatigue, and texture evolution [70]. Here we confine ourselves to length scales of order grain size and hence relevant to polycrystalline materials for which there is significant interest in slip transfer, slip localization, grain boundary sliding, twinning, fatigue crack nucleation, and micro-texture [6, 25, 27, 34, 50, 61, 72, 77, 87]. Also of great interest is the ability to calculate accurately the evolving densities of dislocations, be they geometrically necessary (GND) or statistically stored (SSD), because of the potential roles played in latent hardening, initiation of recrystallisation and nucleation of fatigue to name but three areas. There are now many modelling techniques available in crystal plasticity finite element analysis [69] and for the determination of GND density and their inclusion in modelling studies related to indentation size effects [12, 81], facet fatigue [6, 25, 50, 61] and micro-deformation [17, 18] for example, is widespread. However, what is currently less clear is how well current modelling techniques, and in particular, crystal plasticity finite element methods, properly and accurately capture independent experimentally observed behaviour; that is, at the level of individual grains, the strain and stress distributions, the lattice rotations and the densities of GNDs. Hence the primary aim of this chapter is to present detailed comparisons between length-scale–enhanced crystal plasticity calculation and high resolution EBSD measurement of these quantities in an attempt to assess how well the laudable ambitions referred to above are currently achievable.

The whole area of polycrystal modelling and experimental integration is currently,

rightly, receiving much attention; an example of this is the recent 140$^{\text{th}}$ annual TMS meeting which contained this area as a major theme. One of the earlier detailed studies of CPFE capabilities versus experimental observation was carried out by Kalidindi et al. [44] who made use of pseudo-2D polycrystal experiments with which to carry out detailed strain comparisons with crystal calculations, a technique used later by others [29]. Wang et al. [78], Yang et al. [86] and Zhao et al. [88] have similarly carried out detailed and interesting studies of polycrystal deformation with crystal plasticity but for surface-based measurements, the problem of comparing results with crystal calculations in the absence of knowledge of sub-surface crystallography remains an issue. There is little doubt, however, that Wang et al. [78] and Yang et al. [86] show that much progress is still to be made in order for CPFE predictions to be considered good, though work reported so far is based on conventional crystal plasticity as opposed to that which is gradient enhanced. In particular, he demonstrates the significant difficulty of capturing the important features of grain boundary slip transfer.

Our approach in the present chapter is to attempt to enable as close as possible a tie-up between the experimental model and that used in gradient-enhanced CPFE analyses[1]. We choose an fcc nickel single crystal material to investigate, which after heat-treatment, contains distinct and reasonably separated carbide particles of size $\sim 20\mu$m. The material is then subjected to stress relief by heat treatment at 870°C and subsequent reduction of temperature to 20°C thus generating significant thermal strain at the single crystal particle boundaries by virtue of the differing thermal expansivities of the nickel single crystal and the carbide particles. The difference is large enough in order to cause the development of plastic strain with gradients and hence lattice curvatures and densities of GNDs. Our methodology is to adopt high-resolution EBSD

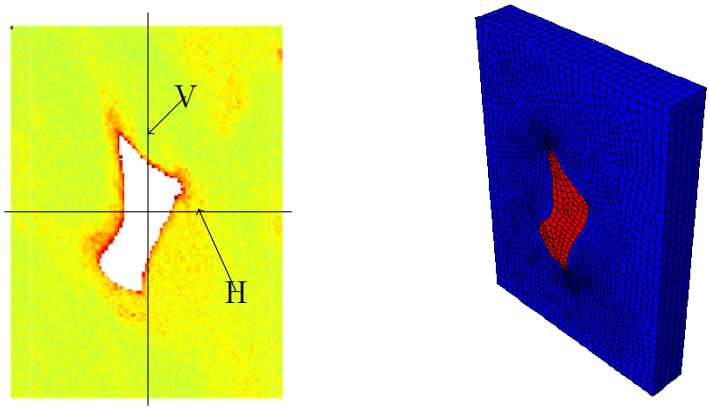
[1]The work in this chapter was done in collaboration with Phani Karamched and Angus Wilkinson of Oxford's Materials Department. The Materials group produced the experimental data used in this chapter, which they also later separately published in [45].

[82] in order to measure the elastic strains developed at the particle together with determination of the distribution of GND density from lattice curvature measurements. Determination of the distribution of GND density from lattice curvature measurements is explained in [13]. We model a nominally identical material and loading using our GND-enhanced crystal plasticity approach and present detailed comparisons of the results obtained. Some of the results of the EBSD study have been published previously [45], so we give a brief description of the problem studied and the EBSD techniques brought to bear. The modelling strategy for GND accumulation, which now accounts for the activity on each individual slip system and dislocation type (edge versus screw) has also been reported in Chapter 4 in the context of hcp polycrystals so is similarly only briefly described here. We then focus on the results obtained from both techniques and present detailed comparisons. Finally, we present the results of the same analysis in which the GND development is de-coupled from the slip rule in order to assess the importance of the coupling.

5.3 Material, experimental EBSD and crystal plasticity methodology

The material studied is a directionally-solidified nickel alloy provided by Rolls-Royce plc. Samples of dimensions $13.5 \times 3 \times 3$mm were cut from the stock provided and subjected to an initial heat treatment of 1100°C for 1 hour followed by ageing by exposure to 870°C for 16 hours twice. The ageing enabled enhanced grain growth and subsequent EBSD analysis revealed that in fact single crystal samples had been obtained containing carbide particles of various shapes of size $\sim 20\mu$m. EBSD also enabled determination of the crystallographic orientation and in the sample studied here, it was found to be $\phi_1 = 83.5°$, $\phi = 91.5°$, $\phi_2 = 0°$ in Bunge notation. Following cooling

from 870°C, high-resolution EBSD was again used in order to quantify the elastic strain distributions which resulted from the mismatch in thermal expansivities of the nickel single crystal material and the carbide particle. Full details of the EBSD technique and the determination of the full strain field tensor components, lattice rotations and GND density may be found in [45]. The particular particle-matrix combination to be studied is shown in Figure 5.1(a). Its dimensions are $27 \times 37\mu$m. In the experimental study described in [45], the samples were subsequently also subjected to four-point bend fatigue tests but we confine ourselves in this chapter to the thermal loading problem for the specific particle-matrix combination shown in Figure 5.1(a). An advantage of analysing such a system is that in many respects, it becomes pseudo-two-dimensional in that there is no (or little) variation of crystallographic orientation through the depth. In addition, because it is single crystal, the often-encountered issue of 3D polycrystal surface measurements is largely eliminated, though the potential variation of the particle geometry through the thickness of the sample remains.



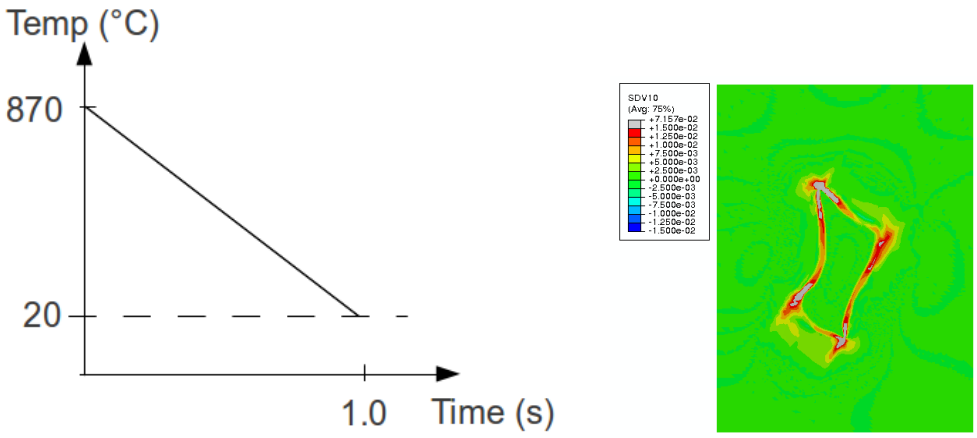
(a) EBSD (b) CPFE

Figure 5.1: (a) $27 \times 37\mu$m EBSD image of nickel alloy single crystal matrix containing a large carbide particle subjected to thermal loading and (b) the corresponding $28 \times 38 \times 5\mu$m 3D crystal plasticity finite element model.

5.3.1 Crystal plasticity model

The corresponding geometric finite element representation of the problem is shown in Figure 5.1(b). Its dimensions are $28 \times 38 \times 5\mu$m. A full three-dimensional model is

developed comprising 11000 20-noded quadratic 3D finite elements and results obtained from the front, free-surface are representative of those for a state of plane stress. The same assumption has been used in order to determine the full strain tensor from the EBSD analysis. In the finite element model, the boundaries are all assumed to be free though analysis has shown that changing the conditions (eg such that all planar boundaries remain so) has very limited impact on results obtained local to the particle, which are those of interest here. The thermal loading is applied in the model as shown in Figure 5.2(a). The temperature range imposed is identical to that in the experiments but the time-scale used in the modelling is arbitrary since although the crystal model incorporates rate sensitivity, these effects are likely to be negligibly small since for most of the cooling, the matrix material behaviour remains elastic. It is only at the end of the cooling process that the thermal strains developed are large enough to cause the onset of plasticity.



(a) Loading (b) p

Figure 5.2: (a) The temperature history to which the Ni particle/matrix have been subjected and (b) the resulting predicted accumulated plastic strains which develop local to the particle but within the Ni single crystal matrix

A full presentation of the length scale dependent, elastically anisotropic, physically-based and rate-dependent crystal plasticity model is given in [26], which is used here with changes as detailed in Chapter 2. The slip rate for the single-crystal nickel alloy is similar to the general form given in Chapter 1 equation 1.8 and is repeated below in

equation 5.1 to facilitate the discussion that follows.

$$\dot{\gamma}^{\kappa} = \rho_S^m \nu b^{\kappa 2} \exp\left(\frac{-\Delta F}{kT}\right) \sinh\left(\frac{(\tau^{\kappa} - \tau_c^{\kappa})\gamma_0^{\kappa}\Delta V^{\kappa}}{kT}\right) \tag{5.1}$$

This slip rate was developed on the basis of planar slip occurring through release and pinning of gliding, statistically stored dislocations with density ρ_{ssd}^m, with an activation energy ΔF associated with the pinning by sessile, geometrically necessary and statistically stored dislocations with densities ρ_{gnd} and ρ_{ssd}^{im} respectively over an activation volume $\Delta V = b^2\lambda_p$. The pinning distance λ_p is taken to be $\lambda_p = 1/\sqrt{\psi\left(\rho_{ssd}^{im} + \rho_{gnd}\right)}$ in which ρ_{ssd}^{im} is the density of immobile statistically stored dislocations, ρ_{gnd} the density of geometrically necessary dislocations and ψ is a coefficient that indicates that not all sessile dislocations (SSDs or GNDs) necessarily act as pinning points. In the present work, for simplicity, the densities of mobile and immobile SSDs are taken to be equal. GNDs are addressed below. In the slip rule, b is Burgers vector magnitude, ν the frequency of dislocation jumps, successful or otherwise, k the Boltzman constant, T the temperature, τ^{κ} the resolved shear stress on system κ, τ_c the critical resolved shear stress and γ_0 the shear strain that is work conjugate to the resolved shear stress. The values of the material properties for the nickel alloy studied, including the thermal expansivities of the single-crystal nickel and the carbide, are given in Table 5.1. Where slip rule parameters, in the table, are not fixed according to the crystal lattice structure requirements they have been selected so as to minimise rate sensitivity effects. The carbide particle is assumed, reasonably, to deform elastically only.

In the slip rule in equation 5.1, the density of GNDs is coupled through the activation volume term ΔV such that any increase in GND density impacts directly upon the slip rate. In the analyses presented later, results are obtained in using the fully coupled slip rule and also the case in which the GND density is decoupled. That is, for the

Table 5.1: Material properties

Slip Rule							
τ_c MPa	$b\mu$m	k JK^{-1}	ΔF J	νs^{-1}	$\rho^m_{ssd} = \rho^{im}_{ssd}\mu$m^{-2}	γ_0	ψ
230	3.5072e−4	1.38e−23	3.456e−20	10^{11}	0.05	8.33e−6	1.5e−4
Elastic Moduli							
			E MPa		ν		
Nickel single crystal			207.0e3		0.28		
Carbide particle			207.0e4		0.28		
Thermal Expansivities							
Nickel single crystal			$20 \leq \theta$°C ≤ 800		13.0e−6 $\leq \alpha$°C$^{-1} \leq$ 15.0e−6		
Carbide particle			$20 \leq \theta$°C ≤ 800		$\alpha = 4.5e$−6°C^{-1}		

decoupled analysis, in equation 5.1, while the GND density is calculated, ρ_{gnd} is taken to be zero in the slip rule. The GND density for the fcc nickel system is determined for each active and independent slip system, taking full account of the edge or screw nature of the dislocation. The techniques employed are described in detail in Chapter 4 for an hcp crystal system hence are not reproduced here, but a brief summary is given to clear the difference in the relevant equations applied to an fcc crystal system. Geometrically necessary dislocations on the κ^{th} slip system can be represented as those with dislocation line directions parallel with the slip direction, $\boldsymbol{s}^\kappa$ (screw type), and parallel with the plane normal, $\boldsymbol{n}^\kappa$, and $\boldsymbol{m}^\kappa = \boldsymbol{n}^\kappa \times \boldsymbol{s}^\kappa$ directions (edge type) such that the total density is

$$\sum_\kappa \left(\rho_e^\kappa \boldsymbol{n}^\kappa + \rho_s^\kappa \boldsymbol{s}^\kappa\right) = \sum_\kappa \boldsymbol{\rho}^\kappa_{\text{gnd}} = \boldsymbol{\rho}_{\text{gnd}} \tag{5.2}$$

The evolution of geometrically necessary dislocation density is determined as detailed in Chapter 4 from

$$\sum_\kappa \left(\boldsymbol{b}^\kappa \otimes \boldsymbol{\rho}^\kappa_{\text{gnd}}\right) = (\text{curl}\boldsymbol{F}^p)^T \tag{5.3}$$

in which $\boldsymbol{F}^p$ is the plastic deformation gradient and $\boldsymbol{b}^\kappa$ the Burgers vector with di-

rection parallel to the corresponding slip direction. The well-known non-uniqueness problem [4] is addressed by use of a least-squares minimization of the dislocation densities in equation 5.3 implemented as the Moore-Penrose pseudo-inverse as detailed in Chapter 4 in Section 4.3.3. The analysis results in knowledge of the edge and screw type GND densities on all active slip systems (see Chapter 4 for a discussion on how the screw components are shared between the active slip systems having corresponding slip direction). From this, the magnitude of the dislocation vector $\boldsymbol{\rho}_{gnd}$ is calculated and it is this result which is then used in the slip rule, equation 5.1.

5.4 Strain, lattice rotation and GND density analyses of Ni sample

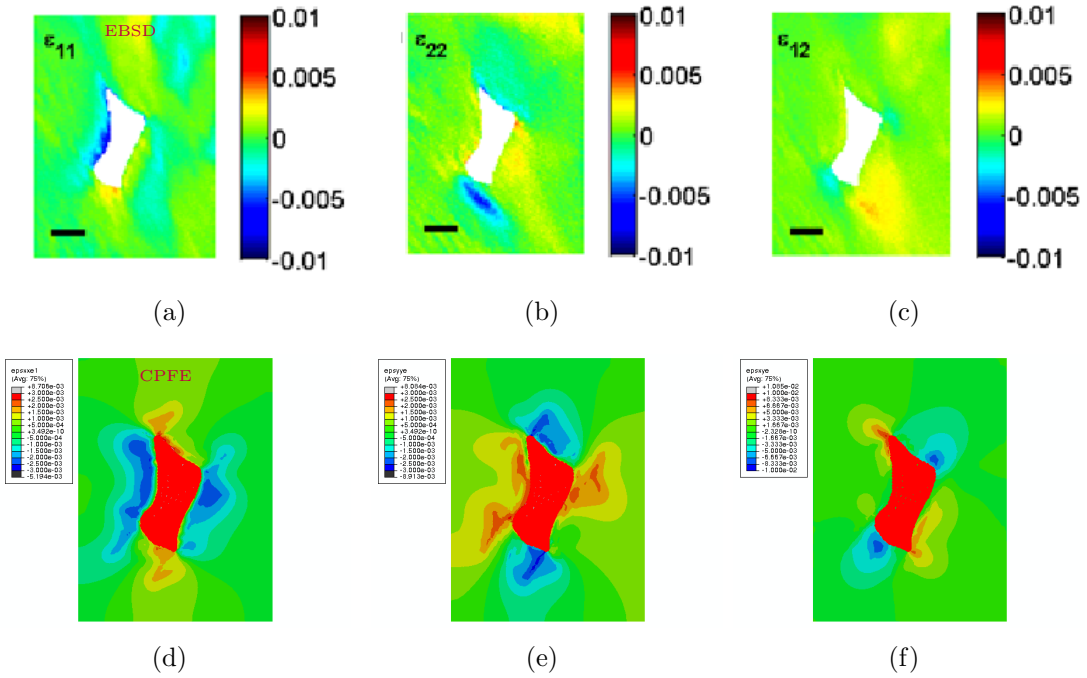
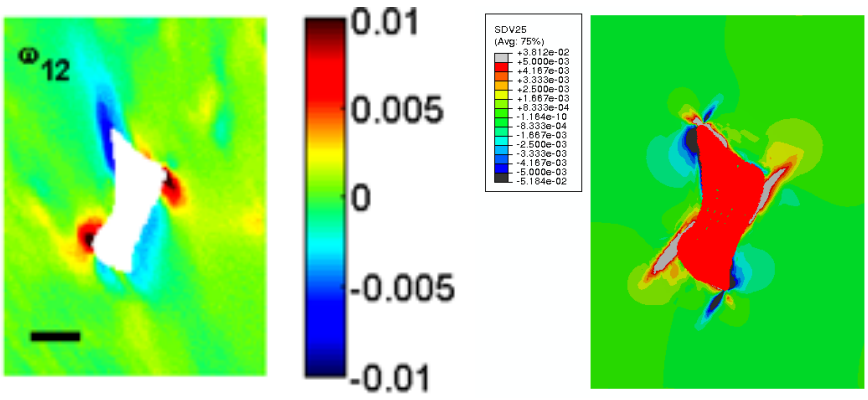


Figure 5.3: Field plots of components (as indicated) of elastic strains (a) - (c) experimentally determined and (d) - (f) those predicted from the crystal plasticity finite element model. There is no direct correspondence of colour.

On cooling the particle/Ni matrix material from 870°C to 20°C, the mismatch in thermal expansivity between the single-crystal matrix and carbide particle leads to the establishment of thermal strains and hence stresses. In fact, the difference in ex-

pansivity (see Table 5.1) is large enough, given the temperature change, to cause the development of plastic strains local to the particle. The extent of the predicted plastic straining, obtained from the crystal plasticity finite element (CPFM) modelling, is shown in Figure 5.2(b). As a result of the heterogeneous nature of the particle geometry, quite considerable variations and indeed gradients in plastic strain develop and it is therefore anticipated that corresponding variations in lattice rotation and GND development will as a result be observed. An important objective of the current chapter is to establish to what extent the detailed experimental observations can be captured accurately by the gradient-enhanced crystal model presented above. In Figure 5.3, the results of high-resolution EBSD to determine the elastic strains local to the particle, on the material free surface, are shown (Figure 5.3(a) to 5.3(c)) together with the corresponding CPFE results (Figure 5.3(d) to 5.3(f)). In the figures, the colour scale bar relates to the experimental measurements and there is no one to one correspondence with the colour scales in the predicted elastic strains. In the latter, the range of strain has been chosen to show to best effect the calculated strain distributions therefore providing, firstly, a qualitative comparison with the measurements. Quantitative comparison is presented later. The thermal strains developed are, in the absence of geometrical constraint, dilatational in nature, and are not therefore captured in the EBSD-determined strain fields. Hence, in order to compare like with like, in the calculated results, the purely dilatational strain has been subtracted from the total (for the direct components; this is not necessary for the shear strains) in order to give the differential strains. In addition, the EBSD-measured strains are, of course, the elastic strains so that again, in ensuring we compare like with like, the plastic strains have been removed from the total strain components in order to give just the elastic strains. Comparison of the figures indicates good agreement in a qualitative sense between measured and predicted elastic strains, i.e. considering the spread of colours local to the

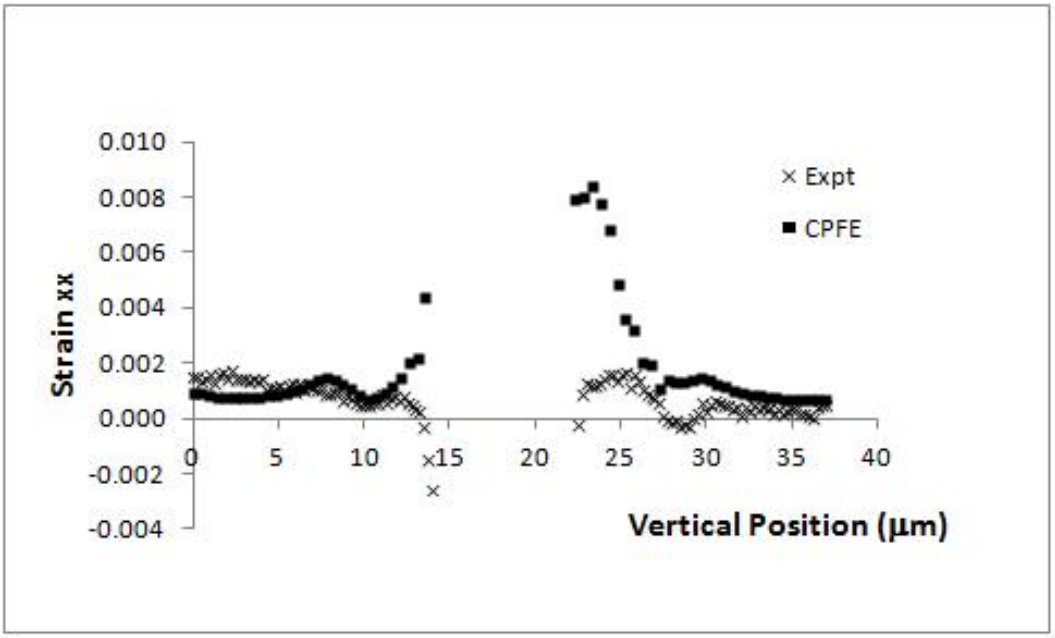
particle. Figure 5.4 shows the experimentally measured and predicted in-plane lattice rotations. Again, good qualitative agreement is observed.



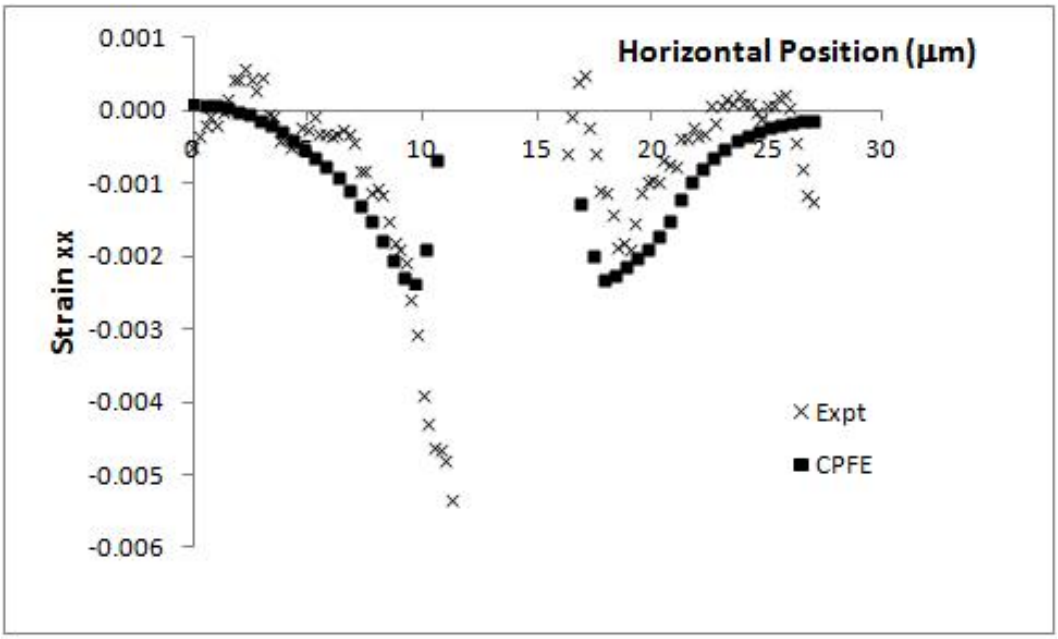
(a) (b)

Figure 5.4: Field plots of component (as indicated) of lattice rotations (a) experimentally determined and (b) those predicted from the crystal plasticity finite element model. There is no direct correspondence of colour.

In order to carry out a more quantitative assessment, two lines have been introduced in Figure 5.1(a). All the elastic strain components and lattice rotations along the vertical and horizontal lines have been extracted from both the experimental measurements and CPFE model predictions and are shown in Figures 5.5(a) to 5.8(b). It is apparent that there are some aspects of the strain and lattice rotations which are in good agreement but clearly others for which this is not the case. For example, along the vertical line in Figure 5.1(a), the direct strains are found to be significantly over-predicted in magnitude particularly very close to the particle. In contrast, along the horizontal, the predicted elastic strains are under-predicted close to the particle. Some of the shear strain distribution characteristics are captured; others are clearly not. Lattice rotations, however, shown in Figures 5.8(a) and (b) are quite well captured by the model in both magnitude and distribution along the two lines shown in Figure 5.1(a). A particular implication of this is for the CPFE model predictions for the GND densities, which are measured directly from the gradients of the lattice rotations. The predicted GND density distribution developed as a result only of the thermal



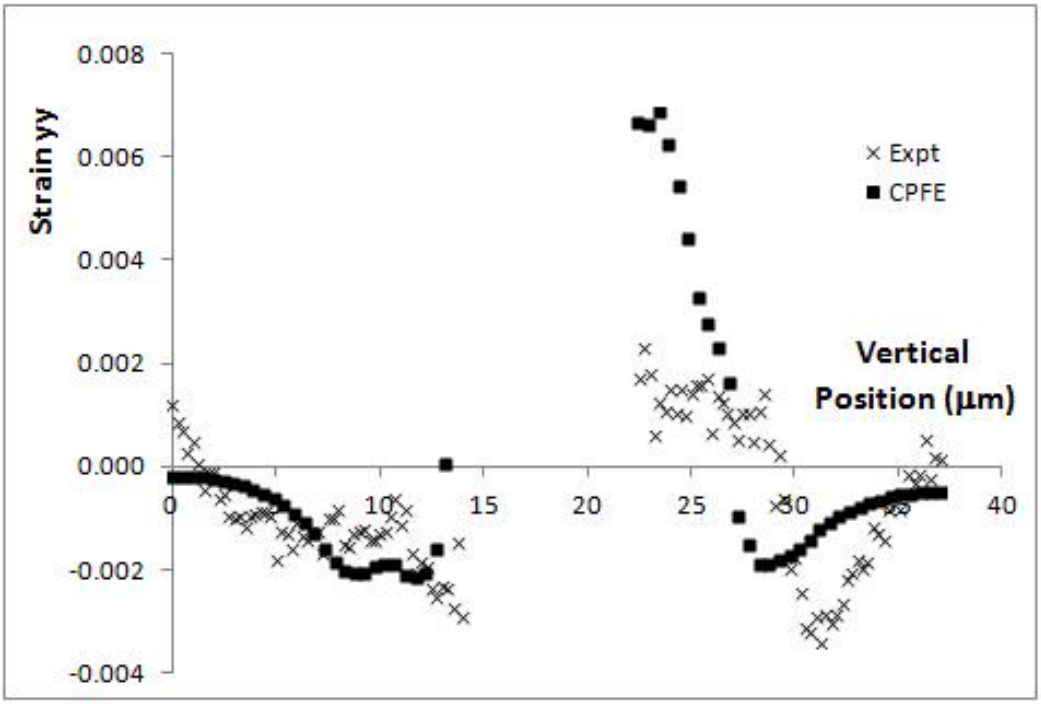
(a)



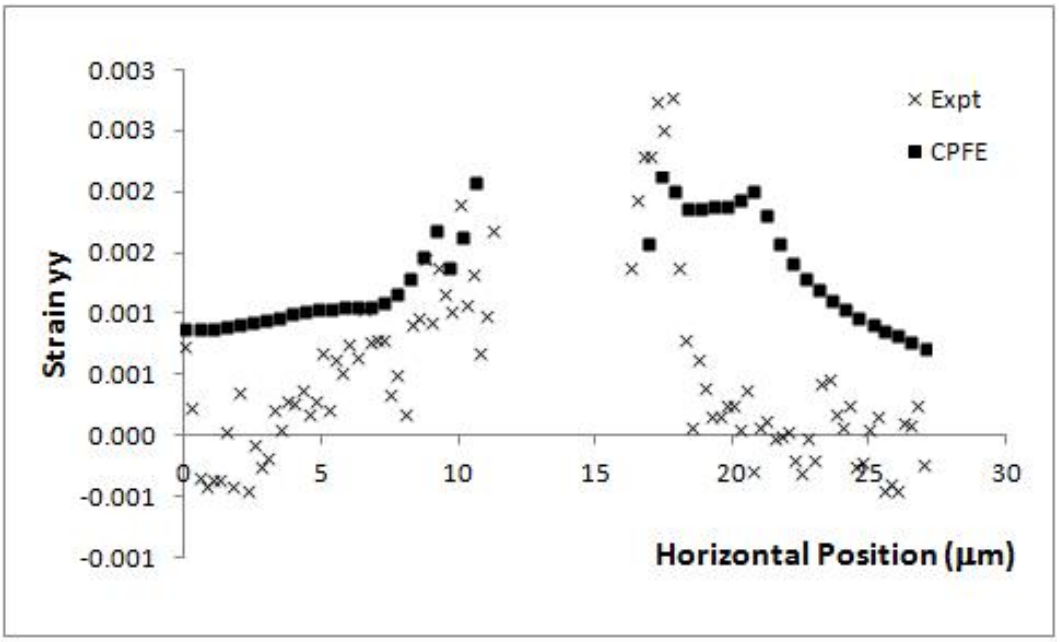
(b)

Figure 5.5: Graphs showing crystal plasticity finite element calculations and experimental EBSD measurements for the nickel/particle system subject to thermal loading. Results are shown along the vertical and horizontal lines given in Figure 5.1(a) as follows: elastic strains ε_{xx} along (a) the vertical and (b) horizontal line.

excursion is shown in Figure 5.9 together with that determined from EBSD measurements taken from the sample free surface. Again, reasonable qualitative agreement is obtained but a more quantitative comparison is shown in Figure 5.10 in which again,



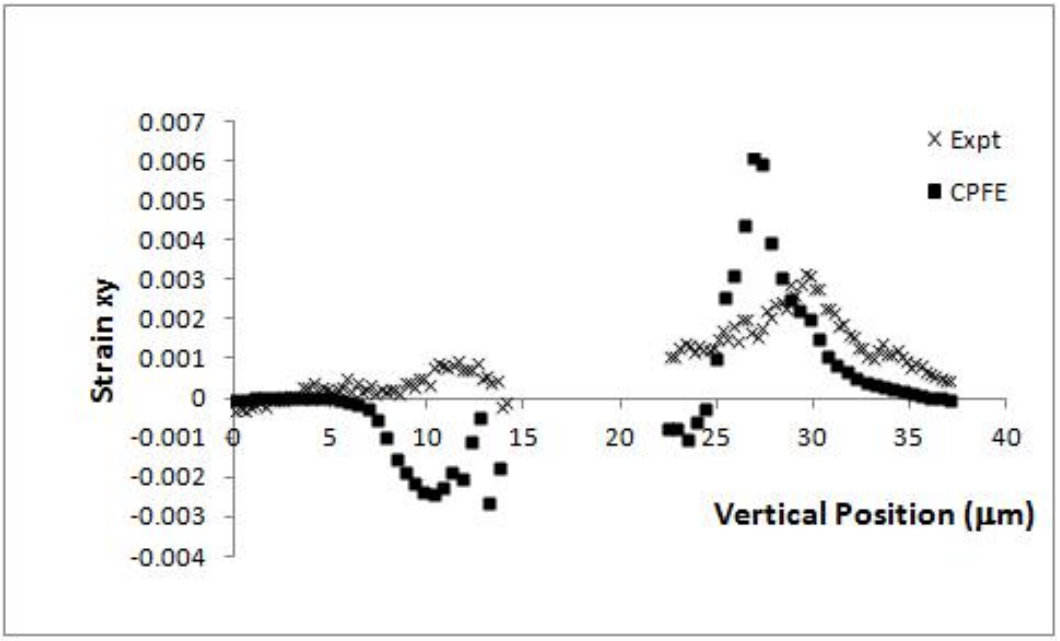
(a)



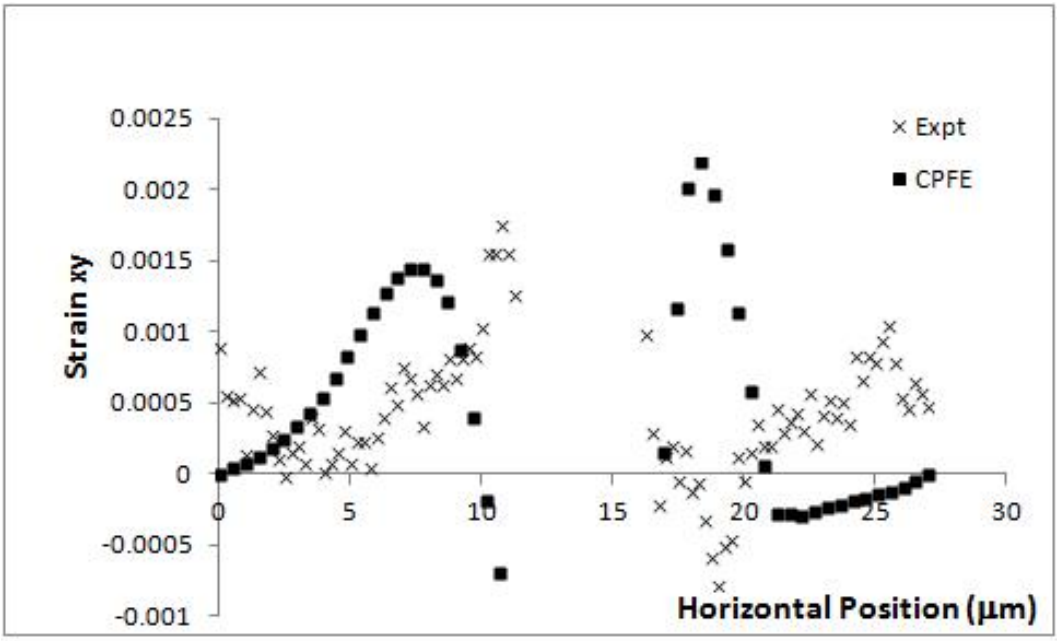
(b)

Figure 5.6: Graphs showing crystal plasticity finite element calculations and experimental EBSD measurements for the nickel/particle system subject to thermal loading. Results are shown along the vertical and horizontal lines given in Figure 5.1(a) as follows: elastic strains ε_{yy} along (a) the vertical and (b) horizontal line.

the variation of the experimentally determined and CPFE predicted GND densities along the vertical and horizontal lines shown in Figure 5.1(a) are given. The maximum values of GND density are shown in Table 5.3, compared for experiment and CPFE. Here, reasonable agreement can be seen both in terms of GND density magnitude and



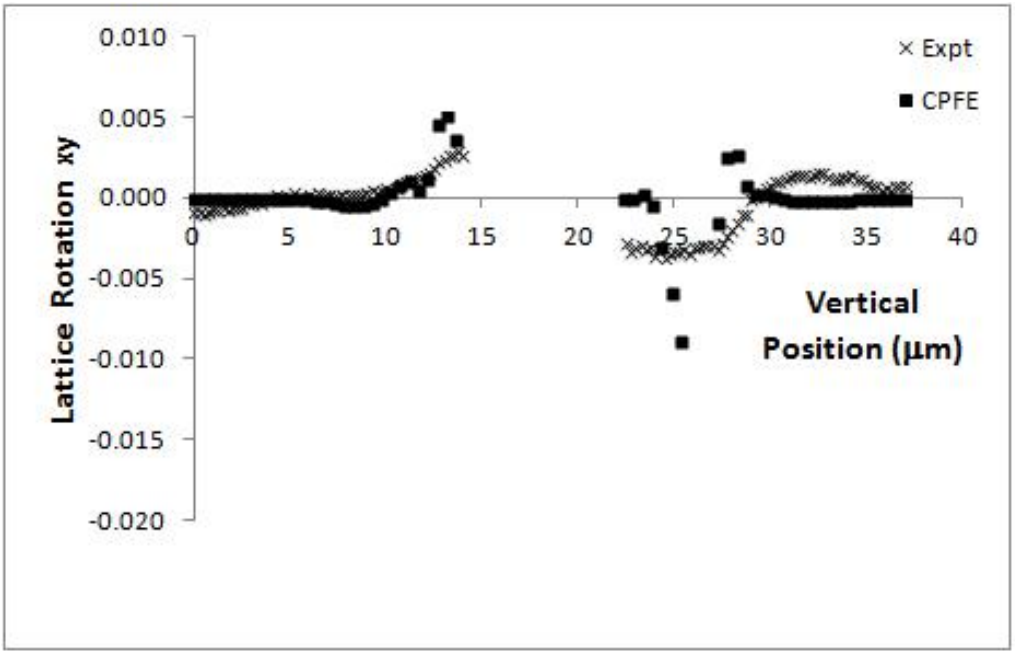
(a)



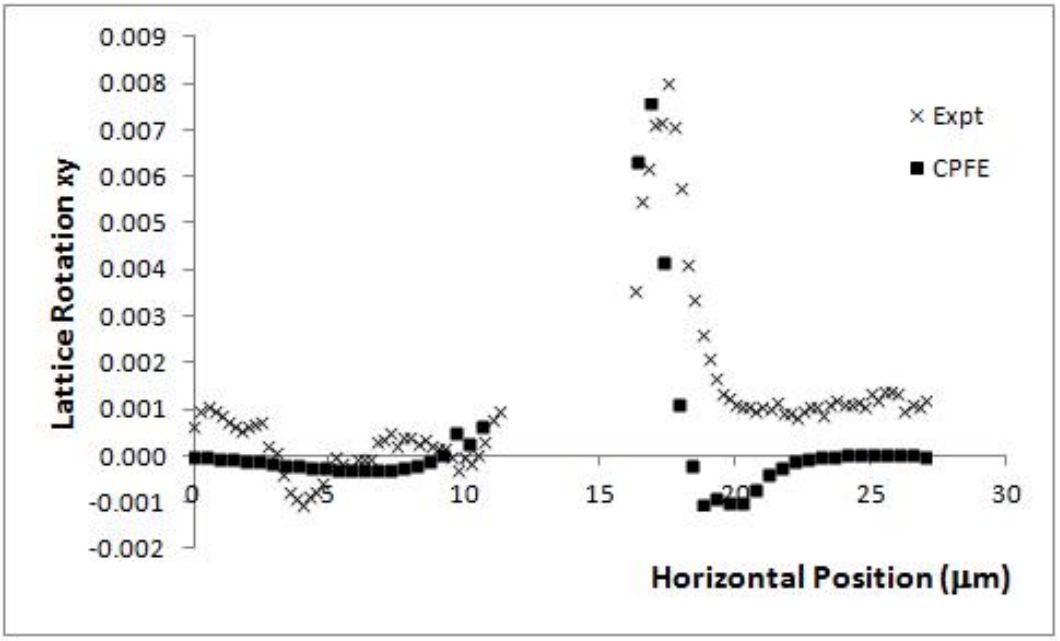
(b)

Figure 5.7: Graphs showing crystal plasticity finite element calculations and experimental EBSD measurements for the nickel/particle system subject to thermal loading. Results are shown along the vertical and horizontal lines given in Figure 5.1(a) as follows: elastic shear strains ε_{xy} along (a) the vertical and (b) the horizontal line.

the expected nature of the distribution - especially along the horizontal line.



(a)

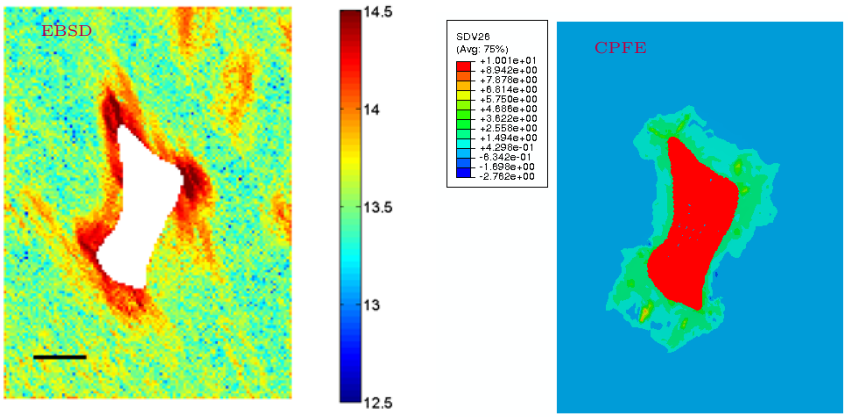


(b)

Figure 5.8: Graphs showing crystal plasticity finite element calculations and experimental EBSD measurements for the nickel/particle system subject to thermal loading. Results are shown along the vertical and horizontal lines given in Figure 5.1(a) as follows: lattice rotations ω_{xy} along (a) the vertical and (b) horizontal line.

	Expt		CPFE	
	Rotation	Location	Rotation	Location
Vertical	61.4	28.3	106.2	28.2
Horizontal	117.9	16.5	110.2	17.8

Table 5.2: Maximum values of GND density (μm^2) and corresponding locations (μm) compared for experiment and coupled CPFE results. Refer to Figure 5.10 for corresponding plots.



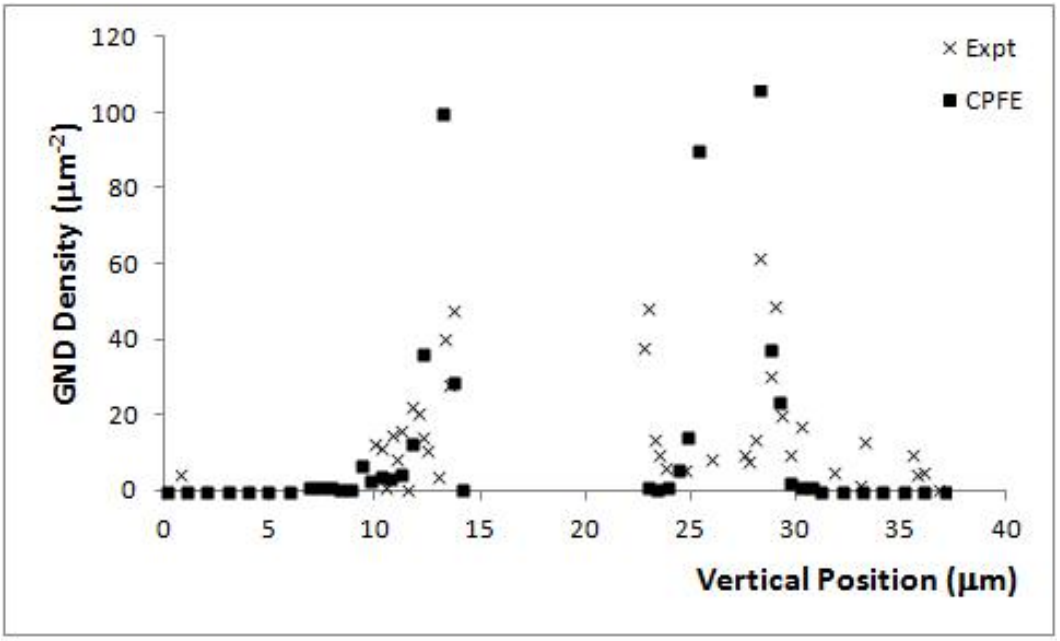
(a) (b)

Figure 5.9: Field plots of density of geometrically necessary dislocations (GNDs) (a) experimentally determined and (b) those predicted from the crystal plasticity finite element model. The range is the same for both figures but there is no direct correspondence of colour.

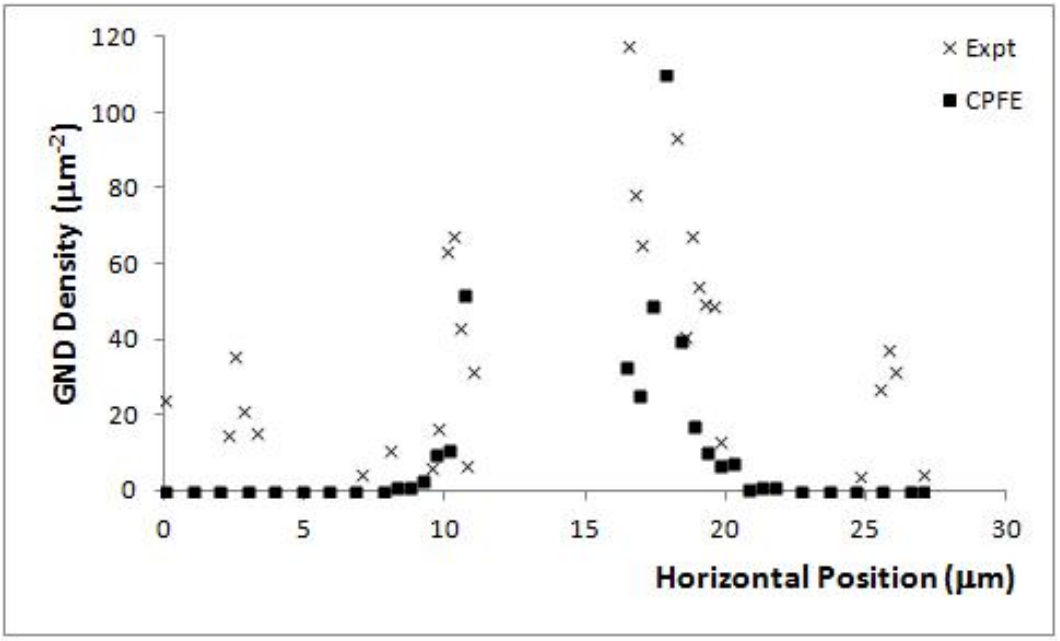
5.4.1 Comparison between the GND coupled and uncoupled models

It is sometimes argued in the literature that the coupling between the evolving GND density and its effect on subsequent plastic slip is crucial in ensuring the accuracy of crystal plasticity predictions. It is therefore of interest to test this assertion particularly in the light of the quality (or otherwise!) of gradient-enhanced CPFE predictions and their comparison with experimental data at a micro-mechanical level. Hence, the CPFE analysis of the particle thermal problem discussed above has been repeated but on this occasion, the GND coupling with the slip rate shown in equation 5.1 is removed. That is, the GND density is calculated from equation 5.3 just as it was in the earlier analysis, but this is not reflected in the slip rule in which now, the activation volume, ΔV, is assumed to be constant and unaffected by the GND density such that its value remains fixed at

$$\Delta V = b^2 \lambda_p = \frac{b^2}{\sqrt{\psi \left(\rho_{ssd}^{im} + \rho_{gnd}\right)}} = \frac{b^2}{\sqrt{\psi \rho_{ssd}^{im}}} \tag{5.4}$$



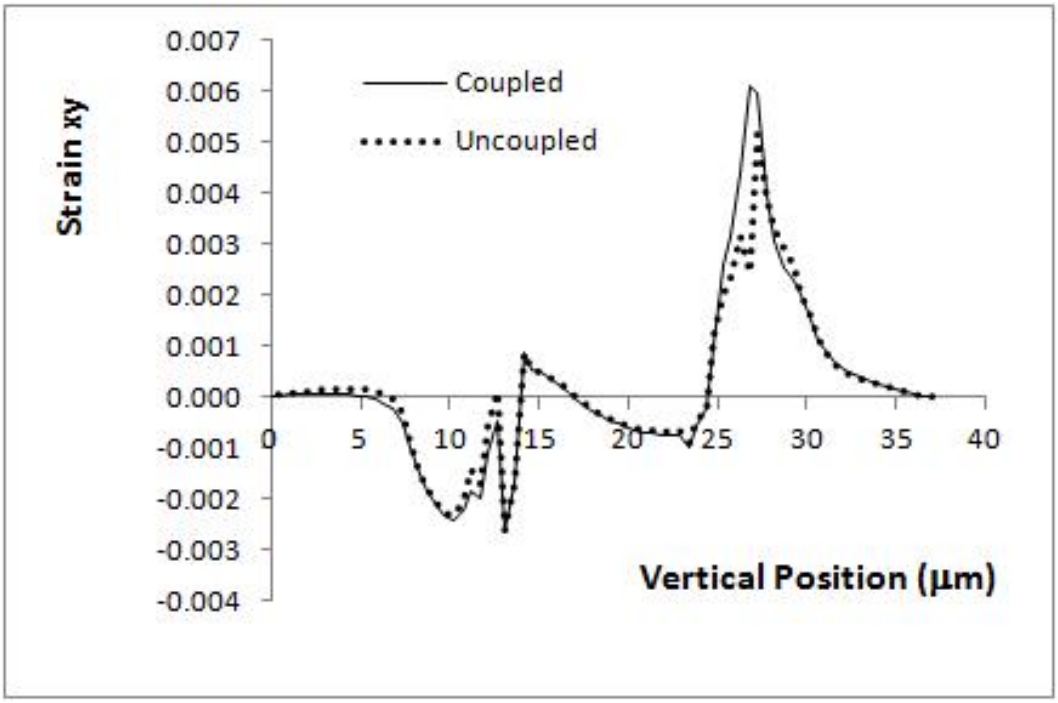
(a)



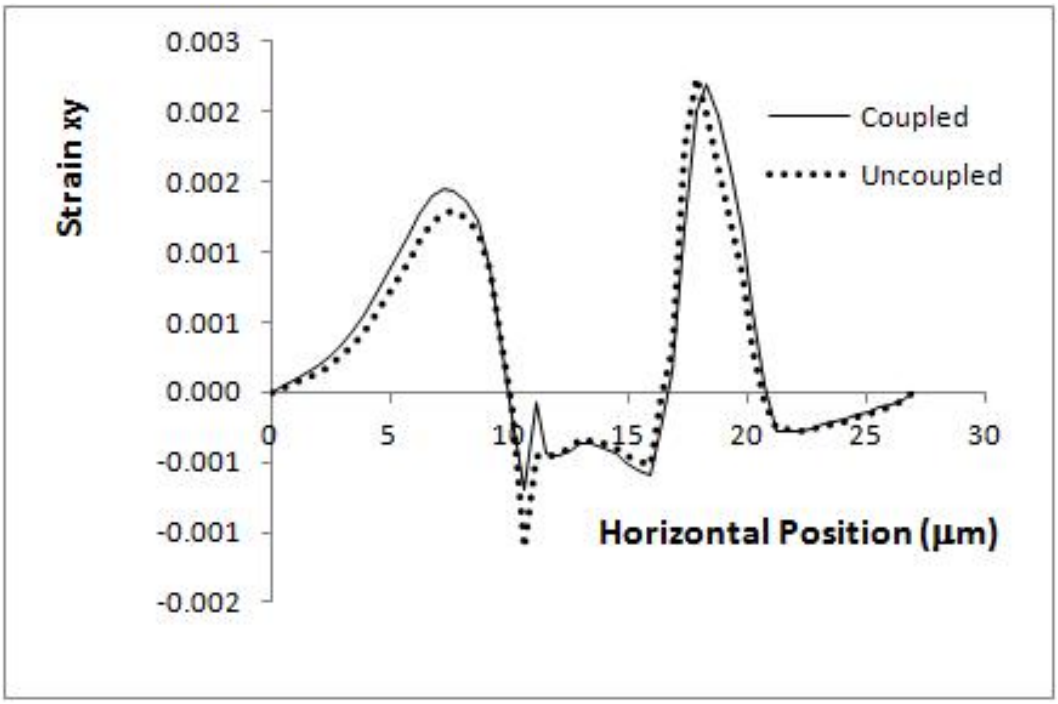
(b)

Figure 5.10: Graphs showing crystal plasticity finite element calculations and experimental EBSD measurements for the nickel/particle system subject to thermal loading. Total GND density is shown along the (a) vertical and (b) horizontal lines given in Figure 5.1(a). See text for interpreting experimental data.

where the terms take the values previously used and given in Table 5.1. Thus, the results obtained are those for a conventional crystal plasticity formulation as opposed to one which is gradient-enhanced. The comparisons of the results obtained for the elastic shear strains, lattice rotations and effective plastic strains along the vertical and

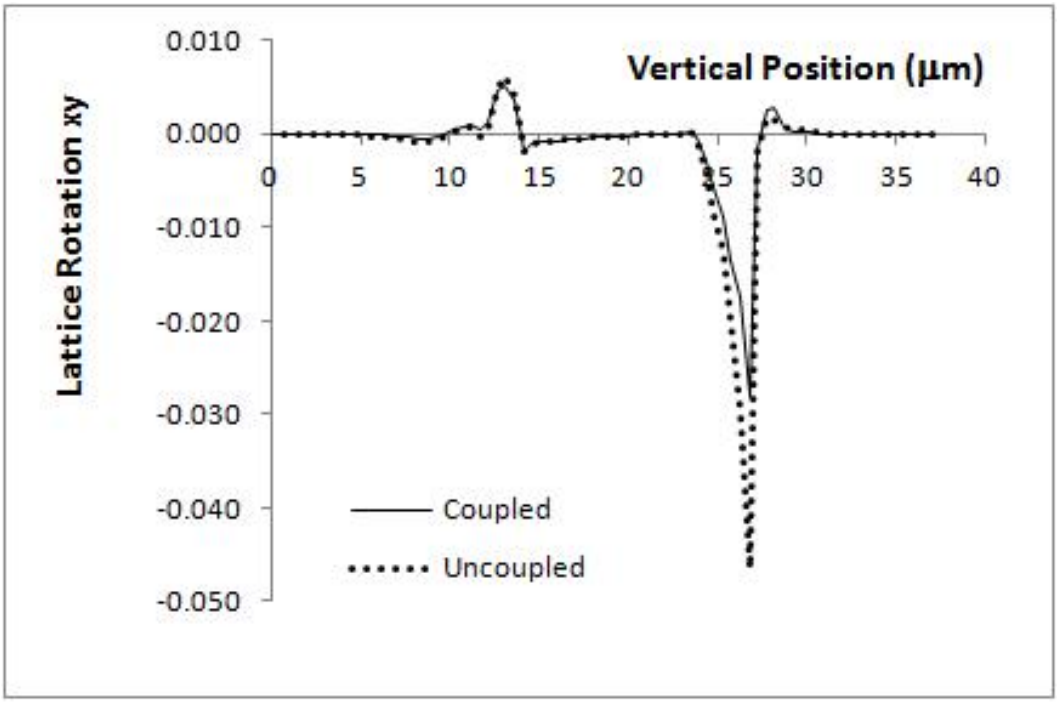


(a)

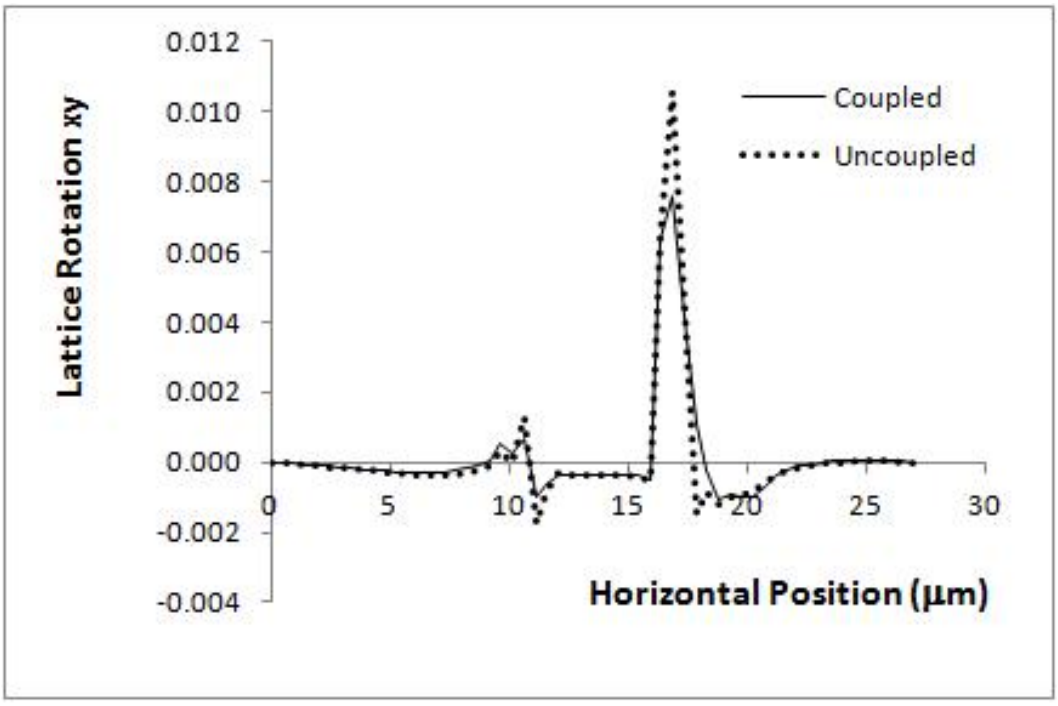


(b)

Figure 5.11: Graphs showing crystal plasticity finite element calculations for the nickel/particle system subject to thermal loading for the case of GND density coupled and uncoupled with the slip rule. Results are shown along the vertical and horizontal lines given in Figure 5.1(a) as follows: elastic shear strains xy (a) along the vertical and (b) horizontal line

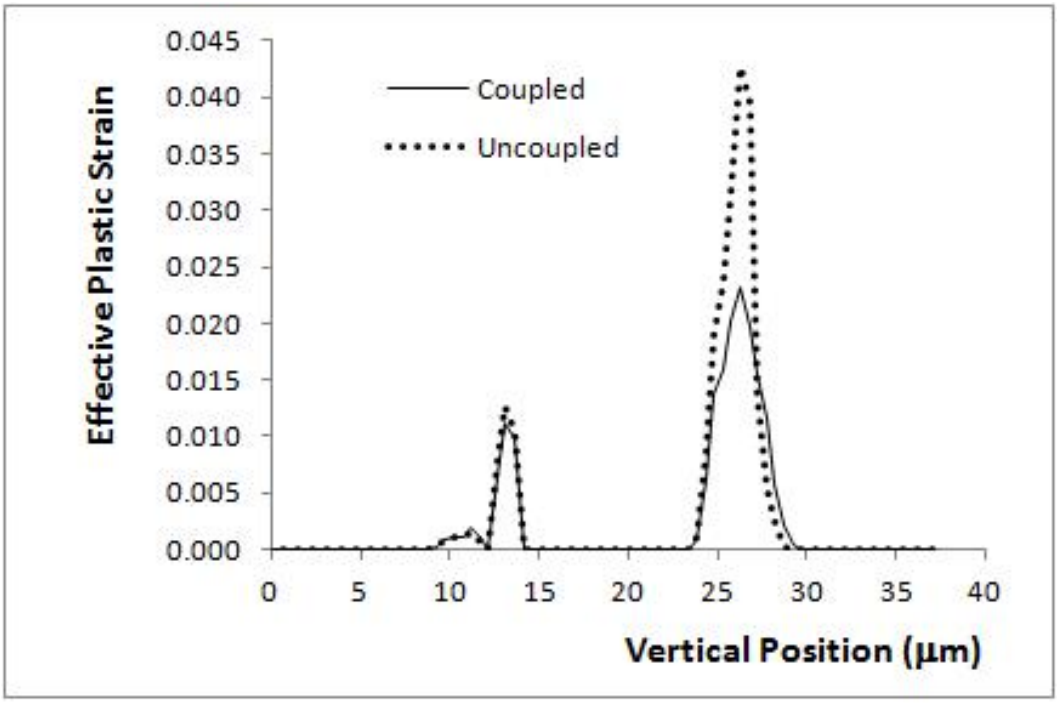


(a)

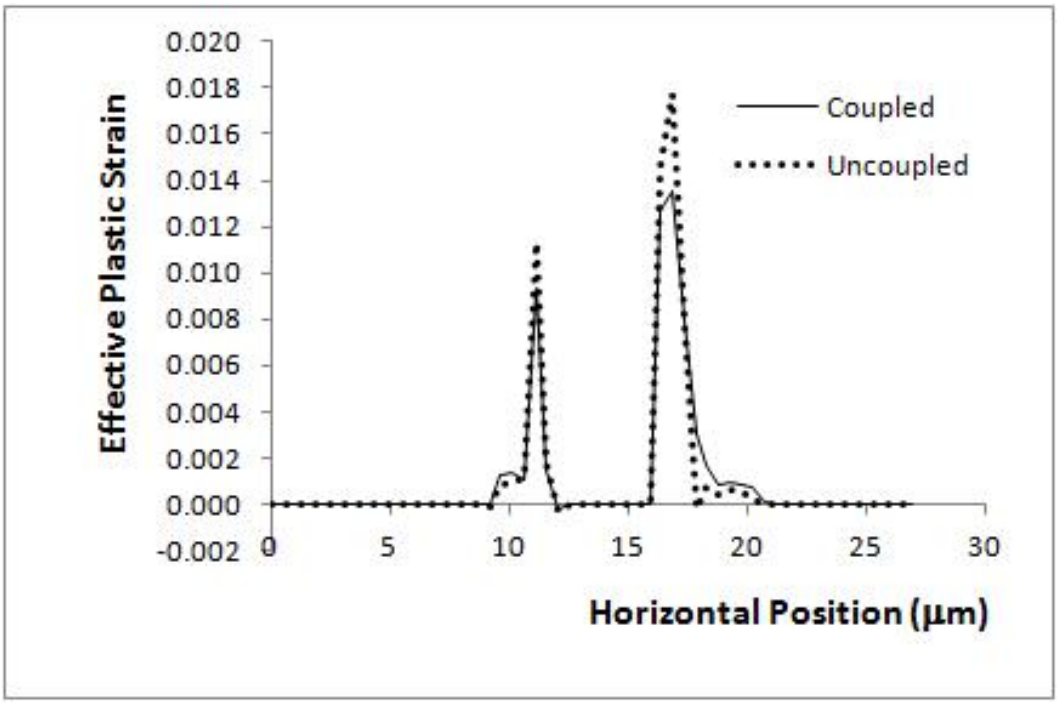


(b)

Figure 5.12: Graphs showing crystal plasticity finite element calculations for the nickel/particle system subject to thermal loading for the case of GND density coupled and uncoupled with the slip rule. Results are shown along the vertical and horizontal lines given in Figure 5.1(a) as follows: lattice rotations ω_{xy} (a) along the vertical and (b) horizontal line.



(a)



(b)

Figure 5.13: Graphs showing crystal plasticity finite element calculations for the nickel/particle system subject to thermal loading for the case of GND density coupled and uncoupled with the slip rule. Results are shown along the vertical and horizontal lines given in Figure 5.1(a) as follows: effective plastic strains (a) along the vertical and (b) along the horizontal line.

horizontal lines shown in Figure 5.1(a) for the Ni single crystal/particle material are given in Figures 5.11(a) to 5.13(b).

The elastic shear strains are shown in Figures 5.11(a) and (b), and interestingly, the differences observed for the coupled and uncoupled analyses are really quite small. The lattice rotations, however, particularly close to the particle/matrix interface, do show quite substantial differences (almost a factor of 2) with the coupled model predicting substantially smaller rotations at the interface. The experimentally measured lattice rotations at the interface, shown in Figures 5.8(a) and (b), are in fact much closer to the coupled predictions than the uncoupled model results, and this suggests that the GND coupling is important for lattice rotation (and hence GND density) determination at locations of significant heterogeneity eg at grain boundaries, triple points and so forth. The maximum values of lattice rotations are shown in Table 5.3, compared for experimental, coupled CPFE and uncoupled CPFE. It has long been argued that conventional crystal plasticity has been successful at capturing bulk grain deformation but has been shown to be problematic at grain boundaries eg [44]. The results presented here provide direct evidence that gradient effects at locations of considerable heterogeneity do at least contribute to some of the differences observed in the past.

Figures 5.13(a) and (b) show the distributions of effective plastic strain in which the effect of the coupling can be seen to inhibit the development of plasticity, particularly close to the particle/matrix interface. This, of course, is the location at which, from Figures 5.9 and 5.10, at which the highest density of GNDs is seen to develop and naturally, through the slip rule coupling, this inhibits subsequent plasticity development relative to the uncoupled model. Quite substantial differences in magnitudes of plastic strain can be seen to be obtained from the two models indicating that at regions of heterogeneity, conventional crystal plasticity is likely to overestimate the extent of plasticity.

	Expt		Coupled		Uncoupled	
	Rotation	Location	Rotation	Location	Rotation	Location
Vertical	-3.70×10^{-3}	24.5	-2.82×10^{-2}	26.8	-4.66×10^{-2}	26.8
Horizontal	8.00×10^{-3}	17.5	7.58×10^{-3}	16.4	1.06×10^{-2}	16.4

Table 5.3: Maximum values of lattice rotations (rad) and corresponding locations (μm) compared for experiment, coupled CPFE, and uncoupled CPFE results. Refer to Figures 5.8 and 5.12 for corresponding plots.

5.5 Discussion and conclusions

In this chapter, we have attempted to provide detailed comparisons of the results of gradient-enhanced crystal plasticity predictions with EBSD measurements in a model, heterogeneous material system under thermal loading. GND effects are now included in a large range of model analyses for crack nucleation and growth, for the initiation of recrystallization and for the nucleation of twinning, for example. It is therefore of considerable importance to demonstrate that the quantities of importance at the appropriate length scale are in fact being determined correctly and ideally accurately. Hence, we have aimed to test the ability of gradient crystal plasticity at a particular microstructural heterogeneity.

Some of the observed differences in the measured and predicted results inevitably originate from the modelling assumptions made. For example, while free-surface modelling results have been compared appropriately with free-surface EBSD measurements, in the model, the particle is assumed prismatic sub-surface; this is unlikely to be the case in reality. In addition, in the experimental Ni alloy material, while it is known that the carbide particles are well-dispersed such that inter-particle effects are likely to be small, they cannot be eliminated and the possibility always exists that additional particles, not visible in Figure 5.1(a), exist below the free surface and unfortunately close to the analysed particle. Further, the matter of boundary conditions is always important in these analyses; the region of the material, Figure 5.1(a), modelled in Figure 5.1(b) is in fact contained within a larger material sample and the correct boundary

conditions are therefore difficult to reproduce. However, studies with various different boundary conditions show that the effects close to the particle are in fact small.

In summary, we find that the prediction of elastic micro-straining is qualitatively reasonable but not completely accurate. Lattice rotations, however, and GND densities, are found to be better predicted, in a quantitative sense, by gradient-enhanced crystal plasticity and that conventional, non-gradient plasticity is likely to be more in error particularly where gradient effects are important at, for example, phase interfaces, grain boundaries and triple points.

There remains the important need to continue to challenge and to test the abilities of crystal plasticity modelling techniques by means of detailed comparison of predicted results with micro-mechanical testing at the appropriate length scale. Only in this way can confidence in its use for problems of significance be developed.

Chapter 6

Texture evolution modelling

6.1 Executive summary

This chapter achieves three things: (i) develops a stress update algorithm that is fit for simulating any desired strain, thus overcoming the limits encountered previously in Chapter 2; (ii) develops a methodology for tracking texture development; (iii) outlines a systematic methodology for calibrating the slip rule, specifically the power law, based on experimental data.

6.2 Introduction

There are several modelling approaches for texture development (e.g. self-consistent methods, enhanced Mises plasticity, polycrystal plasticity) all with associated advantages and disadvantages. These approaches mainly differ by virtue of the consideration given to boundary conditions with regard to stress and strain, i.e. equilibrium and compatibility. Finite element (FE) plasticity formulations are, however, made to ensure that both equilibrium and compatibility are satisfied and are therefore a good alternative approach to modelling texture evolution. The FE method does not only take the interactions between adjacent elements into account (i.e. the grain-to-first-neighbour interactions), but also long range interactions [76]. Various authors (e.g. [7, 76]) have compared finite element methods (FEM) with some of the models available and concluded that finite element predictions are better.

In this work, a physically-based approach is adopted using single crystal plasticity theory (implemented in a finite element code as a UMAT for the Abaqus FE package). In the approach, individual crystals, with their associated crystallographic orientations,

are explicitly represented within the model. This approach is advantageous as it is known to give good predictions of texture at least in single-phase materials in which the predominant deformation mechanism is slip. However, problems may arise where significant twinning or recrystallization occur - both are not modelled in the work presented in this chapter. The disadvantage of this approach is it is not usually (if ever) possible to develop crystal plasticity finite element models which incorporate every grain within a material undergoing processing; such models while possible in principle, are simply far too large even given predicted future computing speed. As a result, a 'multi-scale' approach may be adopted as follows.

Process deformation analysis is carried out using a continuum elasticity-plasticity modelling approach. Critical points (or hotspots) within the structure at which texture information is required are identified and their local deformation histories extracted from the continuum analysis using point tracking. The initial texture (in the form of hkl data, or Bunge angles) which exists before deformation processing commenced is assumed to have been obtained by prior EBSD. Knowledge of the initial texture is employed to generate a representative volume element (RVE) for a selected hotspot; that is, a finite element model is developed (using ABAQUS/Standard) and computational techniques used to assign the initial EBSD measured texture to this finite element model where it is used in the single crystal plasticity finite element (CPFE) code to define the initial crystallographic orientation. The point tracking file can then be used to determine approximately the deformation history which is applied as the loading conditions imposed on the RVE, enabling the CPFE RVE model to capture the initial material texture and loading conditions representative of the deformation process at the critical points of interest (each point requiring its own RVE). The deformation analysis of the RVE then permits the determination of texture related to the points of interest within the component. Following the deformation analysis, the resulting pole

figures and Kearn's factors are determined from the deformed RVE.

The first problem to address in this chapter is the need to develop a code that is capable of simulating large deformation with Abaqus/Standard in order to study texture evolution in comparison with large deformation (up to 90% true strain) experimental texture data received from Rolls-Royce, which is the subject of the next chapter, i.e. Chapter 7. In the past we have attempted to solve this problem by implementing a stress-update algorithm based on the Cauchy stress (see Section 2.4). This approach is fine for simulating relatively small deformations ($< 10\%$) but has, up to this point in the project, continued to present numerical difficulties requiring the use of continuation simulations when large deformations are required, i.e. a series of simulations where a previous simulation's output is used as input for a following simulation. Another way around this problem would be to implement remeshing algorithms but this is also neither easy nor void of problems, especially with regard to mapping of data between an old mesh and a new one after remeshing.

In this chapter we develop and test a new single crystal plasticity finite element code to enable us simulate large deformations. We start with the implementation described by Kalidindi et al. [43], avoiding any assumptions about the effect of elastic strains on the rigid body rotations, we initially embed in it the slip rule given in equation 1.8, and define a relevant material jacobian using an approach that naturally follows from the stress-update algorithm, which is unlike that used by Kalidindi et al. [43]. The material jacobian defined here is straight forward to implement in the FE code given the implementation of the stress update scheme. We also investigate the effect of the slip rule on convergence and address the determination of the parameters needed in the slip rule that is finally adopted from experimental data.

6.3 New stress and texture update methodology

Previous attempts to model large deformations, of the magnitude required to capture texture evolution, resulted in mesh distortion problems that required the use of continuation simulations to overcome, i.e. results would be extracted at the end of one simulation for which a small displacement was applied and used as initial conditions for a new (continuation) simulation with the new mesh. The process would be repeated until the total sum of the small displacements equals the required total displacement for large deformation. This approach also did not return the expected results for various reasons, for example, the geometry at the start of a continuation simulation did not match that at the end of the preceeding simulation. Additionally a number of days would be required to simulate to, for example, an applied nominal strain of 10%, for a medium-sized RVE. This section presents a new solution (a different stress update methodology) that eliminates the need for continuation simulations altogether.

The previous attempts involved modifying a finite element (FE) code that was originally developed for simulating small deformations (see Chapter 2 Section 2.4). This involved updating stress based on the Jaumann rate of Cauchy stress. However the code thus developed presented numerical difficulties whenever very large deformations were required (even for strains as small as 10%). The numerical difficulties resulted from the way the stress contribution due to rigid body rotation was handled with regard to the implicit integration of the constitutive equations.

In this section we develop and test a new FE code to enable us better handle very large deformations. We start with the stress update methodology described by Kalidindi et al. [43] and fill in the necessary gaps to make it complete for our use here, and for other users to be able to follow what we have written in the code itself. This formulation uses the second Piola-Kirchoff stress, S, which is very well suited for very

large deformation modelling. The main factor that makes S more suitable than the Cauchy stress, σ, for modelling large deformations is σ changes in response to pure rigid body rotations while S does not - see e.g. [8].

6.3.1 Stress update

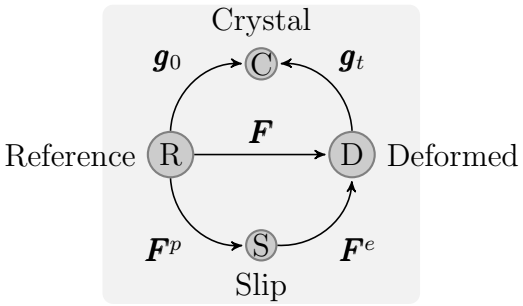


Figure 6.1: Multiplicative decomposition of the deformation gradient $\boldsymbol{F}$ into the components $\boldsymbol{F}^e$ and $\boldsymbol{F}^p$ showing the relationship of the crystal frame (C) to the reference (R) and deformed (D) frames via the orientation matrix $\boldsymbol{g}$ from which equation 6.20 is derived.

At any strain increment in the finite element code we calculate the current value of the deformation gradient $\boldsymbol{F}$, using the Abaqus/Standard UEL implementation, and obtain a value of its plastic part $\boldsymbol{F}^p$ from the previous increment. We use these two to obtain an estimate of the elastic part of the deformation gradient $\boldsymbol{F}^e$ and, with the assumption that all rigid body rotation is lumped into $\boldsymbol{F}^e$, obtain the rotation part $\boldsymbol{R}^e$ using the polar decomposition as follows (nb: It was noted during studies of thermal expansivity that the assumption that elastic strains are small so that $\boldsymbol{R}^e \approx \boldsymbol{F}^e$ led to noticeable errors in the values of Kearn's factors obtained. Additionally, avoiding this assumption allows the code to be usable for both small and large deformation modelling.):

$$\boldsymbol{F}^e = \boldsymbol{F}\boldsymbol{F}^{p-1}, \qquad \boldsymbol{R}^e = \boldsymbol{F}^e\boldsymbol{U}^{e-1}, \quad \text{and} \quad \boldsymbol{U}^e = \sqrt{\boldsymbol{F}^{eT}\boldsymbol{F}^e} \tag{6.1}$$

The fourth order elasticity tensor $\boldsymbol{C}$ and other properties such as the slip directions and

normals are specified in the crystal's reference frame (C). The C-frame is mapped onto the initial undeformed reference frame (R) by the specified initial orientation given by the initial orientation matrix $\boldsymbol{g}_0$ - this is defined from the initial EBSD measured texture. $\boldsymbol{g}_0$ is thus used to transform all the relevant properties to the R-frame and the intermediate frame (I), as shown in Figure 6.1, for example as

$$\boldsymbol{D}_R = \boldsymbol{T}_\sigma^{-1} \boldsymbol{C} \boldsymbol{T}_\varepsilon \tag{6.2}$$

where $\boldsymbol{D}_R$ is the fourth order elasticity tensor referred to the R-frame, and $\boldsymbol{T}_\sigma^{-1}$ and $\boldsymbol{T}_\varepsilon$ are the appropriately sized rotation matrices obtained from $\boldsymbol{g}_0$ as described in appendix C of Dunne et al. [26]. As should be expected, we store the Cauchy stress $\boldsymbol{\sigma}$ for viewing. This is converted to the second Piola-Kirchoff stress $\boldsymbol{S}$ referred to the I-frame, hence $\boldsymbol{S}^e$, for the calculations as follows

$$\boldsymbol{S}^e = J^e \boldsymbol{F}^{e-1} \boldsymbol{\sigma} \boldsymbol{F}^{e-T}, \qquad J^e = \det(\boldsymbol{F}^e) \tag{6.3}$$

The Green strain $\boldsymbol{E}^e$, which is the work conjugate to $\boldsymbol{S}^e$, is also calculated as

$$\boldsymbol{E}^e = \frac{1}{2} \left(\boldsymbol{A} - I \right), \qquad \boldsymbol{A} = \boldsymbol{F}^{e^T} \boldsymbol{F}^e \tag{6.4}$$

The trial stress $\boldsymbol{S}^{e^{tr}}$, after relevant vectorisation, can then be obtained as

$$\boldsymbol{S}^{e^{tr}} = \boldsymbol{D}_R \boldsymbol{E}^e \tag{6.5}$$

It should be noted that $\boldsymbol{E}^e$ is zero if the deformation is a pure rigid body rotation. Consequently $\boldsymbol{S}^{e^{tr}}$ would also be zero. This property makes $\boldsymbol{S}$ and $\boldsymbol{E}$ a perfect work conjugate pair for large deformation modelling as material straining is properly handled

and differentiated from any rotation (unlike in the case discussed in Chapter 2). At this point the resolved shear stress τ^α on any slip system α can be obtained as

$$\tau^\alpha = \boldsymbol{S}^e \boldsymbol{n}_0^\alpha \cdot \boldsymbol{s}_0^\alpha = \boldsymbol{M}_0^{\alpha^T} : \boldsymbol{S}^e, \quad \text{where} \quad \boldsymbol{M}_0^\alpha = \boldsymbol{s}_0^\alpha \otimes \boldsymbol{n}_0^\alpha \tag{6.6}$$

where $\boldsymbol{n}_0^\alpha$ and $\boldsymbol{s}_0^\alpha$ are the initial non-updated slip normal and direction respectively, as defined in the R-frame. τ^α can be used to determine if any slip system is active by comparing it with the prescribed critical resolved shear stress τ_c^α. If any slip system is found to be active, the new stress is calculated, via a Newton implicit integration scheme (IIS), as follows:

$$\boldsymbol{S}_{n+1}^e(t+1) = \boldsymbol{S}_n^e(t+1) - \boldsymbol{J}_{\psi_n}^{-1}\boldsymbol{\psi} \tag{6.7}$$

$$\boldsymbol{\psi} = \boldsymbol{S}_n^e(t+1) - \boldsymbol{S}^{e^{tr}}(t+1) + \boldsymbol{Q} \tag{6.8}$$

$$\boldsymbol{Q} = \sum_\alpha \dot{\gamma}^\alpha \Delta t \boldsymbol{C}^\alpha; \qquad \boldsymbol{C}^\alpha = \boldsymbol{D}_R\left(\frac{1}{2}\boldsymbol{B}^\alpha\right); \qquad \boldsymbol{B}^\alpha = \boldsymbol{A}\boldsymbol{M}_0^\alpha + \boldsymbol{M}_0^{\alpha^T}\boldsymbol{A} \tag{6.9}$$

$$\boldsymbol{J}_{\psi_n} = \boldsymbol{I} + \Delta t \sum_\alpha \left(\boldsymbol{C}^\alpha \otimes \frac{\partial \dot{\gamma}^\alpha}{\partial \boldsymbol{S}_n^e(t+1)}\right) \tag{6.10}$$

where n is counter for the number of iterations in the IIS. $\boldsymbol{S}_n^e(t+1)$ is set equal to $\boldsymbol{S}^e(t)$ at the beginning of the IIS, i.e. when $n = 1$. The variation of the slip rate, with the slip rule written in the following compressed form, leads to the following derivative of the slip rate with respect to stress $\boldsymbol{S}_n^e$

$$\dot{\gamma}^\alpha = \beta_1^\alpha \sinh \beta_2^\alpha \left(\tau^\alpha - \tau_c^\alpha\right), \quad \text{and} \quad \boldsymbol{L}^p = \sum_\alpha \dot{\gamma}^\alpha \boldsymbol{M}_0^\alpha \tag{6.11}$$

$$\delta\dot{\gamma}^\alpha = \beta_1^\alpha \beta_2^\alpha \cosh \beta_2^\alpha \left(\tau^\alpha - \tau_c^\alpha\right) \delta\tau^\alpha = \beta_1^\alpha \beta_2^\alpha \cosh \beta_2^\alpha \left(\tau^\alpha - \tau_c^\alpha\right) \boldsymbol{M}_0^{\alpha^T} : \delta\boldsymbol{S}_n^e \tag{6.12}$$

$$\therefore \frac{\partial \dot{\gamma}^\alpha}{\partial \boldsymbol{S}_n^e} = \beta_1^\alpha \beta_2^\alpha \cosh \beta_2^\alpha \left(\tau^\alpha - \tau_c^\alpha\right) \boldsymbol{M}_0^\alpha \tag{6.13}$$

Convergence is judged to have been achieved when $|\boldsymbol{\psi}|$ is within the prescribed toler-

ance, $|\boldsymbol{\psi}| \leq 10^{-8}$ in the cases reported here. We define relevant material jacobian $\frac{\partial \boldsymbol{S}^e}{\partial \boldsymbol{E}^e}$ as follows

$$\boldsymbol{S}^e(t+1) = \boldsymbol{S}^{e^{tr}}(t+1) - \sum_\alpha \dot{\gamma}^\alpha \Delta t \boldsymbol{C}^\alpha \tag{6.14}$$

$$\delta\boldsymbol{S}^e(t+1) = \delta\boldsymbol{S}^{e^{tr}}(t+1) - \sum_\alpha \delta\dot{\gamma}^\alpha \Delta t \boldsymbol{C}^\alpha \tag{6.15}$$

$$\delta\boldsymbol{S}^e(t+1) = \delta\boldsymbol{S}^{e^{tr}}(t+1) - \left(\Delta t \sum_\alpha \boldsymbol{C}^\alpha \otimes \frac{\partial \dot{\gamma}^\alpha}{\partial \boldsymbol{S}^e(t+1)}\right) \delta\boldsymbol{S}^e(t+1) \tag{6.16}$$

$$\left[\boldsymbol{I} + \Delta t \sum_\alpha \boldsymbol{C}^\alpha \otimes \frac{\partial \dot{\gamma}^\alpha}{\partial \boldsymbol{S}^e}\right] \delta\boldsymbol{S}^e = \delta\boldsymbol{S}^{e^{tr}} \tag{6.17}$$

$$\delta\boldsymbol{S}^{e^{tr}} = \boldsymbol{D}_R \delta\boldsymbol{E}^e \Rightarrow \boldsymbol{J}_\psi \delta\boldsymbol{S}^e = \boldsymbol{D}_R \delta\boldsymbol{E}^e \tag{6.18}$$

$$\therefore \frac{\partial \boldsymbol{S}^e}{\partial \boldsymbol{E}^e} = \boldsymbol{J}_\psi^{-1} \boldsymbol{D}_R \tag{6.19}$$

6.3.2 Texture development

With this new stress-update scheme, we track texture development by following the evolution of the orientation matrix $\boldsymbol{g}$ at each material point (i.e. integration point) using the following non-incremental approach (see Figure 6.1)

$$\boldsymbol{g}_t = \boldsymbol{g}_0 \boldsymbol{R}^{e^T} \qquad \text{or} \qquad \boldsymbol{g}_t^T = \boldsymbol{R}^e \boldsymbol{g}_0^T \tag{6.20}$$

keeping in mind the assumption that all rigid body rotation is lumped into $\boldsymbol{F}^e$, from which $\boldsymbol{R}^e$ is obtained by polar decomposition. The initial value of the orientation matrix $\boldsymbol{g}_0$ is obtained from the EBSD-measured texture data (after the texture homogenisation process described later in Chapter 7) and entered into the Abaqus input file for each crystallite as quaternions (see Dam et al. [21] for a comprehensive treatment of quaternions and rotation with quaternions).

It is worth noting that unlike in Chapter 1 Section 1.3.3 where texture update is accounted for by directly re-orientating the slip directions and normals (which is a

consequence of updating texture in the deformed configuration) here no slip direction or other quantity gets updated that way. In the present approach it is not necessary to calculate the elastic spin $\boldsymbol{W}^e$ in order to update the various quantities. In fact $\boldsymbol{g}_t$ in equation 6.20 is not used to update any quantity directly but it is 'extracted' merely for purposes of visualising texture evolution, i.e. for constructing pole figures and calculating Kearns factors, and for appropriately rotating the 4^{th} order elasticity tensor for use in calculating the tangent stiffness matrix given in Chapter 2 Section 2.3.1 equation 2.32. The latter rotation operation is not needed if equation 2.20 is used instead. The actual updating of texture results from updating $\boldsymbol{F}^p$, which is done as follows

$$\boldsymbol{F}^p(t+1) = (\boldsymbol{I} + \boldsymbol{L}^p \Delta t)\, \boldsymbol{F}^p(t) \tag{6.21}$$

with $\boldsymbol{I}$ the identity matrix and $\boldsymbol{L}^p$ defined as in equation 1.7. $(t+1)$ and (t) refer to the current and previous time increment respectively. Equation 6.21 can be simply derived as follows

$$\begin{aligned} \boldsymbol{F}^p(t+1) &= \boldsymbol{F}^p(t) + \dot{\boldsymbol{F}}^p \Delta t \\ &= \boldsymbol{F}^p(t) + \boldsymbol{L}^p(t+1)\boldsymbol{F}^p(t)\Delta t \\ &= \{\boldsymbol{I} + \boldsymbol{L}^p(t+1)\Delta t\}\, \boldsymbol{F}^p(t) \end{aligned} \tag{6.22}$$

Equation 6.22 is in fact a good approximation to $\boldsymbol{F}^p(t+1) = \exp\{\Delta t \boldsymbol{L}^p(t+1)\}\, \boldsymbol{F}^p(t)$ which would be the result of a fully-implicit integration of equation 1.7 [43]. With $\boldsymbol{F}^p$ updated and $\boldsymbol{F}$ obtained using the Abaqus UEL implementation (of $\frac{\partial \boldsymbol{x}}{\partial \boldsymbol{X}}$), $\boldsymbol{F}^e$ results from the elastic-plastic multiplicative decomposition of $\boldsymbol{F}$; and its use in locating the intermediate configuration and hence defining the different quantities used in the stress-

update scheme described in this chapter (e.g. $\boldsymbol{S}^e$) automatically accounts for the update of texture. A consequence of this approach is texture development is no longer an optional operation that can be switched on and off, unlike the case with the scheme described in Chapter 1 Section 1.3.3.

6.3.3 Numerical Stability Control

As stated by Kalidindi et al. [43], for low rate sensitivity equation 6.8 (with $\boldsymbol{\psi} = 0$ or equation 6.14) is very stiff, i.e. numerically unstable, making it necessary to apply constraints to the Newton corrections in equation 6.7 and to modify the iterative procedure. The following contraints were applied to the Newton corrections. Let $\Delta\boldsymbol{S} = \boldsymbol{J}_{\psi_n}^{-1}\boldsymbol{\psi}$ be the vector of stress increments calculated between two consecutive Newton iterations and ΔS_{max} the largest component of $\Delta\boldsymbol{S}$. We set a value ΔS_a for the largest allowed increment for any component of $\Delta\boldsymbol{S}$ and ensure that if $\Delta S_{max} < \Delta S_a$, all $\Delta\boldsymbol{S}$ is accepted without any changes. However, if $\Delta S_{max} > \Delta S_a$, ΔS_{max} is set equal to ΔS_a and the other components are set such that

$$\Delta\boldsymbol{S}_i = \Delta S_a \times \Delta\boldsymbol{S}_i / \Delta S_{max} \tag{6.23}$$

i.e., the accepted Newton corrections are kept in the same ratios relative to the largest as the computed corrections and the maximum is limited to ΔS_a. For hcp, keeping the increments in proportion was found to significantly improve the stability of the simulation and to speed up convergence compared to the case where only those components of $\Delta\boldsymbol{S}$ that are greater than ΔS_a are changed (all of them set to ΔS_a) while any components less than ΔS_a are simply accepted without change.

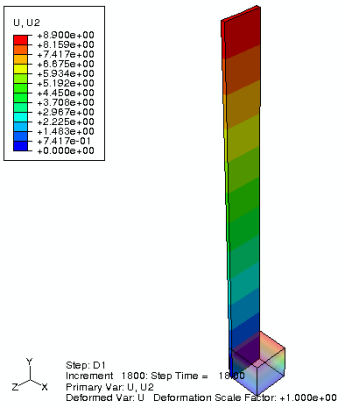
In the current case, it was also necessary to apply a limit on the slip rate ($\dot{\gamma}$) since it rises rapidly, causing the simulation to fail with an illegal floating point error. The limit that gave the best results was as follows. Let $H^\alpha = \tau_i^\alpha / \tau_{c_i}^\alpha - 1.0$ so that

$\dot{\gamma}^\alpha = \beta_1^\alpha \sinh\left(\beta_2^\alpha \tau_{c_i}^\alpha H^\alpha\right)$. Also choose a percentage, J, to which τ may be allowed to go above τ_c, e.g. $J = 0.05$. Then if $H^\alpha > J$, set $H^\alpha = J$; else accept H^α without any changes. In the code validation simulations that follow, $\Delta S_a = 5.0$ and $J = 0.05$ were used unless otherwise stated.

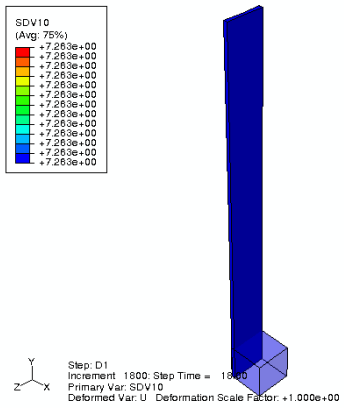
6.4 Model validation: hcp crystal simulations

The code was tested with single crystals and two different single orientations (given by Bunge Euler angles $(\varphi_1, \theta, \varphi_2) = (0, 0, 0)$ and $(\varphi_1, \theta, \varphi_2) = (-45, 90, 0)$) with an applied compression, under displacement control, to a target nominal strain of 90%. The following shows some of the different test cases simulated with some of the results obtained and the final strain obtained.

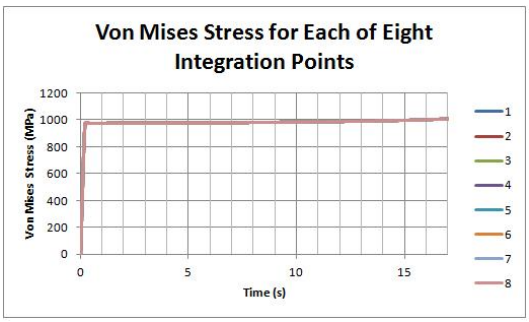
6.4.1 Single crystal uniaxial compression to 90%



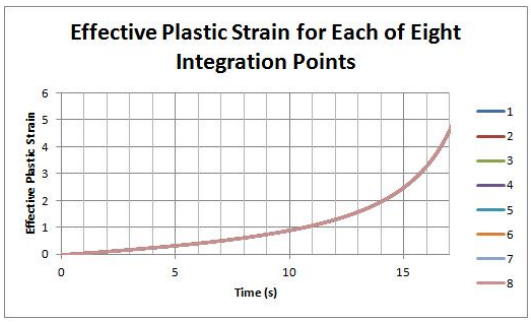
(a) Displacement u_2



(b) Effective plastic strain



(c) Von Mises stress



(d) Effective plastic strain

Figure 6.2: Hcp 1x1x1μm single element under -0.9μm compression. Reference crystal orientation $(\varphi_1, \theta, \varphi_2) = (0, 0, 0)$ is specified (i.e., c-axis parallel to z-axis).

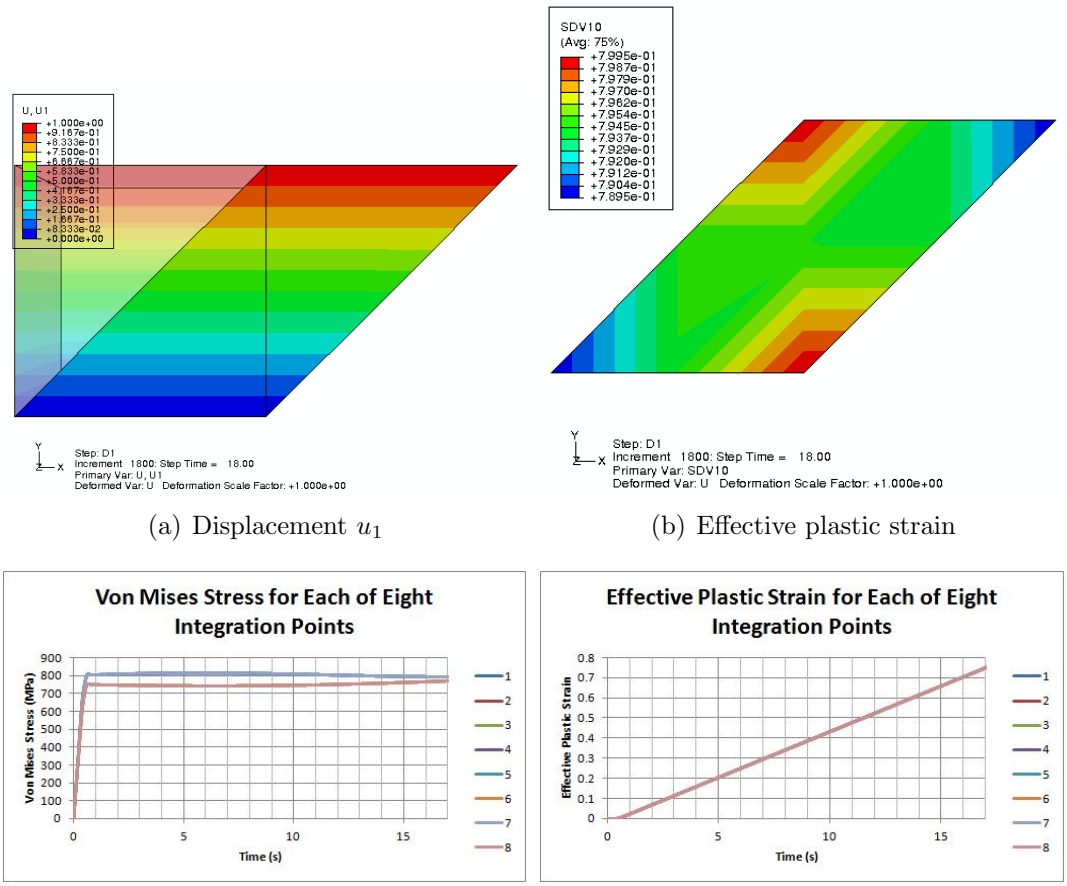
A single element, with crystal (reference) orientation - $(\varphi_1, \theta, \varphi_2) = (0, 0, 0)$, was subjected to uniaxial compression (in the x-direction according to the axes shown in Figure 6.2) to 90% nominal strain. Figure 6.2 shows the y-component of displacement obtained, with the initial undeformed shape included to give an idea of the overall deformation obtained. The figure also gives the accumulated plastic strain, p, both as a field plot and xy plot, and also gives the von Mises stress obtained. No hardening mechanism is included and the evolution of geometrically necessary dislocations has been disabled so that an elastic-perfectly plastic stress response is expected, and this is what is obtained as shown in the figure. The accumulated plastic strain obtained is also uniform as expected.

6.4.2 Single crystal shearing to 45°

The same single element above was also subjected to shearing displacement to 45°, or maximum displacement of $1\mu m$, as indicated in Figure 6.3(a) which shows the final x-component of displacement together with the initial undeformed shape. Figure 6.3 also shows the final effective plastic strain, p, as a field plot and as an xy plot. It also gives a plot of the von Mises stress obtained. The results here are again as expected. It is noteworthy that the effective plastic strain obtained here is much smaller than that obtained in the uniaxial loading case. This is because the deformation in the case of shear loading is mostly rigid body rotation, rather than material straining. This test therefore serves to validate the performance of the new code in the presence of large rigid body rotation - complementing the uniaxial compression test case which only validates performance for large (plastic) strain.

6.4.3 Single crystal uniaxial compression to 65%

In order to test the code's capability to simulate deformation that is more inhomogeneous than the two cases described above, the single element was again subjected



(a) Displacement u_1

(b) Effective plastic strain

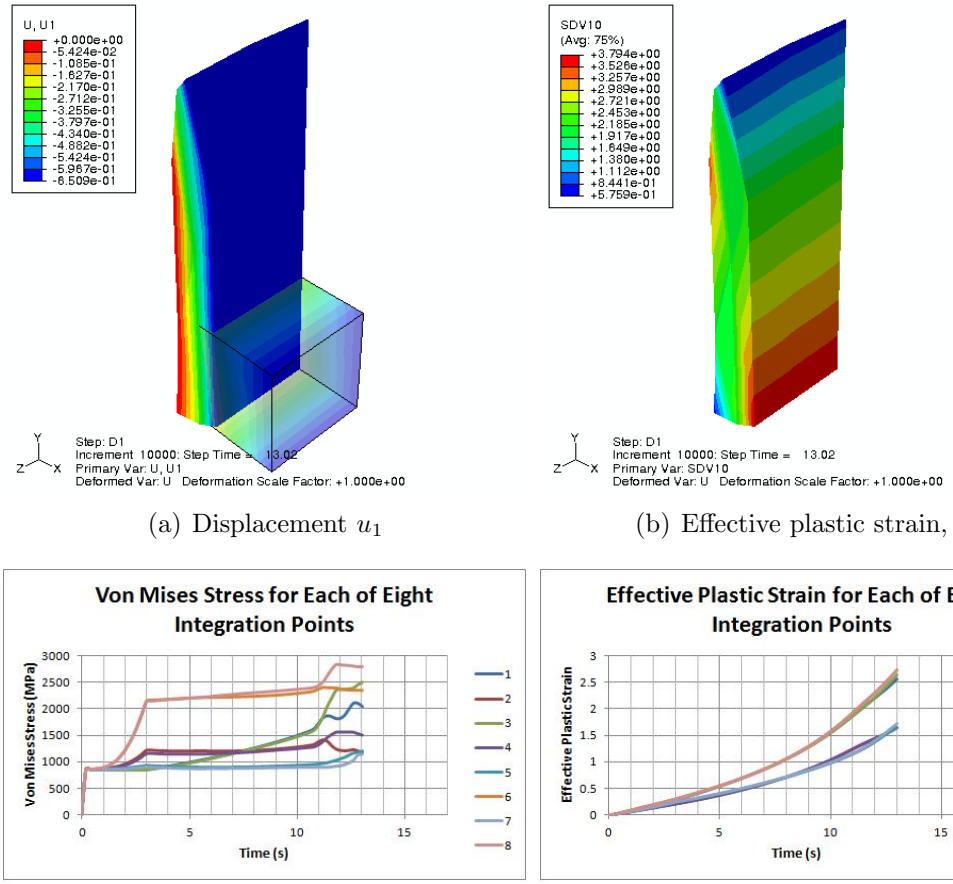
(c) Von Mises stress

(d) Effective plastic strain

Figure 6.3: Hcp 1x1x1μm single element under -0.9μm shear. Reference crystal orientation $(\varphi_1, \theta, \varphi_2) = (0, 0, 0)$ is specified (i.e., c-axis parallel to z-axis).

to the uniaxial compression described above but with the crystallographic orientation specified such that the c-axis is normal to the z-axis and at 45° to both the x- and y-axes, i.e., $(\varphi_1, \theta, \varphi_2) = (-45, 90, 0)$.

Unlike in the reference orientation case in Figure 6.2, the non-reference orientation case in Figure 6.4 exhibits effective plastic strain and von Mises stress that is inhomogeneous (i.e. varies between the different integration points) due the combination of the nature of the hcp crystallography and the prescribed crystallographic orientation. A consequence of this inhomogeneity of deformation was that much smaller time-steps were required compared to the reference orientation case. For this case, the simulation stopped at total applied strain of 65% (instead of the target of 90%) because it had reached the maximum number of increments that had been prescribed (i.e., 10,000).



(a) Displacement u_1

(b) Effective plastic strain, p

(c) Von Mises stress

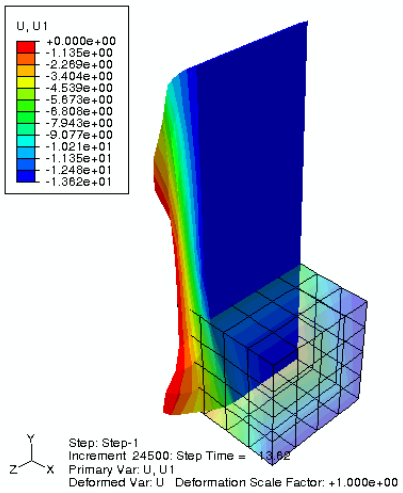
(d) Effective plastic strain

Figure 6.4: Hcp 1x1x1μm single element under -0.9μm compression. Crystal orientation $(\varphi_1, \theta, \varphi_2) = (-45, 90, 0)$ is specified.

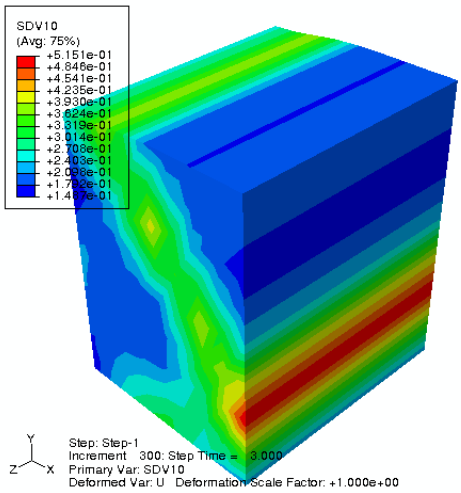
At this time the time-step was steady at $\Delta t = 0.0004271$ and it was completing each increment after about seven iterations on average - as reported in Abaqus/standard's .sta file. This contrasts strongly with the reference orientation case which consistently run at the prescribed maximum time-step of $\Delta t = 0.01$ reaching the prescribed nominal strain of 90% in 1800 increments, and with each increment completed in exactly one iteration. This same orientation when tested on an FCC single crystal produced uniform fields as in the hcp reference orientation case above confirming that the inhomogeneity observed here is directly a consequence of the hcp crystallography.

Aside from the expected variation of the stress between integration points, it is also observed that it rises exponentially in the time interval $t = 1 - 4s$ before exhibiting elastic-perfectly plastic behaviour, Figure 6.4(c). At around $t = 11s$ exponential in-

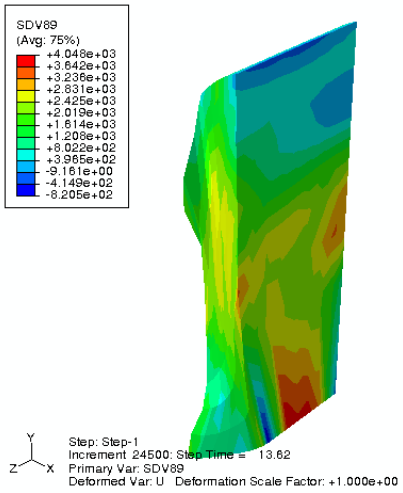
crease in von Mises stress is seen again, followed by softening at some of the integration points of the element. (The strain rate in all the simulations performed for code testing is 0.05/s; hence total nominal strain (%) can quickly be obtained from the time scale on any plot by multiplying the total time (or step time on field plots) by five.)



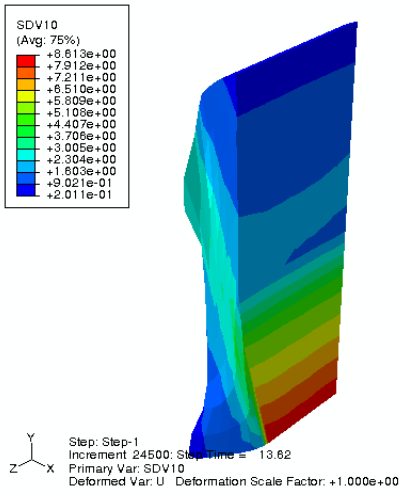
(a) Displacement u_1



(b) Eff. plas. strain at 15% nominal



(c) Von Mises stress at 68% nominal



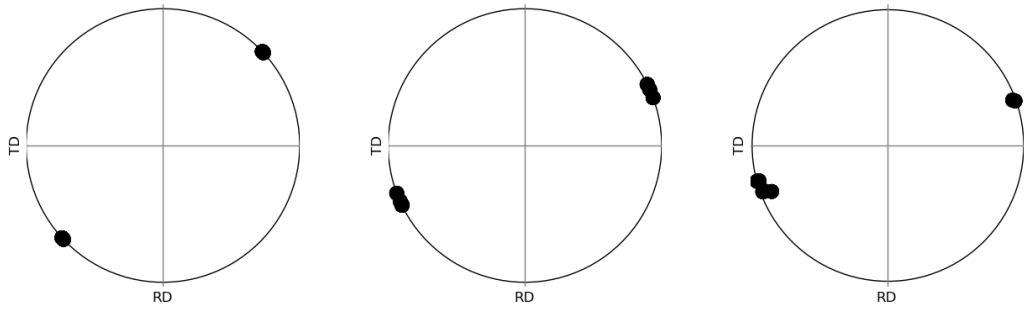
(d) Eff. plas. strain at 68% nominal

Figure 6.5: Hcp 20x20x20μm single crystal under -0.9μm compression in the x-direction. Crystal orientation $(\varphi_1, \theta, \varphi_2) = (-45, 90, 0)$ is specified.

In order to understand whether or not the stress behaviour exhibited by the single element in non-reference orientation is a consequence of the single element's incapacity to correctly capture the stress-strain variation, the single crystal was modelled with a sixty four element model to enable better capturing of the stress-strain variation. The final field distributions for all the quantities in the two Figures 6.4 and 6.5 are

very similar which suggests that the stress behaviour observed was due to something else, i.e. , the interpolation capability of the quadratic reduced integration element is not the reason for the observed stress behaviour. (The 64 element model stopped at a nominal strain of 68% after 24584 increments. It stopped because the required time increment had reached the minimum set: $\Delta t_{min} = 1.0 \times 10^{-5}$)

It was then decided to extract orientation data on an integration point basis - i.e. , without averaging over the element - to ensure that orientation evolution can be followed at each of the element's eight integration points individually. This would enable capturing of the orientation change at the individual integration points for the single element case enabling a more detailed look at the fundamental crystallographic changes resulting from the prescribed loading/orientation combination. Figs 6.6 and 6.7 show

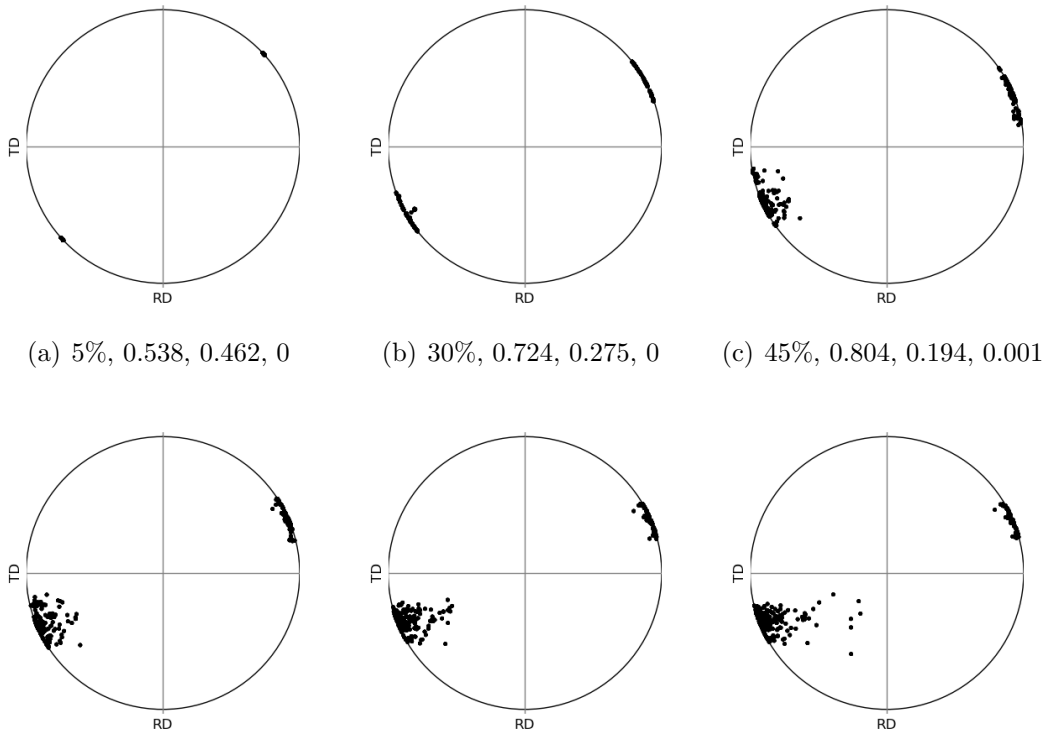


(a) 5%, 0.536, 0.464, 0 (b) 50%, 0.830, 0.170, 0 (c) 65%, 0.892, 0.107, 0.001

Figure 6.6: (0001) pole figures for a single element single crystal with orientation $(\varphi_1, \theta, \varphi_2) = (-45, 90, 0)$. The caption numbers show nominal strain and (0001) Kearn's factors f_1, f_2 and f_3 respectively. The points have have been made with circles of radius 0.05 to ease visibility.

the pole figures obtained for the two single crystal simulations with the prescribed crystal orientation $(\varphi_1, \theta, \varphi_2) = (-45, 90, 0)$; they show the results from the single element and 64 element models respectively. The figures also show the nominal strain and Kearn's factors.

It is evident from the pole figures that the same crystallographic orientation change is taking place for both the single element and the 64 element single crystal models.



(a) 5%, 0.538, 0.462, 0 (b) 30%, 0.724, 0.275, 0 (c) 45%, 0.804, 0.194, 0.001

(d) 55%, 0.836, 0.161, 0.003 (e) 65%, 0.856, 0.136, 0.007 (f) 68%, 0.854, 0.134, 0.012

Figure 6.7: (0001) pole figures for a 64 element single crystal with orientation $(\varphi_1, \theta, \varphi_2) = (-45, 90, 0)$. The caption numbers show nominal strain and (0001) Kearn's factors f_1, f_2 and f_3 respectively. The points have have been made with circles of radius 0.01 to ease visibility.

In both cases the crystal (or eventually crystals - since they eventually become different orientations at the different integration points) starts to rotate from the initial orientation, keeping entirely within the xy-plane (i.e., rotating about the z-axis) until the orientation at some of the integration points changes such that the crystal's c-axis obtains a z-component, as is clear from both the pole figures and Kearn's factors; but the Kearn's factors in both cases indicate that only a few points obtain this orientation, see f_3. Examination of the displacement u_3 (and looking at the deformed shapes e.g. in Figure 6.5) shows that a little bit of material pushes out in the z-direction near the bottom and top, which is perhaps caused by this change in orientation which would make material flow in that direction possible.

Initially, slip occurs on basal slip systems and this is expected to lead to the initial yield observed in the single element (Figure 6.4(c)) between $t = 0 - 2s$: this would in-

deed lead to the kind of effective plastic strain field clearly shown in Figure 6.5(b). The crystal rotation to align the c-axis closer to the z-direction likely leads to orientation, at the affected integration points, where basal slip is limited requiring slip on other slip systems. In the absence of other deformation mechanisms, e.g. twinning, the crystal then may carry more stress at these points if the mix of slip systems favours those that require more stress to slip hence the observed stress rise, and crystal rotation continues until a slip system becomes available. The different integration points in Figure 6.4(c), between $t = 1 - 4s$, experience slip again but at different levels of stress suggesting that various slip systems are involved: potentially a mixture of a- and c+a-slip.

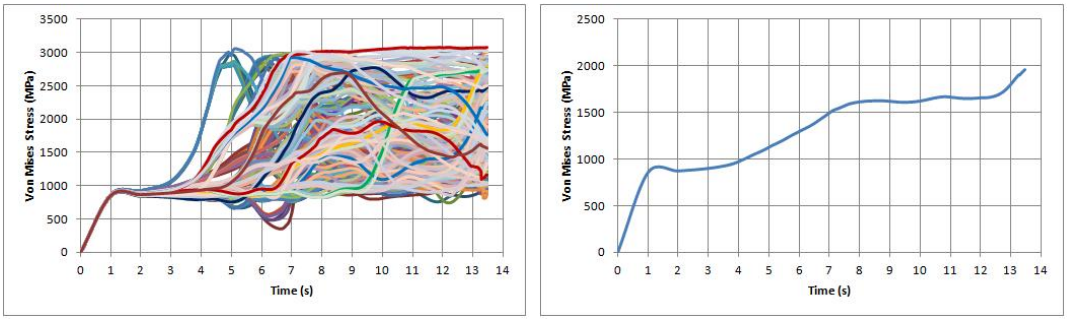
In the code, individual slips ($\gamma = \sum_t \dot{\gamma} \Delta t$) on the first twenty slip systems as well as GNDs for all the slip systems were stored - although GNDs were not coupled into the slip rule for all simulations reported here. Examination of the results reveals that various slip systems activate, and at times deactivate, at the different integration points. The following slip systems, in Table 6.1, are found to activate at the indicated time.

Table 6.1: Activate Slip Systems

Time (s)	**Slip System**
$0 - 2$	$(0001)[\bar{1}2\bar{1}0]$
$2 - 4$	$(1\bar{2}12)[\bar{1}2\bar{1}3]$
5	$(0\bar{1}11)[\bar{2}110]$
$8 - 9$	$(0\bar{1}11)[\bar{2}110]$ - at a different integration point
11	$(0001)[\bar{1}\bar{1}20], (0001)[\bar{2}110], (2\bar{1}\bar{1}2)[\bar{2}113]$
$12 - 13$	$(2\bar{1}\bar{1}2)[\bar{2}113]$

The basal plane ($(0001)[\bar{1}2\bar{1}0]$) is found to be active at all integration points at all time but other slip systems activate and deactivate at different times for the different integration points. Secondary c+a-pyramidal systems activate at three time points: $t = 2 - 4$, $t = \ 11$, and $t = 12 - 13$. At these points we see marked changes in stress levels. It is the a-pyramidal systems that have been seen to switch on and off at various times but this did not cause major shifts in stress level - probably because

they have been prescribed the same critical resolved shear stress as the basal systems. The observation that the stress level at an integration point changes according to the mix of slip systems active at that point suggests that the obtained stress level at any integration point corresponds to an effective yield stress for an effective slip system defined by the combination of slip systems active at that point. This would explain the different stress levels observed for the different integration points in Figure 6.4(c), and gives an indication of how the combination of crystallography and texture may affect the average physical properties of a polycrystal.



(a) (b)

Figure 6.8: Von Mises stress for the 64 element single crystal with orientation $(\varphi_1, \theta, \varphi_2) = (-45, 90, 0)$. The plot in(a) shows the stress for the individual integration points, while that in (b) shows the same results but averaged overall all integration points. Stress was stored much less frequently than in fig 6.4(c).

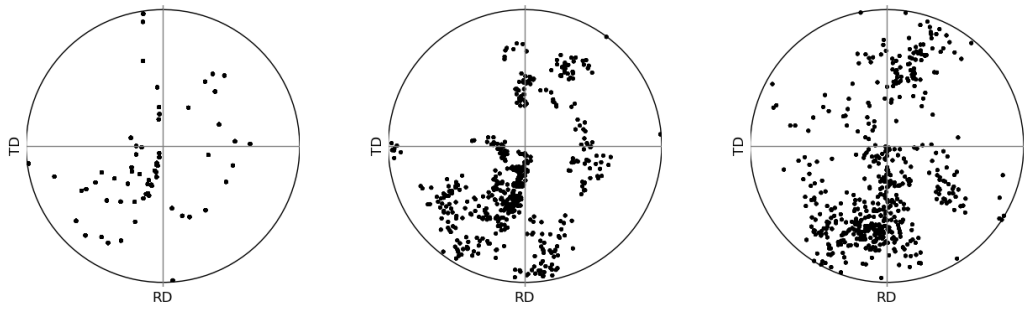
Fig 6.8(a) shows the varying stress levels for the different individual integration points[1] due to the different combinations of active slip systems, but for the multi-element single crystal model in fig 6.5. This should be compared with fig 6.4(c) which is similar but for a single element single crystal model. A snap-shot of the last time point, at $t = 13.62$, from Figure 6.8(a) is shown as a field plot in fig 6.5(c). Fig 6.8(b) shows the same results as fig 6.8(a) but they have now been averaged over all the integration points to show the overall trend of the stress. As has been explained for fig 6.4(c), it may now be understood that the trend of the overall/average stress of

[1]Only 255 out of 512 integration points are shown. 255 is the limit of data series that can be fitted into an Excel plot.

a polycrystal (e.g. in fig 6.8(b)) is a consequence of the stress behaviour at each material/integration point (e.g. in fig 6.8(a)), which in turn is a consequence of the orientation at that point (relative to the loading) which defines the combination of slip systems that may be active at that material point.

It should also be noted that in fig 6.8(b) the average stress behaviour exhibits drops in stress at various points, i.e. stress relaxation. This behaviour would normally be associated with such phenomena as recrystallization but it is evident in this case that the behaviour can also be explained by the switching on and off of various slip systems as crystallographic orientation changes.

6.4.4 Hcp polycrystal test

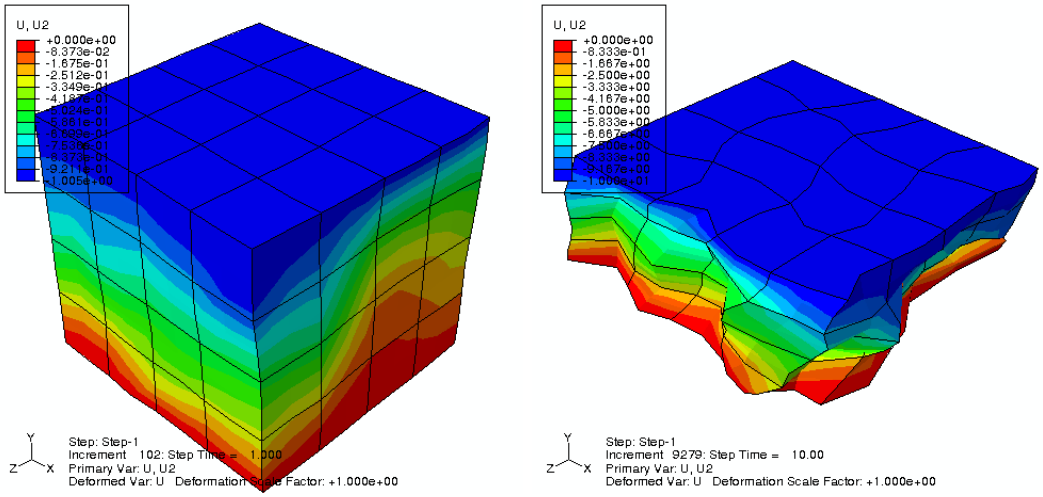


(a) 0%, 0.219, 0.312, 0.469 (b) 20%, 0.185, 0.421, 0.394 (c) 50%, 0.155, 0.532, 0.312

Figure 6.9: (0001) pole figures of an hcp 20x20x20μm polycrystal under -0.9μm compression. The achieved nominal strain and Kearn's factors are also shown in the sub-figure captions.

To further check on the capability of the code to simulate very large deformations in the presence of inhomogeneous deformation, a test simulation was carried out on the deformation of a polycrystal. A relatively small three dimensional polycrystal - not necessarily a representative volume element for any particular larger model - with sixty four orientations was set up. The polycrystal's initial texture and that after deformation is shown by the basal pole figures in Figure 6.9.

Fig 6.10 shows the displacement and deformed shape after the polycrystal was



(a) Displacement u_2 at 5% compression (b) Displacement u_2 at 50% compression

Figure 6.10: Deformed shape of an hcp 20x20x20μm polycrystal under -0.9μm compression.

subjected to 50% nominal strain (the simulation stopped at this point because the time-step had reached the specified minimum of $\Delta t = 1 \times 10^{-5} s$ after 15494 increments, with on average 7 iterations per increment at the time it stopped).

In summary, by moving away from Cauchy stress-based stress update to 2^{nd} Piola-Kirchoff stress-based stress update, and by using appropriate stiff equation control together with a cap on the slip rule (sinh law), we were able to extend the achievable nominal strain range from below 10% to over 50% (c.10%-70% true strain) for polycrystal deformation. This is closer to the range of strain required for RR texture analyses - up to 90% true strain (c.65% nominal). However, at this stage the simulations still required over 15 hours of CPU time for the small polycrystal shown without even achieving the required strain. The next section investigates the next important factor in the quest to achieve higher strain in less time: the slip rule.

6.5 Allowable time-step and the slip rule

In all the non-reference orientation cases discussed above, it was observed that time-steps become very small (order 10^{-5}s) for applied nominal strain of about 50% hence

requiring a large number of increments for very small gain in applied displacement. In fact, cutbacks (or reductions in time-step) start to occur at a nominal strain of 15% in the single element single orientation case reported in Figure 6.4. With all other obvious matters examined, the next potential cause for these very low time-steps appears to be the slip rule.

The slip rule determines the plastic strain increment for a given incremental displacement via the plastic velocity gradient $\boldsymbol{L}^p$. Therefore if, for a small applied incremental displacement (hence increment in total strain), the slip rule defines a very large slip rate, $\dot{\gamma}$, the computed increment in plastic strain may be larger than the applied increment in total strain leading to difficulty in establishing equilibrium. In other words the more non-linear the slip rule is the greater the difficulty in establishing equilibrium. The fact that a cap was required on the slip rate $\dot{\gamma}$ as already described (see Section 6.3.3) supports this view.

```
1     1    1U    0     6     6   0.00        0.00        0.01000
1     1    2     0     9     9   0.00250     0.00250     0.002500
1     2    1     0     1     1   0.00500     0.00500     0.002500
1     3    1     0     1     1   0.00750     0.00750     0.002500
1     4    1U    0     9     9   0.00750     0.00750     0.003750
1     4    2     0     1     1   0.00844     0.00844     0.0009375
1     5    1U    0     7     7   0.00844     0.00844     0.001406
1     5    2     0     1     1   0.00879     0.00879     0.0003516
```

Figure 6.11: Excerpt from an Abaqus/standard .sta file showing multiple equilibrium iterations, failed convergence and consequent cutbacks

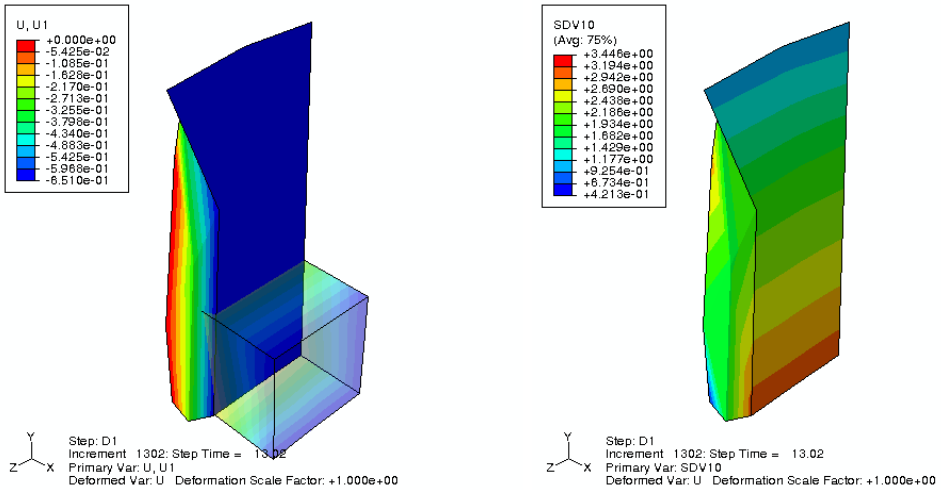
Fig 6.11 shows an example snapshot of a status (.sta) file from an Abaqus/standard simulation showing how a lot of equilibrium iterations (and hence CPU time) are wasted on increments that fail to converge due to a larger than acceptable time increment - indicated by U next to the increment attempts counter. In the case that the increment fails to converge (i.e. equilibrium is not established) the increment is re-attempted with a reduced time-step.

To fully investigate the effect of $\dot{\gamma}$ on the stability of the simulation, we try a simpler

slip rule than the sinh law: we use the power law given in equation 6.24. In the code, equations 6.11 to 6.13 have to be changed accordingly but all else remains as already described. τ_c^α, $\dot{\gamma}_0^\alpha$ and n can generally be determined directly from experimental data.

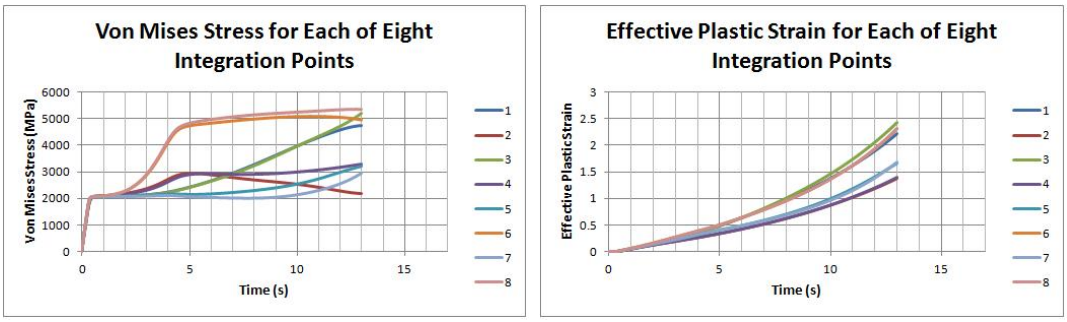
$$\dot{\gamma}^\alpha = \dot{\gamma}_0^\alpha \left| \frac{\tau^\alpha}{\tau_c^\alpha} \right|^n \tag{6.24}$$

Figure 6.12 shows the same model as in Figure 6.4 but simulated with the slip rule



(a) Displacement u_1

(b) Effective plastic strain, p



(c) Von Mises stress

(d) Effective plastic strain

Figure 6.12: Hcp 1x1x1μm single element under -1.0μm compression using the power law slip rule. Crystal orientation $(\varphi_1, \theta, \varphi_2) = (-45, 90, 0)$ is specified. Results shown up to 65% strain to compare with Figure 6.4

in equation 6.24; with $\dot{\gamma}_0^\alpha$ and n arbitrarily chosen to be 10^{-4} and 4 respectively. The same value of $\tau_c = 423.7$MPa is used as in all the previous simulations in this chapter. The model successfully run up to 99.5% nominal strain, at a strain rate of 0.05/s, but

results are shown only up to the same level as in the figure to be compared with.

Unlike the simulation described in Figure 6.4, the simulation in Figure 6.12 continued at the prescribed maximum time-step of $\Delta t = 0.01$ and with exactly one equilibrium iteration per increment up to a nominal strain of 86.5%, continued to a final nominal strain of 99.5% in only 2220 increments (compared to 10000 for 65.0% nominal strain in the former case), with a final time-step of $\Delta t = 0.001372$ just before failure. These simulations therefore demonstrate that the form of the slip rule is critical to the rate of convergence, and thus to the determination of the allowable time-steps.

In summary cutbacks cause loss of CPU time and should be avoided. The allowed time-step in any increment during the simulation is directly influenced by the nature of the slip rule and the choice of parameters for the slip rule. It is also to be noted that the numerical difficulties that necessitated the use of continuation simulations or implementation of remeshing algorithms have been completely eliminated, for any desired level of deformation.

The code developed according to the discussion up to this point, with the power law form of the slip rule, is used to study texture evolution for real experimentally measured textures in the Chapter 7. But first consideration of the determination of the parameters in the slip rule from experimental data is appropriate. This is the subject of the following section.

6.6 Determination of slip rule parameters

Stress-strain data were received for samples taken from an hcp material with the initial texture given in Figure 6.13, deformed under compression at various temperatures and strain rates. The purpose of this section is to determine the parameters $\tau_c^\alpha, \dot{\gamma}_0^\alpha$ and n needed in the slip rule (equation 6.24) in order for the simulated stress-strain behaviour to match the experimentally determined behaviour. (Detailing this process

was also required by Rolls-Royce to enable them determine the parameters needed for their Deform finite element code). All three parameters $\dot{\gamma}_0$, τ_c, and n can be determined directly from experimental stress-strain data. However, there are other relevant considerations in order for the simulated stress-strain behaviour to closely approach that which is experimentally determined. These are also discussed in what follows. The homogenisation scheme described later in Chapter 7 was also used for the simulations presented in the following sections.

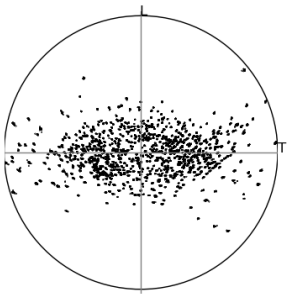


Figure 6.13: (0001) pole figure for raw data as obtained from experiment for a textured sample. All stress-strain curves in this section refer to simulations based on this initial texture.

6.6.1 The yield point: τ_c and $\dot{\gamma}_0$

For a given temperature, the parameters $\dot{\gamma}_0$ and τ_c *together* define the yield point for the simulated polycrystal's stress-strain curve, e.g. as indicated for the $300°C$ data in Figure 6.14. These must be chosen together from data corresponding to a single experimental stress-strain curve.

Assuming that the slip rate $\dot{\gamma}$ is approximately equal to the strain rate $\dot{\varepsilon}$, $\dot{\gamma}_0$ is set equal to a selected strain rate. For example, for a measured stress-strain curve for which the strain rate is $\dot{\varepsilon} = 0.05s^{-1}$, set $\dot{\gamma}_0 = 0.05s^{-1}$ in the CPFE code. τ_c is set equal to $\sigma_y/\sqrt{6}$, where σ_y is the yield stress determined from the experimental stress-strain curve corresponding to the selected strain rate. For HCP crystals $1/\sqrt{6}$ is a good approximation to the Schmidt factor for an equivalent case of single prismatic

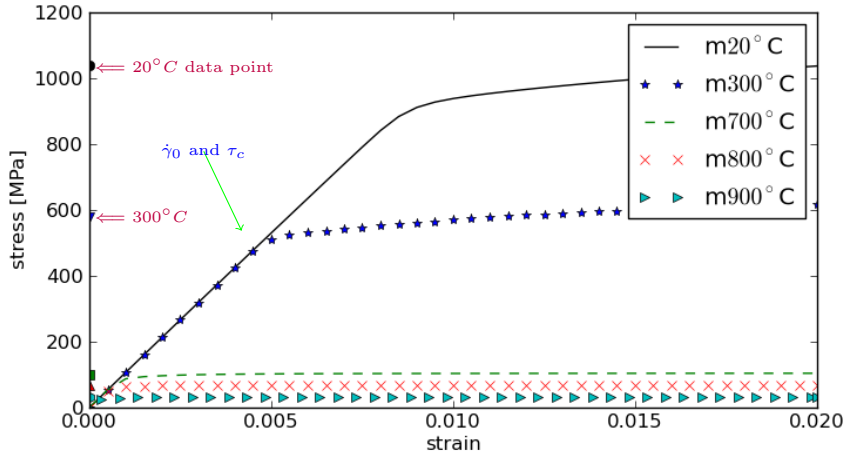


Figure 6.14: Stress-strain curves for compression of an hcp material at five temperatures (as indicated in the legend) for a strain rate of $0.05s^{-1}$ showing initial yield points defined. Single points along the left-hand vertical axis show the data point from the received stress curves that was selected as the yield point to be matched. The curves show the simulation results indicating how well the selected yield point is recovered from the simulation results.

slip with uniaxial loading in reference crystal orientation - it is exact for FCC crystals. Data at any strain rate may be used to set $\dot{\gamma}_0$ and τ_c in the CPFE code provided that both $\dot{\varepsilon}$ and σ_y refer to the same stress-strain curve at the same temperature - this will naturally fit the yield stress for the selected curve. The yield stress at any other strain rate will be recovered by applying the desired straining rate (in the Abaqus input file), without changing the CPFE code settings, provided the rightful rate sensitivity has been set (via n) as described in the next section. For example, having set up the CPFE code parameters for $800°C$ based on experimental data at a strain rate of $0.05s^{-1}$, the yield point at a strain rate of $5s^{-1}$ for $800°C$ automatically matches that which is experimentally determined if the loading rate, as specified in the Abaqus input file, is 100 times faster, without changing the CPFE code settings from those for $0.05s^{-1}$. In other words, for a given temperature, $\dot{\gamma}_0$ and τ_c can be fixed based on a single stress-strain curve and used for all desired strain rates. However, for a fixed strain rate $\dot{\varepsilon}$, hence $\dot{\gamma}_0$, τ_c must be varied if the temperature is varied. All the data in Figure 6.14 are for a strain rate $\dot{\varepsilon}$ of $0.05s^{-1}$, hence $\dot{\gamma}_0 = 0.05s^{-1}$ for all of them. Only τ_c is varied

with temperature.

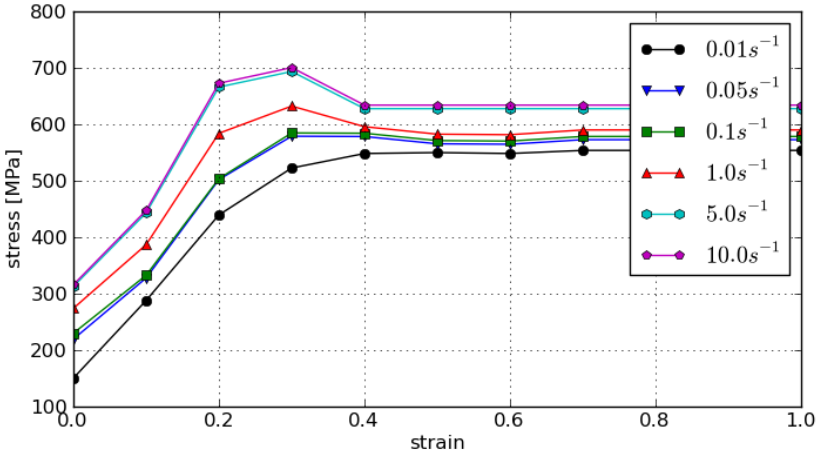


Figure 6.15: Received stress-strain data for for compression at $300°C$ for the strain rate $\dot{\varepsilon}$ shown in the legend. Yield points are not sharply defined for these data.

In cases where the yield point is not sharply defined or in cases where, for example, twinning activity is expected to be significant, e.g. the received data at the lower temperature of $300°C$ (shown in Figure 6.15), it is not easy to decide on a value for σ_y to use with the slip rule. In such cases the results presented later represent an attempt to fit to the stress-strain curve at very large strain (i.e. beyond a strain of 40% in Figure 6.15).

6.6.2 Strain rate sensitivity: n

In the CPFE code, the rate sensitivity is purely determined by n in the slip rule. To calculate n it is necessary to obtain experimental data for at least two strain rates. With the same assumption above about the relationship between strain rate and slip rate, we can define strain rate sensitivity, R_τ, based on the experimental data for the specified temperature and a given strain rate ratio, R_ε, as follows:

$$\frac{\tau^\alpha}{\tau_c^\alpha} = \left(\frac{\dot{\gamma}^\alpha}{\dot{\gamma}_0^\alpha}\right)^{\frac{1}{n}} \Rightarrow \quad R_\tau = \frac{\tau_2^\alpha}{\tau_1^\alpha} = \left(\frac{\dot{\gamma}_2^\alpha}{\dot{\gamma}_1^\alpha}\right)^{\frac{1}{n}} \approx \left(\frac{\dot{\varepsilon}_2}{\dot{\varepsilon}_1}\right)^{\frac{1}{n}} = R_\varepsilon^{\frac{1}{n}} \Rightarrow \quad n = \frac{\log(R_\varepsilon)}{\log(R_\tau)} \tag{6.25}$$

For example, for the 800° data received from RR, the yield stresses at strain rates of

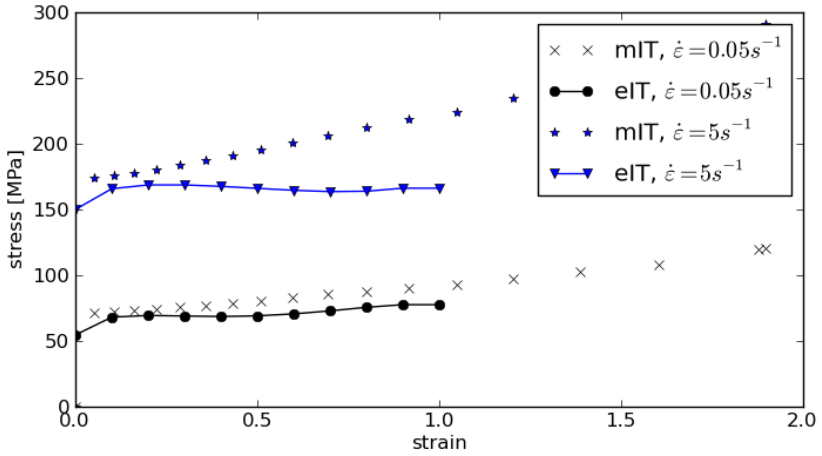


Figure 6.16: Average polycrystal stress-strain response for the initial texture shown in Figure 6.13 for compression at $800°C$ for the strain rate $\dot{\varepsilon}$ shown in the legend for RVE64. Results for the CPFE simulation are marked 'm' and from experiment 'e'

$\dot{\varepsilon}_1 = 0.05/s$ and $\dot{\varepsilon}_2 = 5/s$ are approximately $70MPa$ and $170MPa$ respectively, hence the required strain rate sensitivity is $R_\tau = 170/70 = 2.43$, and the strain rate ratio $R_\varepsilon = 5/0.05 = 100$; which gives $n = 5.19$. The results for this n with $\dot{\gamma}_0 = 0.05s^{-1}$ and $\tau_c = 70/\sqrt{6} = 28.6$ (determined according to the discussion in Section 6.6.1), for RVE64 which can accommodate a maximum of 512 unique orientations, are given in Figure 6.16 for only the data corresponding to the texture in Figure 6.13 to which the available experimental data corresponds. The results for $5.0s^{-1}$ are obtained by raising the straining rate in the input file by a factor of 100. Notice that in Figure 6.16 the target yield stress is obtained for both strain rates but the shapes of the stress-strain curves thereafter deviate from the measured curves. The reasons for this are the subject of the next section. To emphasise the need for $\dot{\gamma}_0$ and τ_c to be selected together, notice that using $\dot{\gamma}_0 = 10^{-4}s^{-1}$ and $\tau_c = 8.63$ MPa would give the same result as $\dot{\gamma}_0 = 0.05s^{-1}$ and $\tau_c = 28.6$ MPa above for the same value of n.

With the above procedures good estimates for all the three parameters can be obtained directly from the experimental data without needing to perform any simulations. The main challenge is deciding which point along the experimentally determined stress-

strain curve to be considered the yield point in cases where it is not sharply defined, as exemplified by by Figure 6.15.

6.6.3 Stress-strain curve shape

As discussed above, the parameters $\tau_c^\alpha, \dot{\gamma}_0^\alpha$ and n only define the yield stress and rate sensitivity. The shape of the stress curve beyond the yield point is otherwise defined by other factors. Among those factors would be the inclusion of the other relevant deformation mechanisms such as twinning into the CPFE model in addition to crystallographic slip which is currently the only mechanism included in our code. Mechanical twinning is known to dominate Zr alloy deformation at lower temperatures, hence capturing the stress-strain curve shape at those temperatures can be expected to be poorer for a model that does not incorporate it.

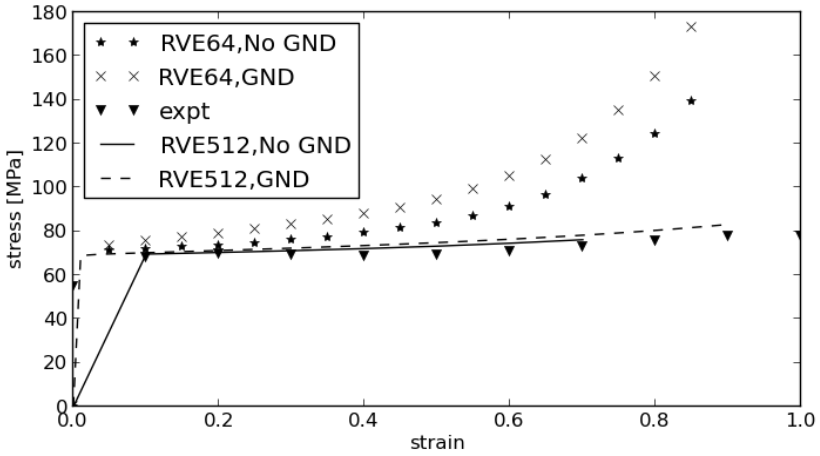


Figure 6.17: Stress-strain curves for compression at a strain rate of $0.05s^{-1}$ showing the effect of the RVE size as well as of including GND work hardening in the model. In the legend 'expt' is the experimental data. The apparent differences in gradients in the elastic regime are due to differences in frequency of data storage and should be ignored. Figure 6.14 gives an idea of what this region looks like. Larger models would take up too much disc space if output data were stored at the same frequency as for the smaller models.

Figure 6.17 demonstrates another factor that influences the shape of the stress-strain curve: the size of the representative volume element (RVE). The figure shows results for the same initial texture (shown in Figure 6.13) but for RVEs of different

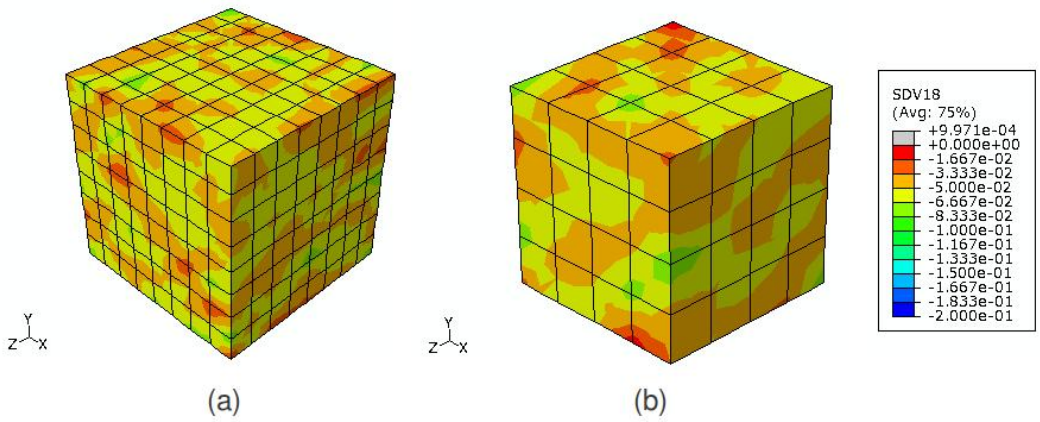


Figure 6.18: Representative volume elements (RVEs) containing twenty-noded 3D finite elements showing FE mesh with strain ε_{yy} for "RVE512,GND" and "RVE64,GND" in Figure 6.17 at a time of 1.0s, i.e. applied compressive nominal strain of 5%: (a) RVE512, (b) RVE64.

sizes: (a) RVE512 (512 elements with capacity of 4096 unique orientations), and (b) RVE64 (64 elements with capacity of 512 unique orientations). The FE meshes of the two RVEs (a) and (b) are shown in Figure 6.18. It is shown in Chapter 7 that both RVEs capture the evolution of texture well but it is clear from Figure 6.17 that they lead to different stress-strain behaviour. To be certain that the difference is not due to the usual geometrically necessary dislocation (GND)-induced size effect, the figure presents both cases with and without GND-Taylor hardening. Taylor hardening is, in this case, incorporated as given in equation 6.26 (see e.g. [5, 46]):

$$\tau_c = \tau_{c_0} + \psi G b \sqrt{\rho} \tag{6.26}$$

where ψ is a correction factor specific to the material, G is the shear modulus - which is G_{12} for a-type slip and G_{13} for c+a-type slip, b the burgers magnitude, ρ the dislocation density and τ_{c_0} accounts for the intrinsic strength of the material. For the data in Figure 6.17 the properties used are summarised in Table 6.2. In this case it is clear that including the GNDs does not significantly affect the stress-strain shape for either RVE. (It has however been noticed that including GNDs in this way increases the stability

of the simulation, i.e. reduces instances of unconverged increments). Figure 6.17 helps

Slip Rule						
$\dot{\gamma}_0(\mathrm{s}^{-1})$	n	$\tau_{c_0}^a$ (MPa)	$\tau_{c_0}^{c+a}$ (MPa)	ψ	$b^a(\mu\mathrm{m})$	$b^{c+a}(\mu\mathrm{m})$
0.05	5.19	28.6	71.5	$1.6e-3$	$3.20e-4$	$5.10e-4$
Elastic Moduli						
E_{11} (GPa)	E_{33} (GPa)	ν_{12}	ν_{13}	G_{12} (GPa)	G_{13} (GPa)	
104.4	143.3	0.48	0.20	35.3	46.7	

Table 6.2: Hcp material properties

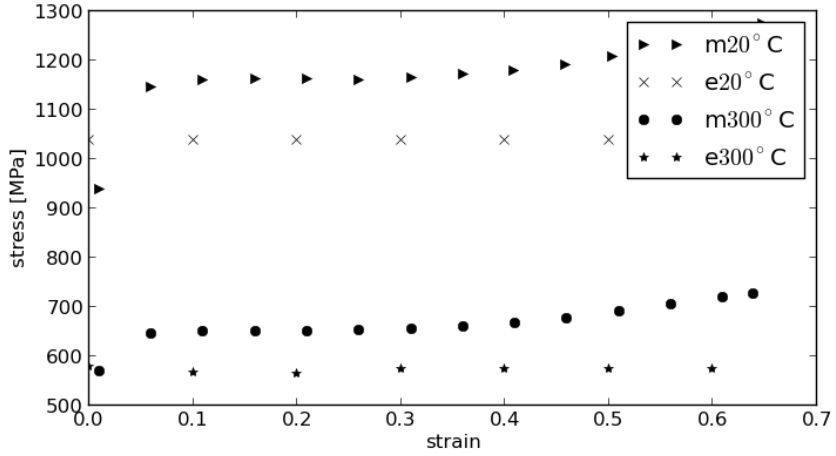
in answering the question: what is a fair representative volume element. The received texture data shown in Figure 6.13 was found to contain 2225 unique orientations (which is much more than 512 but also much less than 4096 - the orientation capacities of the two RVEs above). Figure 6.17 demonstrates that as more of the unique orientations are incorporated into the FE model, the simulated stress-strain curve approaches the experimentally determined curve more closely. The origin of this is obvious: the simulated stress-strain curve represents the average of the behaviour at all the material points (see for example Figure 6.8) so that as more orientations are included the average is shifted towards the measured curve. So defining a fair representative volume element may depend on including a sufficient number of orientations to provide a satisfactory match to the measured stress flow curve, in addition to faithfully representing the measured texture.

Discretisation density is another factor that can help to better match the experimental stress flow curve. That is, as more finite elements are used to discretise the same volume, strains, and hence stresses, will be more accurately captured. For the two RVEs referred to above, the element size is the same ($2\times2\times2\mu$m), and the number of elements per unit volume (i.e. discretisation density) is the same in both the smaller RVE ($8\times8\times8\mu$m) which has 64 elements, and the larger RVE ($16\times16\times16\mu$m) which has 512 elements. In other words volume was increased to accommodate more orientations without changing the discretisation density. Hence the improvement in

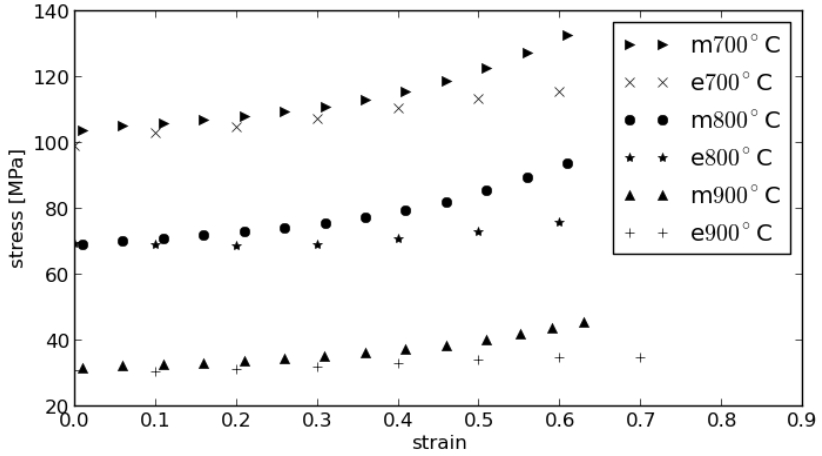
matching the experimental stress flow curve was not due to increased dicretisation density (elements per volume), not a length scale effect (such as GND effects), but it is due to inclusion or representation of more EBSD-measured orientations in the RVE.

6.6.4 Results

The model stress profiles at very low strains are already shown in Figure 6.14. This section presents large strain results for two strain rates: $0.05s^{-1}$ and $1.0s^{-1}$.



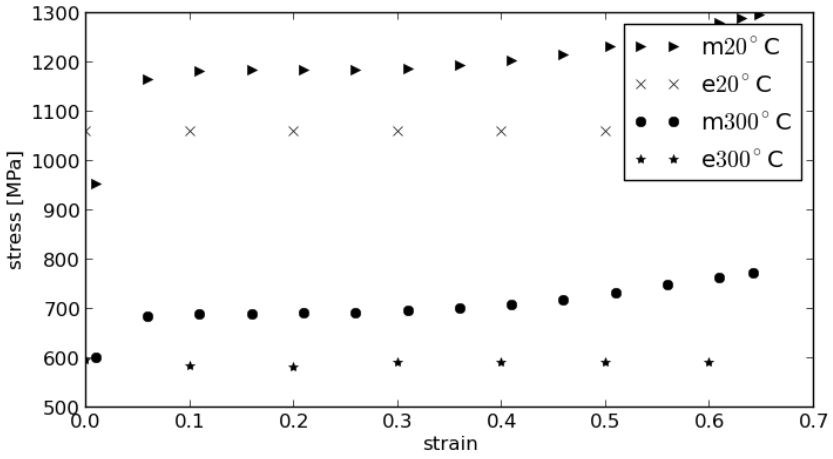
(a) Low Temperature



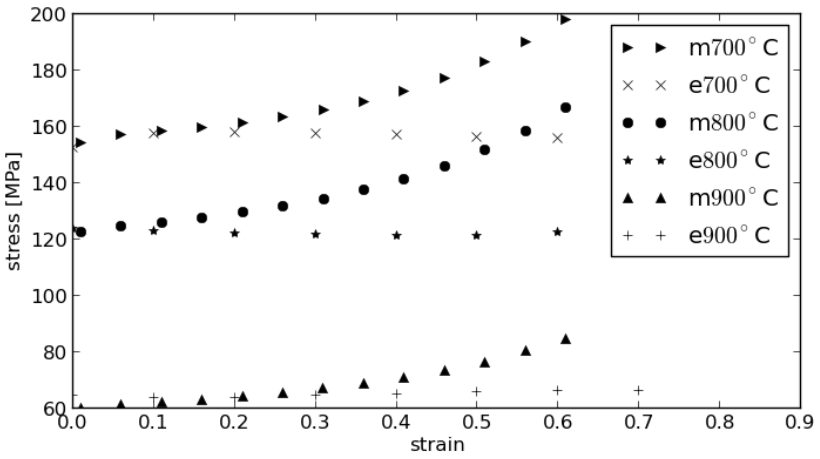
(b) High Temperature

Figure 6.19: Stress-strain curves for compression at five temperatures (as indicated in the legend) for a strain rate of $0.05s^{-1}$. In the legend, "e" and "m" denote experimental and model data respectively.

Figure 6.19 shows the simulated stress-strain profiles for strain rate of $0.05s^{-1}$ against the experimental results at the same strain rate for all the different temperatures (as



(a) Low Temperature



(b) High Temperature

Figure 6.20: Stress-strain curves for compression at five temperatures (as indicated in the legend) for a strain rate of $1.0s^{-1}$. In the legend, "e" and "m" denote experimental and model data respectively.

T (°C)	σ_y (MPa)	τ_c (MPa)	n	$\dot{\gamma}_0$ (s^{-1})
20	1037.8	423.7	154.98	0.05
300	572.8	233.8	50.32	0.05
700	98.9	40.4	7.42	0.05
800	70.0	28.6	5.19	0.05
900	32.8	13.4	4.62	0.05

Table 6.3: Slip rule parameters (from experimental data at a strain rate of $\dot{\varepsilon} = 0.05s^{-1}$). The first two columns list the temperatures and the assumed yield stress values as read from received data respectively. The next three columns give the corresponding values used in the slip rule of equation 6.24 to give the results in Figure 6.19.

indicated in the legend). Figure 6.20 is similar but shows data for the strain of $1.0s^{-1}$. As mentioned in Section 6.6.1 data at the strain rate of $\dot{\varepsilon} = 0.05s^{-1}$ was used for selecting the parameters to use in the slip rule. These parameters are summarised in

Table 6.3 for all temperatures.

Also as mentioned in Section 6.6.3, mechanical twinning is known to dominate Zr alloy deformation at lower temperatures. It can be seen in Figures 6.19 and 6.20 that although the yield point is correctly captured in both the low and high temperature data, the predicted stress-strain curve shape for low temperature data quickly deviates from the experimental data. In the case of Zr alloy this is expected since mechanical twinning has not be included in the CPFE model.

6.7 Conclusion

A new CPFE code has been developed and validated. The new code has been shown to be capable of simulating large deformation. The previously encountered numerical difficulties that necessitated the use of continuation simulations or implementation of remeshing algorithms to overcome have been eliminated for the analyses considered in this chapter. The single most important factor that helped to alleviate the difficulties with modelling large deformations was the choice of appropriate stress-strain measures. Specifically choosing the 2^{nd} Piola-Kirchoff stress over the Cauchy stress for the stress-update scheme was the single most important factor that enabled very large strains to be simulated in one go, i.e. without resorting to continuation simulations.

It has been found that the form of the slip rule, and the choice of the slip rule parameters also plays a significant role in convergence and numerical stability considerations - in addition to the choice of appropriate stress-strain measures. Equally significant for the same considerations is the choice of constraints for Newton corrections.

Finally, a methodology for determination of the slip rule parameters for the power law in order to match experimentally determined stress-strain curves has been outlined. In the following chapter we present results from texture evolution studies where initial texture data and stress-strain data received from Rolls-Royce are used to set initial

conditions for the CPFE models. The results are compared with those obtained from experimental measurements, which have also been received from Rolls-Royce.

Chapter 7

Texture homogenization and evolution

7.1 Executive summary

A texture homogenization technique which relies on interpretation of EBSD data in order to allocate orientation frequencies based on representative area fractions has been coupled with a polycrystal plasticity RVE framework allowing for arbitrarily sized RVEs and corresponding allocation of crystallographic orientation. An assessment has been made of the effect of RVE size on representation of initial, measured texture and of post-deformation predicted texture, together with average stress strain response. Textures have been characterised using both pole figures and Kearns' factors. It has been shown that with really quite crude RVEs, perfectly reasonable qualitative (pole figure) and quantitative (Kearns' factor) texture representations may be obtained. Very good agreement between predictions and EBSD-measurements of deformation textures has also been obtained.

7.2 Introduction

The determination of deformation texture continues to be a key requirement related to component manufacture and particularly so in the context of life-critical components for which knowledge of macro-scale material properties, and their relationship to texture, is essential. This chapter addresses texture development within hexagonal materials focusing particularly on initial texture representation, or homogenization, and crystal plasticity deformation modelling in which homogenization is carried out

using crystallographic orientation assignment within finite element representative volume elements (RVEs).

Many examples of the importance of texture in component processing may be found in the aero-engine and nuclear industries in which hexagonal materials are often utilized. In practice, the loading and temperature regimes adopted in processing hcp materials such as two-phase Ti and Zr alloys are such that a range of mechanisms operate during deformation, which include slip but often, in addition, twinning and recrystallization. Texture prior to deformation processing is often determined (at least on free surfaces at 'hot-spots') by electron back-scatter diffraction (EBSD) [83], but also in critical components, by use of (destructive) sectioning in order to generate improved knowledge about 3D texture prior to processing. The same approach is adopted for critical component post-processing also in order to develop understanding of textures, but after deformation. Texture measurement and representation after deformation processing is reasonably well established and in hcp materials, pole figures are used but in addition, Kearns factors are also often employed since they provide an empirical basis from which macro-level properties (such as stiffness and thermal expansivity) may be correlated.

An overview of homogenization techniques for texture representation has been given by Roters et al. [69], who rightly highlight the importance of computational efficiency in determining the texture methodology adopted since to a large extent, it is this which determines its uptake and practical usage. Tjahjanto et al. [75] present a homogenization technique based on identification of grain clusters. Within the context of crystal plasticity approaches, in which usually aggregates of grains are explicitly considered, Melchior and Delannay [63] examined RVEs made up of equally weighted orientations and divided up the sample texture into regions (or 'grains') of similar orientation containing as many orientations as necessary to match the respective volume fractions

within the grains. They also addressed morphology effects and the number of grains contained within the RVE. Eisenlohr and Roters [30] presented a coupled deterministic-probabilistic scheme for selection of crystallographic orientations in order to sample a given number of equally weighted orientations from a discrete crystal orientation distribution function. Prior to this, Li et al. [54] carried out a quantitative evaluation of deformation textures developed under tensile and compressive uniaxial and shear loading in aluminium plate using the crystal plasticity finite element (CPFE) method. Results were found to improve with finer finite element discretization (in particular, employing multiple elements per grain) and for moderate (rather than large) deformation strains. More recently, Liu et al. [57] have addressed the comparison of finite element and the more recent Fourier transform crystal plasticity methods for texture prediction.

In the present chapter, we focus on hcp systems incorporating basal, prismatic and pyramidal (type I and II) slip adopting the crystal plasticity representative volume element approach to represent initial texture and its subsequent evolution during deformation. In particular, the representation of initial texture, or texture reconstruction or homogenization, from EBSD measurements is addressed and a quantitative assessment given of the number of initial orientations necessary within the RVE in order to give a faithful representation of final predicted deformation texture. RVEs containing 64, 512 and 8000 finite elements are considered. Initial and final predicted textures are characterized using standard pole figures and, because of their prevalence in hcp studies, Kearns factors are also assessed for a number of as-received EBSD measurements of texture, and for the corresponding range of RVEs considered addressing both initial and final predicted textures.

In the following sections, the methodology adopted for texture homogenization from EBSD measurements is outlined. Following this, a specific assessment is made

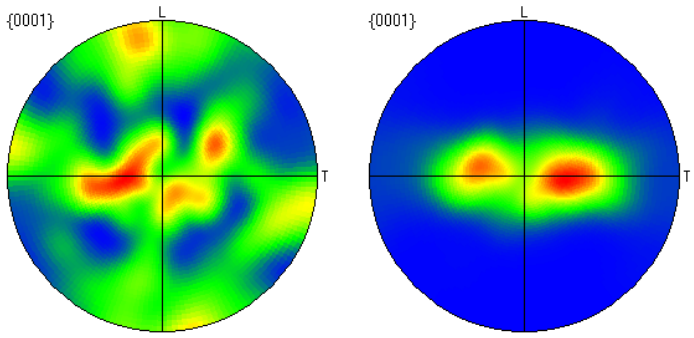
of the RVE size (ie the number of orientations captured) in order to maintain fidelity in predicted texture evolution in hcp materials. Finally, in the context of the texture predictions, the effect of RVE size on macro-scale material stress-strain response is also assessed.

7.3 Texture homogenization from EBSD measurements

Orientation data in the form of Euler angles from EBSD measurements were obtained for two Zr alloy samples: one initially random (IR) and the other textured (IT). For the IT sample, stress-strain history data as well as pole figures showing the final texture after the sample was compressed to 90% true strain at 800°C at strain rates of $0.05s^{-1}$ and $5.0s^{-1}$ are also available. The uniaxial stress-strain behaviour was used to determine the constants in the slip rule given in equation 6.11 (these values are the same as those given in Table 6.2 for the data presented in this chapter), and the measured orientation data (for 62,500 grid locations) were used to assign the initial orientation to representative volume elements (RVEs) developed for the simulation of texture within the crystal plasticity finite element (CPFE) model. Table 7.1 shows Kearns factors obtained from EBSD output alongside those calculated using equations 1.3 in the present study, showing identical values. The corresponding initial pole figures for the random (IR) and textured (IT) samples are shown in Figure 7.1.

Kearns factors	Initially Textured(IT)		Initially Random(IR)	
	Measured	Calculated	Measured	Calculated
f_L	0.056	0.056	0.306	0.306
f_T	0.294	0.294	0.305	0.305
f_N	0.650	0.650	0.389	0.389

Table 7.1: Kearns factors for the (0001) pole for the EBSD measured textures for the initially random (IR) and textured (IT) samples shown in Figures 7.1(b) and 7.1(a). All Kearns factors are arranged according to the original material directions L, T, and N.



(a) Random (b) Textured

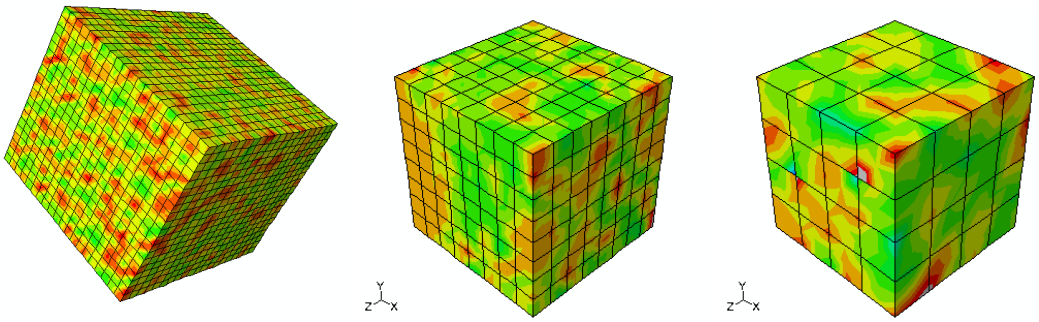
Figure 7.1: (0001) pole figures obtained by EBSD for (a) an initially random and (b) initially textured samples

Representative volume elements (RVEs) are developed for these textures for the CPFE simulation of texture evolution. In order to assign the measured texture data to the RVE, it is necessary to compact the measured orientation data into as many groups as the number of orientations that can be contained in a given RVE. A key question is then what is the minimum number of orientation data points necessary in order to develop an RVE which is truly representative of texture, and this is examined in a systematic way in what follows. Here, orientations have been assigned to the RVE on an integration point basis in order to compact as much orientation data as possible into the RVE. The key consideration is the representation of the initial texture and also, importantly, the quality of the predicted texture after deformation as a function of the RVE size (here meaning the number of orientations stored). Twenty-noded, C3D20R Abaqus finite elements are used in the RVEs each containing eight integration points.

The methodology adopted considers each experimentally obtained EBSD orientation data point and identifies orientation bins into which the same or very similar orientations, according to a tolerance, are assigned. Within each bin, the Euler angles are converted to quaternions which are averaged to give a single mean orientation using the method proposed by Humbert et al. [42]. The number of individual orientations assigned to a given orientation bin, ie the orientation frequency, is also stored, giving a

measure of the area fraction occupied by a given orientation. The unique orientations are then assigned to as many integration points in the RVE as is required to match its area fraction, with knowledge of the frequency. If the specific RVE chosen can only accommodate a smaller number of orientations than the total number of unique orientation bins obtained, those orientations with the lowest area fractions are discarded. In this way, with a given measured texture, a range of RVEs of differing sizes, resulting in widely differing computational run times, can be assessed for their effectiveness in capturing initial texture (in the form of pole figures and Kearns' factors) and final predicted texture.

7.3.1 Representative volume elements

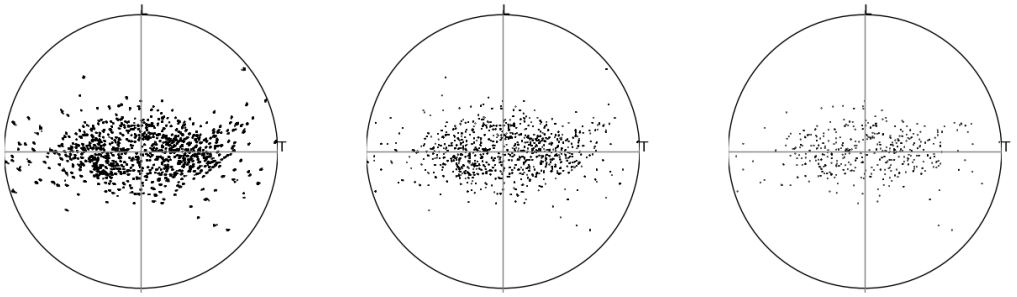


(a) 8000 elements (b) 512 elements (c) 64 elements

Figure 7.2: Representative volume elements (RVEs) containing twenty-noded 3D finite elements as indicated.

Three 'model' RVEs are considered in the present study containing 8000, 512, and 64 finite elements, and labelled RVE8000, RVE512 and RVE64 respectively, and shown in Figure 7.2. The quantity shown in colour is a representative quaternian indicative of crystallographic orientation. The texture considered here is that for the initially textured sample (IT) for which the pole figure is shown in Figure 7.1(b) and the Kearns factors in Table 7.1. Note that this pole figure and the Kearns' factors correspond to the entire measured EBSD data set (containing 62,500 orientation data sets). The texture homogenization technique discussed above has been applied to this data set in

order to develop the three RVEs shown in Figure 7.2. In the case of RVE8000, the total number of integration points is such that all the 62,500 measured orientations can be explicitly incorporated within the RVE. However, this is not the case for RVE512 and RVE64 for which the homogenization process has led to the incorporation of a smaller number of orientations than contained in the measured data.



(a) RVE8000 (b) RVE512 (c) RVE64

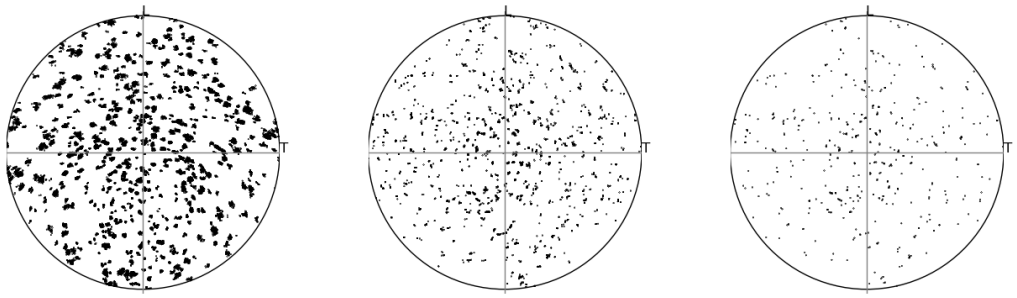
Figure 7.3: Calculated pole figures corresponding to the same nominal texture for the initially textured (IT) sample, but after homogenization for the three RVEs shown in Figure 7.2.

Kearns factors	Initially textured (IT)			Initially random (IR)		
	Measured	RVE64	RVE512	Measured	RVE64	RVE512
f_L	0.056	0.055	0.056	0.306	0.312	0.306
f_T	0.294	0.296	0.294	0.305	0.302	0.305
f_N	0.650	0.648	0.650	0.389	0.386	0.389

Table 7.2: EBSD-measured and homogenized Kearns' factors for representative volume elements RVE64 and RVE512 shown in Figure 7.2 for the initially textured (IT) and random (IR) samples.

The resulting pole figures now determined independently and directly from the three RVEs are shown in Figures 7.3(a) to (c), which should also be compared to the original smoothed pole figure from the EBSD data shown in Figure 7.1(b). The major differences between the pole figures largely relate to intensity and not to orientation distribution; this qualitatively indicates that the RVEs are all capable of capturing the texture at least in terms of pole figures. However, Table 7.2 shows a quantitative comparison between the Kearns' factors obtained directly from the EBSD measurements

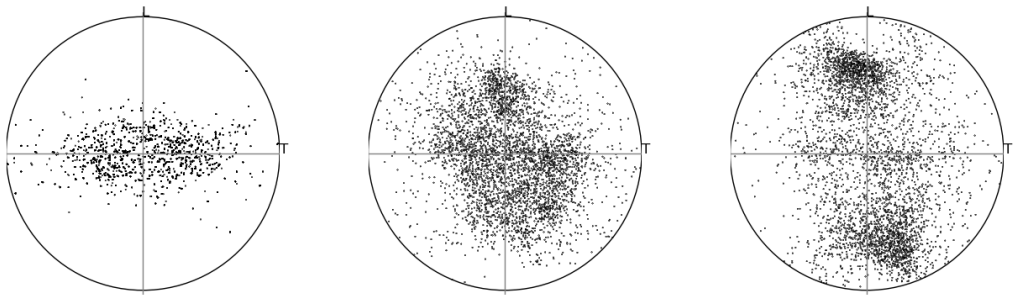
and those calculated from the RVEs (those for RVE8000 are not shown simply because they are identical to the EBSD measured values). For both the initial textured (IT) and for the random sample (IR), the three RVEs capture very closely the Kearns' measure of texture. In particular, RVE8000 and RVE512 capture identically the measured Kearns' factors while even RVE64 does a very reasonable job. The corresponding pole figures for the initially random sample, calculated from the three RVEs after homogenization, are shown in Figures 7.4(a) to (c), for which the Kearns' factors are given in Table 7.2.



(a) RVE8000 (b) RVE512 (c) RVE64

Figure 7.4: Calculated pole figures corresponding to the same nominal texture for the initially random (IR) sample, but after homogenization for the three RVEs.

7.3.2 Texture evolution using homogenized RVEs



(a) $\varepsilon_L = 0\%$ (b) $\varepsilon_L = 92\%$ (c) $\varepsilon_L = 190\%$

Figure 7.5: Pole figures for the initially textured sample RVE512 loaded in the L-direction relative to the texture at the strains indicated.

The RVEs representing textures after homogenization, described above, are sub-

jected to uniaxial deformation up to large strain (∼190%) at rates of $0.05s^{-1}$ and $5.0s^{-1}$ at a temperature of 800°C, for which the slip rule in eqn 6.11 has been calibrated. The post-deformation textures obtained for two RVEs, namely RVE512 and RVE64, are assessed together with the Kearns' factors, in the context of three initial textures. Firstly, however, the initially textured sample, for which the homogenized texture is shown in Figure 7.2(b), corresponding to RVE512, is analysed during simulated deformation and the predicted pole figures are shown in Figure 7.5 for conditions of (a) zero, (b) 92% and (c) 190% strain. The initial texture shown in (a) is largely transverse to the loading direction; that is, the majority of orientations are such that their c-axes lie normal to the loading direction. With deformation, these are expected to rotate progressively with strain until they approach the loading direction, and this can be seen to be developing in Figures 7.5(b) and (c). A large strain (190%) is needed in order to achieve this since the initial texture favours predominantly a-type slip and it is in effect the initial texture farthest from the final texture corresponding to c-axes parallel to the loading.

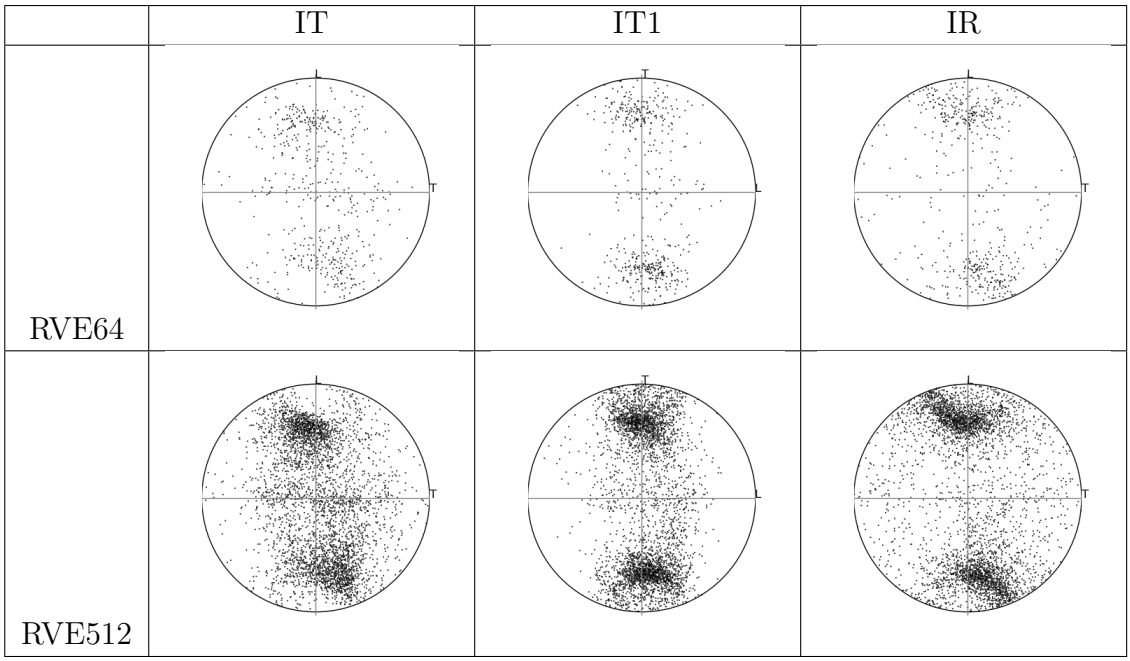


Figure 7.6: Predicted texture pole figures after ∼190% imposed strain for initially textured (IT and IT1) samples, and for the initially random (IR) sample using two RVE representations (RVE64 and RVE512)

	IT Sample		IT1 Sample		IR Sample	
f	RVE64	RVE512	RVE64	RVE512	RVE64	RVE512
f_L	0.536	0.539	0.077	0.079	0.703	0.703
f_T	0.166	0.154	0.722	0.709	0.139	0.142
f_N	0.298	0.307	0.201	0.212	0.158	0.155

Table 7.3: Kearn's factors for the initially textured (IT and IT1) and initially random textured (IR) samples after uniaxial straining to ∼190% for the two FE RVEs, namely RVE64 and RVE512

With knowledge of the final texture shown in Figure 7.5(c) for the initially textured (IT) sample, using RVE512, we analyse the same problem but using RVE64, with very reduced texture representation. This is carried out for the initially textured (IT) sample and the initially random (IR) sample together with a third initial texture (designated IT1) which in fact is identical to the initially textured (IT) sample shown in Figure 7.5(a) but rotated through 90° such that the loading direction becomes the transverse direction (labelled T in Figure 7.5(a)). The resulting, predicted, texture pole figures are shown in Figure 7.6 and the corresponding Kearns' factors in Table 7.3. The notable feature is that the reduced RVE, namely RVE64, provides very similar post-deformation pole figures to RVE512 and that this is quantitatively demonstrated by the Kearns' factors given in Table 7.3. Comparison of Kearns' factors in Tables 7.2 and 7.3, together with comparisons of the post-deformation pole figures in Figure 7.6 with the pre-deformation poles in Figures 7.3(a) and 7.4(a), show that very significant texture changes have taken place as a result of the deformation and that both the reduced (RVE64) and intermediate (RVE512) representations provide perfectly reasonable representations of the final textures. It's also interesting to note that despite starting from three quite different textures, the imposed uniaxial strain to large deformation has led to the development of really quite similar post-deformation textures, at least qualitatively, since the Kearns' factors given in Table 7.3 show that there remain some quantitative differences.

7.4 Measured texture after deformation

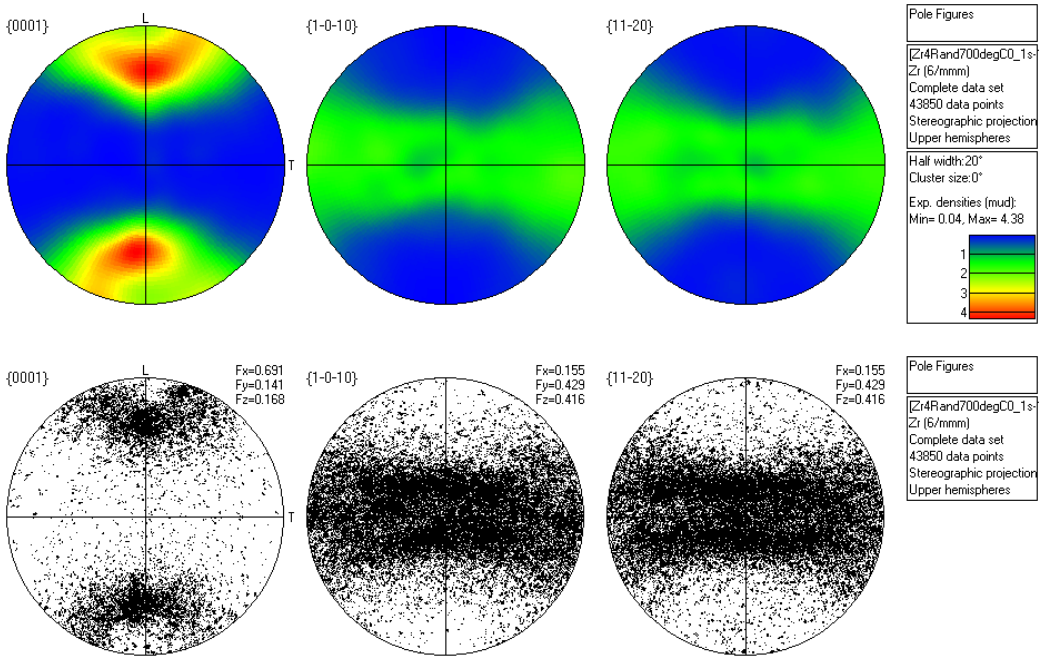
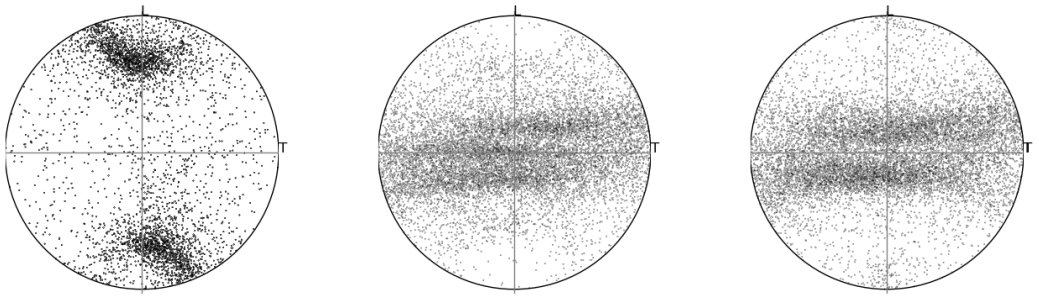


Figure 7.7: Measured pole figures obtained by EBSD for an initially nominally random specimen of Zircaloy-4 that was compressed to 90% true strain at 700°C and a strain rate of $1s^{-1}$.



(a) 0001 (b) $10\bar{1}0$ (c) $11\bar{2}0$

Figure 7.8: Predicted texture pole figures after ∼190% imposed strain for the initially random sample, IR in Figure 7.6, using RVE512 showing all three poles as indicated for comparison with Figure 7.7

Figure 7.7 shows measured pole figures obtained by EBSD for an initially nominally random specimen of Zircaloy-4, see Figure 7.1(a), that was compressed to 90% true strain at 700°C and a strain rate of $0.1s^{-1}$, with no post-deformation heat treatment. This is compared with Figure 7.8 which shows the complete set of (three) predicted pole

figures, (0001), $(10\bar{1}0)$, and $(11\bar{2}0)$, for the IR sample shown in Figure 7.6 corresponding to RVE512.

For all the predicted textures already reported, simulations were performed at two strain rates of $0.05s^{-1}$ and $5.0s^{-1}$ but it was found that the textures obtained for the two strain rates were identical for all stored time frames for all three textures IT, IT1 and IR. This implies that the texture evolution is independent of the strain rate. Additionally, from Chapter 6 it was observed, from Figures 6.19 and 6.20, that the data for 700°C and 800°C, which relate to the IT sample referred to above, are very similar for all the strain rates considered. These observations make it reasonable to compare the above 700°C at $0.1s^{-1}$ measured texture with that predicted for 800°C at $0.05s^{-1}$.

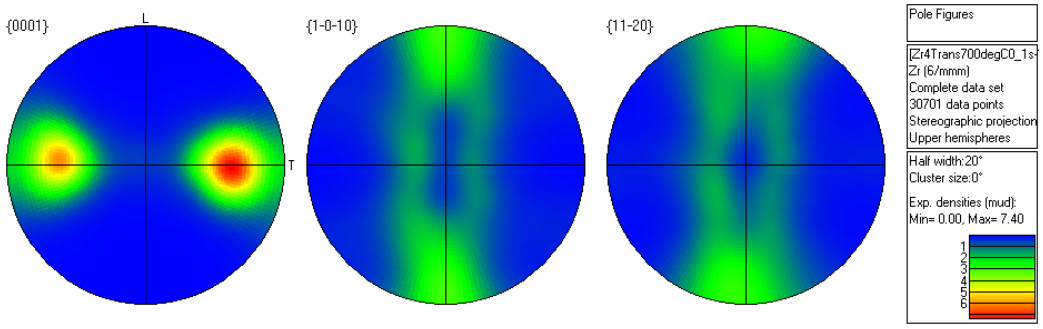
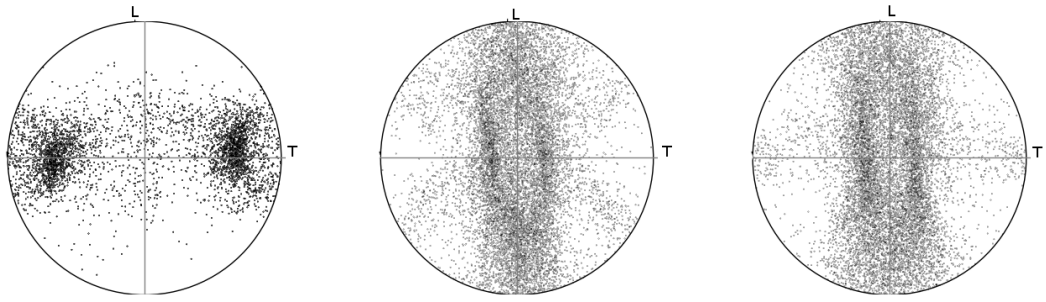


Figure 7.9: Measured pole figures obtained by EBSD for an initially textured specimen of Zircaloy-4 that was compressed to 90% true strain at 700°C and a strain rate of $1s^{-1}$, with the loading applied in the transverse material direction.



(a) 0001 (b) $10\bar{1}0$ (c) $11\bar{2}0$

Figure 7.10: Predicted texture pole figures after ∼190% imposed strain for the initially textured sample, IT1 in Figure 7.6, using RVE512 showing all three poles as indicated for comparison with Figure 7.9.

Figure 7.9 shows results obtained under exactly the same conditions as explained for Figure 7.7 except that the initial texture is that given in Figure 7.1(b) but with compression applied in the horizontal T-direction on the pole figure, hence IT1. Figure 7.10 shows the predicted texture to be compared with Figure 7.9.

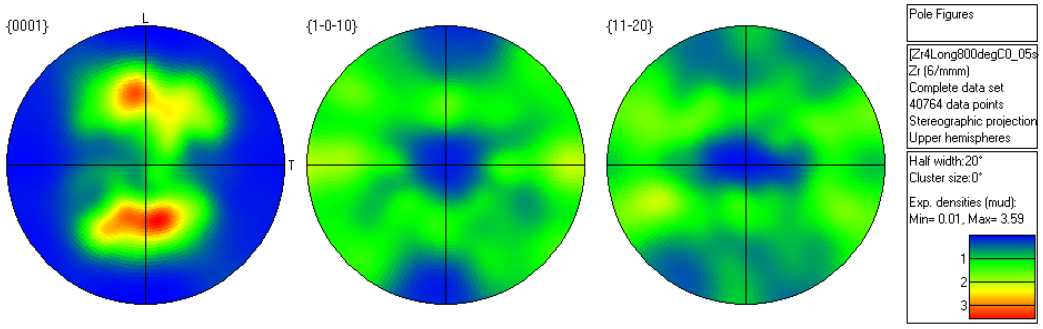
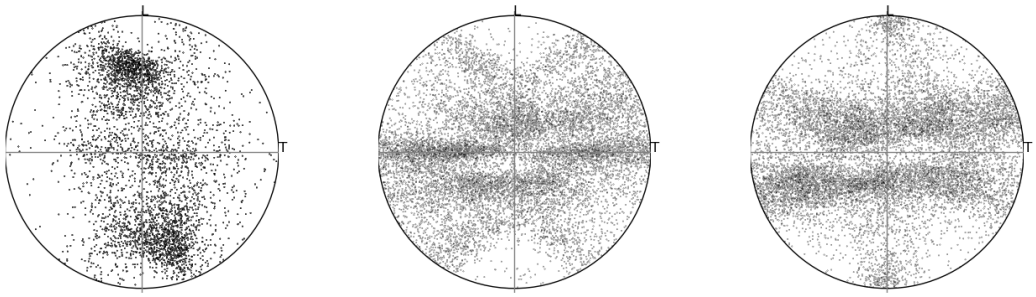


Figure 7.11: Measured pole figures obtained by EBSD for an initially textured specimen of Zircaloy-4 that was compressed to 90% true strain at 800°C and a strain rate of $0.05s^{-1}$, with the loading applied in the longitudinal material direction.



(a) 0001 (b) $10\bar{1}0$ (c) $11\bar{2}0$

Figure 7.12: Predicted texture pole figures after ∼190% imposed strain for the initially textured sample, IT in Figure 7.6, using RVE512 showing all three poles as indicated for comparison with Figure 7.11

Finally, Figure 7.11 shows the final measured texture for which the initial texture is that given in Figure 7.1(a) with the compression applied in the L-direction. Figure 7.12 shows its prediction under the same conditions of temperature and strain rate. Table 7.4 summarises the results of Figures 7.7 to 7.12 in terms of Kearns factors. Note that for each case the predicted Kearns factors for the loading direction are higher than the experimental values due to the higher applied compressive strain in the simulation, i.e. ∼85% nominal strain for simulation compared to ∼60% nominal strain for experi-

ment. The results presented in this section demonstrate very good agreement between simulation and experiment for all the initial textures considered.

	IT Sample		IT1 Sample		IR Sample	
f	Expt	RVE512	Expt	RVE512	Expt	RVE512
f_L	0.374	0.539	0.051	0.079	0.691	0.703
f_T	0.170	0.154	0.667	0.709	0.141	0.142
f_N	0.456	0.307	0.281	0.212	0.168	0.155

Table 7.4: Comparison of final Kearns factors between experimental results and RVE512 for the initially textured (IT and IT1) and initially random textured (IR) samples.

7.5 RVE dependence of average stress-strain response

So far, the effects of RVE size on maintaining fidelity of texture prior to and following large deformations have been assessed but nothing has yet been said about the RVE-dependence of the macro, or average stress strain response. In this section, the two initially textured samples (IT and IT1) and the initially random sample models are employed to assess uniaxial average stress-strain response at two strain rates and in particular, to examine the differences which result in using the two RVEs, namely RVE512 and RVE64. The previous studies have shown that both RVEs are capable of allowing reasonable representation of texture both before and after deformation and here, we examine if this holds true for average stress strain behaviour. Naturally, if the two RVEs are truly representative, then one would expect not to see any differences in the results obtained from them for the identical loading conditions. However, RVE64 is unlikely to be truly representative because of its limited size.

Figure 7.13 shows the model computed average stress strain response for uniaxial straining of the polycrystal representation using RVE512 at the two strain rates of $0.05s^{-1}$ and $5.0s^{-1}$, which result in the final textures shown in Figure 7.6 for the smaller strain rate. Also shown in this figure are the experimentally obtained macro stress strain curves at the two strain rates, from which the slip properties in eqn 6.11

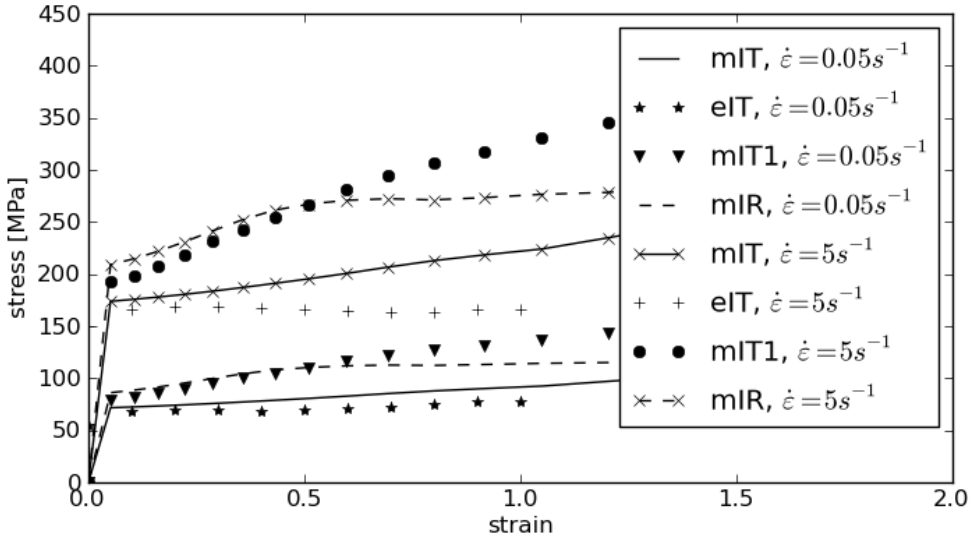


Figure 7.13: Stress-strain curves for RVE64 simulations and experiments (denoted by "e" preceeding "IT") for the initially textured (IT) and random (IR) samples for the strain rates shown. L and T in the legend indicate the loading direction relative to the original material directions: L > longitudinal, T > transverse. The apparent difference in Elastic moduli is a result of not storing data frequently enough and should therefore be ignored. In all cases the model loading direction corresponds to loading in the transverse material direction.

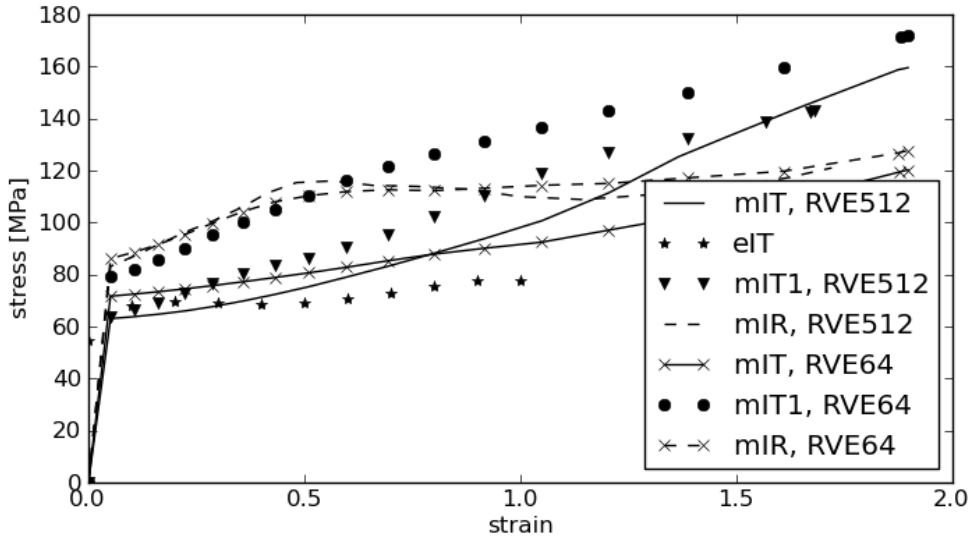


Figure 7.14: Stress-strain RVE64 and RVE512 at a loading strain of 0.05/s.

were determined. Considering the smaller strain rate first, the initially textured sample (IT) shows the lowest stress response because the initial texture, shown in Figure 7.5(a) is the most favourable for a-type slip for which the critical resolved shear stress is considerably lower than for c+a-type slip. Hence for sample IT1, for which the initial

texture contains considerable grain orientations with their c-axes parallel to the loading direction, the macro-stress response is higher. The same general trends are repeated at the higher strain rate of $5.0s^{-1}$. The same computations have been carried out at the lower strain rate but employing the reduced RVE64, and the average stress strain response for this RVE together with that for RVE512 is shown in Figure 7.14. The overall behaviour is such that both RVEs capture the initial yielding reasonably, where the differing yield and flow stresses result from the different initial textures, but it is apparent that there are some differences obtained by virtue of the two RVEs employed, confirming in particular that RVE64 is unlikely to be truly representative. However, the stress differences resulting from the two RVEs are not so large as to render the computations useless. On the contrary, it is argued that both texture representation and evolution during large deformations together with the macro stress strain behaviour may be perfectly reasonably captured by computer time-efficient but simple RVEs. This is potentially useful since full polycrystal texture analyses, using crystal plasticity modelling, remain implausible for process design but are being considered in parallel with standard Mises plasticity component process modelling in which texture analyses are carried out only for a sub-set of hotspots identified from the conventional process modelling. The scale of the texture modelling for the hotspots then becomes a key question, and it is argued that early-stage process design could reasonably rely on simplistic RVE (and hence efficient) polycrystal representations which are capable of satisfactory texture prediction. Naturally, more detailed design would then require more lengthy analysis using better RVE polycrystal representations in order to confirm texture predictions.

7.6 Conclusions

A texture homogenization technique which relies on interpretation of EBSD data in order to allocate orientation frequencies based on representative area fractions has been coupled with a polycrystal plasticity RVE framework allowing for arbitrarily sized RVEs and corresponding allocation of crystallographic orientation. A crystallographic slip rule for hcp zirconium has been developed which allows for basal, prismatic, and types I and II pyramidal slip, and accounts for the differing a- and c+a-type slip system strengths. Slip rule properties and rate sensitivity have been determined from average uniaxial experimental data.

An assessment has been made of the effect of RVE size on representation of initial, measured texture and of post-deformation predicted texture, together with average stress strain response. Textures have been quantified using both pole figures and Kearns' factors. It has been shown that with really quite crude RVEs, perfectly reasonable qualitative (pole figure) and quantitative (Kearns' factor) texture representations may be obtained. This potentially provides for the possibility of a texture process design methodology combining conventional deformation process modelling from which hotspots are identified, for which the strain histories are extracted and used to carry out polycrystal RVE texture analyses in order to determine post-deformation texture.

It has been found that for simulations at the specified temperature to very large strains the final texture is largely determined by the loading direction and is independent of the initial texture. However for relatively low straining, the texture observed is dependent on the initial texture, particularly dependent on the misorientation of the c-axes away from the loading direction.

Comparison of predictions with EBSD-measured textures showed very good agreement. This shows that the large deformation model developed in Chapter 6 together

with the homogenized RVEs developed in the present chapter comprise a good model for texture evolution prediction.

Bate and Quinta da Fonseca [7] studied the need for multiple elements to represent a grain, i.e. orientation, for effective representation of texture in CPFEM. The methodology used to assign orientation here is more coarse than they described, that is, rather than at least one element per grain, we are using one quadratic element for eight orientations (or one integration point per orientation) and yet the texture development is properly captured according to the comparison with experiment. Moreover this is true even for true strains greater than 100%. It is, therefore, not necessary to have more than one element per grain in order to model texture evolution properly. Having many elements is in fact a waste of computing resources.

The fact that we are using 3D models for surface-based EBSD measured texture and yet capturing its evolution satisfactorily in comparison to experimental data, even with the fact that we assign the orientation on an integration point basis suggests that the role of morphology in modelling texture evolution may be somewhat limited.

For the RVE64, simulations were performed for two different strain rates, 0.05/s and 5/s. For both strain rates, the resulting textures were identical for any given initial texture at all levels of strain. This suggests that rate effects have minimal effect on texture development. Instead it is modelling the expected deformation mechanisms that is of import. In this case the temperature considered was chosen to minimise any effects of twinning, hence with only slip as the included mode of deformation, the textures are well predicted. At lower temperatures it may be necessary to include twinning deformation for Zr in order to correctly predict texture evolution at a comparable strain level with experimental measurements. Recrystallisation was also not included, and similarly the model does not explicitly account for static thermally activated softening, which might be important at elevated temperatures

Chapter 8

Texture effects on polycrystal physical properties

8.1 Executive summary

HCP single crystals have anisotropic thermal expansivities and in Ti and Zirconium alloys, the expansivity in the c-axis direction may be approximately 0.6 times that for the a-direction. This chapter employs crystal elasticity-plasticity analyses of polycrystals in order to investigate the resulting development of 'type II' thermal strains which are generated from temperature change. It is shown that the strains may be sufficiently large in order to cause localized plasticity. A study has been carried out to investigate the resulting effects of crystallographic texture on the thermal expansivities of Zirconium alloy polycrystals, and the corresponding changes which occur to expansivity as a result of the onset of plasticity.

Kearns factors have long been employed to represent texture (particularly for nuclear HCP materials) and to enable the determination of thermal expansivity (and other physical properties) based on an averaging process. The chapter presents an assessment of the Kearns approach and a rigorous crystal elasticity-plasticity methodology for determination of thermal expansivity in Zirconium alloy polycrystals. It is demonstrated that errors in thermal expansivities of up to 15% may occur using the Kearns representation of texture and that the effects of texture dominate over morphological variations. The error in expansivity is sufficiently large to make this result of technological significance in the nuclear industry in which knowledge of expansivity is necessary in component design.

8.2 Introduction

Predicting material properties, for both single crystals and polycrystalline aggregates, is an issue of great interest to industry where materials design is of great importance. Significant work has already been done in the area of determining material properties for single crystals [34] but moving from the knowledge garnered in such work to its application for polycrystal aggregates has remained a challenge.

For the industrialist, establishing a quantitative link between crystallographic texture and material properties has proved far from trivial. In critical applications where texture is known to play an important role, a fixed method of manufacture is typically adopted to ensure consistency with the original certified product. However, for statistical process control and in order to allow manufacturing change, some form of numerate relationship, or ideally, predictive capability for relating texture to key properties [39, 49, 74] is desirable. This allows decisions to be made, where appropriate, on the basis of texture measurements alone, rather than extensive, time consuming and expensive mechanical tests. This issue is particularly prevalent in HCP metals where relatively large elastic and plastic anisotropy can exhibit a wide range as determined by their manufacturing route. In the case of Zirconium and Titanium alloys for nuclear and aerospace use respectively, macroscopic textures are deliberately induced in selected components to optimise component behaviour in service. Control of both 'mean' and 'scatter' in texture is significant given the safety critical applications of these alloy systems.

In the case of zirconium alloys, processing routes are optimised in order to provide some protection against through cracking of fuel cladding. Significant concerns for the designer then arise as a result of the anisotropic properties. In addition to the obvious influence on elastic modulus, changes in expansion coefficients modify thermally

induced stress levels and dimensional changes occur in the components, through life, as a result of irradiation growth. These effects are significant as an example, in the case of CANDU [80] pressure tubes, a length increase of 50mm of a 4m long tube is possible via irradiation growth. The use of Kearns factors [3, 35, 47, 74], where the basal poles are resolved to give 'volume fractions' of the crystal planes in three perpendicular directions, have been, and are widely used in industry. However, more accurate, physically based models would be highly desirable to predict material behaviour as a function of starting texture.

Simplistic averaging approaches fail to capture some key aspects related to the intrinsic nature of a polycrystal. In particular, the grain to grain interactions [49, 74] arising from incompatibility strains and the potential for local stress state change if local plasticity occurs in favourably orientated grains with suitably orientated neighbours [27] cannot be captured by simplistic averaging approaches. It is important to note that in HCP metals that typically deform by a mixture of twinning and slip during manufacture, the mean misorientation distribution [39, 42] between grains may be high. This chapter aims to explore systematically the variability of thermal expansion coefficient as calculated explicitly using crystal plasticity modelling and via Kearns factors for a range of different, experimentally measured starting textures. In addition, the role of grain morphology is explored for a fixed starting texture. Crystal plasticity modelling is shown to be a technique well suited to this application, highlighting the significant errors encountered using the Kearns averaging approach.

Texture representation by pole figures, ODFs, and Kearns factors has been discussed in Section 1.1. Texture information as presented on a pole figure or by an ODF represents the volume fractions of the constituent orientations but not morphology, that is, it has no information about such mechanical factors as grain shape, size, spatial distribution, or grain interaction.

The quantitative nature of the Kearns factors and the ODF's led to interest in using them to average material properties [3, 55, 74]. There are at least four separate factors that need to be considered when averaging properties for a polycrystal based on its constituent crystallites: orientation (of any given crystallite), orientation spatial distribution (i.e. the nature of neighbouring orientation), sizes of crystallites with a given orientation (hence volume fraction of that orientation), and the shapes of the crystallites. Orientation and size (as volume fraction) are encapsulated in Kearns texture factors, but orientation spatial distribution and grain shape are not. The connection between shape, size and orientation spatial distribution will set the nature of grain interaction that occurs locally, and the distribution of this localised behaviour will ultimately influence the form of the averaged properties. The effect of orientation spatial distribution (which determines the nature of neighbouring orientations) has been systematically studied and shown to be an important factor for fatigue facet formation in Ti alloys [27].

In the next sections, an overview is presented of the determination of the average thermal expansivity of a polycrystal based on Kearns factors and on the rigorous crystal elasticity-plasticity modelling strategy. We then present the results from a systematic study of texture effects on thermal expansivity, modulus, Poisson's ratio and yield under conditions of elastic and plastic material behaviour.

8.3 Thermal expansivity calculation

The stress and texture update methodologies used in this chapter are those detailed in Chapter 6. The power law form of the slip rule is used with the following parameters: $\dot{\gamma}_0^\alpha = 10^{-4}s^{-1}$, $n = 5.19$ and the critical resolved shear stress τ_c^α is 8.63 MPa for a-type slip and 21.6 MPa for c+a-type slip. These were obtained by fitting to experimental stress flow curves for zirconium alloy compressed at strain rates of $0.05s^{-1}$ and $5.0s^{-1}$

at $800°C$ as described in Section 6.6.2. This temperature was chosen because for the specific experimental dataset it was known that slip is the dominant deformation mechanism, unlike lower temperatures where significant twinning would occur. τ_c and n are temperature dependent (generally increasing as temperature decreases) but are assumed constant for simplicity in this case; properties for the stiffness matrix are $E_{11} = 104.4GPa$, $E_{33} = 143.3GPa$, $G_{13} = 46.7GPa$, $\nu_{12} = 0.48$, and $\nu_{13} = 0.20$.

Like the elastic moduli, the thermal expansivity in HCP materials is also known to be anisotropic (see e.g. [23]). In [23], and other works by the same authors (e.g. [22]), thermal expansivities have been measured for various materials including HCP materials using X-ray techniques. The measurements show a clear distinction in the expansivities in the a-direction (α_a) and c-direction (α_c) for HCP materials. Their measurements also show that α_a and α_c are temperature dependent. In this study, we assume that α_a and α_c are constant with temperature for simplicity. The values used here for these are $\alpha_a = 9.5 \times 10^{-6} K^{-1}$ and $\alpha_c = 0.5895\alpha_a$.

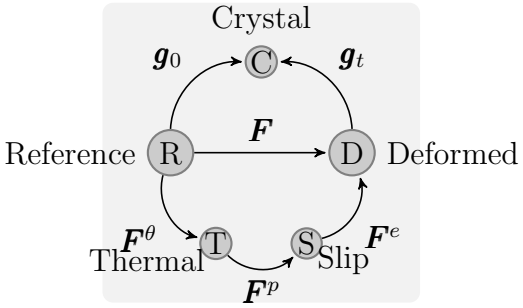


Figure 8.1: Multiplicative decomposition of the deformation gradient $\boldsymbol{F}$ into the components $\boldsymbol{F}^e$, $\boldsymbol{F}^p$, and $\boldsymbol{F}^\theta$ the elastic, plastic and thermal contributions to the deformation gradient respectively. Also shown is the relationship of the crystal frame (C) system to the reference (R) and deformed (D) frames via the orientation matrix.

The thermal strain, for any crystal, with respect to its crystallographic axes (C in

Figure 8.1) $\boldsymbol{\varepsilon}_c^\theta$ is given as

$$\boldsymbol{\varepsilon}_c^\theta = \begin{bmatrix} \alpha_a & 0 & 0 \\ 0 & \alpha_a & 0 \\ 0 & 0 & \alpha_c \end{bmatrix} \theta \tag{8.1}$$

where θ is the temperature change. $\boldsymbol{\varepsilon}_c^\theta$ is mapped to the undeformed (reference) configuration thermal strain $\boldsymbol{\varepsilon}^\theta$ by the initial orientation $\boldsymbol{T}$ $(= \boldsymbol{g}_0^{-1})$ according to

$$\boldsymbol{\varepsilon}^\theta = \boldsymbol{T}\boldsymbol{\varepsilon}_c^\theta \boldsymbol{T}^T \tag{8.2}$$

With thermal loading, the deformation gradient can be multiplicatively decomposed as shown in equation 8.3 and illustrated in Figure 8.1.

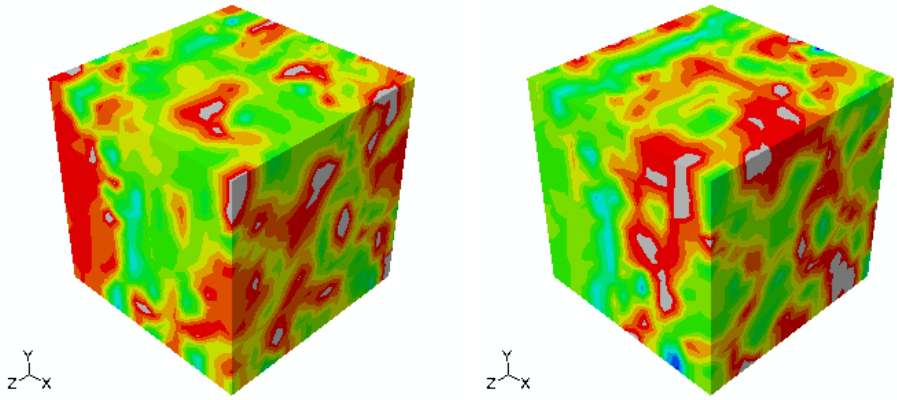
$$\boldsymbol{F} = \frac{\partial \boldsymbol{x}}{\partial \boldsymbol{X}} = \boldsymbol{F}^e \boldsymbol{F}^p \boldsymbol{F}^\theta \tag{8.3}$$

For a single crystal, thermal loading alone only leads to expansion but does not result in any rigid body rotation. Therefore the contribution to the deformation gradient from thermal loading is a pure a stretch, and can be defined as follows

$$\boldsymbol{F}^\theta = \boldsymbol{U}^\theta = \boldsymbol{I} + \boldsymbol{\varepsilon}^\theta \tag{8.4}$$

With $\boldsymbol{F}$ obtained using ABAQUS's UEL implementation, $\boldsymbol{F}^p$ obtained as in equation 1.7 and $\boldsymbol{F}^\theta$ obtained as in equation 8.4, $\boldsymbol{F}^e$ can be obtained for the implicit integration of equations, calculation of the Jacobian, and for tracking texture development as detailed in Chapter 6.

Figure 8.2 shows a representative volume element (RVE) in which the crystallographic orientations are depicted using quaternions. Figure 8.3 shows the different



(a) q_2 (b) q_3

Figure 8.2: A $16 \times 16 \times 16 \mu m$ representative volume element used for plasticity simulations. Fixed in the x direction on the -x face, y on the -y face, and z on the -z face. Field plots show two of the four quaternion components (with limits $-1 \leq q \leq 1$) giving an idea of the field distribution of orientation. The model can accommodate up to 4096 unique orientations.

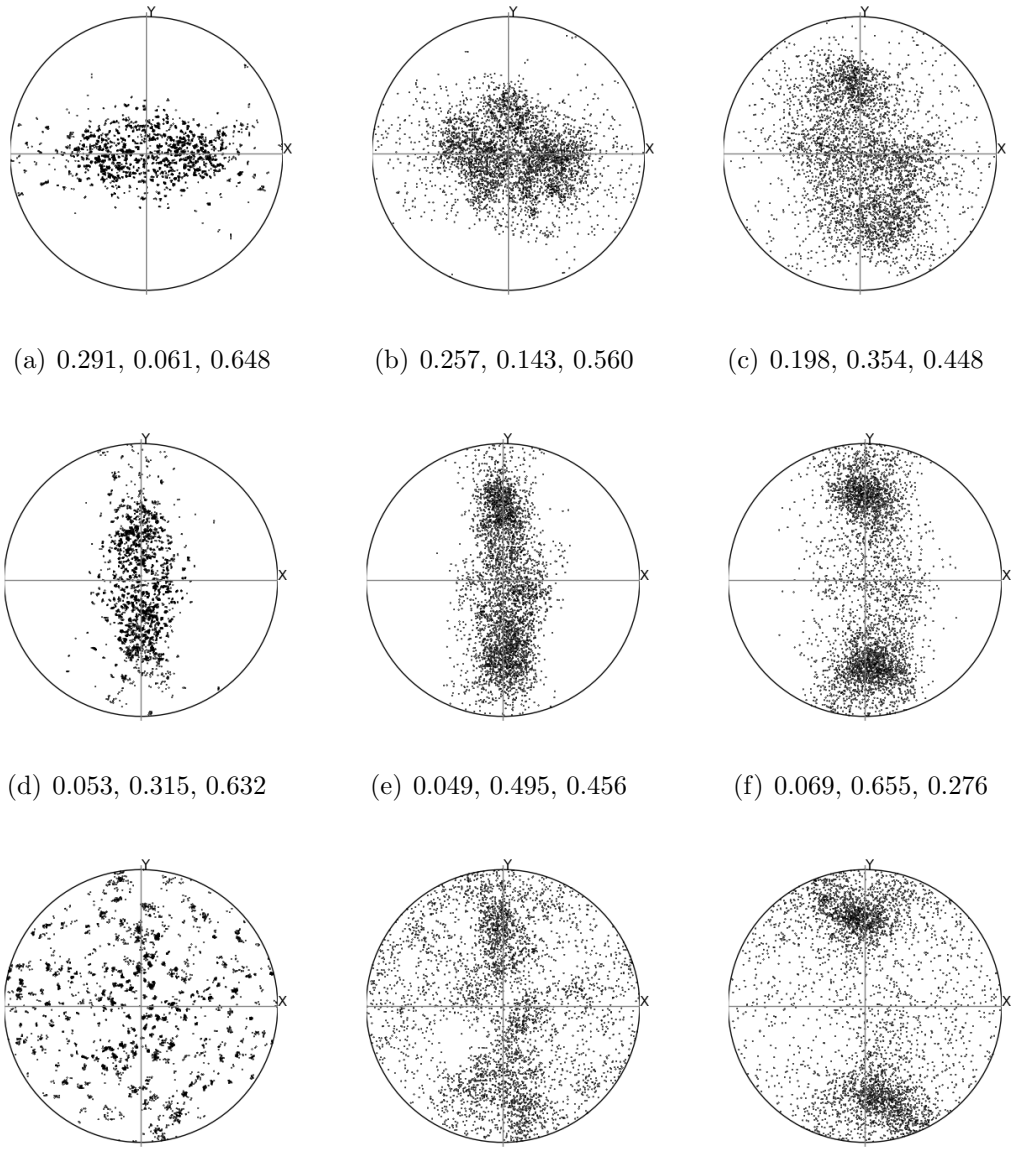
initial textures assigned to the RVE in Figure 8.2, and which will be the subject of the discussion in this chapter - the texture shown as a field plot in Figure 8.2 is representative of that in Figure 8.3(a). Figures 8.3(a), 8.3(d), and 8.3(g) represent measured textures from experimental Zirconium alloy samples, while the others represent evolved versions of those initially measured.

The loading involves subjecting the model shown in Figure 8.2 to cooling from $1143K$ to $293K$ in 2.125 seconds, hence the maximum temperature change is $-850K$ and the cooling rate is $400Ks^{-1}$. Each RVE and initial texture is simulated both with all free faces constrained to remain flat and without any constraints.

At any time t in the simulation, the displacements u_1, u_2, u_3 from the free x, y, z-faces respectively are obtained and used to compute the (nominal) macro-strains as follows:

$$\varepsilon_1 = \frac{u_1}{L_1}, \quad \varepsilon_2 = \frac{u_2}{L_2}, \quad \varepsilon_3 = \frac{u_3}{L_3} \tag{8.5}$$

In the case where the free faces are not constrained to remain flat the displacements u



(a) 0.291, 0.061, 0.648 (b) 0.257, 0.143, 0.560 (c) 0.198, 0.354, 0.448

(d) 0.053, 0.315, 0.632 (e) 0.049, 0.495, 0.456 (f) 0.069, 0.655, 0.276

(g) 0.297, 0.326, 0.377 (h) 0.235, 0.485, 0.280 (i) 0.163, 0.655, 0.182

Figure 8.3: Initial textures as pole figures and corresponding Kearns factors (f_1, f_2, f_3) for the three reference directions (X, Y, Z). Each pole figure shows 4096 orientations (each of which are not necessary unique as is obvious from the figures), according to the capacity of the RVE in Figure 8.2.

represent the mean displacement of the nodes on a given free face. The corresponding temperature drops, at time t, are also obtained. A Python script is then used to compute the differential changes in both the displacements and the temperature, enabling the calculation of the thermal expansivities as follows:

$$\alpha_1^\epsilon = \frac{d\varepsilon_1}{d\theta}, \quad \alpha_2^\epsilon = \frac{d\varepsilon_2}{d\theta}, \quad \alpha_3^\epsilon = \frac{d\varepsilon_3}{d\theta} \tag{8.6}$$

where the superscript ϵ merely indicates that these values of α have been obtained directly from the strains. At each time, the orientation distribution is also retrieved and used to compute the Kearns factors.

Tempest [74] provides a thorough review of the physical basis for the estimation of polycrystal bulk physical properties by averaging single crystal properties (emphasising applicability only to those properties relating two vector quantities or a tensor with a scalar quantity but not properties dependent on tensor-tensor relationships such as Young's modulus). This can be summarised, with reference to thermal expansivity, as follows. For a single crystal, the thermal expansivity in some reference direction, which makes an angle ϕ with the basal pole, can be found as

$$\alpha_{ref}(\phi) = \alpha_c \cos^2 \phi + \alpha_a (1 - \cos^2 \phi) \tag{8.7}$$

and if, in a polycrystal, each crystallite (i) is assumed to contribute to the bulk thermal expansivity in proportion to its volume fraction (V_i) then the average thermal expansivity is given by

$$\begin{aligned} \alpha_{ref} &= \alpha_c \sum_i V_i \cos^2 \phi_i + \alpha_a \sum_i V_i \left(1 - \cos^2 \phi_i\right) \\ &= \alpha_c f + \alpha_a (1 - f), \quad \text{with} \quad f = \sum_i V_i \cos^2 \phi_i \end{aligned} \tag{8.8}$$

f in equation 8.8 is the Kearns factor with respect to the normal direction (cf. f_3 in equation 1.3) for that reference direction. It can also be defined as a continuous function, and evaluated for the three orthogonal directions as given in equations 1.3.

The corresponding thermal expansivities in the three directions are thus given as

$$\alpha_1^f = \alpha_c f_1 + \alpha_a(1 - f_1)$$
$$\alpha_2^f = \alpha_c f_2 + \alpha_a(1 - f_2)$$
$$\alpha_3^f = \alpha_c f_3 + \alpha_a(1 - f_3) \tag{8.9}$$

In order to validate the implementations for the texture factors and thermal expansivity, the polycrystal in Figure 8.2 was converted into a single crystal (i.e. uniform orientation) and simulations performed for three simple cases for which the result is obvious, with the thermal loading described above. The following crystallographic orientations were assigned: (i) c-axis parallel to z-axis, (ii) c-axis parallel to y-axis, and (iii) c-axis parallel to z-axis. Expected texture factors for the three cases are: (i) $f_1 = f_2 = 0, f_3 = 1$, (ii) $f_1 = f_3 = 0, f_2 = 1$, and (iii) $f_1 = 1, f_2 = f_3 = 0$. These were all obtained as expected.

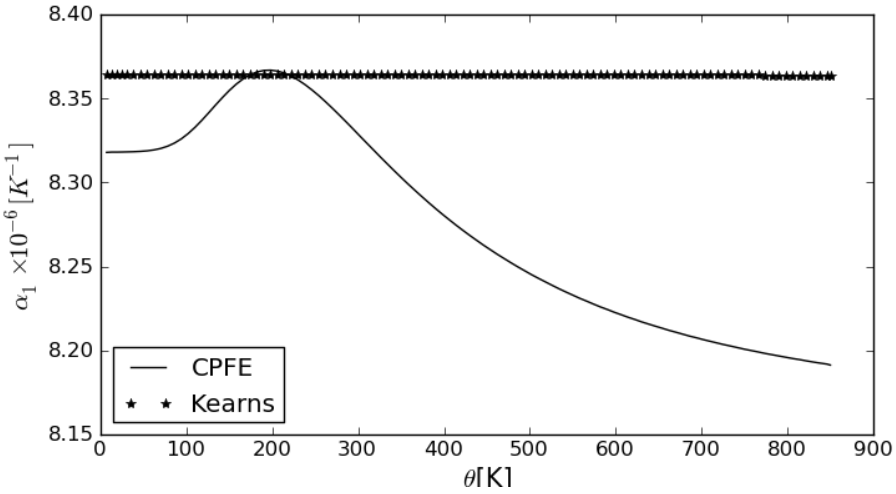
8.4 Systematic study of texture effects on expansivity

This section presents results from the CPFE simulation of polycrystals subjected to thermal loading for the different initial textures (Figure 8.3) as described in Section 8.3. Results are presented for comparisons between the thermal expansivity obtained from the rigorous polycrystal plasticity calculations given in equation 8.6 and those calculated from the empirical Kearns relationships given in equation 8.9. In all cases studied, the results for the case where the free faces of the model were constrained to remain flat were found to be essentially the same as those for which no constraints were applied. All the results relating to thermal expansivity below relate to the model whose faces are constrained to remain flat.

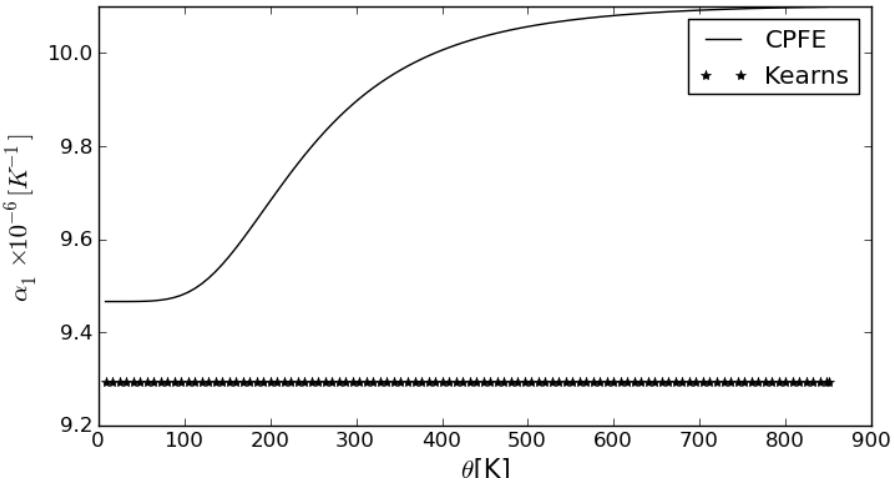
In the polycrystal if it were the case that the thermal expansivities were not anisotropic, the resulting strain and stress fields in the polycrystal would be homogeneous and uniform and the magnitudes of the stress zero. However, the anisotropic thermal expansivities lead to strain mismatch and a heterogeneous distribution of strain throughout the polycrystal. With sufficiently large temperature change, the thermal strain mis-match is big enough to cause the stress at some locations to exceed the yield stress, and hence the overall polycrystal behaves elasto-plastically. The anisotropy of the thermal expansivities is a consequence of the HCP crystal structure. This is important to remember in interpreting subsequent results.

Figure 8.4 shows comparisons of results of thermal expansivity from the two different methods, as described in Section 8.3, i.e. the rigorous CPFE method and the Kearns factor method, for three of the nine textures. In all cases it is observed that the rigorously calculated thermal expansivity is constant in the elastic regime but starts to vary as plasticity sets in. The expansivity predicted from the Kearns factors remains essentially constant through the plastic regime, which is not surprising since the thermally-induced elastic-plastic deformation leads to negligible texture change so that the Kearns numbers remain nearly constant.

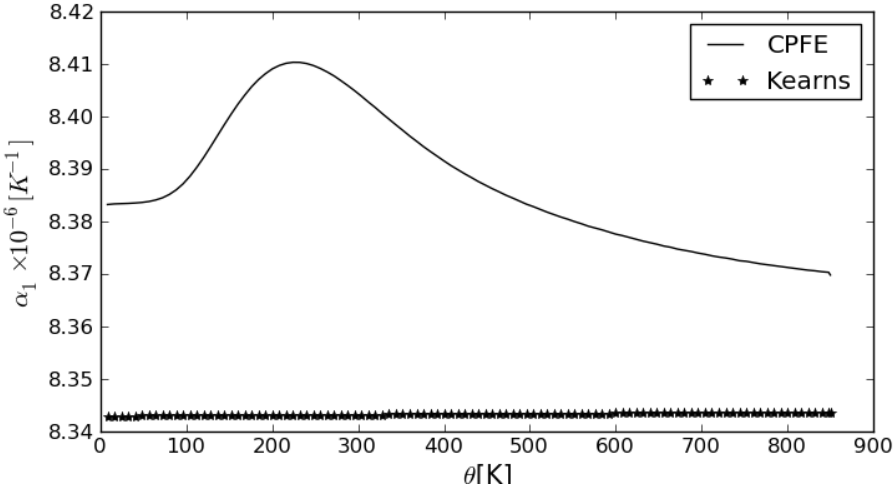
Figure 8.5 shows the percentage difference $\alpha_d = \left(\frac{\alpha^f}{\alpha^\epsilon} - 1\right) \times 100\%$ between the rigorously calculated thermal expansivity and that predicted from the Kearns texture factors for all the nine textures, and for the three orthogonal directions. It is clear that errors that result vary significantly with the initial textures, especially in the plastic regime. It is interesting to note that these errors can be larger than 15%. The labels on the legend of the figure match the labelling of the textures in Figure 8.3 so that each curve can be easily related to the texture from which it originates. It is observed that the errors in Figure 8.5(a), which shows errors in the estimation of α_1, exhibit a decreasing trend in keeping with the f_1 Kearns factors given in Figure 8.3. That is,



(a) fig 8.3(a), α_1

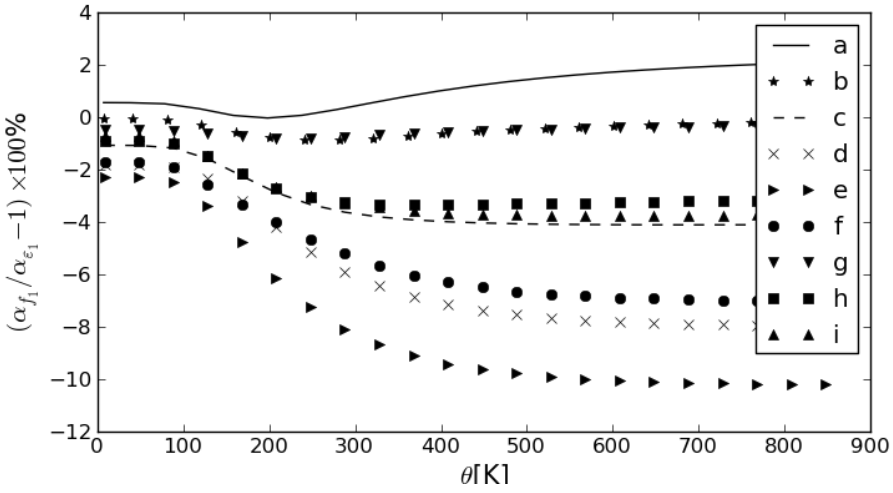


(b) fig 8.3(d), α_1

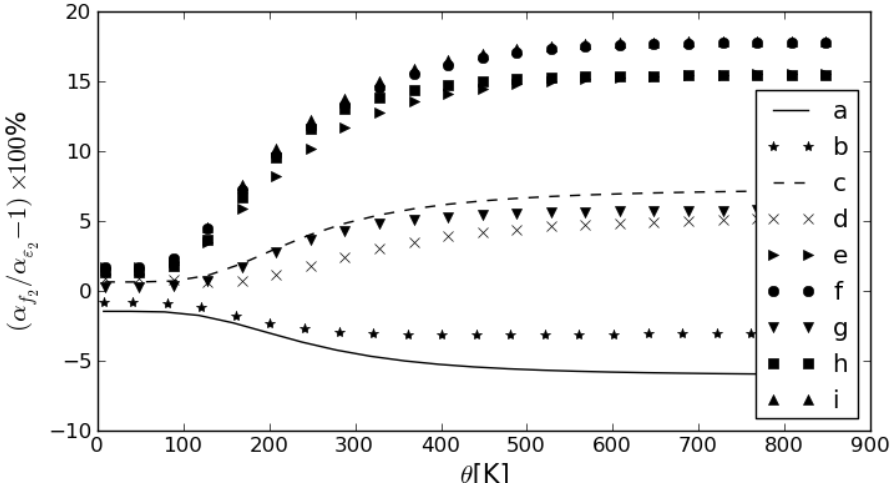


(c) fig 8.3(g), α_1

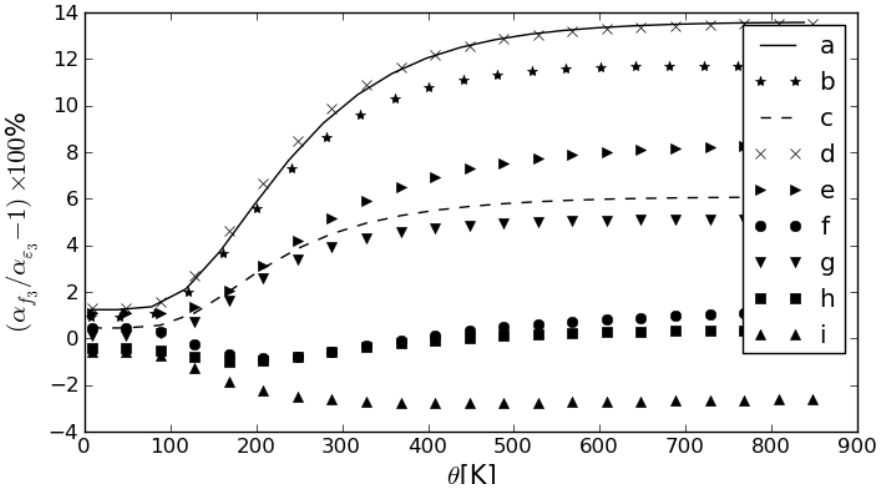
Figure 8.4: Rigorously calculated thermal expansivity (CPFE) versus temperature compared to that predicted from Kearns factors for the initial textures shown in Figures 8.3(a), 8.3(d) and 8.3(g). Only α_1 is shown for the three textures, i.e direction X.



(a) α_1



(b) α_2



(c) α_3

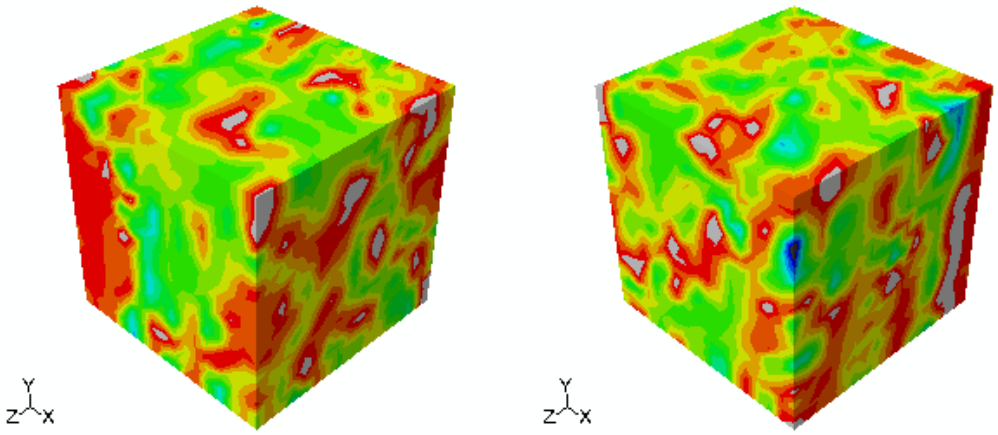
Figure 8.5: Percentage difference between rigorously calculated thermal expansivity and that predicted from Kearns factors, i.e. $\alpha_d = \left(\frac{\alpha^f}{\alpha^\epsilon} - 1\right) \times 100\%$, for all the nine textures in no particular order.

as f_1 increases, so does α_d. The same is true between α_2 and f_2 (Figure 8.5(b)), and between α_3 and f_3 (Figure 8.5(c)). The random texture of Figure 8.3(g) has relatively low errors for all three thermal expansivities α_1, α_2, and α_3. Hence the more textured the sample is, the greater the errors from the Kearns factor method.

Aside from variation of thermal expansivity with initial texture, it is observed, from both Figures 8.4 and 8.5, that the rigorously calculated thermal expansivity in the plastic region for any texture varies non-linearly and at times non-monotonically as the polycrystal is cooled before eventually attaining a nearly-steady value as the whole polycrystal becomes plastic. Bearing in mind that the resulting strains for the applied thermal loading are small (less than 1%) so that no noticeable texture evolution has occurred, it is evident that there is another factor other than overall crystallographic texture that the prediction based on Kearns factors fails to capture. This variation of expansivity is probably a result of initially localised shape changes as crystallites in different parts of the polycrystal transition from elastic to plastic deformation. These local changes lead to an overall change in the dimensions of the polycrystal (with the greatest effect in the direction of the highest Kearns factors) but since they do not induce much texture change, they are not captured by the Kearns factor-based method. The plasticity locally develops as a result of the synergy between the HCP crystal structure and the crystallographic texture.

8.4.1 Investigating texture realisation effects

To investigate further the effect of orientation distribution realisations on the prediction of thermal expansivity we take the same initial texture (Figure 8.3(a)) and use it to study two different realisations (Figure 8.6). A texture realisation is said to be different from another if any grain's neighbours have different crystallographic orientation (and/or size and shape) than in a reference set-up for the same initial overall



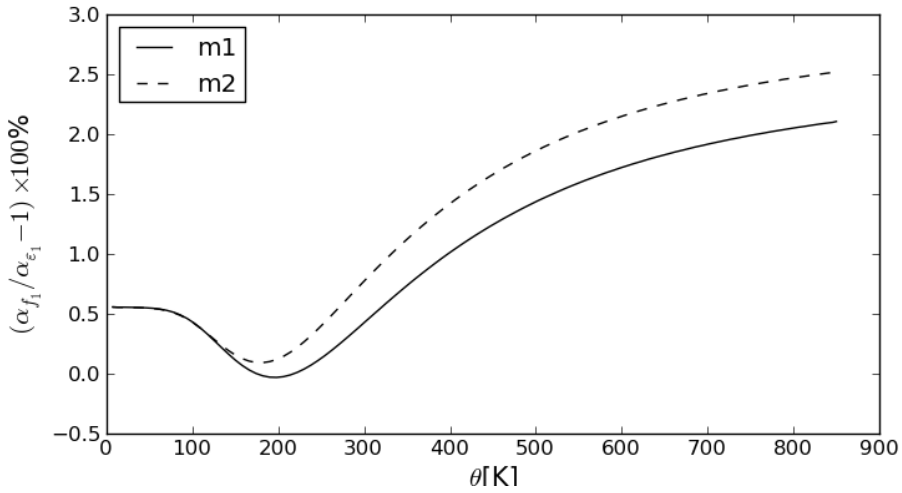
(a) m1 (b) m2

Figure 8.6: Two different orientation distribution realisations for the same texture shown in Figure 8.3(a). The fields show the q_2 quaternion component, limited to $-1 \leq q_2 \leq 1$, in both cases giving an idea of the distribution of crystallographic orientation.

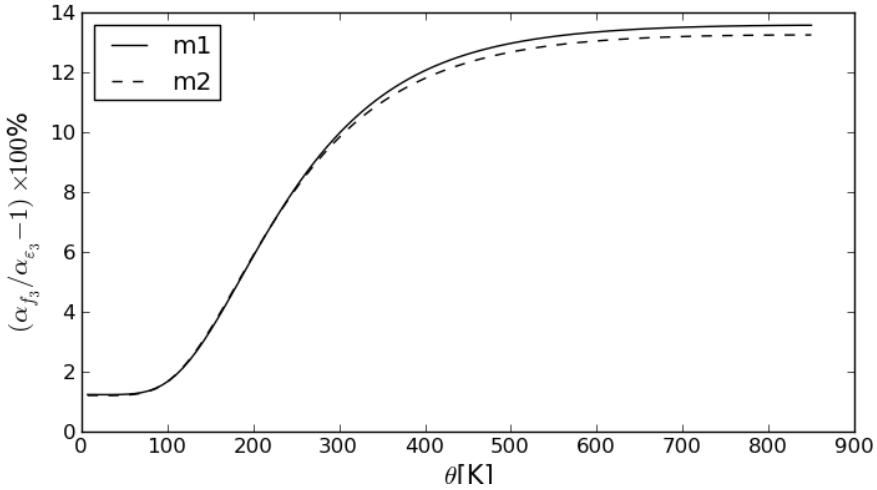
texture - where a grain is simply defined as a region of uniform crystallographic orientation. Hence the texture realisation effect is due to the resulting misorientation (i.e. relative crystallographic orientation of adjacent crystallites). The fields in Figure 8.6 show the q_2 quaternion component giving an idea of the distribution of crystallographic orientations for the two texture realisations.

Figure 8.7 shows the percentage difference α_d between the rigorously calculated thermal expansivity and that predicted from the Kearns texture factors for the two realisations in Figure 8.6. Note that m1 in Figure 8.7 shows the same information as texture a in Figure 8.5. For this texture, which is an extreme case according to Figure 8.5, it was observed that texture realisation differences alone contributed only about 0.5% error.

Although the models used in the above results are large enough potentially to accommodate 4096 unique orientations, they are still relatively small by comparison to industrial component sizes. At larger length scales where continuum assumptions apply, it can be expected that texture realisation effects would completely disappear as the component's shortest dimension gets significantly larger than the average grain



(a) α_1



(b) α_3

Figure 8.7: Percentage difference between rigorously calculated thermal expansivity and that predicted from Kearns factors, i.e. $\alpha_d = \left(\frac{\alpha^f}{\alpha^\epsilon} - 1\right) \times 100\%$, for the two orientation distribution realisations (Figure 8.6) of the same texture in Figure 8.3(a).

size. Note that length scale effects such as the evolution of geometrically necessary dislocations [28] have not been included in this study. Crystallographic mis-orientation between crystallites can be particularly pronounced in metals with an HCP crystal structure. This may arise as a result of twinning being a potentially significant deformation mechanism during manufacture, where crystal rotations near to 90° may be common, causing a high degree of mis-orientation between twinned and untwined grains of similar starting orientation. In addition, the transformation of alpha to beta phase and subsequent dual phase field hot working common for many titanium alloys

produces macro-zones that commonly exhibit mis-orientation that is variable, dependent on processing route but that can reach extreme levels [71]. In these circumstances it is therefore likely that morphological effects will become significant since macro-zone size is often of a significant length scale compared to component size.

8.5 Texture effects on mechanical properties

The polycrystals were also subjected to mechanical loading to study the effect of the initial texture on the polycrystal's mechanical properties: Young's modulus, E; Poisson's ratio, ν; and yield stress, σ_y. The Young's modulus and Poisson's ratios were calculated as

$$E_{22} = \frac{d\sigma_{yy}}{d\varepsilon_{yy}}, \quad \nu_{21} = -\frac{d\varepsilon_{xx}}{d\varepsilon_{yy}}, \quad \nu_{23} = -\frac{d\varepsilon_{zz}}{d\varepsilon_{yy}} \tag{8.10}$$

where σ and ε are stress and strain respectively. Figure 8.8 shows the overall polycrystal stress-strain response obtained for the different initial textures given in Figure 8.3 when the polycrystals were subjected to compression in the y-direction, which corresponds to the Y-direction on the pole figures. It is clear from the Figure 8.8 that the different initial textures lead to different polycrystal elastic modulii and yield stress: the yield stress is difficult to determine because it is not sharply defined - a consequence of progressive yield through the polycrystal. It is taken to be the stress at the the last data point shown in Figure 8.8 (at 0.4% strain) at which point all material is expected to have yielded so that the stress has stabilised. The labelling for the legend has been arranged according to the magnitude of the stress. a2 in Figure 8.8 refers to a different model than that used for the cases a to i. It refers to a $40 \times 40 \times 40\mu m$ model that is capable of accommodating 64000 unique orientations whose initial texture is similar to that given in Figure 8.3(a) and whose Kearns factors were $f_1 = 0.294$, $f_2 = 0.056$ and

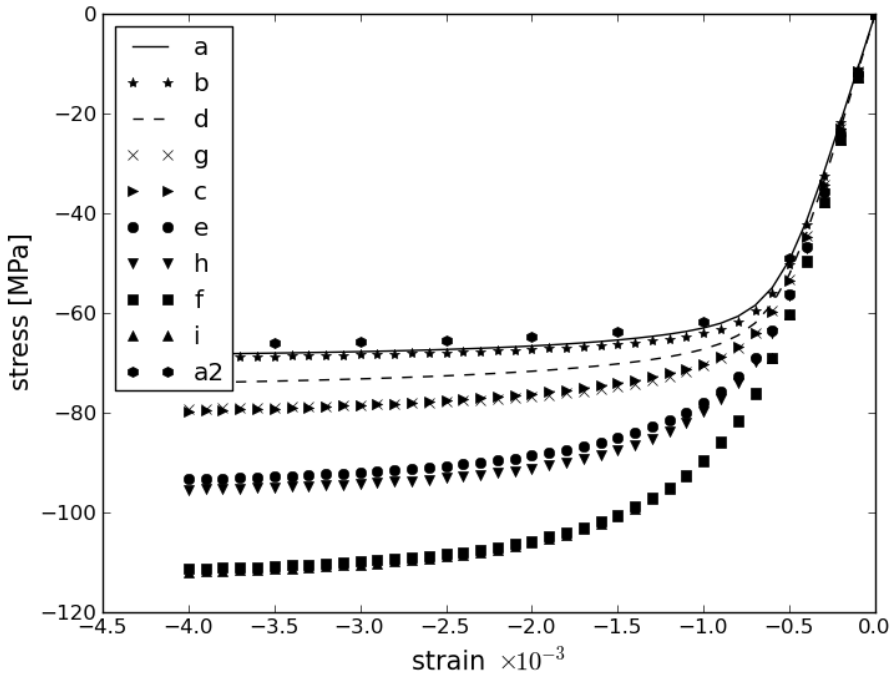
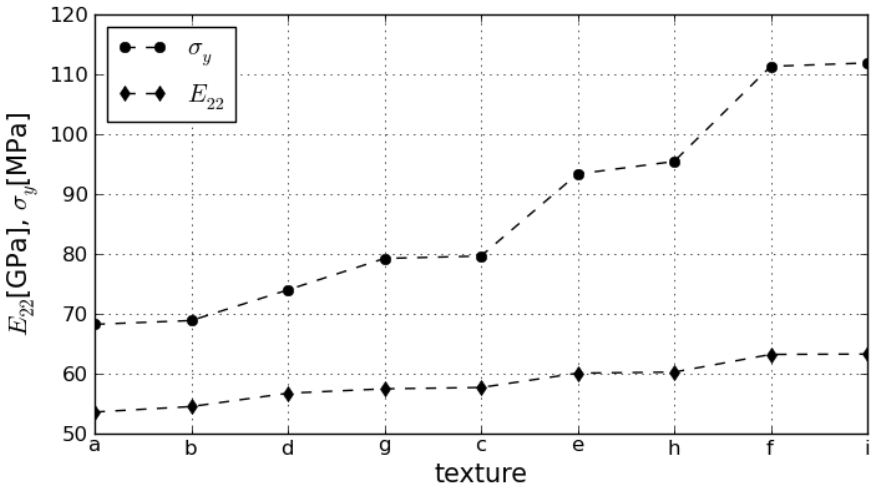


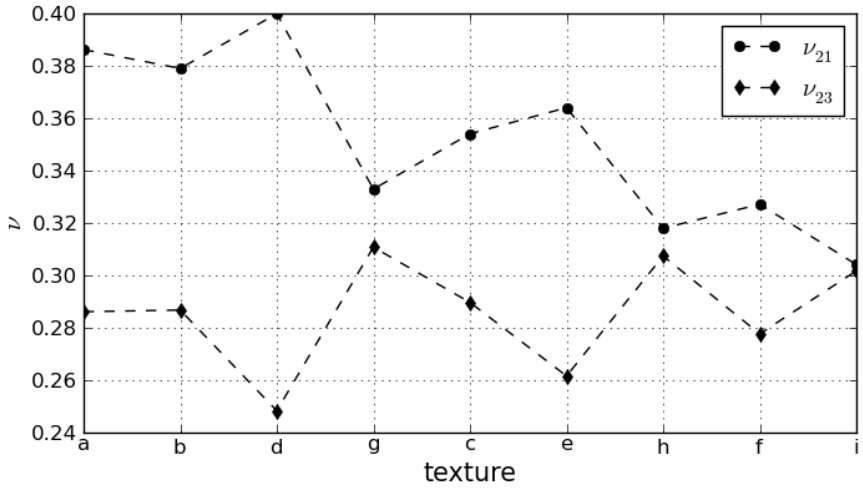
Figure 8.8: Stress-strain response to yy-compression for the different initial textures in Figure 8.3. The labelling for the legend has been arranged according to the magnitude of the stress. The labels a, b, c, etc. correspond to the labelling of the textures in Figure 8.3. a2 refers to a much larger model with the same initial texture as a.

$f_3 = 0.650$, which are the experimentally determined Kearns factors for that texture. This much larger model was set up in order to ascertain whether the models used in the rest of the cases were sufficient to define representative volume elements (RVEs). The comparison of the stresses for a and a2 in Figure 8.8 shows that a is of sufficient size for an RVE. Since RVEs a to i are the same size, the comparison between a and a2 suggests that the rest of the models are indeed appropriate RVEs.

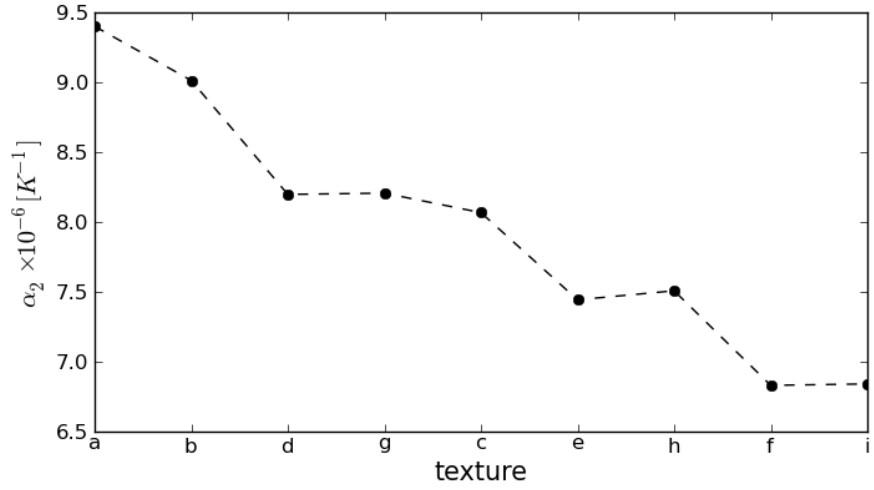
Figure 8.9 shows the predicted polycrystal mechanical properties as well as thermal expansivity in the elastic region for the different textures. The predicted polycrystal yield stress and Young's modulus also follow the trend of the f_2 Kearns factors in Figure 8.3. This is because for HCP materials slip is more difficult in the c-direction due to the much higher CRSS than in the a-direction as indicated by the properties given in Section 8.3. Hence the initial textures with a higher component of c-axes in the loading direction (and hence larger Kearns factors in the same direction) carry more



(a) E, σ_y



(b) ν_{21}, ν_{23}



(c) α_2

Figure 8.9: Predicted polycrystal mechanical properties: (a) Young's modulus E_{22} (GPa) and yield stress σ_y (MPa), (b) Poisson's ratios ν_{21}, ν_{23}. (c) shows the predicted polycrystal thermal expansivities α_2 for elastic deformation. Results are plotted against texture, with the labels a, b, c, etc. on the horizontal axis corresponding to the labelling of the textures in Figure 8.3, arranged according to the f_2 Kearns factors.

stress in that direction. The predicted Poisson's ratios do not appear to follow Kearns factors the same way. They are however consistent with the crystallography implied by the textures. For example, the two Poisson's ratio for texture Figure 8.3(i) are almost equal, which is consistent with implied overall crystallography for that texture that is similar to loading an HCP single crystal along the c-axis such that both Poisson's ratios refer to effects of a-direction strain relative to the c-direction, according to the Poisson's ratio-strain relations of equation 8.10. By contrast, texture Figure 8.3(a) has overall crystallography similar to loading a single crystal along an a-direction so that one of the Poisson's ratios (the lower one) relates strain in the c-direction to the a-direction (ν_{23}) while the other relates strain in the a-direction to another a-direction. The thermal expansivities follow the reverse trend to the Kearns factors. This is also appropriate given that single crystal thermal expansivity is smaller in the c-direction so that as f, and hence c-axes volume fraction, increases in a given direction the polycrystal thermal expansivity should decrease in the same direction.

8.6 Conclusions

Crystal elasticity and plasticity calculations for an HCP polycrystal have demonstrated that texture plays an important role in determining average polycrystal mechanical and thermal physical properties as a result of the anisotropy in these properties at the single crystal level in HCP materials. It has also been shown that with sufficiently large, but technologically relevant temperature changes, the thermal strains developed can be sufficiently large to generate localized plasticity. As a result, thermal expansivity then becomes dependent on the level of straining (or equivalently, temperature change) with maximum changes of about 10% from what would be determined from purely elastic deformation.

Nine textured polycrystals, subjected to thermal loading, have been analysed and

the average thermal expansivities for each polycrystal determined using both the rigorous crystal elasticity-plasticity method and the empirical, averaging approach previously reported in the literature using Kearns factors. It has been shown that expansivities determined using the latter technique can be in error by up to 15%; this results from the failure of this technique to impose properly the requirements of equilibrium and compatibility which are rigorously applied in the crystal elasticity-plasticity model. The magnitude of the error is potentially of technological importance since the Kearns approach is currently used in the nuclear industry.

The nine textured polycrystals have also been subjected to mechanical loading and analysed to study the the effect of crystallographic texture on their average mechanical properties: Young's modulus, Poisson's ratio and yield stress. The results have demonstrated that texture indeed has a significant role in determining the average mechanical properties of a polycrystal, with the average properties having a strong correlation with the density of c-axes oriented in the loading direction for the HCP Zirconium alloys studied.

Chapter 9

Two-phase texture evolution

9.1 Executive summary

Previous chapters have addressed the modelling of texture evolution for single phase material systems. However most engineering alloys are dual-phase in nature. This chapter extends the methods in the previous chapters to dual-phase material systems and investigates the effect of the second phase on the texture evolution and stress-strain response of the first. It has been found that the second phase (bcc) does not have a significant constraining effect on the texture development of the main (hcp) phase, but that it serves to moderate the average stress-stress response of the polycrystal. It appears that this average response may be obtained via a simple linear mixing of the single phase responses of the constituent phases based on their volume fractions.

9.2 Introduction

Much work has been done on single-phase modelling in the literature but very little exists for dual-phase texture. However most engineering alloys in industrial applications are multi-phase in nature, i.e. contain a mixture of materials which generally have more than one crystal type, e.g Zr-2.5Nb for which Zr is mainly hcp while Nb is bcc. In fact in some cases the same material may exist in multiple phases as a result of phase transformations, e.g. as well as hcp, Zr can exist as a metastable bcc phase which can transform to Nb during autoclaving [15].

Chapters 6, 7 and 8 addressed texture evolution modelling for a single phase (hcp Zr) material. The present chapter extends this to a two-phase material system. The experimental data used in this chapter was obtained from Rolls-Royce plc for the two-

phase alloy of Zr-4 with 2.5wt%Nb. This chapter investigates the effect of the second phase (bcc) on the texture evolution and stress-strain response of the main hcp phase.

9.3 Dual phase material model

The relevant slip systems for the bcc crystal type are given in appendix B. Only the first twenty four of these are used. It is generally noted in the literature that the included {110} and {112} families of slip planes are the most important, and it may also be deduced that they are sufficient to describe any possible strain state that a bcc single crystal may experience since a set of five independent slip systems [48] can be obtained from them; where any two slip systems are defined as independent iff they produce different pure strains, and five such systems are needed because there are a maximum of five independent terms in the pure strain tensor, which in rate form is essentially the symmetric part of the plastic velocity gradient $\boldsymbol{L}^p$. The power law form of the slip rule is used as described in Section 6.6 and the properties applicable to the hcp phase are those specified in Table 6.2. The extra properties relevant to the bcc phase are summarised in Table 9.1, where b is set according to standard bcc crystallography and τ_{c0}, in the absence of experiementally measured single crystal bcc material properties, defines the bcc phase to have a much lower critical resolved shear stress compared to the hcp phase.

Table 9.1: Bcc material properties

Slip Rule		
τ_{c_0} (MPa)	ψ	$b(\mu\text{m})$
10.2	$1.6e-3$	$2.48e-4$
Elastic Moduli		
E (GPa)	ν	G (GPa)
70.0	0.3	26.9

9.4 Experimental data

This section presents the data from experimental measurements used as initial texture for the simulation results in this chapter. As before, the pole figure software developed in this project was also used to plot the figures in order to see if the received pole figures could be reproduced. This exercise is useful (and worth doing every time) because it makes it possible to know if there are mismatches in the definition of reference axes used between the experimental measurements and Abaqus reference coordinate system. The difference if not detected and accounted for could result in effectively working with different initial textures without realising it hence not comparing like with like.

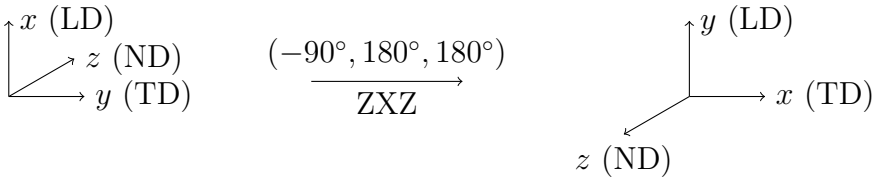


Figure 9.1: Reference axes: Rolls-Royce experimental Euler angle measurements (left) and the Abaqus reference system in which simulations are performed (right). The angles $(90°, 180°, 180°)$ are needed to map the reference systems to each other.

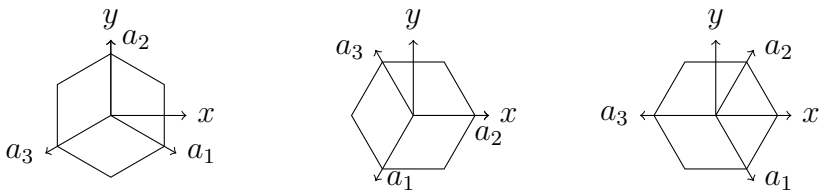
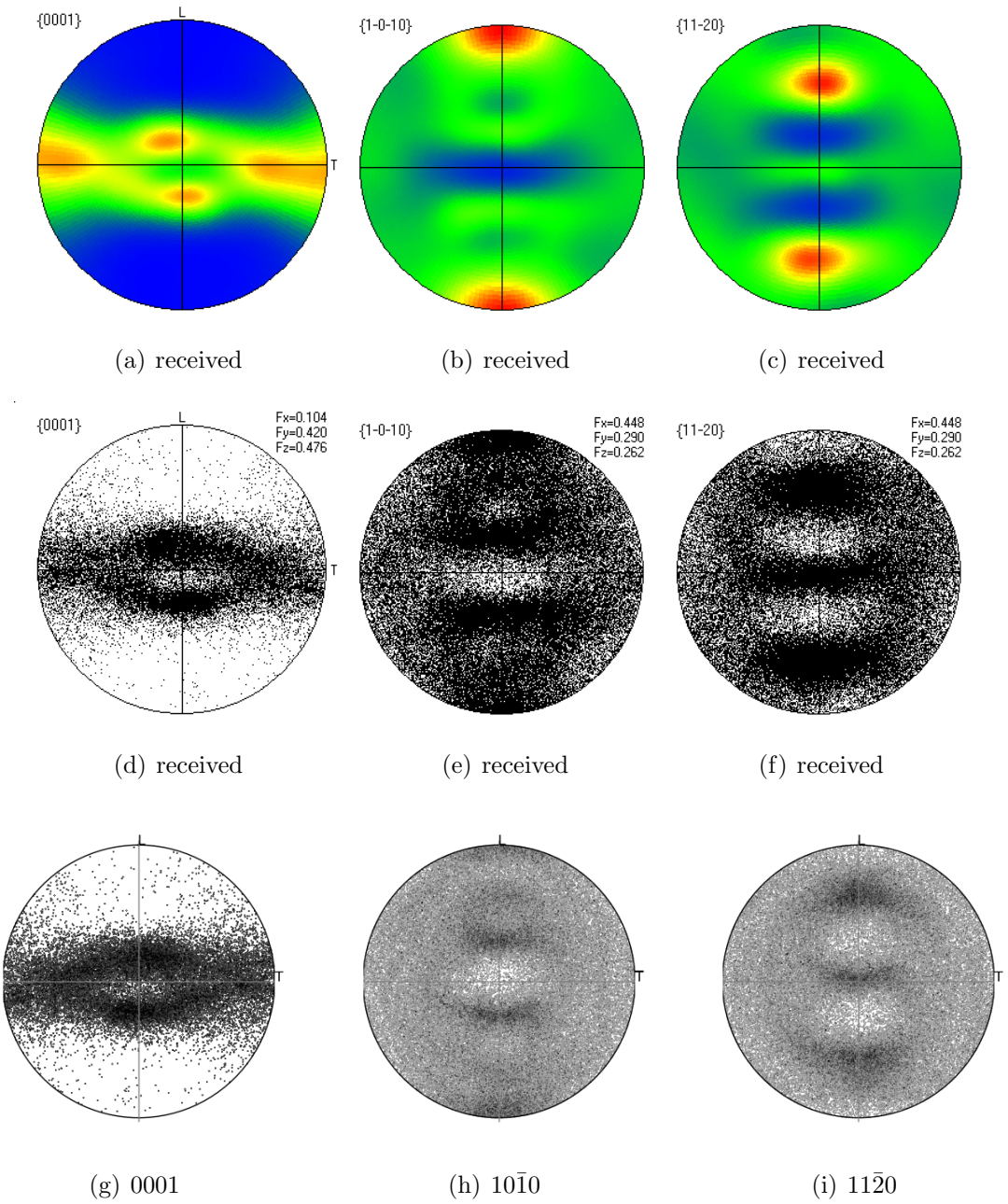


Figure 9.2: Crystal natural coordinates in reference system. The leftmost system is required to faithfully represent received pole figures. The other alternative configurations are given for completeness and comparison.

Figure 9.1 shows the reference axes used in the experimental measurements and the Abaqus reference system; as well as the Bunge Euler angles needed to map the two systems to each. This basically means that these angles $(-90°, 180°, 180°)$ must be added to all the experimentally measured Euler angles for them to be compatible



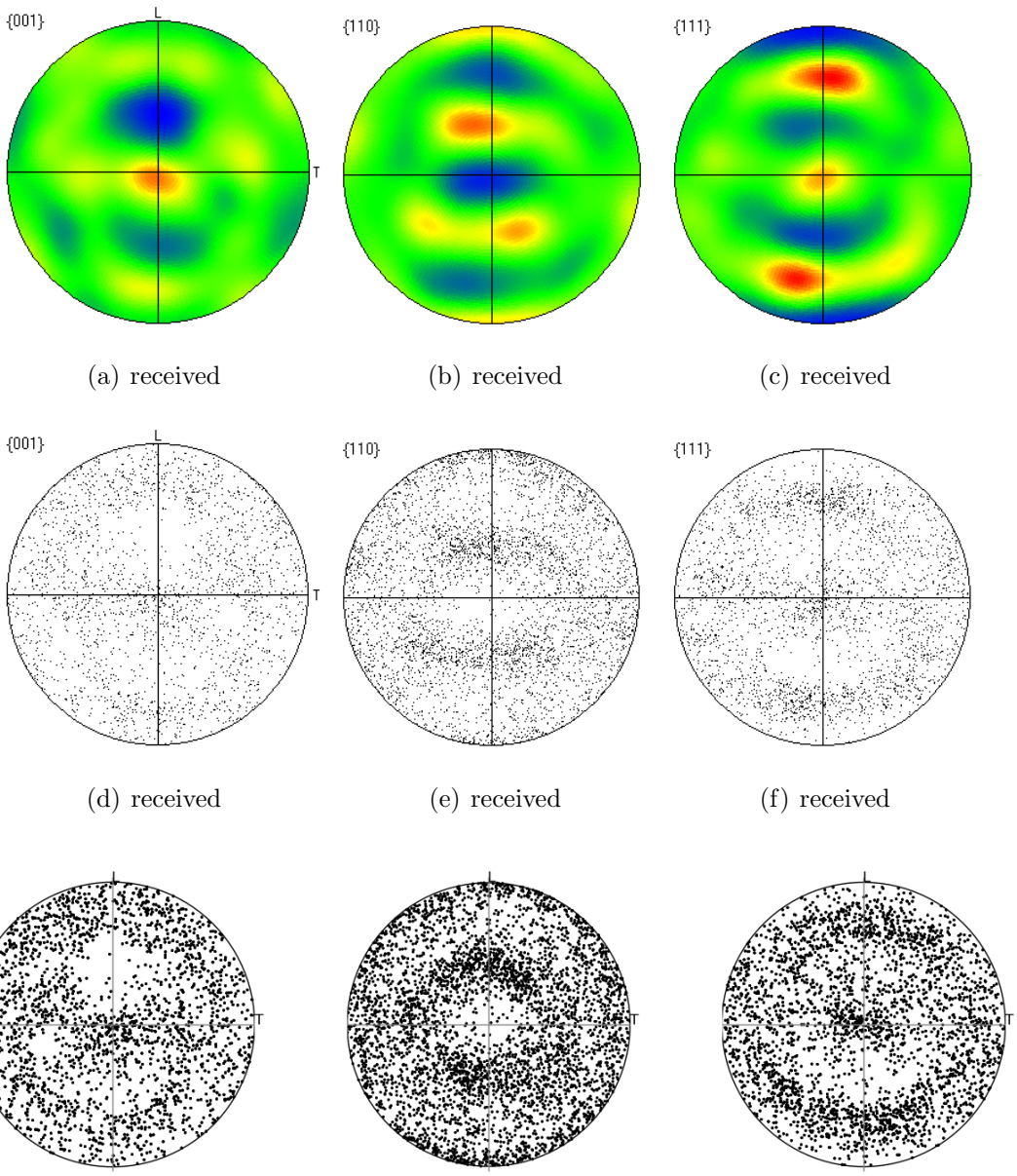
(a) received (b) received (c) received

(d) received (e) received (f) received

(g) 0001 (h) $10\bar{1}0$ (i) $11\bar{2}0$

Figure 9.3: Hcp received and calculated pole figures. The (received and calculated) basal Kearns factors are $0.420, 0.104, 0.476$.

with the Abaqus reference system in which the simulations are performed. The angles $(90°, 180°, 180°)$ would give the same final position of the axes but the difference in path in Euler space that they define would cause the resulting pole figures to be plotted such that the lower and upper hemispheres are swapped. Additionally Figure 9.2 shows the different axes in the crystal's reference system (relative to the crystal's natural axes (a_1, a_2, a_3), of the three axes systems as detailed in Chapter 3, that need to be used in order to represent the received Rolls-Royce data faithfully. Using the wrong set of



(a) received (b) received (c) received

(d) received (e) received (f) received

(g) 001 (h) 110 (i) 111

Figure 9.4: Bcc received and calculated pole figures

axes causes the two non-basal (hcp) pole figures to be swapped. Figures 9.3 and 9.4 show the received and calculated hcp and bcc pole figures respectively.

9.5 Two-phase texture homogenisation

Texture homogenisation in the case of two-phase texture data files is carried out in a similar way to that described in Chapter 6. First the orientation data is separated into two datasets according to the constituent phases. Each dataset is then operated

on separately to obtain its set of unique orientations and their corresponding volume fractions relative to the phase's dataset. These are then sieved through according to the volume fraction of each orientation as previously described. The overall volume fraction of each phase determines the total number of orientations that are allowed for that phase. This can be determined directly from the measured data; or in cases where we want to represent the same texture but different phase volume fractions than the measured ones, it can be separately defined. For the present study, the desired volume fraction (as communicated by Rolls-Royce) is around 30% bcc to run at 800°; this is used in what follows unless otherwise stated. The original data have a bcc volume fraction of 2.4%. These data actually represent post rolling texture, indexed by EBSD at room temperature, but for the present study they will suffice to use as the initial texture instead of generating some other random textures. It has already been shown (see Chapter 6) that for very large strain, the final texture is generally independent of the initial texture.

After the homogenisation process, it is necessary to combine the datasets for the two-phases for assigning to the FE model. For this, a list of elements (which may belong to several separate element sets) must be provided for one of the phases - bcc in this case. The length of this list (i.e. the number of elements) must be consistent with the desired volume fraction for the specified phase. This element list forms the basis for mixing the phases, i.e. defining how the specified phase is spread out through the other, for example the next section examines two cases: (i) where the bcc phase covers the core of the model - referred to as block phase assignment; and (ii) where bcc phase is uniformly spread out through the model - referred to as uniform phase assignment.

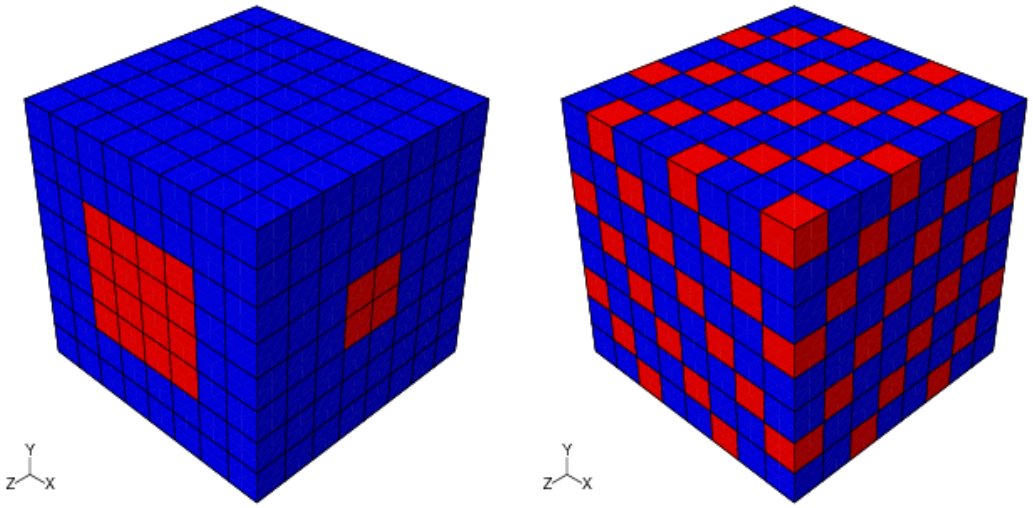
9.6 Two-phase (hcp+bcc) texture evolution

In considering dual-phase texture evolution, if the second phase is expected to have an effect on the texture evolution of the first and on the stress-strain response, then it can be expected that the order in which the phases are assigned, i.e. mixed together, is important. For any predefined volume fraction of the second phase, it is possible to either assign that phase as a block embedded in or surrounding the first, as uniformly dispersed through the first, or a variation between these two extremes. If the second phase had a significant constraining effect on the first, then the choice of the assignment from the above options may be expected to affect the overall result. In the present section we examine only the two extreme cases defined above: block and uniform phase assignment.

9.6.1 Block vs. uniform phase assignment

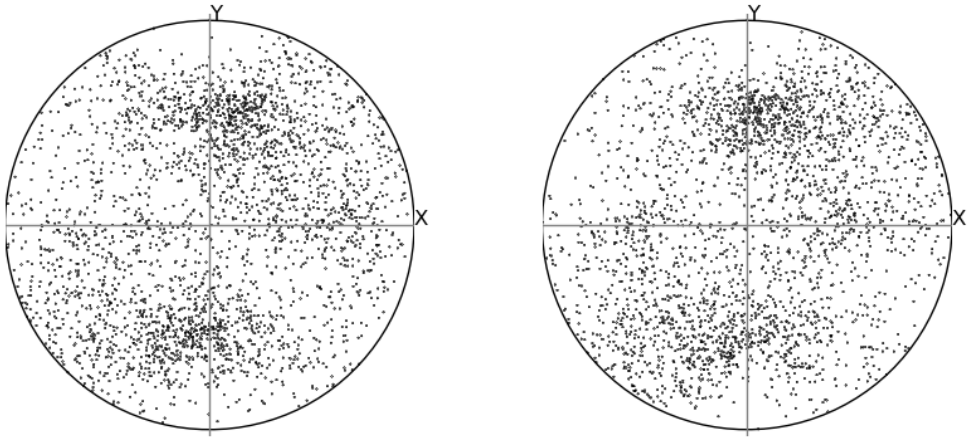
This section examines the effect of phase assignment on the predicted texture and the overall stress-strain response for a case where the bcc phase volume fraction is ∼30%. Figure 9.5 shows the field plots of bcc and hcp phase distribution. The bcc volume fractions for the block, Figure 9.5(a), and uniform, Figure 9.5(b), phase assigned cases are 28.1% and 29.1% respectively. These are both close enough to the desired 30%. In Figure 9.5(a) the bcc core is narrower parallel to the x-axis than parallel to the z-axis purely because it was preferred to keep the volume fraction as close as possible to the 30%. The models have 512 elements and the dimensions are $16 \times 16 \times 16\mu$m. The initial texture assigned to both cases is that given in Figures 9.3 and 9.4.

Figures 9.6 and 9.7 show the simulated final texture for the hcp and bcc phases respectively after compression to nominal strain of 65%. The figures show minor differences between the block and uniform phase assignment results suggesting that the nature of phase assignment does not (qualitatively) have a significant effect on the



(a) block (b) uniform

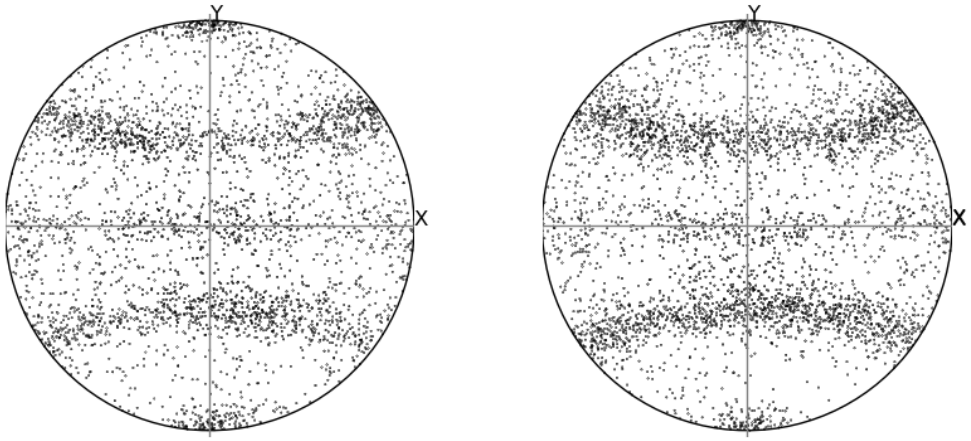
Figure 9.5: Field plots of bcc (red) and hcp (blue) phase distribution. The bcc volume fractions for the block and uniform cases are 28.1% and 29.1% respectively. These are both close enough to the desired 30%. The models have 512 elements and the dimensions are $16 \times 16 \times 16 \mu$m



(a) block (b) uniform

Figure 9.6: (0001) pole figures for the hcp phase showing the simulated final texture after compression of the two models in Figure 9.5 to nominal strain of 65%. The final Kearns factors, (f_1, f_2, f_3), for the block and uniform cases are (0.274, 0.359, 0.367) and (0.263, 0.355, 0.382) respectively. The initial texture for hcp is that shown in Figure 9.3

final texture. The final Kearns factors, (f_1, f_2, f_3), are (0.274, 0.359, 0.367) and (0.263, 0.355, 0.382) for the block and uniform cases respectively. These show a small (quantitative) difference in the final predicted texture but, as with the pole figures, this difference is not significant.



(a) block (b) uniform

Figure 9.7: (001) pole figures for the bcc phase showing the simulated final texture after compression of the two models in Figure 9.5 to nominal strain of 65%. The initial texture for bcc is that shown in Figure 9.4

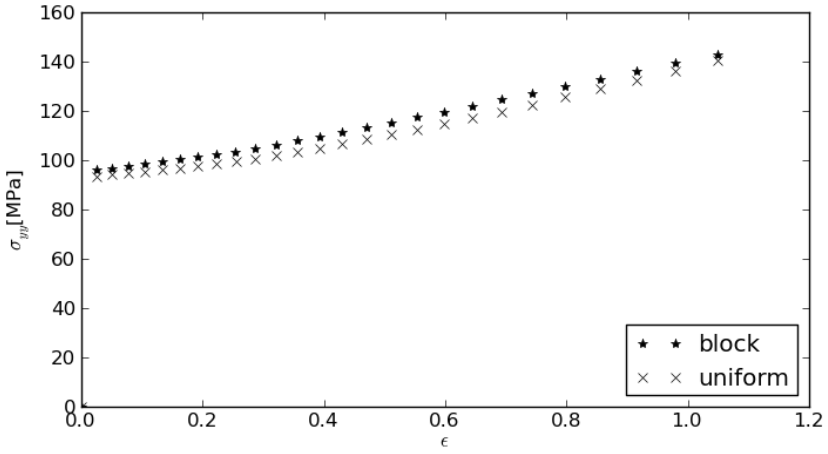
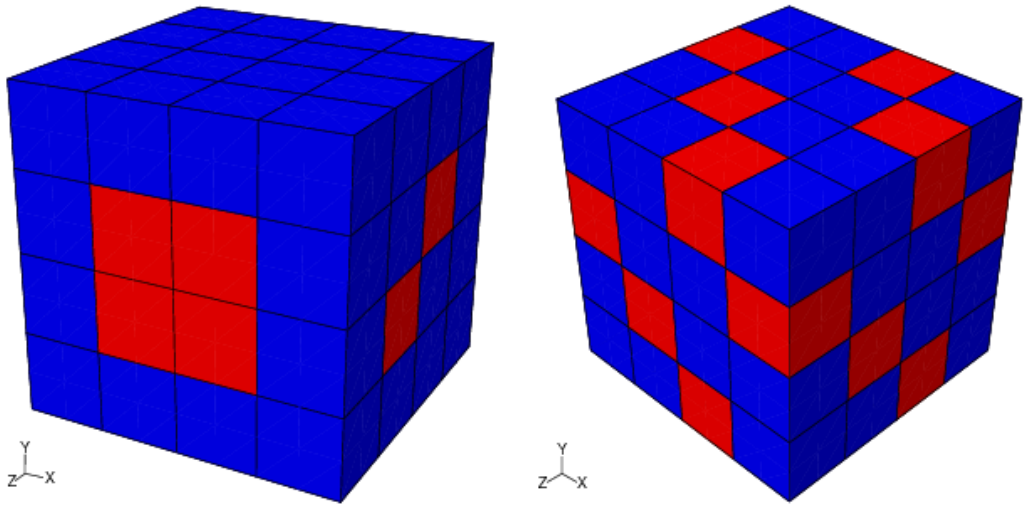


Figure 9.8: Stress-strain response of the two models in Figure 9.5 to nominal strain of 65%. Compression was carried out at a strain rate of $1.0s^{-1}$.

Figure 9.8 shows a comparison of the overall stress-strain response between block and uniform phase assignment. It is observed here that block phase assignment leads to a marginally higher stress response than the uniform case. This is also an insignificant difference and is consistent with the pole figures and Kearns factors. Moreover this marginal difference in overall stress can be accounted for by the marginal difference in the hcp volume fraction used for the two forms of phase assignment. It is concluded, therefore, that both block and uniform phase assignments are essentially equally good

since the results from both are not significantly different.

9.6.2 RVE size effect on texture evolution



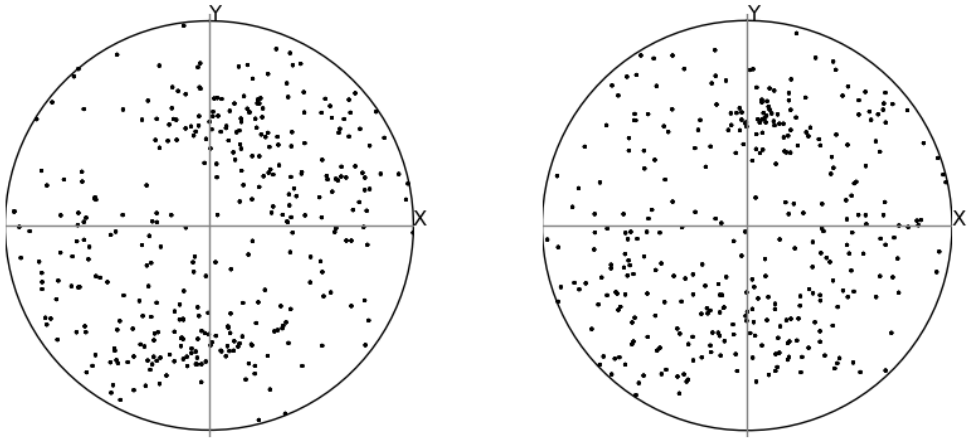
(a) block (b) uniform

Figure 9.9: Field plots of bcc (red) and hcp (blue) phase distribution. The bcc volume fractions for the block and uniform cases are 31.3% and 32.8% respectively. These are both close enough to the desired 30%. The models have 64 elements and the dimensions are $8 \times 8 \times 8\mu$m

This section explores the effect of the RVE size on the predicted texture evolution, for both the block and uniform phase-assigned models. The RVEs in Figure 9.9 are each made of 64 elements (i.e. RVE64) and are compared with those in Figure 9.5 which are each made of 512 (i.e. RVE512). In Chapter 6 it was demonstrated that RVE512 was a sufficient RVE to represent the stress profile (see for example Figure 6.18 under Section 6.6.3) for a single phase system. Together with Chapter 7, RVE64 was then shown to give reasonable texture predictions. However, its stress-strain predictions generally differed from those for RVE512. In the present section we compare texture predictions between RVE512 and RVE64 but for a dual-phase system.

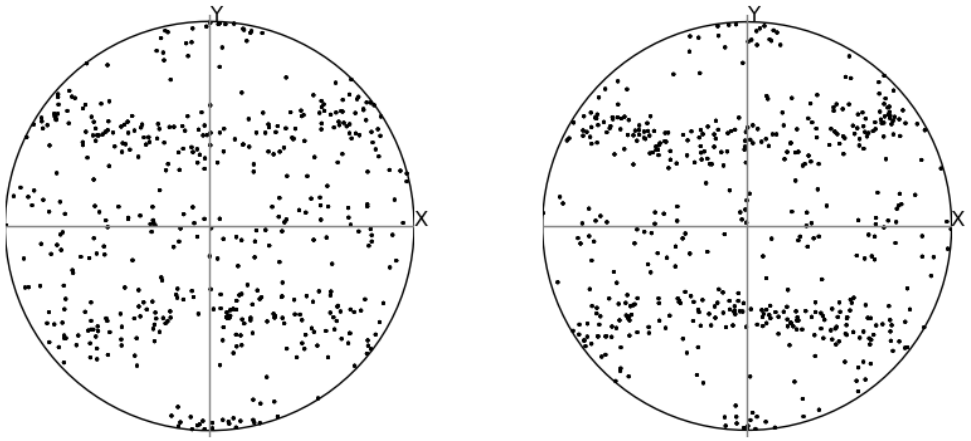
The reader is reminded at this point that RVE size here refers to the number of orientations represented (see Chapter 6 Section 6.6.3) and not mesh refinement. RVE64 and RVE512 can represent up to $(64 \times 8 =)$ 512 and $(512 \times 8 =)$ 4096 individual

orientations respectively. Compared to RVE64, RVE512 merely increases the model volume to accommodate more orientations without changing the discretisation density, i.e. number of finite elements per unit volume.



(a) block (b) uniform

Figure 9.10: (0001) pole figures for the hcp phase showing the simulated final texture after compression of the two models in Figure 9.9 to nominal strain of 65%. The final Kearns factors, (f_1, f_2, f_3), for the block and uniform cases are (0.280, 0.354, 0.366) and (0.289, 0.346, 0.366) respectively.



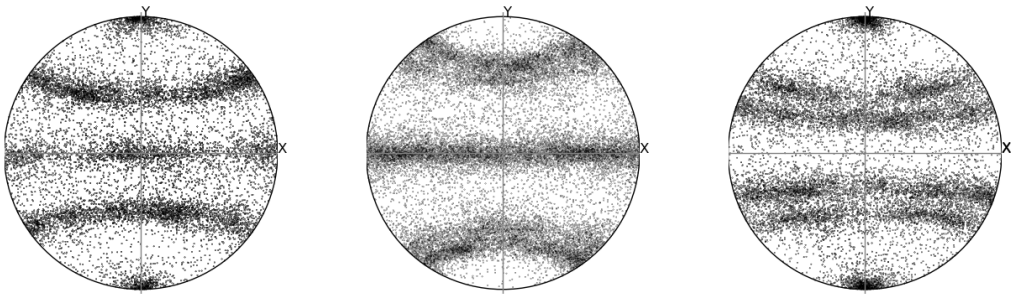
(a) block (b) uniform

Figure 9.11: (001) pole figures for the bcc phase showing the simulated final texture after compression of the two models in Figure 9.9 to nominal strain of 65%.

Figures 9.10 and 9.11 show the final texture for the hcp and bcc phases respectively after compression to nominal strain of 65% with RVE64. Ignoring the differences

in the number of plotted points in the figures, which are a result of the differing number of orientations accounted for, Figures 9.10 and 9.11 show very similar results to Figures 9.6 and 9.7 respectively. In other words the RVE64 models still capture the overall features of the final pole figures satisfactorily. The final Kearns factors, (f_1, f_2, f_3), for the block and uniform cases are (0.280, 0.354, 0.366) and (0.289, 0.346, 0.366) respectively for RVE64. Those for RVE512 were (0.274, 0.359, 0.367) and (0.263, 0.355, 0.382) respectively. There are some differences between the RVE64 and RVE512 results; and as already noted for RVE512, there are also some differences between block and uniform phase assignment for RVE64. Overall, it is clear that RVE64 gives sufficiently indicative texture results for design purposes.

9.7 Bcc single phase texture evolution



(a) 001 (b) 110 (c) 111

Figure 9.12: Final texture for a single phase bcc case with RVE512 after compression to a nominal strain of 65% (i.e. 105% true strain), where the initial texture is that given in Figure 9.4.

Before we can fully understand the constraining effect that the bcc phase imposes on the hcp phase in a dual-phase system and make fuller sense of the dual-phase results already presented in the cases studied above it is instructive to first examine the bcc phase on its own. Previous chapters (6, 7, and 8) have already examined the single phase hcp behaviour.

Figure 9.12 shows the final texture for a single phase bcc model with RVE512 after

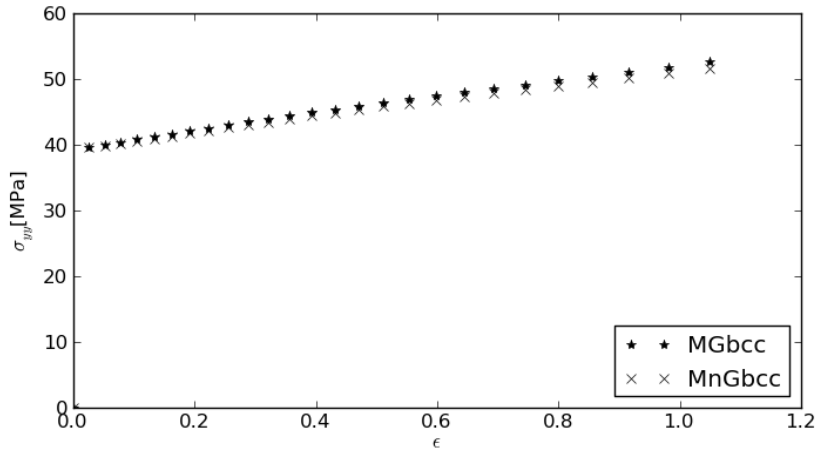


Figure 9.13: Stress-strain response of a single phase bcc case after compression to a nominal strain of 65% (i.e. 105% true strain), where the initial texture is that given in Figure 9.4. Comparison is made between the response with GND-Taylor hardening (MGbcc) and without it (MnGbcc). In the legend 'M' indicates that RVE512 was used, 'nG' indicates the absence of GND hardening while 'G' indicates its presence, 'bcc' indicates the phase under consideration.

compression to a nominal strain of 65% (i.e. 105% true strain). The initial texture is that given in Figure 9.4 with the correspondence between the initial and final textures in Figures 9.4 and 9.12 as follows: (g)-(a), (h)-(b), and (i)-(c) respectively.

Figure 9.13 shows the stress-strain response that corresponds to the texture evolution resulting in Figure 9.12. This stress-strain response shows hardening behaviour. In order to understand the source of this apparent hardening the simulation was performed with GND-Taylor hardening (MGbcc in the legend) and without it (MnGbcc), where the GND-Taylor hardening was implemented as described in equation 6.26 of Chapter 6 Section 6.6.3, with the relevant parameters described in Table 9.1. The final textures for both cases (with and without Taylor hardening) were identical and they are as shown in Figure 9.12. The stress-strain profile also shows that the impact of Taylor hardening is negligible. The apparent hardening observed may therefore be explained in terms of the bcc crystallography as was done for the hcp crystallography in Chapters 6, 7, and 8. The relevant slip systems for bcc crystallography are given in appendix B.1. Only the {110} and {112} families of slip planes have been included in

the bcc slip model implemented in the present code.

9.8 The effect of the second phase

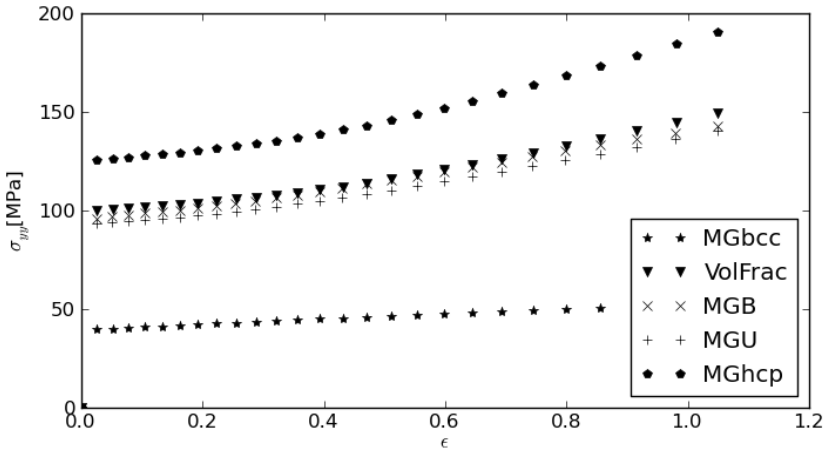


Figure 9.14: Stress-strain response of dual-phase models alongside the single phase models model for the same initial textures given in Figures 9.3 and 9.4. In the legend 'M' indicates that RVE512 was used, 'G' indicates the presence of GND hardening, 'bcc' and 'hcp' indicate the phase under consideration, 'B' and 'U' refer to block and uniform phase assignment respectively for the dual-phase models. 'VolFrac' is data obtained by linearly combining the stress responses of the two pure phases.

Figure 9.14 shows the stress-strain response of dual-phase models alongside single phase models for the same initial textures. RVE512 was used in all the simulations in the figure and Taylor hardening was included as indicated in the figure's legend. The initial textures for the four models represented in the figure are as follows: (i) MGhcp - hcp single phase texture Figure 9.3 (g-i), (ii) MGbcc - bcc single phase texture of Figure 9.4 (g-i), (iii) MGB - block phase-assigned dual-phase texture combining the textures of Figures 9.3 and 9.4 as described for Figure 9.5(a), and (iv) MGU - same as (iii) except for uniform phase assignment as described for Figure 9.5(b).

As expected, MGbcc provides a lower bound while MGhcp provides an upper bound for the stress-strain response. Note that the MGbcc plot is exactly the same in this figure and in Figure 9.13, suggesting that the bcc-crystal geometry hardening effect discussed in the previous section is almost insignificant when compared to the hcp-

crystal geometry hardening effect.

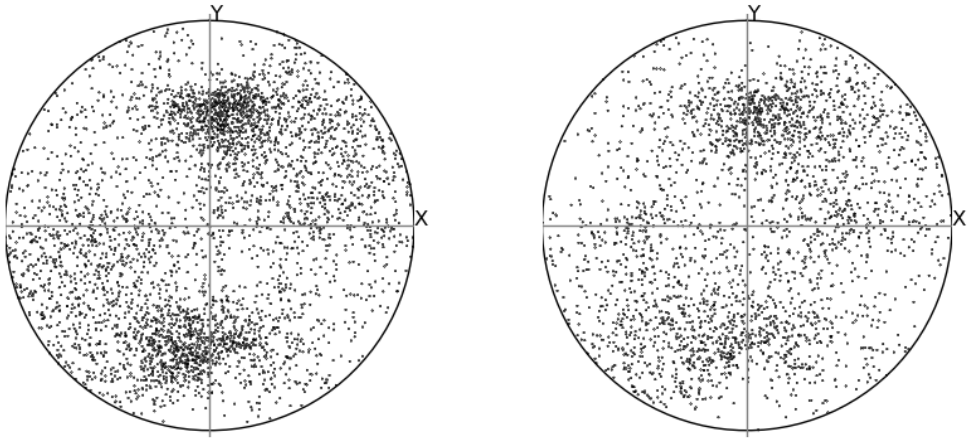
The MGB and MGU dual-phase stress-strain profiles are also not surprising: they lie between the single phases' profiles. A visual inspection of Figure 9.14 suggests that the MGB/U profiles are at about a third of the way between the MGhcp and MGbcc responses, from the former, which is consistent with the ∼30% bcc volume fraction and suggests that *a linear mixing rule* may apply to the stress-strain response for these two phases.

The VolFrac data in Figure 9.14 shows the result of implementing the suspicion of a linear mixing rule as suggested in the previous paragraph. This data, $\sigma_{volfrac}$, was obtained by linearly combining the single phase hcp stress, σ_{hcp}, (labelled MGhcp) and the single phase bcc stress, σ_{bcc}, (labelled MGbcc) according to equation 9.1, which assumes that bcc volume fraction is 30%.

$$\sigma_{volfrac} = 0.3\sigma_{bcc} + 0.7\sigma_{hcp} \tag{9.1}$$

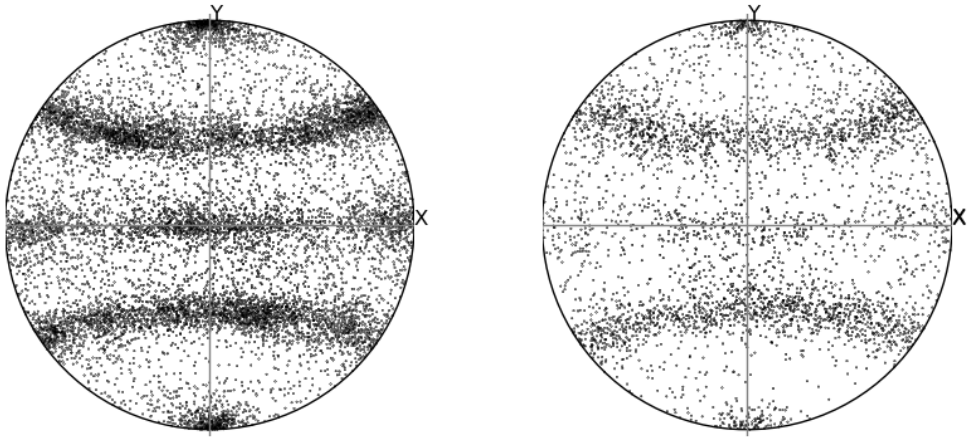
It is evident from the figure that this result (VolFrac) is a reasonably accurate estimate to the dual-phase stress profiles MGB and MGU obtained directly from the simulations. This result suggests that if the single phase responses of an alloy's components are known, the stress response of the alloy may be estimated from the constituents according to their volume fractions. It is noted in passing that this linear mixing is applied to the von Mises stress for the individual phases and not to the 3D stress tensors or to the underlying mechanical properties as is normally done when estimating the mechanical properties of composites. It is interesting that the mixing can be carried out at the von Mises stress level.

Figures 9.15(a) and 9.15(b) show the hcp final textures corresponding to MGhcp and MGU in Figure 9.14 respectively. Similarly Figures 9.16(a) and 9.16(b) show the



(a) hcp (b) hcp+bcc (uniform)

Figure 9.15: (0001) pole figures for the hcp phase showing the simulated final texture after compression to nominal strain of 65%. (a) and (b) correspond to single and dual-phase models respectively. In both cases the initial texture for hcp is that shown in Figure 9.3 (g-i). The final Kearns factors, (f_1, f_2, f_3), for (a) and (b) are (0.309, 0.445, 0.246) and (0.263, 0.355, 0.382) respectively. The initial texture for hcp is that shown in Figure 9.3



(a) bcc (b) hcp+bcc (uniform)

Figure 9.16: (001) pole figures for the bcc phase showing the simulated final texture after compression to nominal strain of 65%. (a) and (b) correspond to single and dual-phase models respectively. In both cases the initial texture for bcc is that shown in Figure 9.4 (g-i).

bcc final textures corresponding to MGbcc and MGU in Figure 9.14 respectively. The single and dual-phase pole figures are almost identical with the difference in intensity resulting from the reduced number of orientations per phase represented in the dual-

phases cases since the overall model size (RVE512) was kept the same in both the single and dual-phase cases.

Figures 9.15 and 9.16 provide contrast to Figure 9.14 because they suggest that unlike the stress-strain profile for which a mixing rule for the two phases is apparent, the texture evolution for each phase in the dual-phase cases appears to proceed independently of the second phase. Hence the dual-phase textures look like those for single phase, irrespective of how the phases are mixed together in the model. In other words, *the effect of the second phase (bcc) on the first (hcp) is to moderate the stress response without significantly affecting its texture development.*

9.9 Discussion and conclusions

Observations from the two extreme ways of assigning phase distribution indicate that the method of mixing the two phases does not have a significant effect on the resulting texture evolution and stress-strain response. Of course, local effects exist as evidenced by the minor differences between the block and uniform phase-assigned results of Section 9.6.1 in Figures 9.5 to 9.8. Such local effects may be important in local studies requiring phase/grain boundary-level resolution, but the results here indicate that such local effects can be ignored with impunity for texture and average stress analysis.

Even in the case of bcc single phase where all slip systems have the same strength and for which the single crystal is orthogonally isotropic, the stress profile can undulate in a similar way to that for hcp phase as a result of crystallographic orientation and its effect in determining the number of slip systems that may activate at a given material point.

Predicted stress-strain response suggests that the dual-phase stress-strain response can be obtained from the responses of the single phases via a simple linear mixing rule

that is consistent with the volume fractions of the individual phases.

Additionally it has been found that the development of texture during uni-axial compression in a dual-phase polycrystal proceeds in the same way as in single phase polycrystals with the texture for each phase evolving as it would in a single phase setting, i.e. independently of the second phase.

Based on the above observations, it may be concluded that the effect of the second phase (bcc) on the first (hcp) is to moderate the stress response without significantly affecting its texture development.

Chapter 10

Conclusions and future work

10.1 Conclusions

This DPhil project is set in the context of single crystal elasticity-plasticity finite element modelling. Its core objective was to develop and implement a methodology for predicting the evolution of texture in single and dual-phase material systems. This core objective has been successfully achieved. Modelling texture evolution entails essentially modelling large deformations accurately and taking account of the deformation mechanisms that cause texture to change. The most important deformation mechanisms are slip and twinning. Slip has been modelled in this project and care has been taken to explore conditions where it is the dominant deformation mechanism for the materials studied. Modelling slip demands that one also models dislocations since slip is assumed to occur by the movement of dislocations. In this project a model for geometrically necessary dislocations has been developed and validated against experimental measurements. A Python program has also been developed for drawing pole figures and calculating Kearns factors.

The thesis contributes to the following areas of micro-mechanics materials research: (i) 3D small deformation crystal plasticity finite element (CPFE) modelling, (ii) geometrically necessary dislocation modelling, (iii) 3D large deformation CPFE modelling, (iv) texture homogenisation methods, (v) single and dual phase texture evolution modelling, (vi) prediction of polycrystal physical properties, (vii) systematic calibration of the power law for slip based on experimental data, and (viii) texture analysis software development (pole figures and Kearns factors).

10.1.1 Geometrically necessary dislocation modelling

The geometric dislocation tensor has been derived in forms suitable for both deformed and undeformed configuration formulations, and reconciled with the various suggestions of its form in the literature. The result, together with Nye's slip-systemwise-discrete tensor, has been implemented in crystal plasticity finite element code to enable determination of GND accumulation on the active and independent a-type basal, prismatic and pyramidal and c+a-type pyramidal slip systems in hcp crystals. The GND density is fully coupled with the crystal slip rule. A model near-α Ti polycrystal under deformation has been analysed using this approach to determine the GND densities developing on the a- and c+a-type slip systems and compared with independent experimental observations. Good agreement is obtained and in particular the experiments support the model prediction that c+a-type slip system GND densities are an order of magnitude lower than those for a-type slip.

10.1.2 GND effects in micro-deformation modelling

A single-crystal nickel alloy sample containing carbide particles of size $\sim$30μm has been subjected to cooling from 870°C to 20°C from a nominally stress-free state thus causing the development of thermal mismatch strains as a result of the differing thermal expansivities of the Ni matrix and the carbide particle. High-resolution EBSD has been employed to determine the resulting elastic strains, lattice rotations and densities of geometrically necessary dislocations (GNDs) close to a particular carbide particle. A representative gradient-enhanced crystal plasticity finite element (CPFE) model has been developed for the same sample and loading conditions, and detailed comparisons of the predicted strains, rotations and GND densities are presented. In addition, the same analysis is carried out in which the GND density is decoupled from the crystal slip rule, and the results obtained also compared with those from the gradient-enhanced model

and with the experimental data. Qualitatively good agreement is achieved between the coupled and decoupled model elastic strains with the EBSD measurements, but lattice rotations and GND densities are quantitatively well-predicted by the coupled crystal model but are less well captured by the decoupled model. In addition, the GND coupling is found to lead to reduced lattice rotations and plastic strains in the region of highest heterogeneity close to the Ni matrix/particle interface, which are in agreement with the experimental measurements. The results presented provide objective evidence of the effectiveness of gradient-enhanced CPFE and demonstrate that GND coupling is required in order to capture strains and lattice rotations in regions of high heterogeneity.

The success of the GND model (which is based on field concepts) and its effectiveness in quantitatively predicting deformation in regions of high heterogeneity provides motivation to also develop a robust field-based model for statistically stored dislocations. This would improve quantitative prediction of deformation variables that are less dependent on GNDs, e.g. deformation away from the regions of high heterogeneity.

10.1.3 Texture homogenisation and evolution modelling

A texture homogenization technique which relies on interpretation of EBSD data in order to allocate orientation frequencies based on representative area fractions has been coupled with a polycrystal plasticity RVE framework allowing for arbitrarily sized RVEs and corresponding allocation of crystallographic orientation. An assessment has been made of the effect of RVE size on representation of initial, measured texture and of post-deformation predicted texture, together with average stress-strain response. Textures have been characterised using both pole figures and Kearns' factors. It has been shown that with really quite crude RVEs, perfectly reasonable qualitative (pole figure) and quantitative (Kearns' factor) texture representations may be obtained.

A stress update algorithm that is fit for simulating any desired strain (e.g. up to

190% true strain simulated in this thesis) together with a methodology for tracking texture development have been developed. Additionally a systematic methodology for calibrating the slip rule, specifically the power law, based on experimental data has been outlined. Hence a robust 3D CPFE code has been developed that is able to achieve the ultimate aim of the thesis: to develop and implement a methodology for predicting the evolution of texture in single and dual-phase material systems.

Good agreement between predictions from the developed CFPE model and EBSD-measurements of single-phase deformation textures has been obtained. Additionally it has been found that for simulations at a specified temperature to very large strains the final texture is largely determined by the loading direction and is independent of the initial texture. However for relatively low straining, the texture observed is dependent on the initial texture, particularly dependent on the misorientation of the c-axes away from the loading direction.

The CPFE model has been extended to enable modelling of multi-phase material systems. Hence a dual-phase (bcc+hcp) Zr alloy material system has been studied to investigate the effect of the second phase (bcc) on the texture development and stress-strain response of the first (hcp). It has been found that the second phase does not have a significant constraining effect on the texture development of the main (hcp) phase, but that it serves to moderate the average stress-strain response of the polycrystal. It appears that this average response may be obtained via a simple linear mixing of the single phase responses of the constituent phases based on their volume fractions.

10.1.4 Texture effects on physical properties

The development of 'type II' thermal strains in hcp polycrystals which result from the anisotropy of their thermal expansivity, which also results from the hcp crystal geometry, has been investigated. It has been shown that the strains may be sufficiently

large in order to cause localized plasticity. A study has been carried out to investigate the resulting effects of crystallographic texture on the thermal expansivities of Zirconium alloy polycrystals, and the corresponding changes which occur to expansivity as a result of the onset of plasticity. An assessment of the Kearns approach and a rigorous crystal elasticity-plasticity methodology for determination of thermal expansivity in Zirconium alloy polycrystals has been carried out. It has been demonstrated that errors in thermal expansivities using the Kearns representation of texture can be sufficiently large making the results obtained of technological significance to the nuclear industry. It has also been confirmed that texture indeed has a significant role in determining the average mechanical properties of a polycrystal: Young's modulus, yield stress and Poisson's ratio.

10.2 Future work

10.2.1 Orientation distribution realisations

The method of orientation assignment used in all the texture development studies in this thesis has been designed to maximise the number of individual orientations represented while maintaining their volume fractions and with the aim to keep computation time low. Hence elements were not pre-grouped into large sets before orientation assignment. Instead the orientation was assigned on an integration point basis. Fundamentally even if orientation is assigned to elements as sets, it will ultimately be used by the finite element code on an integration point basis. The approach adopted in this thesis merely exploits that fact. Consequently the resulting arrangement of orientation groups (shape, size, and spatial arrangement) may not be directly mapped to a measured EBSD-map. The results obtained demonstrate that the developed meshes are sufficient for our purposes. However if we had more time or more powerful computers it would be interesting to see the differences that would result if we were to define grain

shapes exactly as measured (e.g. by 3D EBSD) while representing at least as many orientations and maintaining volume fractions. Software from Simpleware Ltd [58] can be purchased to generate meshes directly from measured data.

10.2.2 Deformation mechanisms

It has been noted throughout the work that modelling the deformation mechanisms that are expected to be in operation is of great importance when modelling texture development. While working with experimental data, care has been taken to keep within temperature regimes where slip was known to be the dominant mechanism. However it would be beneficial to model other mechanisms such as twinning, phase transformations and dynamic recrystallisation in our CPFE code. This would enable us to work with a wider range of temperatures and would give greater insight into the micro-mechanics of the materials considered. There are however still other outstanding research questions that would need to be addressed before benefit from the above can be fully realised. For example a physically based criteria for initiating twinning has not yet been fully defined. With regard to slip, it would be useful to also develop a model for statistically stored dislocations. This could be done as a relatively short project with the already developed GND model as a starting point.

10.2.3 Temperature dependence of physical properties

During thermal cooling studies the single crystal thermal expansivities and elastic mechanical properties were assumed to be constant with temperature. This was because data regarding the temperature dependence of these properties is not readily available and because such detailed study into these properties lies outside the scope of the project. This is however not expected to cause much difference to the conclusions drawn since plasticity results from the anisotropy of the thermal expansivity which also results from the hcp crystal geometry rather than from the absolute value of expansiv-

ities themselves, i.e. the same temperature reduction applied to the same textures but for an isotropic crystal type would not result in any plasticity. In addition, it is noted that the plastic strain for any single crystal/crystallite results from the constraining effect of its neighbours which prevent its free contraction (to maintain compatibility). Consider, for example, thermal contraction of a free hcp crystal along one of its axes, for which thermal expansivity α and Young's modulus E apply, by thermal strain $\alpha\theta$. Any neighbouring crystals preventing this contraction must exert a stress of magnitude $E\alpha\theta$. For cooling, E will increase but α will decrease. Therefore net change to the exerted stress $E\alpha\theta$ due to temperature dependence of E and α is generally minimised. Similarly the temperature dependence of CRSS only delays or speeds up the onset of plasticity. This dependence needs to be significant to change the results significantly. Nevertheless it would be interesting to be able to quantify such changes in future.

Appendix A

Euler angles

A.1 Roe, Bunge and Kocks angles

The table below presents the equivalence of the Bunge and Roe angle notation systems for Euler angles used to describe orientation relationships between crystal axes and external reference axes. The table is taken from Hosford [40], and the third column is from Kocks et al. [49]. The Roe angles θ, ψ, and φ are defined in appendix A.2. The Bunge system uses the angles φ_1, Φ and, φ_2. A third Euler angle nomenclature in common use is the symmetric (Kocks) angles: θ, ψ, and ϕ.

Table A.1: Euler angle notation equivalence

Roe	**Bunge**	**Kocks**
ψ	$\varphi_1 - \pi/2$	ψ
θ	Φ	θ
φ	$\varphi_2 + \pi/2$	$\pi - \phi$
$\psi + \pi/2$	φ_1	$\psi + \pi/2$
θ	Φ	θ
$\varphi - \pi/2$	φ_2	$\pi/2 - \phi$

A.2 Roe's system

The desciption of Roe's system presented here is adapted from Hosford [40]. In Roe's system, the crystallographic axes ([100],[010],[001]) are designate X, Y, Z and the external axes are designated x, y, z. The X, Y, Z axes can be generated from the x, y, z by three rotations, θ, ψ, and φ. Starting with the x, y, z axis system:

First, rotate the x and z axes counterclockwise about y through an angle θ to form a set of axes, x', $y' = y$, and z'; $x \rightarrow x'$, $z \rightarrow z'$.

Second, rotate the x',y', and z' axes counterclockwise about z, note that it is the original z, through an angle ψ to form a set of axes x'', y'', and z''; $x' \rightarrow x''$, $y' \rightarrow y''$,

$z' \rightarrow z'' = Z$.

(Thus $90° - \theta$ and ψ can be considered the north latitude and east longitude of Z on a globe with z being the North Pole and x on the equator at the meridian through Greenwich.)

Third, rotate the x'' and y'' axes counterclockwise about $z'' = Z$ through an angle φ to form the X, Y, Z axes; $x'' \rightarrow X$, $y'' \rightarrow Y$.

(Note that the above describes the rotations that generate the crystal axes starting with the external coordinates rather the reverse.)

The angular relations between the axes are given by the direction cosines in Tables A.2 and A.3. For cubic crystals, given an ideal orientation, $(hkl)[uvw]$, the

Table A.2: Direction cosines between x, y, z and x'', y'', z''

	x''	y''	z''
x	$cos\theta cos\psi$	$-sin\psi$	$sin\theta cos\psi$
y	$cos\theta sin\psi$	$cos\psi$	$sin\theta sin\psi$
z	$-sin\theta$	0	$cos\theta$

Table A.3: Direction cosines between x'', y'', z'' and X, Y, Z

	$X = 1$	$Y = 2$	$Z = 3$
x''	$cos\varphi$	$-sin\varphi$	0
y''	$sin\varphi$	$cos\varphi$	0
z''	0	0	1

Roe angles can be calculated as follows.

$$cos\psi = w(h^2 + k^2 + l^2)^{1/2}/[(u^2 + v^2 + w^2)(h^2 + k^2)]^{1/2}, \qquad h \neq 0, k \neq 0$$

$$cos\theta = \frac{1}{(h^2 + k^2 + l^2)^{1/2}}$$

$$cos\varphi = -h(h^2 + k^2)^{1/2}, \qquad h \neq 0, k \neq 0$$

For the special case in which $h = k = 0$,

$$cos(\psi + \varphi) = u/(u^2 + v^2 + w^2)^{1/2}$$

Alternatively, the ideal orientation can be found from the angles using

$$h = -sin\theta cos\varphi, \qquad k = sin\theta sin\varphi, \qquad l = cos\theta$$

$$u = cos\psi cos\theta cos\varphi - sin\psi sin\varphi$$

$$v = -cos\psi cos\theta sin\varphi - sin\psi cos\varphi$$

$$w = +cos\psi sin\theta$$

Appendix B

Slip systems

B.1 BCC Slip Systems

There are fourty eight possible slip systems for body-centred cubic crystals. Twelve of the {110} family, twelve of {112} and twenty four of {123}. All of them have $< 111 >$ slip directions. This gives maximums of 48 possible edge and 4 screw types.

B.1.1 {110} family

Slip system	Slip plane	Slip Direction	Screw group
1	(110)	$[\bar{1}11]$	s1
2	(110)	$[1\bar{1}1]$	s2
3	$(\bar{1}01)$	[111]	s3
4	$(\bar{1}01)$	$[1\bar{1}1]$	s2
5	$(\bar{1}10)$	[111]	s3
6	$(\bar{1}10)$	$[11\bar{1}]$	s4
7	$(01\bar{1})$	[111]	s3
8	$(01\bar{1})$	$[\bar{1}11]$	s1
9	(011)	$[1\bar{1}1]$	s2
10	(011)	$[11\bar{1}]$	s4
11	(101)	$[\bar{1}11]$	s1
12	(101)	$[11\bar{1}]$	s4

B.1.2 {112} family

Slip system	Slip plane	Slip Direction	Screw group
13	(112)	$[11\bar{1}]$	s4
14	$(\bar{1}12)$	$[1\bar{1}1]$	s2
15	$(1\bar{1}2)$	$[\bar{1}11]$	s1
16	$(11\bar{2})$	[111]	s3
17	(121)	$[1\bar{1}1]$	s2
18	$(\bar{1}21)$	$[11\bar{1}]$	s4
19	$(1\bar{2}1)$	[111]	s3
20	$(12\bar{1})$	$[\bar{1}11]$	s1
21	(211)	$[\bar{1}11]$	s1
22	$(\bar{2}11)$	[111]	s3
23	$(2\bar{1}1)$	$[11\bar{1}]$	s4
24	$(21\bar{1})$	$[1\bar{1}1]$	s2

B.1.3 {123} family

This family is said to be the least important by some authors, i.e. it can be left out without affecting results significantly.

Slip system	Slip plane	Slip Direction	Screw group
25	(123)	$[11\bar{1}]$	s4
26	$(\bar{1}23)$	$[1\bar{1}1]$	s2
27	$(12\bar{3})$	$[\bar{1}11]$	s1
28	(123)	$[111]$	s3
29	(231)	$[1\bar{1}1]$	s2
30	$(\bar{2}31)$	$[11\bar{1}]$	s4
31	$(2\bar{3}1)$	$[111]$	s3
32	$(23\bar{1})$	$[\bar{1}11]$	s1
33	(132)	$[1\bar{1}1]$	s2
34	$(\bar{1}32)$	$[11\bar{1}]$	s4
35	$(1\bar{3}2)$	$[111]$	s3
36	$(13\bar{2})$	$[\bar{1}11]$	s1
37	(213)	$[11\bar{1}]$	s4
38	$(\bar{2}13)$	$[1\bar{1}1]$	s2
39	$(2\bar{1}3)$	$[\bar{1}11]$	s1
40	$(21\bar{3})$	$[111]$	s3
41	(321)	$[\bar{1}11]$	s1
42	$(\bar{3}21)$	$[111]$	s3
43	$(3\bar{2}1)$	$[11\bar{1}]$	s4
44	$(32\bar{1})$	$[1\bar{1}1]$	s2
45	(312)	$[\bar{1}11]$	s1
46	$(\bar{3}12)$	$[111]$	s3
47	$(3\bar{1}2)$	$[11\bar{1}]$	s4
48	$(31\bar{2})$	$[1\bar{1}1]$	s2

B.2 FCC Slip Systems

In FCC, slip happens along $< 110 >$ directions on $\{111\}$ planes. There are twelve slip systems. This gives maximums of 12 possible edge and 6 screw types.

B.3 HCP Slip Systems

HCP crystals have 30 possible slip systems. Three basal systems (a-slip) of the kind $\{0001\} < 11\bar{2}0 >$, three prismatic systems (a-slip) of the kind $\{10\bar{1}0\} < 11\bar{2}0 >$, six pyramidal systems (a-slip) of the kind $\{10\bar{1}1\} < 11\bar{2}0 >$, twelve primary pyramidal

Slip system	Slip plane	Slip Direction	Screw group
1	(111)	$[1\bar{1}0]$	s1
2	(111)	$[01\bar{1}]$	s2
3	(111)	$[10\bar{1}]$	s3
4	$(\bar{1}11)$	$[110]$	s4
5	$(\bar{1}11)$	$[01\bar{1}]$	s2
6	$(\bar{1}11)$	$[101]$	s5
7	$(1\bar{1}1)$	$[110]$	s4
8	$(1\bar{1}1)$	$[011]$	s6
9	$(1\bar{1}1)$	$[10\bar{1}]$	s3
10	$(11\bar{1})$	$[1\bar{1}0]$	s1
11	$(11\bar{1})$	$[011]$	s6
12	$(11\bar{1})$	$[101]$	s5

systems (c+a-slip) of the kind $\{10\bar{1}1\} < 11\bar{2}3 >$, and six secondary pyramidal systems (c+a-slip) of the kind $\{11\bar{2}2\} < 11\bar{2}3 >$ [38]. Only six of the kind $\{10\bar{1}1\} < 11\bar{2}3 >$ are given in the table below, which includes only the 24 systems used in this report. This gives maximums of 24 edge and 9 screw dislocations.

Slip system	Slip plane	Slip Direction	Screw group
1	(0001)	$[\bar{1}\bar{1}20]$	s1
2	(0001)	$[\bar{1}2\bar{1}0]$	s2
3	(0001)	$[\bar{2}110]$	s3
4	$(\bar{1}100)$	$[\bar{1}\bar{1}20]$	s1
5	$(10\bar{1}0)$	$[\bar{1}2\bar{1}0]$	s2
6	$(0\bar{1}10)$	$[\bar{2}110]$	s3
7	$(\bar{1}101)$	$[\bar{1}\bar{1}20]$	s1
8	$(10\bar{1}1)$	$[\bar{1}2\bar{1}0]$	s2
9	$(0\bar{1}11)$	$[\bar{2}110]$	s3
10	$(1\bar{1}01)$	$[\bar{1}\bar{1}20]$	s1
11	$(\bar{1}011)$	$[\bar{1}2\bar{1}0]$	s2
12	$(01\bar{1}1)$	$[\bar{2}110]$	s3
13	$(\bar{1}101)$	$[1\bar{2}13]$	s4
14	$(10\bar{1}1)$	$[\bar{2}113]$	s5
15	$(0\bar{1}11)$	$[11\bar{2}3]$	s6
16	$(1\bar{1}01)$	$[\bar{1}2\bar{1}3]$	s7
17	$(\bar{1}011)$	$[11\bar{2}3]$	s8
18	$(01\bar{1}1)$	$[\bar{2}113]$	s9
19	$(\bar{1}2\bar{1}2)$	$[1\bar{2}13]$	s4
20	$(2\bar{1}\bar{1}2)$	$[\bar{2}113]$	s5
21	$(1\bar{1}22)$	$[11\bar{2}3]$	s6
22	$(1\bar{2}12)$	$[\bar{1}2\bar{1}3]$	s7
23	$(\bar{1}122)$	$[11\bar{2}3]$	s8
24	$(2\bar{1}\bar{1}2)$	$[\bar{2}113]$	s9

References

[1] A. Acharya and J. L. Bassani. Lattice incompatibility and a gradient theory of crystal plasticity. *Journal of the Mechanics and Physics of Solids*, 48:1565–1595, 2000.

[2] Amit Acharya. A counterpoint to Cermelli and Gurtin's criteria for choosing the 'correct' geometric dislocation tensor in finite plasticity. *Proceedings of the IUTAM Symposium, South Africa*, 11:99–105, 2008.

[3] A. Anderson, R. Thompson, and C. Cook. Ultrasonic measurement of the kearns texture factors in zircaloy, zirconium, and titanium. *Metallurgical and Materials Transactions A*, 30:1981–1988, 1999.

[4] A. Arsenlis and D. M. Parks. Crystallographic aspects of geometrically-necessary and statistically-stored dislocation density. *Acta Metallurgica et Materialia*, 47: 1597–1611, 1999.

[5] M. F. Ashby. The deformation of plastically non-homogeneous materials. *Philosophical Magazine*, 21(170):399–424, 1970.

[6] M. R. Bache and F. P. E. Dunne. Experimental and crystal plasticity studies of deformation and crack nucleation in a titanium alloy. *Journal of strain analysis*, 45:391–399, 2010.

[7] P. S. Bate and J. Quinta da Fonseca. Texture development in the cold rolling of IF steel. *Material Science and Engineering A*, 380:365–377, 2004.

[8] Klaus-J"urgen Bathe. *Finite element procedures in engineering analysis*. Prentice-Hall International, London, 1982.

[9] A. J. Beaudoin and O. Engler. Deformation Processing: Texture Evolution. *Encyclopedia of Materials - Science and Technology*, 1-11:2014–2022, 2001.

[10] H. K. D. H. Bhadeshia. *Worked examples in the Geometry of Crystals*. The Institute of Metals, London, 2001.

[11] Susan Blackford. Linear Least Squares (LLS) Problems. http://www.netlib.org/lapack/lug/node27.html, 1999.

[12] T. B. Britton, H. Liang, F. P. E. Dunne, and A. J. Wilkinson. The effect of crystal orientation on the indentation response of commercially pure titanium: experiments and simulations. *Proc. R. Soc.*, 466:695–719, 2010.

[13] T. Ben Britton, Soran Birosca, Michael Preuss, and Angus J. Wilkinson. Electron backscatter diffraction study of dislocation content of a macrozone in hot-rolled ti-6al-4v alloy. *Scripta Materialia*, 62(9):639 – 642, 2010.

[14] E. P. Busso, F. T. Meissonnier, and N. P. O'Dowd. Gradient-dependent deformation of two-phase single crystals. *Journal of the mechanics and physics of solids*, 48:2333–2361, 2000.

[15] S. Cai, M.R. Daymond, R.A. Holt, M.A. Gharghouri, and E.C. Oliver. Evolution of interphase and intergranular stresses in zr2.5nb during room temperature deformation. *Materials Science and Engineering: A*, 501(12):166 – 181, 2009.

[16] Paolo Cermelli and Morton E. Gurtin. On the characterization of geometrically necessary dislocations in finite plasticity. *Journal of the Mechanics and Physics of Solids*, 49:1539–1568, 2001.

[17] K. S. Cheong, E. P. Busso, and A. Arsenlis. A study of microstructural length scale effects on the behaviour of fcc polycrystals using strain gradient concepts. *International Journal of Plasticity*, 21:1797–1814, 2005.

[18] Ke-Shen Cheong and Esteban P. Busso. Effects of lattice misorientations on strain heterogeneities in fcc polycrystals. *Journal of the Mechanics and Physics of Solids*, 54(4):671 – 689, 2006. doi:10.1016/j.jmps.2005.11.003.

[19] P. C. Chou and N. J. Pagano. *Elasticity: Tensor, Dyadic, and Engineering Approaches*. Dover Publications, New York, 1992.

[20] M. A. Crisfield. *Non-linear Finite Element Analysis of Solids and Structures*, volume 2: Advanced Topics. John Wiley & Sons, England, 2001.

[21] Erik B. Dam, Martin Koch, and Martin Lillholm. Quaternions, interpolation and animation. Technical report, University of Copenhagen, Denmark, 1998.

[22] V. T. Deshpande and Ramrao Pawar. X-ray determination of the thermal expansion of tungsten. *Current Science*, 31(12):497–499, Dec 1962.

[23] V. T. Deshpande and S. V. Suryanarayana. Thermal expansion of strontium molybdate. *Acta Crystallographica Section A*, 28(1):94–95, Jan 1972.

[24] University of Cambridge DoITPoMS. Shape changes arising from dislocation glide and deformation twinning (a shear transformation). http://www.doitpoms.ac.uk/ldplib/shape_memory/background.php. Accessed: 24 May 2013.

[25] F. P. E. Dunne and D. Rugg. On the mechanisms of fatigue facet nucleation in titanium alloys. *Fatigue & Fracture of Engineering Materials & Structures*, 31: 949–958, 2008.

[26] F. P. E. Dunne, D. Rugg, and A. Walker. Lengthscale-dependent, elastically anisotropic, physically-based hcp crystal plasticity: Application to cold-dwell fatigue in Ti alloys. *International Journal of Plasticity*, 23:1061–1083, 2007.

[27] F. P. E. Dunne, A. Walker, and D. Rugg. A systematic study of hcp crystal orientation and morphology effects in polycrystal deformation and fatigue. *Proceedings of the Royal Society A*, 463:1467–1489, 2007.

[28] F. P. E. Dunne, R. Kiwanuka, and A. J. Wilkinson. Crystal plasticity analysis of micro-deformation, lattice rotation and geometrically necessary dislocation density. *Proceedings of the Royal Society A: Mathematical, Physical and Engineering Science*, 468:2509–2531, 2012. doi:10.1098/rspa.2012.0050.

[29] F.P.E. Dunne, A.J. Wilkinson, and R. Allen. Experimental and computational studies of low cycle fatigue crack nucleation in a polycrystal. *International Journal of Plasticity*, 23(2):273 – 295, 2007.

[30] Philip Eisenlohr and Franz Roters. Selecting a set of discrete orientations for accurate texture reconstruction. *Computational Materials Science*, 42(4):670 – 678, 2008.

[31] N. A. Fleck, G. M. Muller, M. F. Ashby, and J. W. Hutchinson. Strain gradient plasticity: theory and experiment. *Acta Metallurgica et Materialia*, 42:475–487, 1994.

[32] N.A. Fleck, M.F. Ashby, and J.W. Hutchinson. The role of geometrically necessary dislocations in giving material strengthening. *Scripta Materialia*, 48:179–183, 2003.

[33] G. B. Gibbs. Thermodynamic analysis of dislocation glide controlled by dispersed local obstacles. *Materials Science and Engineering*, 4:313–328, 1969.

[34] Jicheng Gong and Angus J. Wilkinson. Anisotropy in the plastic flow properties of single-crystal α titanium determined from micro-cantilever beams. *Acta Materialia*, 57(19):5693 – 5705, 2009.

[35] J.A. Gruber, S.A. Brown, and G.A. Lucadamo. Generalized kearns texture factors and orientation texture measurement. *Journal of Nuclear Materials*, 408(2):176 – 182, 2011.

[36] C-S Han, A Ma, F Roters, and D Raabe. A finite element approach with patch projection for strain gradient plasticity formulations. *International Journal of Plasticity*, 23:690–710, 2007.

[37] N. Hansen. Plastic Behaviour of Metals: Large Strains. *Encyclopedia of Materials - Science and Technology*, Volumes 1-11:7040–7050, 2001.

[38] Vikas Hasija, S. Ghosh, Michael J. Mills, and Deepu S. Joseph. Deformation and creep modeling in polycrystalline Ti–6Al alloys. *Acta Materialia*, 51:4533–4549, 2003.

[39] E.A. Holm, G.N. Hassold, and M.A. Miodownik. On misorientation distribution evolution during anisotropic grain growth. *Acta Materialia*, 49(15):2981 – 2991, 2001.

[40] William F. Hosford. *The Mechanics of Crystals and Textured Polycrystals*. Oxford University Press, Oxford, 1993.

[41] D. Hull and D. J. Bacon. *Introduction to dislocations*. Butterworth Heinemann, Oxford, 2001. ISBN 0750646810,9780750646819.

[42] M. Humbert, N. Gey, J. Muller, and C. Esling. Determination of a mean orientation from a cloud of orientations. application to electron back-scattering pattern measurements. *Journal of Applied Crystallography*, 29(6):662–666, 1996.

[43] S. R. Kalidindi, C. A. Bronkhorst, and L. Anand. Crystallographic texture evolution in bulk deformation processing of fcc metals. *Journal of the Mechanics and Physics of Solids*, 40:537–569, 1992.

[44] Surya R. Kalidindi, Abhishek Bhattacharyya, and Roger D. Doherty. Detailed analyses of grain-scale plastic deformation in columnar polycrystalline aluminium using orientation image mapping and crystal plasticity models. *Royal Society of London Proceedings Series A*, 460(2047), 2004.

[45] Phani S. Karamched and Angus J. Wilkinson. High resolution electron backscatter diffraction analysis of thermally and mechanically induced strains near carbide inclusions in a superalloy. *Acta Materialia*, 59(1):263 – 272, 2011.

[46] M.E Kassner. Taylor hardening in five-power-law creep of metals and class m alloys. *Acta Materialia*, 52(1):1 – 9, 2004.

[47] J. J. Kearns. On the relationship among 'f' texture factors for the principal planes of zirconium, hafnium and titanium alloys. *Journal of Nuclear Materials*, 299(2): 171 – 174, 2001.

[48] A. Kelly and G. W. Groves. *Crystallography and Crystal defects*. Longman Group Limited, London, 1970.

[49] U. F. Kocks, C. N. Tome, and H. R. Wenk. *Texture and Anisotropy. Preferred Orientations in Polycrystals and their Effect on Materials Properties*. Cambridge University Press, Cambridge, UK, 1998.

[50] A. M. Korsunsky, D. Dini, F. P. E. Dunne, and M. J. Walsh. Comparative assessment of dissipated energy and other fatigue criteria. *International journal of fatigue*, 29(9-11):1990 – 1995, 2007.

[51] E. Kroner. Allgemeine kontinuumstheorie der versetzungen und eigenspannungen. *Archive for Rational Mechanics and Analysis*, 4:273 – 334, 1960.

[52] J.W. Kysar, Y. Saito, M.S. Oztop, D. Lee, and W.T. Huh. Experimental lower bounds on geometrically necessary dislocation density. *International Journal of Plasticity*, 26(8):1097 – 1123, 2010.

[53] E. H. Lee. Elastic plastic deformation at finite strain. *ASME Journal of Applied Mechanics*, 36:1 – 6, 1969.

[54] Saiyi Li, Paul Van Houtte, and Surya R Kalidindi. A quantitative evaluation of the deformation texture predictions for aluminium alloys from crystal plasticity finite element method. *Modelling and Simulation in Materials Science and Engineering*, 12(5):845, 2004.

[55] Yan Li and R. Bruce Thompson. Relations between elastic constants c_{ij} and texture parameters for hexagonal materials. *Journal of Applied Physics*, 67(5): 2663 – 2665, 1990.

[56] Hong Liang. *Crystal Plasticity Modelling of Lengthscale Effects in Deformation and Nano-Indentation*. PhD thesis, University of Oxford, UK, 2008.

[57] B Liu, D Raabe, F Roters, P Eisenlohr, and R A Lebensohn. Comparison of finite element and fast fourier transform crystal plasticity solvers for texture prediction. *Modelling and Simulation in Materials Science and Engineering*, 18(8):085005, 2010.

[58] Simpleware Ltd. The fast, easy and robust way to convert 3d images into models. http://www.simpleware.co.uk/. Accessed: December 2012.

[59] Lawrence E. Malvern. *Introduction to the mechanics of a continuous medium*. Prentice-Hall, Englewood Cliffs, N.J., 1969. ISBN 0134876032.

[60] T. Mayama, T. Ohashi, and R. Kondou. Geometrically necessary dislocation structure organization in fcc bicrystal subjected to cyclic plasticity. *International Journal of Plasticity*, 25(11):2122 – 2140, 2009.

[61] D. L. McDowell and F. P. E. Dunne. Microstructure sensitive computational modelling of fatigue crack formation. *International Journal of Fatigue*, 32(9): 1521–1542, 2010.

[62] F. T. Meissonnier, E. P. Busso, and N. P. O'Dowd. Finite element implementation of a generalised non-local rate-dependent crystallographic formulation for finite strains. *International Journal of Plasticity*, 17:601–640, 2001.

[63] Maxime A. Melchior and Laurent Delannay. A texture discretization technique adapted to polycrystalline aggregates with non-uniform grain size. *Computational Materials Science*, 37(4):557 – 564, 2006.

[64] Edward M. Mielnik. *Metalworking science and engineering*. McGraw-Hill, 1991.

[65] A. Molinari. Mechanics-based Crystal Plasticity. *Encyclopedia of Materials - Science and Technology*, Volumes 1-11:5311–5320, 2001.

[66] J.F. Nye. Some geometrical relations in dislocated crystals. *Acta Metallurgica*, 1: 153–162, 1953.

[67] Dierk Raabe and Franz Roters. Using texture components in crystal plasticity finite element simulations. *International Journal of Plasticity*, 20:339–361, 2004.

[68] Valerie Randle and Olaf Engler. *Introduction to Texture Analysis*. Taylor & Francis Ltd CRC Press Inc, second edition, 2009.

[69] F. Roters, P. Eisenlohr, L. Hantcherli, D.D. Tjahjanto, T.R. Bieler, and D. Raabe. Overview of constitutive laws, kinematics, homogenization and multiscale methods in crystal plasticity finite-element modeling: Theory, experiments, applications. *Acta Materialia*, 58(4):1152 – 1211, 2010. doi:10.1016/j.actamat.2009.10.058.

[70] D. Rugg, M. Dixon, and F. P. E. Dunne. Effective structural unit size in titanium alloys. *Journal of Strain Analysis*, 2007.

[71] D Rugg, D Furrer, and N Brewitt. Texture in titanium – an industrial perspective on deformation, transformation and properties. *Materials Processing and Texture, Ceramic Transactions, Volume 200, A Collection of Papers Presented at the 15th International Conference on Textures of Materials (ICOTOM 15) June 1-6, 2008 Pittsburgh, Pennsylvania Edited by A. D. Rollett.*, 2008.

[72] M. A. Rust and R. I. Todd. High resolution surface studies of superplastic deformation in shear and tension. *Materialwissenschaft und Werkstofftechnik*, 39(4-5): 289–292, 2008.

[73] S. Sun, B. L. Adams, and W. E. King. Observations of lattice curvature near the interface of a deformed aluminium bicrystal. *Philosophical magazine A*, 80:9–25, 2000.

[74] P.A. Tempest. Preferred orientation and its effect on bulk physical properties of hexagonal polycrystalline materials. *Journal of Nuclear Materials*, 92(2-3):191 – 200, 1980.

[75] D D Tjahjanto, P Eisenlohr, and F Roters. A novel grain cluster-based homogenization scheme. *Modelling and Simulation in Materials Science and Engineering*, 18(1):015006, 2010.

[76] P. Van Houtte, L. Delannay, and S. R. Kalidindi. Comparison of two grain interaction models for polycrystal plasticity and deformation texture prediction. *International Journal of Plasticity*, 18:359–377, 2002.

[77] L. Wang, Y. Yang, P. Eisenlohr, T.R. Bieler, M.A. Crimp, and D.E. Mason. Twin nucleation by slip transfer across grain boundaries in commercial purity titanium. *Metallurgical and Materials Transactions A*, 41:421–430, 2010. 10.1007/s11661-009-0097-6.

[78] L. Wang, R.I. Barabash, Y. Yang, T.R. Bieler, M.A. Crimp, P. Eisenlohr, W. Liu, and G.E. Ice. Experimental characterization and crystal plasticity modeling of heterogeneous deformation in polycrystalline α-ti. *Metallurgical and Materials Transactions A*, 42(3):626–635, 2011.

[79] Wikipedia. Euler angles.

[80] Wikipedia. Candu reactor. http://en.wikipedia.org/w/index.php?oldid=500660167, 2012. Accessed: 09 July 2012.

[81] A. J. Wilkinson and D. Randman. Determination of elastic strain fields and geometrically necessary dislocation distributions near nanoindents using electron back scatter diffraction. *Philosophical Magazine*, 90(9):1159–1177, 2010. doi:10.1080/14786430903304145.

[82] A. J. Wilkinson, E. E. Clarke, T. B. Britton, P. Littlewood, and P. S. Karamched. High-resolution electron backscatter diffraction: an emerging tool for studying local deformation. *Journal of Strain Analysis for Engineering Design*, 45(5):365 – 376, 2010.

[83] Angus J. Wilkinson, Graham Meaden, and David J. Dingley. High-resolution elastic strain measurement from electron backscatter diffraction patterns: New levels of sensitivity. *Ultramicroscopy*, 106(45):307 – 313, 2006.

[84] Angus J. Wilkinson, Benjamin Britton, and Philip Littlewood. Research group communication, University of Oxford, 2009.

[85] J. R. Willis. Second-order effects of dislocations in anisotropic crystals. *International Journal of Engineering Science*, 5:171–190, 1967.

[86] Y. Yang, L. Wang, T. Bieler, P. Eisenlohr, and M. Crimp. Quantitative atomic force microscopy characterization and crystal plasticity finite element modeling of heterogeneous deformation in commercial purity titanium. *Metallurgical and Materials Transactions A*, 42:636–644, 2011.

[87] L. G. Zhao, E. P. Busso, and N. P. O'Dowd. Computational modelling of crack initiation in a single crystal superalloy under fatigue-oxidation conditions. *Materials Science and Technology*, 23(12):1433–1438, 2007.

[88] Z. Zhao, M. Ramesh, D. Raabe, A.M. Cuitio, and R. Radovitzky. Investigation of three-dimensional aspects of grain-scale plastic surface deformation of an aluminum oligocrystal. *International Journal of Plasticity*, 24(12):2278 – 2297, 2008.

[89] O. C. Zienkiewicz. *The Finite Element Method in Engineering Science*. McGraw-Hill, London, UK, second edition, 1977.

[90] O. C. Zienkiewicz and R. L. Taylor. *The Finite Element Method for Solid and Structural Mechanics*. Elsevier Butterworth-Heinemann, Oxford, UK, six edition, 2005.